Cost-Effective Spectrally-Efficient Optical Transceiver Architectures for Metropolitan and Regional Links

Mustafa Sezer ERKILINÇ

A thesis submitted to the University College London (UCL) for the degree of Doctor of Philosophy

Optical Networks Group
Department of Electronic and Electrical Engineering
University College London (UCL)

December 2015

I, Mustafa Sezer Erkılınç, confirm that the work presented in this thesis is my own. Where information has been derived from other sources, I confirm that this has been indicated.

To my mother, ***Şengül Ergünü***, the strongest woman that I know,
for her immense support in every aspect of my life.

To my father, ***Gürsel Erkılınç***,
for broadening my vision and keep whispering to me to become an international person.

To my grandparents, ***Huriye & Mustafa Ergünü***,
for their love and sacrifice.

Abstract

The work presented herein explores cost-effective optical transceiver architectures for access, metropolitan and regional links. The primary requirement in such links is cost-effectiveness and secondly, spectral efficiency. The bandwidth/data demand is driven by data-intensive Internet applications, such as cloud-based services and video-on-demand, and is rapidly increasing in access and metro links. Therefore, cost-effective optical transceiver architectures offering high information spectral densities (ISDs $>$ 1 (b/s)/Hz) need to be implemented over metropolitan distances. Then, a key question for each link length and application is whether coherent- or direct (non-coherent) detection technology offers the best cost and performance trade-off. The performance and complexity limits of both technologies have been studied.

Single polarization direct detection transceivers have been reviewed, focusing on their achievable ISDs and reach. It is concluded that subcarrier modulation (SCM) technique combined with single sideband (SSB) and high-order quadrature amplitude modulation (QAM) signaling, enabled by digital signal processing (DSP) based optical transceivers, must be implemented in order to exceed an ISD of 1 (b/s)/Hz in direct-detection links. The complexity can be shifted from the optical to the electrical domain using such transceivers, and hence, the cost can be minimized.

In this regard, a detailed performance comparison of two spectrally-efficient direct detection SCM techniques, namely Nyquist-SCM and OFDM, is presented by means of simulations. It is found out that Nyquist-SCM format offers the transmission distances more than double that of OFDM due to its higher resilience to signal-signal beating interference. Following this, dispersion-precompensated SSB 4- and 16-QAM Nyquist-SCM signal formats were experimentally demonstrated using in-phase and quadrature (IQ)-modulators at net optical ISDs of 1.2 and 2 (b/s)/Hz over 800 km and 323 km of standard single-mode fibre (SSMF), respectively. These demonstrations represent record net optical ISDs over such distances among the reported single polarization wavelength division multiplexed (WDM) systems.

Furthermore, since the cost-effectiveness is crucial, the optical complexity of Nyquist-SCM transmitters can be significantly reduced by using low-cost modulators and high-linewidth lasers. A comprehensive theoretical study on SSB signal generation using IQ- and dual-drive Mach-Zehnder modulators (DD-MZMs) was carried out to assess their performance for WDM direct detection links. This was followed by an experimental demonstration of WDM transmission over 242 km of SSMF with a net optical ISD of 1.5 (b/s)/Hz, the highest achieved ISD using a DD-MZM-based transmitter.

Following the assessment of direct detection technology using various transmitter designs, cost-effective simplified coherent receiver architectures for access and metro networks have been investigated. The optical complexity of the conventional (polarization- and phase-diverse) coherent receiver is significantly simplified, *i.e.*, consisting of a single 3dB coupler and balanced photodetector, utilizing heterodyne reception and Alamouti polarization-time block coding. Although the achievable net optical ISD is halved compared to a conventional coherent receiver due to Alamouti coding, its receiver sensitivity provides significant gain over a direct detection receiver at M-ary QAM formats where $M \geq 16$.

Acknowledgements

First and foremost, with my utmost sincerity, I wish to thank Dr. Robert Killey for his faith in my ability, giving me the opportunity to follow my passion and pursue a Ph.D. degree in fibre-optic communication in Optical Networks Group (ONG) at University College London (UCL). His continuous guidance, assistance and patience were the key elements during my Ph.D. study. I could not have imagined having a better supervisor and mentor for myself. I would also like to express my gratitude to my second supervisor, Prof. Polina Bayvel. Her demanding attitude and encouragement, asking for my best all the time, taught me many lessons. Her support, especially in my last year of PhD, was tremendous, and therefore, I am deeply thankful to her. Without my supervisors' support, none of this work would have been possible. It has been a pleasure and an honor being your Ph.D. student.

Besides my supervisors, my sincere thanks go to Dr. Benn C. Thomsen for his great generosity with his time to explain numerous topics. His expertise and assistance helped me to improve my problem solving and lab skills remarkably. I feel very fortunate to learn from a 'teacher' like him who is thirsty for teaching all the time. I would also like to thank Dr. Seb J. Savory for giving me a chance to work in coherent communication systems under his supervision, and sharing his valuable ideas and suggestions.

I would like to express and show my deep appreciation to my colleagues, Dr. Robert Maher, Dr. Domaniç Lavery, Dr. Rachid Bouziane, Dr. Kai Shi, Sean Kilmurray, and Zhe Li. They have been extremely patient and positive with me while offering their valuable time, experiences and knowledge. It was a 'pure joy' working with them. I am also thankful all the members of ONG group for their kindness and friendship.

I would like to acknowledge the funding provided by the European Commission's Framework Programme 7 and PIANO+ IMPACT, and thank Dr. Stephan Pachnicke, Dr. Helmut Griesser, and Dr. Jöerg-Peter Elbers from ADVA Optical Networking SE for their stimulating discussions, feedback and support throughout my Ph.D. study.

I could not finish thanking to my girlfriend, Lucrezia Morvilli, and my dearest friends in London, Jan Frederick Rohweder, Andrea Patrick Buchenau, Kai Shi, Ömer Önal, Kareem Sheik Al Sagha, Yazan Hamadeh, and Arturs Tiesnesis. They have been always with me on this journey, and hence, my experience in London has been nothing short of amazing and unforgettable.

Lastly, I feel blessed to have my mother who have loved, cared and supported me all the way, and thus, my PhD thesis is firstly dedicated to her.

Mustafa Sezer Erkılınç

Contents

List of Figures

List of Tables

Chapter 1

Introduction

Optical fibre became the transmission medium of choice instead of copper in long-haul telecommunication networks due to its potential for enabling high capacity and cost-effective transmission [1]. During the 1980s, the first generation fibre-optic communication systems, also referred to as lightwave systems, became commercially available by the telephone companies, operating at wavelengths around 0.8 μm at a bit rate of 45 Mb/s and with a re-generator spacing of up to 10 km. Towards the end of the decade, in the second generation systems, the data rates were increased to 2 Gb/s, using a repeater spacing of 50 km and standard single mode fibre (SSMF), operating at 1.3 μm [2]. The fibre loss at this wavelength (typically 0.5 dB/km) was the main limitation for the repeater spacing. The loss of the silica fibre was reduced to 0.2 dB/km at wavelengths near 1.55 μm. Consequently, the lightwave systems operating at 1.55 μm and a bit rate of up to 2.5 Gb/s, termed as third generation, using dispersion shifted fibre (DSF) became commercially available in 1990 [1]. From the 1970s to the 1990s, although the lightwave device technology developed at a high rate resulting in components such as powerful lasers, faster modulators and photodetectors, *etc.*, the data rate in lightwave systems did not increase at the same rate until the introduction of optical amplifiers. From the mid 1990s, to meet the increasing demand, lightwave systems were revolutionized by the invention of optical amplification, in particular the Erbium-doped fibre amplifier (EDFA). These fourth generation systems made use of wavelength division multiplexing (WDM), filling up the available optical bandwidth with data channels in order to increase system capacity, and were able to meet the demands economically [1].

Moreover, the use of digital signal processing (DSP), thanks to innovations in digital/wireless communication, and forward error correction (FEC) were the most important factors in increasing the system capacity after 2000 [3]. At this point, optical communication started to shift from physics to communication engineering in order to use the optical bandwidth (typically, the conventional (C) band (1530-1565 nm) and long (L) band (1565-1625 nm) more efficiently, *i.e.,* to transmit more information (bits-per-second) within a certain bandwidth (Hz) which is defined as information spectral density (ISD). Optical communication researchers started to investigate the modulation techniques inherited from digital/wireless communication using directly detected optical signals operating at 10, 40 and 100 Gb/s. Overall, total capacity of commercial lightwave systems increased from approximately 1 Gb/s in the mid-1980s to roughly 1 Tb/s by 2000 [4].

The main motivation behind all these series of developments and innovations is both the commercial and consumer demand for high data rate communications, especially after the development of the Internet (email and World Wide Web) in the 1990s. The growth in Internet protocol (IP) data traffic is estimated to

be exponential [3]. The trend in global Internet traffic between 2000 and 2020 is shown in Fig. 1.1. More specifically, global IP traffic has increased more than fourfold between 2008 and 2012, and is expected to increase threefold over the next five years at a compound annual growth rate (CAGR) of 23 percent. Furthermore, the forecasts of communication technology developers indicate that annual global IP traffic will grow to 1.1 zettabyte per year (1 zettabyte = 1000 exabytes = 10^{21} bytes) by 2016 and reach 2.0 zettabyte by 2019 [5]. The biggest contribution to IP traffic is made by video-on-demand applications such as NetFlix, YouTube and Skype, continuously increasing with mobile data usage. It is predicted that the Internet video traffic will contribute to 70% of the entire Internet data traffic by 2019, which was 57% in 2014 [5]. Thus, the throughput of the lightwave systems offered by the communication technology providers must be increased. The next section presents a brief overview about a typical optical telecommunication network structure.

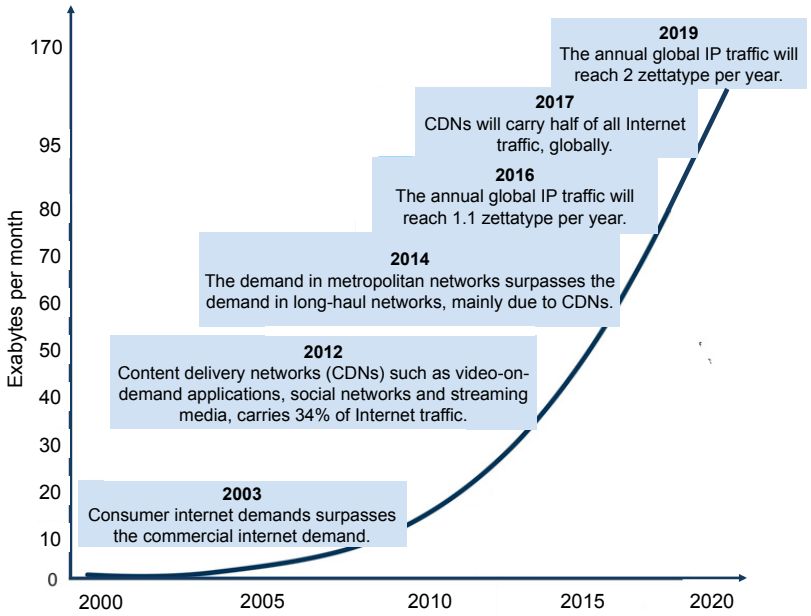

Fig. 1.1: The trend in Internet (IP and mobile) traffic [5].

1.1 Brief overview: Optical telecommunication network structure

The structure of an optical telecommunication network is depicted in Fig. 1.2. It is worth noting that a public fibre-optic network in a real scenario is more complex than depicted because there are different service providers operating at different parts of the network. The central offices (telephone exchanges) behave as the node of a network. The links between the nodes can be a single fibre or bundle of fibres, deployed in ducts underground. Typically, an optical network can be classified within the three different network types, namely a long-haul (sometimes called core), a metropolitan (metro or regional) or an access network, as illustrated in Fig. 1.2. Each network has different technical and operational requirements, such as transmission distance (reach), capacity, cost, dispersion tolerance or footprint.

Long-haul links/networks interconnect different continents and regions, covering transoceanic distances ($\geq$800 km). Achieving high transmission distance and high ISD (throughput divided by the bandwidth - bits/s/Hz) are the most important requirements in such links. To meet the rapidly increasing data and bandwidth demands in long-haul optical networks, the system capacity has been already upgraded from a bit rate of 10 Gb/s to 40 Gb/s and 100 Gb/s by the use of multi-level phase and amplitude

modulation techniques such as quadrature phase-shift keying (QPSK) or 16-quadrature amplitude modulation (QAM) combined with polarization- and phase- coherent receivers [6]. This is due to the fact that coherent detection gives the ability to recover the full optical field, the amplitude, phase and state of polarization (SoP). Consequently, this allows high spectral efficiency and gives the capability to mitigate transmission impairments by utilizing advanced DSP techniques, implemented using high-speed silicon complementary metal oxide semiconductor (CMOS) digital circuits [7]. Therefore, currently, polarization- and phase-diverse coherent receivers have become the standard in long-haul communication links.

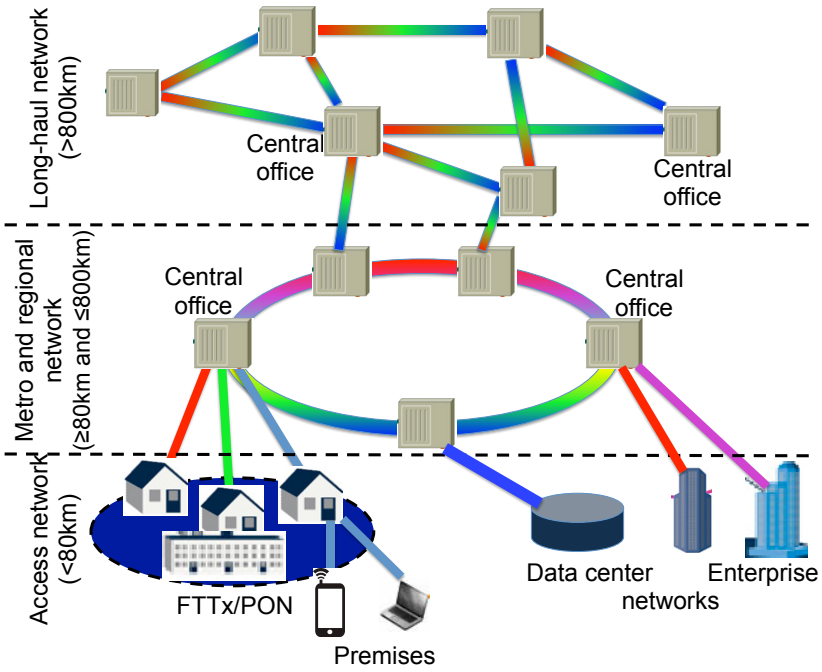

Fig. 1.2: Overview of a typical optical telecommunication network structure.

A metro link/network interconnects the central offices in a large city or connects the cities in a region (metro-core). It typically spans from 80-100 km to 500-800 km. The total volume of metro traffic worldwide surpassed long-haul traffic in 2014, and is predicted to comprise 62% of total IP traffic by 2019 since it is growing almost two times faster than long-haul traffic from 2014 to 2019 (Table 7 in [5]). This is due in part to the important role of content delivery networks (34% in 2014 and 62% by 2019) which constitute a large portion of the Internet content today, including web and downloadable objects, streaming media, and social networks [5]. Therefore, metro links/networks are becoming increasingly essential for communication technology.

An access link/network is the "last mile" of an optical network that connects a node in a metro network to the subscriber premises, such as data-centers, large enterprises or campuses, or individual users of a telecom service provider, referred to as Fibre to the Node, Curb, Building or Home (FTTx). In other words, the metro network carries the data traffic to the customers' premises via access nodes. The links in an access network are typically a few tens of kilometers. These nodes are connected to each other with different topologies, depending on the individual network design considerations. There are several network topologies, as discussed in [8].

The primary requirement for short and medium reach links is cost-effectiveness. Therefore, direct detection receivers may be an attractive solutions for such optical links, *e.g.,* data centers and interconnect

applications, typically up to 10 km, and medium reach optical links, *e.g.,* access and wireless back-haul links as well as metro and regional distances. Typical transmission distances of different types of WDM optical links are listed in Table 1.1 [9]. The cost and footprint could be significantly reduced by the use of a direct detection receiver due to the lower number of optical components required. In such a receiver, there is no need for a polarization beam splitter (PBS), 90^o optical hybrids and local oscillator (LO) laser. It also relaxes the laser linewidth requirements, and lowers the DSP complexity at the receiver. The following section briefly discusses the system considerations for the three types of optical links described above, and presents the question investigated in this thesis.

Tab. 1.1: Classification of WDM systems based on the transmission distances.

Class	System	Distance (km)
Ultra Short-haul	Interconnects	$<$ 10 km
Short-haul	Data centers	$<$ 40 km
Short-/Medium-haul	Access	$<$ 80 km
Medium-haul	Metro & Back-haul	100 - 300 km
Medium-haul	Regional	300 - 800 km
Long-haul	Terrestrial	800 - 3000 km
Ultra long-haul	Submarine & Transoceanic	$>$ 3000 km

1.2 Thesis problem

ISD versus reach for a variety of optical communication links are plotted in Fig. 1.3. Since coherent detection with polarization multiplexing using polarization- and phase-diverse coherent receivers enable the highest achieved bit rates ($\geq$100 Gb/s per channel) and information spectral densities (ISDs) ($\geq$4 bits/s/Hz), nowadays, it is a well-established technology for long-haul optical transmission systems [6,10, 11]. On the other hand, the intensity modulation (IM)/direct detection (DD) technique is more practical and feasible in (ultra) short reach applications due to the tight budget and footprint (size and packaging) constraints. Hence, the modulation formats, such as 4-pulse amplitude modulation (PAM), orthogonal frequency division multiplexing (OFDM)/discrete multi-tone (DMT) and carrierless amplitude/phase modulation (CAP), are studied extensively to achieve 100 Gb/s using a single wavelength (λ), $2\lambda\times$50 Gb/s, $4\lambda\times$25 Gb/s, or $10\lambda\times$10 Gb/s in IM/DD links over $\leq$40 km of SSMF [12–15]. Typically, the achieved net ISDs in these studies are limited to $\leq$1 bits/s/Hz.

Although the cost-effectiveness is the primary requirement in access and metro links, spectral efficiency and dispersion tolerance in metro links are expected to be higher than the access links. The large portion of the cost in an optical communication link comes from the optical components rather than electrical ones, considering the rapid cost and performance innovations in CMOS technology. Thus, modulation techniques that can be implemented using DSP-based externally modulated transmitters and direct detection receivers, *i.e.,* minimizing the cost of the optical components, need to be investigated. They should offer ISDs greater than 1 bits/s/Hz with a transmission distance larger than 100 km in order to meet the ongoing increase in bandwidth demand. Consequently, researchers are seeking an answer for the question, *what signal formats offer the highest ISDs and maximum transmission distances in direct*

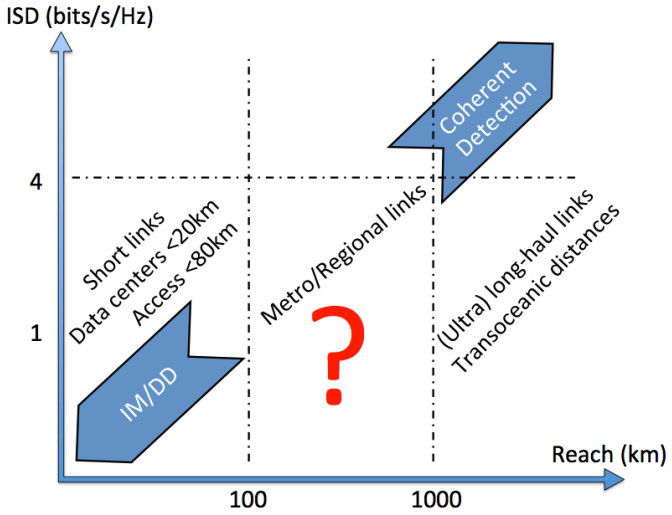

Fig. 1.3: ISD and transmission distance requirements for the access, metro and long-haul links.

detection links.

Alternatively, cost-effective simplified coherent receiver architectures can be studied in order to be employed in metropolitan links. Although their performance is superior than direct detection receivers, *i.e.,* offering high ISD with larger transmission margins, their optical complexity is a major obstacle to be considered in such links. Thus, it needs to be minimized with a minimum performance degradation.

Therefore, the aim of the research described in this thesis was to study and experimentally demonstrate spectrally-efficient and dispersion tolerant modulation formats that can be recovered using a direct detection receiver over metro and regional distances ($\geq$100 km). Moreover, a simplified coherent receiver design was explored and demonstrated which can provide a significant optical signal-to-noise ratio (OSNR) gain, and hence, higher transmission distance in metropolitan links or higher splitting ratios (1:128 or 1:1:256) at an affordable price in LR-PON over a SSMF.

1.3 Thesis outline

The main focus of the thesis is to design cost-effective optical transceivers for metropolitan links ($\geq$100 km) achieving high ISD. To achieve cost-effectiveness, the transceivers need to have low optical complexity with reasonable DSP complexity, considering that the continuing reduction in the cost and footprint, and increase in the performance of silicon complementary metal oxide semiconductor (CMOS) technology. This implies that higher sampling rate/bandwidth electronics will become increasingly applicable to low-cost applications. Therefore, initially, a direct detection receiver, consisting of a single-ended photodiode, is employed instead of a coherent receiver. In the transmitter side, the performance of spectrally-efficient subcarrier modulation (SCM) formats is assessed and compared using Lithium Niobate ($LiNbO_3$) in-phase and quadrature (IQ) and dual-drive MZ (DD-MZ) modulators. Due to its simpler structure compared to an IQ-modulator, as discussed in section 2.2, dual-drive MZM can lower the cost of an optical transmitter. There are also other advantages of employing a dual-drive Mach-Zehnder modulator (dual-drive MZM) such as smaller footprint, lower insertion loss yielding an increase in the power budget, and lower power consumption due to lower half-wavelength (V_π) and drive voltages.

Although $LiNbO_3$-based modulators potentially provide the highest performance (ISD (bits/s/Hz) $\times$

distance (km)), they might not be sufficiently cost-effective for metro space. On the other hand, Indium Phosphide (InP)-based modulators might be more attractive for some metro applications due to the following reasons: They 1) provide lower power consumption, *i.e.,* smaller required drive voltage, 2) have compact footprint and are compatible with the integration of a tunable laser source, and 3) are suitable for high volume production due to its easier integration and simplified packaging processes, compared to $LiNbO_3$-based modulators. The results and findings regarding the various transmitter architectures using such modulators are discussed in section 4.5.

Following this, coherent detection approach is investigated in chapter 5. The recent development in coherent systems proposed for long-haul links requires high optical complexity and footprint, *i.e.,* expensive and bulky devices such as coherent receivers. Thus, a monolithically integrated coherent receiver is preferable due to its low-cost and compact footprint. However, the high optical complexity of a polarization- and phase-diverse intradyne coherent receiver makes its full monolithic integration challenging, mainly due to the size of a PBS. Thus, hybrid implementations (typically using free-space optical components) are commonly employed to implement it. To date, although there are few reported studies regarding the fully monolithically integrated intradyne coherent receiver, they are not sufficiently mature and cost-effective for volume production yet. However, if the PBS is removed from the polarization diversity intradyne receiver, the SoP of the incoming signal needs to be tracked optically, requiring endless feedback loops. This implies that the implementation of a polarization-insensitive, *i.e.,* independent, coherent receiver needs to be achieved which is explored in chapter 5.

The remainder of this thesis is organized as follows: Chapter 2 discusses the theory of optical channel impairments during transmission over metro distances, namely attenuation, chromatic dispersion, amplified spontaneous emission (ASE)-noise, polarization rotation and fibre nonlinearities. Additionally, the optical modulators and detection schemes for optical signal generation and detection are described in detail.

Chapter 3 reviews the literature regarding the previously proposed modulation formats for non-coherent links. The tables listing the notable single polarization WDM direct detection experiments are also presented in this chapter. Following the literature review, the transmitter and receiver DSP architectures of two spectrally-efficient SCM formats, namely single sideband (SSB) Nyquist-SCM and single sideband OFDM (SSB-OFDM), are outlined.

Chapter 4 first provides the description of experimental setups using three modulators, a $LiNbO_3$ IQ-modulator, $LiNbO_3$ and InP dual-drive MZM. In addition, the simulation models, developed in MATLAB during the course of the PhD research, are outlined. After the experimental setups with their corresponding simulation models are given, a performance comparison between SSB Nyquist-SCM and SSB-OFDM is presented by means of simulations. They are compared in terms of their tolerance to signal-signal beating interference (SSBI), back-to-back and transmission performance. Following this, the single channel and WDM experimental demonstrations for the SSB Nyquist-SCM QPSK and 16-QAM signal formats, supported by simulation results, using the optical modulators are presented at bit rates of 14 Gb/s and 25 Gb/s per channel, respectively. Finally, the back-to-back and transmission performance of the modulators is experimentally compared.

Chapter 5 discusses the simplified coherent receiver approach for long-reach access and metropolitan links. Following a description of various types of coherent receivers, a dual-polarization (DP)-OFDM signal format combined with a polarization-time block coding (PTBC) technique is outlined and the

experimental setup used to assess the signal performance is described. OSNR performance of the simplified coherent receiver for the single channel and WDM systems in back-to-back operation are discussed, followed by a performance comparison with the direct detection receiver.

Finally, conclusions that are based on the obtained results discussed in chapters 4 and 5 are drawn in chapter 6. Besides this, potential research topics for future work are provided.

1.4 Original contributions of this thesis

The novelties and original contributions carried out during the course of the research described in this thesis are summarized as follows:

- The investigation of signal waveform symmetric clipping effect on the performance of dispersion-precompensated Nyquist pulse-shaped QPSK SCM in uncompensated DD links. This work resulted in the following publication [19].
- Performance comparison of spectrally-efficient subcarrier modulation (SCM) schemes in direct detection links. In particular, the assessment of single sideband (SSB) Nyquist-SCM and orthogonal frequency division multiplexing (OFDM) signal formats' tolerance to signal-signal beating interference, resulting from square-law detection. The results were reported in [20].
- Generation, transmission and detection of spectrally-efficient SSB Nyquist-SCM with QAM signaling. Numerical simulations and experimental demonstration of WDM SSB Nyquist pulse-shaped QPSK and 16-QAM SCM transmission
  - ⋆ using Lithium Niobate ($LiNbO_3$) IQ-modulators [16–18, 22]
  - ⋆ using $LiNbO_3$ dual-drive Mach-Zehnder modulator (dual-drive MZM) [21, 23]
  - ⋆ using Indium Phosphide (InP)-based tunable transmitter assembly (TTA), consisting of a wideband tunable digital supermode distributed Bragg reflector (DS-DBR) laser and an InP dual-drive MZM. The TTA used in this work was manufactured by Oclaro Inc., UK [24]

  in direct detection (DD) links. Dispersion compensation was achieved utilizing electronic predistortion (EPD) in all these studies.
- Investigation of the impact of the finite extinction ratio of the $LiNbO_3$ IQ-modulator and DD-MZM, in relation to the optical sideband suppression in SSB signal generation, and the resulting crosstalk between neighboring WDM channels, reported in [23].

  All the results and findings from the aforementioned studies, which are discussed in chapter 4, were performed in collaboration with Dr. S. Pachnicke and Dr. H. Griesser from ADVA Optical Networking, Germany. During the course of these studies, Dr. R. Maher and Dr. M. Paskov assisted with the experimental setup, S. Kilmurray assisted with the implementation of EPD technique at DSP stage, and Dr. R. Bouziane assisted with the field programmable gate array (FPGA) settings. Dr. M.J. Thakur provided the $LiNbO_3$ dual-drive MZM.
- Experimental demonstration of the simplified (polarization insensitive (PI)) coherent receiver, *i.e.*, consisting of a single balanced photodiode with a single analogue-to-digital converter (ADC), without the need for a PBS or 90^o optical hybrids.

- ⋆ Implementation of PI coherent receiver utilizing a combination of polarization-time block coding (PTBC) and heterodyne detection.
- ⋆ Performance comparison of direct detection and PI coherent receiver.

This work was completed with Dr. S. Savory and Dr. D. Lavery. The obtained results were presented in [25, 26] and in chapter 5.

1.5 Published papers in the course of the research in this thesis

The following is the list of publications, arised from the work presented in this thesis.

1. **M.S. Erkılınç**, D. Lavery, K. Shi, B.C. Thomsen, P. Bayvel, R.I. Killey, and S.J. Savory, "**Polarization-insensitive single balanced photodiode coherent receiver for long-reach WDM-PONs**", in *IEEE Journal of Lightwave Technology*, pre-print, 2015.
2. **M.S. Erkılınç**, M.P. Thakur, S. Pachnicke, H. Griesser, J. Mitchell B.C. Thomsen, P. Bayvel, and R.I. Killey, "**Spectrally-efficient WDM Nyquist pulse-shaped subcarrier modulation using a dual-drive Mach-Zehnder modulator and direct detection**", in *IEEE Journal of Lightwave Technology*, pre-print, 2015.
3. **M.S. Erkılınç**, D. Lavery, R. Maher, M. Paskov, B.C. Thomsen, P. Bayvel, R.I. Killey, and S.J. Savory, "**Polarization-insensitive single balanced photodiode coherent receiver for passive optical networks**", in *Proceedings of the 41th European Conference on Optical Communications*, 2015.
4. **M.S. Erkılınç**, S. Pachnicke, H. Griesser, B.C. Thomsen, P. Bayvel and R.I. Killey, "**Spectrally-efficient single sideband 16-QAM Nyquist-subcarrier modulation-based WDM transmission using an InP dual-drive Mach-Zehnder modulator and direct-detection**", in *Proceedings of the 41th European Conference on Optical Communications*, 2015.
5. **M.S. Erkılınç**, S. Pachnicke, H. Griesser, B.C. Thomsen, P. Bayvel and R.I. Killey, "**Dispersion-precompensated direct-detection Nyquist pulse-shaped subcarrier modulation using a dual-drive Mach-Zehnder modulator**", JTuA.42 in *Proceedings of the 20th OptoElectronics and Communications Conference*, 2015.
6. **M.S. Erkılınç**, Z. Li, S. Pachnicke, H. Griesser, B.C. Thomsen, P. Bayvel, and R.I. Killey, "**Spectrally-efficient WDM Nyquist pulse-shaped 16-QAM subcarrier modulation transmission with direct detection**", *IEEE Journal of Lightwave Technology*, vol.33, no.15, pp.3147-3155, 2015.
7. **M.S. Erkılınç**, S. Pachnicke, H. Griesser, B.C. Thomsen, P. Bayvel, and R.I. Killey, "**Performance comparison of single sideband direct-detection Nyquist-subcarrier modulation and OFDM**", *IEEE Journal of Lightwave Technology*, vol.33, no.10, pp.2038-2046, 2015.
8. **M.S. Erkılınç**, S. Pachnicke, H. Griesser, B.C. Thomsen, P. Bayvel and R.I. Killey, "**Effect of clipping on the performance of Nyquist-shaped dispersion-precompensated subcarrier modulation transmission with direct detection**", Tu3.3.1 in *Proceedings of the 40th European Conference on Optical Communications*, 2014.

9. **M.S. Erkılınç**, S. Kilmurray, R. Maher, M. Paskov, R. Bouziane, S. Pachnicke, H. Griesser, B.C. Thomsen, P. Bayvel and R.I. Killey, "**Nyquist-shaped dispersion-precompensated subcarrier modulation with direct detection for spectrally-efficient WDM transmission**", *OSA Optics Express*, vol.22, no.8, pp. 9420-9431, 2014.

10. **M.S. Erkılınç**, S. Kilmurray, S. Pachnicke, H. Griesser, B.C. Thomsen, P. Bayvel and R.I. Killey, "**Nyquist-shaped dispersion-precompensated subcarrier modulation with direct detection**", Th3K.4 in *Proceedings of the Optical Fiber Communication Conference*, 2014.

11. **M.S. Erkılınç**, R. Maher, M. Paskov, S. Kilmurray, S. Pachnicke, H. Griesser, B.C. Thomsen, P. Bayvel and R.I. Killey, "**Spectrally-efficient single-sideband subcarrier-multiplexed quasi-Nyquist QPSK with direct detection**", Tu3C.4 in *Proceedings of the 39th European Conference on Optical Communications*, 2013.

1.6 References

[1] G.P. Agrawal, "Applications of nonlinear fiber optics," 3rd edition, *Academic press*, 2010.

[2] A.H. Gnauck, R.W. Tkach, A.R. Chraplyvy, and T. Li, "High-capacity optical transmission systems," *J. Lightw. Technol.*, vol. 26, no. 9, pp. 1032–1045, 2008.

[3] E.B. Desurvire, "Capacity demand and technology challenges for lightwave systems in the next two decades," *J. Lightw. Technol.*, vol. 24, no. 12, pp. 4697–4710, 2006.

[4] R.W. Tkach, "Scaling optical communications for the next decade and beyond," *J. Bell Labs Technical*, vol. 14, no. 4, pp. 3–9, 2010.

[5] Cisco, "Cisco Visual Networking Index: Forecast and Methodology, 2014—2019," 2015 [Online]. Available:http://www.cisco.com/c/en/us/solutions/collateral/service-provider/ip-ngn-ip-next-generation-network/white_paper_c11-481360.pdf (retrieved on August 2nd 2015).

[6] P. Winzer, "High spectral-efficiency optical modulation formats," *J. Lightw. Technol.*, vol. 30, no. 24, pp. 3824–3835, 2012.

[7] S.J. Savory, "Digital coherent optical receivers: algorithms and subsystems," *J. Selected Topics in Quantum Electron.*, vol. 16, no. 5, pp. 1164–1179, 2010.

[8] C. Lam, "Passive Optical Networks," *Academic press*, 2007.

[9] P. Winzer, and R.-J. Essiambre "Advanced modulation formats for high-capacity optical transport networks," *J. Lightw. Technol.*, vol. 24, no. 12, pp. 4711–4728, 2006.

[10] M. Mazurczyk, "Spectral shaping in long haul optical coherent systems with high spectral efficiency," *J. Lightw. Technol.*, vol. 32, no. 16, pp. 2915–2924, 2014.

[11] J.X. Cai, "100G transmission over transoceanic distance with high spectral efficiency and large capacity," *J. Lightw. Technol.*, vol. 30, no. 24, pp. 3845-3856, 2012.

[12] J. Wei, J. Ingham, D. Cunningham, R. Penty, and I. White, "Performance and power dissipation comparisons between 28 Gb/s NRZ, PAM, CAP, and optical OFDM systems for data communication applications," *J. Lightw. Technol.*, vol. 30, no. 20, pp. 3273–3280, 2012.

[13] V Vujicic, P.M. Anandarajah, C. Browning, and L.P. Barry, "WDM-OFDM-PON based on compatible SSB technique using a mode locked comb source," *IEEE Photon. Technol. Lett.*, vol. 25, no. 21, pp. 2058–2061, 2013.

[14] J.C. Cartledge, and A.S. Karar, "100 Gb/s intensity modulation and direct detection," *J. Lightw. Technol.*, vol. 32, no. 16, pp. 2809–2814, 2014.

[15] A. Dochhan, H. Grieser, M. Eiselt, and J.-P. Elbers, "Flexible bandwidth 448 Gb/s DMT transmission for next generation data center inter-connects," in *Proc. IEEE European Conference on Optical Communication (ECOC)*, 2014, paper P.4.10.

[16] M.S. Erkilinc, R. Maher, M. Paskov, S. Kilmurray, S. Pachnicke, H. Griesser, B.C. Thomsen, P. Bayvel, and R. Killey, "Spectrally-efficient single-sideband subcarrier-multiplexed quasi-Nyquist QPSK with direct detection," in *Proc. IEEE European Conference on Optical Communication (ECOC)*, 2013, paper Tu3C4.

[17] M. S. Erkilinc, S. Kilmurray, R. Maher, M. Paskov, R. Bouziane, S. Pachnicke, H. Griesser, B.C. Thomsen, P. Bayvel, and R. Killey, "Nyquist-shaped dispersion-precompensated subcarrier modulation with direct detection," in *Proc. IEEE/OSA Optical Fiber Communication Conference (OFC)*, 2014, paper Th3K.4.

[18] M.S. Erkılınç, S. Kilmurray, R. Maher, M. Paskov, R. Bouziane, S. Pachnicke, H. Griesser, B.C. Thomsen, P. Bayvel, and R.I. Killey, "Nyquist-shaped dispersion-precompensated subcarrier modulation with direct detection for spectrally-efficient WDM transmission," *Optics Express*, vol. 22, no. 8, pp. 9420–9431, 2014.

[19] M. S. Erkilinc, S. Pachnicke, H. Griesser, B.C. Thomsen, P. Bayvel, and R. Killey, "Effect of clipping on the performance of Nyquist-shaped dispersion-precompensated subcarrier modulation transmission with direct detection," in *Proc. IEEE European Conference on Optical Communication (ECOC)*, 2014, paper Tu.3.3.1.

[20] M.S. Erkılınç, S. Pachnicke, H. Griesser, B.C. Thomsen, P. Bayvel, and R. Killey, "Performance comparison of single sideband direct detection Nyquist-subcarrier modulation and OFDM," in *J. Lightw. Technol.*, vol. 33, no. 10, pp. 2038–2046, 2015.

[21] M.S. Erkılınç, S. Kilmurray, R. Maher, M. Paskov, R. Bouziane, S. Pachnicke, H. Griesser, B.C. Thomsen, P. Bayvel, and R.I. Killey, "Dispersion-precompensated direct-detection Nyquist-pulse-shaped subcarrier modulation using a dual-drive Mach-Zehnder modulator," in *Proc. IEEE OptoElectronics and Communication Conference (OECC)*, 2015, paper JTuA.42.

[22] M.S. Erkılınç, Z. Li, S. Pachnicke, H. Griesser, B.C. Thomsen, P. Bayvel, and R. Killey, "Spectrally-efficient WDM Nyquist-pulse-shaped 16-QAM subcarrier modulation transmission with direct detection," in *J. Lightw. Technol.*, vol. 33, no. 15, pp. 3147–3155, 2015.

[23] M.S. Erkılınç, M.P. Thakur, J. Mitchell, S. Pachnicke, H. Griesser, B.C. Thomsen, P. Bayvel, and R.I. Killey, "Spectrally-efficient WDM Nyquist-pulse-shaped subcarrier modulation using a dual-drive Mach-Zehnder modulator and direct detection," in *J. Lightw. Technol.*, pre-print, 2015.

[24] M.S. Erkılınç, S. Pachnicke, H. Griesser, B.C. Thomsen, P. Bayvel, and R.I. Killey, "Spectrally-efficient single sideband 16-QAM Nyquist-subcarrier modulation-based WDM transmission using an InP dual-drive Mach-Zehnder modulator and direct-detection," in *Proc. IEEE European Conference on Optical Communication (ECOC)*, 2015, paper PA5.2.

[25] M.S. Erkılınç, D. Lavery, R. Maher, M. Paskov, B.C. Thomsen, P. Bayvel, R.I. Killey and S.J. Savory, "Polarization-insensitive single balanced photodiode coherent receiver for passive optical networks," in *Proc. IEEE European Conference on Optical Communication (ECOC)*, 2015, paper Th.1.3.3.

[26] M.S. Erkılınç, D. Lavery, K. Shi, B.C. Thomsen, P. Bayvel, R.I. Killey and S.J. Savory, "Polarization-insensitive single balanced photodiode coherent receiver for long-reach WDM-PONs," in *J. Lightw. Technol.*, pre-print, 2015.

Chapter 2

Theory

This chapter outlines the requisite theory for the work detailed in this thesis. In section 2.1, the discussion is focused on the noise and linear impairments which occur during transmission through fibre links, namely amplified spontaneous emission (ASE)-noise, fibre attenuation, chromatic dispersion (CD) and polarization rotation since they are the main impairments and limitations to be considered for access, metropolitan and regional optical links. Furthermore, although the non-linear effects during optical transmission in metro links are not the main limitation unlike in long-haul (transoceanic) links, they are briefly discussed since their effects can become significant over transmission distances of more than 500 km. Following this, the optical modulators and detection schemes, that are used in the experiments outlined in this thesis, are described in sections 2.2 and 2.3, respectively.

2.1 Optical fibre channel impairments

In this section, the noise and impairments, amplified spontaneous emission (ASE) noise, fibre attenuation, chromatic dispersion (CD) and polarization rotation that exhibit a linear behaviour during an optical transmission over a fibre are explained. Then, non-linear impairments, self-phase modulation (SPM), cross-phase modulation (XPM) and four-wave mixing (FWM), incurred by the Kerr effect, are briefly discussed in the second part.

2.1.1 Linear impairments

2.1.1.1 Fibre attenuation

In optical transmission, the loss of a fibre attenuates the signal and reduces the power of the transmitted signal. Therefore, attenuation can be a limiting factor since an optical receiver requires a minimum power level to detect the signal. Under these conditions, the amplitude of an optical field propagating along the fibre denoted as A is described by

$$\frac{\partial A}{\partial z} + \frac{\alpha}{2} A = 0 \tag{2.1}$$

where α is the attenuation coefficient and z is the propagation direction. The solution of the first-order differential equation, denoted in Eq. 2.1 for α is given by

$$P_o = P_i \exp(-\alpha L) \tag{2.2}$$

$$\alpha(\text{dB/km}) = -\frac{10}{L}\log\left(\frac{P_o}{P_i}\right) \approx 4.343\alpha, \tag{2.3}$$

where P_i is the launch (input) power into the fibre, P_o is the output power and L is the fibre length. Attenuation along the fibre is a wavelength-dependent parameter, with α reaching its minimum values between 1460 and 1625 nm, typically 0.2 dB/km for a standard single mode fibre (SSMF). Thus, according to the International Telecommunication Union (ITU), today's optical communication systems employ the short (short-wavelength) band from 1460 to 1530 nm, conventional-wavelength band, referred to as C-band, from 1530 to 1565 nm and long-wavelength band (L-band) from 1565 to 1625 nm as the optical transmission wavelengths [1]. Throughout the thesis, transmission in the C-band is considered at which wavelengths Erbium-doped fibre amplifiers (EDFAs) are used for optical amplification. The loss spectrum of a typical SSMF is shown in Fig. 2.1 (taken from [2] - see Fig.4).

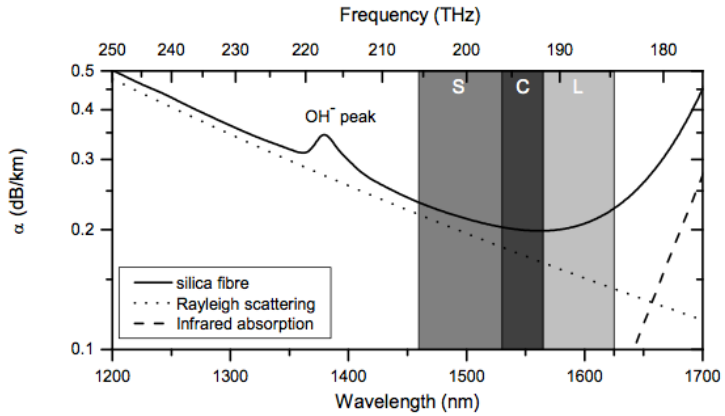

Fig. 2.1: Loss profile of a SSMF as a function of wavelength and frequency. S-(1460-1530 nm), C-(1530-1565 nm) and L-transmission bands (1565-1625 nm) are highlighted.

2.1.1.2 Chromatic dispersion

In medium- and long-haul lightwave systems using SSMF, besides the decrease in signal power due to the fibre loss, pulse broadening, induced by group-velocity dispersion (GVD) of the fibre, limits the performance of the system, as depicted in Fig. 2.2. This broadening effect causes a decrease in signal power, referred to as dispersion-induced fading in signal power. In the time domain, the broadened pulse, represented as '1' (light-on), starts interfering with the neighboring pulses, shown as the shaded regions in Fig. 2.2. This effect is referred to as inter-symbol interference (ISI) which increases the likelihood of an error during symbol decision stage based on threshold, denoted as '*Th*' in Fig. 2.2. In the frequency domain, the GVD is a frequency/wavelength-dependent delay (walk-off), *i.e.,* different frequency components of a signal travel with different velocities. Since the resulting phase shift process is quadratic assuming linear delay with frequency, the walk-off at high frequencies (at high bit-rates) can be observed more significantly compared to low frequencies (low bit-rates). For instance, the CD effect on a 40 GHz signal is 16 times more than on a 10 GHz signal.

Analytically, if the effect of CD is approximated by a Taylor series expanded around the carrier frequency $\omega = \omega_c$ up to the third term, Eq. 2.1 can be re-written as follows:

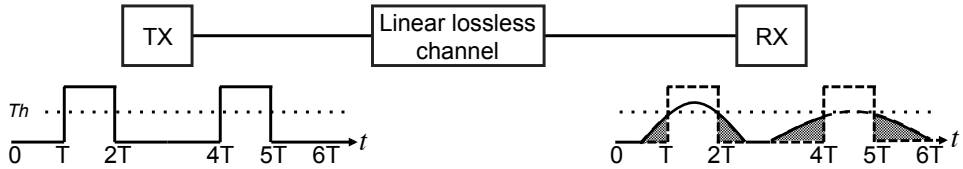

Fig. 2.2: Dispersion effect on a signal.

$$\frac{\partial A}{\partial z}+\frac{\alpha}{2}A+\beta_1\frac{\partial A}{\partial t}+\frac{i}{2}\beta_2\frac{\partial^2 A}{\partial t^2}-\frac{1}{6}\beta_3\frac{\partial^3 A}{\partial t^3}=0, \tag{2.4}$$

where β_1 is inversely proportional to the group velocity v_g, β_2 is the GVD parameter and β_3 is the GVD slope parameter, also referred to as third-order dispersion (ToD). β_1 can be denoted as

$$\beta_1=\frac{1}{v_g}=\frac{1}{c_0}\left(n+\omega\frac{dn}{d\omega}\right), \tag{2.5}$$

where c_0 is the speed of light, n is the linear refractive index profile of the employed fibre and, ω is the angular optical frequency. To simplify Eq. 2.4, β_1 can be eliminated under the assumption of a frame of reference moving with the pulse at v_g. Furthermore, β_3 can be neglected when β_2 is sufficiently high such as is the case with SSMF within the C-band at 1545 nm [3]. Since β_2 is the main parameter that causes pulse broadening, Eq. 2.4 can be simplified to

$$\frac{\partial A}{\partial z}+\frac{\alpha}{2}A+\frac{i}{2}\beta_2\frac{\partial^2 A}{\partial t^2}=0, \tag{2.6}$$

where β_2 is defined as follows:

$$\begin{aligned}\beta_2=\frac{d\beta_1}{d\omega}&=\frac{d}{d\omega}\left[\frac{1}{c_0}\left(n+\omega\frac{dn}{d\omega}\right)\right]\\&=\frac{1}{c_0}\left(2\frac{dn}{d\omega}+\omega\frac{d^2n}{d\omega^2}\right).\end{aligned} \tag{2.7}$$

Additionally, the dispersion parameter (D_{SMF}) of a SSMF can be defined as the first derivative of β_1 with respect to the wavelength λ,

$$D_{SMF}=\frac{d\beta_1}{d\lambda}=\frac{d(1/v_g)}{d\lambda}=\frac{d}{d\lambda}\left[\frac{1}{c_0}\left(n+\omega\frac{dn}{d\omega}\right)\right]=\frac{-2\pi c_0}{\lambda^2}\beta_2. \tag{2.8}$$

The solution of Eq. 2.6 for lossless ($\alpha=0$) channel is

$$H(L,\omega_c)=\exp\left(-\frac{j}{2}L\beta_2\omega_c^2\right)=\exp\left(-jL\frac{D_{SMF}\lambda_0^2}{4\pi c_0}\omega_c^2\right) \tag{2.9}$$

where λ_0 is the carrier wavelength, D_{SMF} is the dispersion parameter at wavelength λ_0, ω_c is the angular optical center frequency and, L is the length of the full transmission link.

The dispersion of an optical fibre is dependent on the operating wavelength, *e.g.,* $D\approx 0$ ps/km/nm at 1310 nm and $D\approx 17$ ps/km/nm at 1550 nm, as shown Fig. 2.3 (taken from [2] - see Fig.5). The total dispersion profile of an optical fibre is the sum of the material and waveguide dispersion. Although the material dispersion cannot be changed for a given fibre, the waveguide dispersion and subsequently, dispersion parameter can be modified by changing the refractive index profile of the fibre, such as dispersion

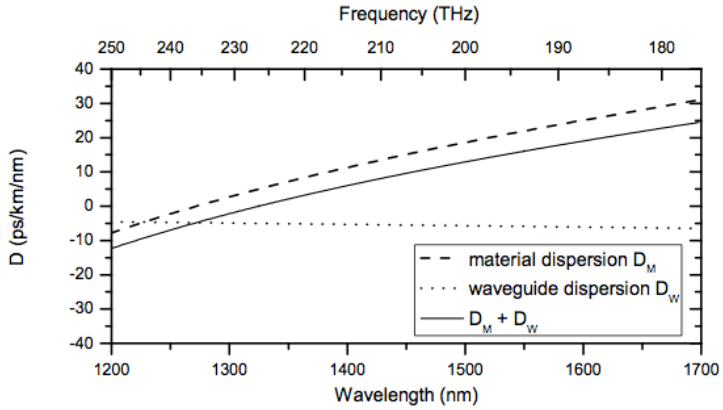

Fig. 2.3: Dispersion of a typical SSMF as a function of wavelength and frequency.

shifted fibre (DSF) and dispersion compensating fibre (DCF).

2.1.1.3 Amplified spontaneous emission (ASE)-noise

To compensate the loss of a fibre whilst transmitting the signal over a distance of typically more than 80 km, optical amplification is required. In amplified optical transmission links, the dominant form of noise emission is ASE-noise which is introduced by EDFAs along the link. The Erbium ions are first excited so that the majority of the ions are in the higher-energy state than the lower-energy state, referred to as population inversion. Whilst the excited ions are returning to a lower-energy state to reach the equilibrium state, they transfer their energy to the optical signal field in the form of additional photons with the same phase, frequency, polarization and direction, through stimulated emission, *i.e.,* the process of amplification of the incoming signal. However, during this process, some Erbium ions in the excited energy-state release their energy to the optical signal field in the form of photons with random phase, frequency, polarization and direction, through spontaneous emission. Some of these photons are guided within the fibre and interact with other dopant ions. Therefore, this spontaneously emitted light is amplified in the same manner as the signal, an effect referred to as amplified spontaneous emission (ASE) [4], which degrades the optical signal-to-noise ratio (OSNR).

ASE-noise can be modeled as independent and identically distributed (i.i.d.) Gaussian random process. The power of spontaneous emission noise (P_{sp} [W]) from an EDFA is nearly constant (white noise) and is defined as

$$P_{sp} = En_{sp}(G-1)BW_{res}, \qquad \text{where} \qquad n_{sp} = \frac{N_2}{N_2 - N_1} = 0.5 \times 10^{NF/10} \quad \text{and} \quad G = \frac{P_{out}}{P_i}, \tag{2.10}$$

where $E = h\nu$ is the energy of a photon at the considered optical frequency (Planck's constant $h = 6.626 \times 10^{34}$ Joules and ν is the frequency of a photon), G denotes the optical amplifier's gain (P_{out} and P_i are output and input powers of continuous wave (CW) signal being amplified), and n_{sp} is the spontaneous emission or population inversion factor, which is typically considered as 1.5. N_1 and N_2 represent the population densities for the ground and excited states, respectively. BW_{res} is the optical bandwidth over which the ASE-noise power is being measured, referred to as resolution bandwidth. It is assumed to be 0.1 nm (=12.5 GHz). The noise figure (F) of an EDFA is approximately $2n_{sp}$, typically 5 dB [5].

Since ASE-noise is an unpolarized optical field, *i.e.,* equal power in both polarizations, and has uniformly distributed phase, it affects both the in-phase (I) and quadrature (Q) components of the optical signal in both polarizations ($[E_x, E_y]$) in the same way. In the case of coherently detected signals, ASE-

noise appears as a symmetrical spread around symbol points on the signal constellation. Therefore, the ASE-noise tolerance of a given modulation format is determined by the closest Euclidean distance between the symbols.

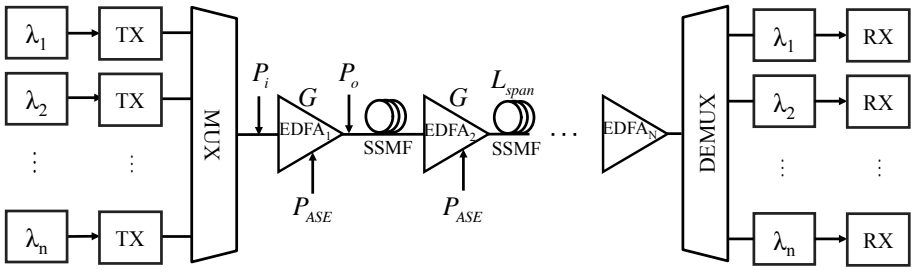

Fig. 2.4: Typical optical transmission link using distributed amplification scheme.

In long-haul links, multiple EDFAs are cascaded to compensate for the loss of the previous span, as shown in Fig. 2.4. Therefore, ASE-noise accumulates from one to another amplifier that reduces the OSNR gradually, as given in Eq. 2.11. A detailed discussion on the ASE-noise with different amplification schemes can be found in [5]. The optical OSNR can be defined as the ratio of output signal power (P_o) to the ASE-noise power (P_{ASE}) resulted from an EDFA

$$\text{OSNR} = \frac{P_o}{P_{ASE}}. \tag{2.11}$$

By plugging Eq.2.10 into Eq.2.11, OSNR can be re-written as follows:

$$\text{OSNR} = \frac{GP_i}{2n_{sp}(G-1)h\nu BW_{res}} \approx \frac{P_i}{2n_{sp}h\nu BW_{res}}, \tag{2.12}$$

for large gains $G \gg 1$. Plugging the values for $h\nu$ and BW_{res}, and taking the logarithm of both sides, Eq.2.12 becomes

$$\text{OSNR(dB)} \approx 58 + P_i(\text{dBm}) - F(\text{dB}), \tag{2.13}$$

where $F = 10\log_{10}(2n_{sp})$ is the noise figure of the amplifier (for large gains). In an optical point-to-point link, consisting of N amplifiers and $N-1$ fibre spans, each amplifier in a chain adds noise, and hence, OSNR keeps decreasing in a lightwave system, as shown in Fig. 2.4. Assuming that each amplifier is identical (F for each amplifier is the same along the link) and compensates exactly for the loss of the each fibre span ($G(\text{dB}) = \alpha(\text{dB/km}) \times L_{span}(\text{km})$), the final OSNR at the end of link is given by

$$\text{OSNR(dB)} \approx 58 + P_i(\text{dBm}) - F(\text{dB}) - 10\log_{10}(N) - 10\log_{10}(M), \tag{2.14}$$

where M is the number of WDM channels.

2.1.2 Polarization rotation

A SSMF supports two polarization modes, referred to as X- and Y-polarization, which are orthogonal to each other. They can vary in amplitude and frequency, implying that they can be modulated with different data. The asymmetry of an optical fibre, mechanical stress and/or temperature fluctuations causes random polarization rotation, polarization mode dispersion (PMD) and polarization dependent loss (PDL). Assuming that the OSNR is sufficiently high and chromatic dispersion compensation is

achieved with negligible penalty, PMD and PDL can reduce the OSNR, and consequently, severely degrade the system performance in single polarization direct detection links over long distances (>800 km) at a bit rate of 10 Gb/s with high PMD legacy fibre or ≥40 Gb/s [6–10]. Since such transmission distances are beyond the scope of this thesis, the discussion in this section is focused on the impact of polarization rotation.

The random variations in the axes of the two orthogonal polarization modes ($[E_x, E_y]$) along the fibre are described by the 2×2 Jones matrices. The Jones matrix for a random rotation by an angle θ, denoted as $R(\theta)$), and a random phase shift (a phase shift of $\phi/2$ along the fast, let's say x-, axis and a phase shift of $-\phi/2$ along the slow, let's say y-, axis) T(ϕ), can be written as follows:

$$\mathbf{E}' = R(\theta)T(\phi)\mathbf{E} \tag{2.15}$$

$$\begin{bmatrix} E'_x \\ E'_y \end{bmatrix} = \begin{bmatrix} \cos(\theta) & -\sin(\theta) \\ \sin(\theta) & \cos(\theta) \end{bmatrix} \begin{bmatrix} e^{j\phi/2} & 0 \\ 0 & e^{-j\phi/2} \end{bmatrix} \begin{bmatrix} E_x \\ E_y \end{bmatrix}, \tag{2.16}$$

where E'_x and E'_y are the resultant polarization modes after polarization rotation and, θ and ϕ are uniformly distributed over $[-\pi, \pi]$. To represent different polarization states of light in real three dimensional space, the Poincaré sphere tool is utilized [11]. On the Poincaré sphere, any given polarization state is represented with a unique point that is defined by the (real-valued) Stokes parameters (S_0, S_1, S_2 and S_3). They are given by

$$\begin{aligned} S_0 &= E_{0x}^2 + E_{0y}^2 \\ S_1 &= E_{0x}^2 - E_{0y}^2 \\ S_2 &= 2E_{0x}E_{0y}\cos(\phi) \\ S_3 &= 2E_{0x}E_{0y}\sin(\phi), \end{aligned} \tag{2.17}$$

where E_{0x} and E_{0y} are the real maximum amplitudes of X-and Y-polarization modes and ϕ is the phase difference between the modes. S_0 represents the total intensity of light and S_1 indicates the difference between the X-polarization (linearly horizontal polarized light) and Y-polarization (linearly vertical polarized light) modes. S_2 represents the intensity difference between linearly 45°- and -45°- polarized light. Finally, S_3 represents the intensity difference between the right and left circularly polarized light. If the light is totally polarized ($S_0 = 1$), the state of polarization of a signal is a point on the Poincaré sphere. Otherwise, it is within the sphere (partially polarized light). The center of the sphere represents unpolarized light ($S_0 = 0$). The points on the equator correspond to linear polarization states ($S_2 = 0$ and $S_3 = 0$) whereas the left and right-hand circularly polarized light are shown by the South and North Poles of the sphere ($S_1 = 0$), respectively. The rest of the points on the sphere represent elliptical polarization states.

The cancellation of the polarization rotation effect is described for single carrier systems in [12] and for multi-carrier systems in [13], assuming that the full optical field is recovered using a polarization-diverse coherent receiver. However, if only a single polarization is detected using a coherent receiver with no polarization diversity (having no polarization beam splitter (PBS) or optical polarization tracking unit), then the receiver should have the ability to detect the signal regardless of the state of polarization of the incoming signal, referred to as polarization-insensitive coherent receiver. This problem is explored in chapter 5.

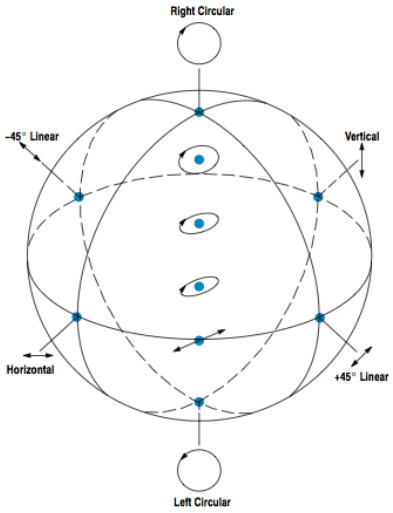

Fig. 2.5: The Poincaré sphere with the fundamental states of polarization (taken from http://www.newport.com/Tutorial-Polarization-in-Fiber-Optics/849671/1033/content.aspx).

2.1.3 Nonlinear impairments (Kerr-effect)

In section 2.1.1.2, the refractive index profile of an optical fibre (n) was assumed to be power independent. However, in reality, it is dependent on the optical intensity of the signal propagating through the fibre, referred to as the Kerr effect. The nonlinear refractive index is given by

$$n' = n + n_2(P/A_{eff}), \tag{2.18}$$

where n_2 is the nonlinear-index coefficient, P is the optical power in the fibre and A_{eff} is the effective mode area. This effect distorts the signal in propagation and causes a time-dependent non-linear phase shift [3]. The nonlinear Schrödinger equation (NLSE) that governs the Kerr-effects during the light propagation along the fibre is given as follows:

$$\frac{\partial A}{\partial z} + \frac{\alpha}{2}A + \frac{i}{2}\beta_2\frac{\partial^2 A}{\partial t^2} = i\gamma|A|^2A, \qquad \text{where} \qquad \gamma = \frac{n_2\omega}{c_0 A_{eff}}, \tag{2.19}$$

where γ is the nonlinear coefficient, and A is the total amplitude of the optical fields, propagating in the fibre. If the optical phase shift is self-induced (due to the optical intensity of a channel of interest), it is called self-phase modulation (SPM). It leads to an instantaneous frequency chirp depending on optical intensity, broadens the signal bandwidth and can limit the system performance. The refractive index depends not only on the optical intensity of the propagating channel of interest, but also on the intensity of the signal propagating in the neighboring wavelength division multiplexing (WDM) channels, an effect termed cross-phase modulation (XPM). Additionally, when the amplitudes of three optical fields in A, let's say A_1, A_2 and A_3 with carrier frequencies of $\omega_{c_1}, \omega_{c_2}$ and ω_{c_3}, are co-propagating in an optical fibre simultaneously, they mix and generate new optical fields (with amplitude A_4) with carrier frequencies $\omega_{c_4} = \omega_{c_1} \pm \omega_{c_2} \pm \omega_{c_3}$. These mixing frequency components interfere with the channel of interest, and the effect is called FWM. All these nonlinear propagation effects (Kerr-effects) can be represented in the NLSE by extending Eq.2.19 as follows:

$$\frac{\partial A_1}{\partial z}+\frac{\alpha}{2}A_1+\frac{i}{2}\beta_2\frac{\partial^2 A_1}{\partial t^2}=\underbrace{i\gamma|A_1|^2A_1}_{\text{SPM}}+\underbrace{2i\gamma(|A_2|^2+|A_3|^2)A_1}_{\text{XPM}}+\underbrace{i\gamma A_2^2A_3^*}_{\text{FWM}}, \tag{2.20}$$

However, Eq.2.20 assumes that the optical field of each WDM channel is simulated as separate vectors. This operation significantly increases the computational complexity in numerical simulations. Therefore, for the sake of simplicity in simulations, all the optical fields, *e.g.,* A_1, A_2 and A_3, are combined into a single optical field, $A = A_1 + A_2 + A_3$, and subsequently, Eq.2.19 is used in simulations throughout the thesis.

2.2 Optical modulators

An optical modulator converts the electrical signal (typically over a bandwidth of tens of GHz) into an optical signal by modulating the signal on an optical carrier at the frequencies of hundreds of THz. The optical modulation can be performed directly by modulating the laser drive current. However, this type of modulation is not preferable for more than 20 km of SSMF transmission links since it causes a frequency chirp on the modulated optical signal [7]. To avoid the chirping effect, external modulation in which the laser acts as a CW source should be employed. In external modulation, the data is modulated onto an optical carrier by controlling its phase.

The fundamental component in high-speed optical modulators is a phase modulator (PM). An optical PM consists of an optical waveguide in an electro-optic modulator substrate, *e.g.,* Lithium Niobate ($LiNbO_3$) or Indium Phosphide (InP) crystal. InP photonic integration has compact footprint, low power consumption (smaller required drive voltage) and simplified production and packaging processes [14–16]. The refractive index profile of the substrate can be changed by applying an electric voltage. This allows the electrical field to be modulated on the phase of an optical carrier [7, 17]. For InP-based devices, the phase of an optical carrier is nonlinearly dependent on the applied voltage $V(t)$ whereas it can be assumed to be linear for the $LiNbO_3$-based devices. This effect is further discussed in section 4.2.1.3. Nevertheless, InP-based devices might be more attractive for cost-effective optical transceivers. The required driving voltage in order to achieve π-phase shift is defined as V_π. Hence, the relation between an input optical signal (E_i) and output phase modulated signal (E_o) can be represented as

$$E_o = E_i e^{j\phi(t)} = E_i e^{j\frac{V(t)}{V_\pi}\pi}. \tag{2.21}$$

A dual-drive Mach-Zehnder modulator is the combination of two phase modulators that are driven independently. The incoming light (E_i) is split into two paths and passed through the phase modulators in parallel. The splitting ratio of a modulator depends on its extinction ratio which is discussed in chapter 4. After the incoming light in both paths is phase modulated, two optical fields are coupled and the output optical signal is generated in polar coordinates form. The transfer function of a dual-drive Mach-Zehnder modulator (dual-drive MZM) with the driving voltages of $V_1(t)$ and $V_2(t)$ is given by

$$E_o = E_i \left[\gamma_{sp} e^{j\phi_1(t)} + (1-\gamma_{sp}) e^{j\phi_2(t)} \right]$$
$$= E_i \left[\gamma_{sp} e^{j\frac{V_1(t)}{V_\pi}\pi} + (1-\gamma_{sp}) e^{j\frac{V_2(t)}{V_\pi}\pi} \right], \tag{2.22}$$

where $\phi_1(t)$ and $\phi_2(t)$ represent the phase shifts in the first and second arms of the modulator, respectively, and γ_{sp} is the splitting ratio, determines the extinction ratio of the modulator. It is crucial whilst generating a single sideband (SSB) signal. How γ_{sp} and extinction ratio of a modulator affect the quality of a SSB signal is further discussed in section 4.5.2.2. If V_1 is set equal to V_2 in Eq. 2.22, the dual-drive MZM operates as a single phase modulator. The relation between an output and input optical signal in Eq. 2.22 can be re-written in the normalized form of

$$E_o = \frac{E_i}{2} \left[e^{j\frac{V_1(t)}{V_\pi}\pi} - e^{j\left(\frac{V_2(t)}{V_\pi}\pi+\pi\right)} \right]$$
$$= \frac{r_{\max}}{2} \left(e^{j\phi_1} - e^{j\phi_2} \right), \tag{2.23}$$

where $\phi_1 = \pi V_1/V_\pi$, $\phi_2 = \pi(V_2/V_\pi + \pi)$ and $r_{\max}$ is the maximum amplitude among the modulated optical symbols. Eq. 2.23 gives the geometric representation of an optical field modulated by a dual-drive MZM.

Any M-ary signal constellation can be written in polar coordinates as follows:

$$s_i = r_i e^{j\theta_i}, \tag{2.24}$$

where $r_i > 0$, $0 \le \theta_i < 2\pi$ and $r_{\max} = \max\{r_i\}$ while $i = 0, \ldots, M-1$. Hence, in this coordinate system, two driving signals (corresponding phases) for a dual-drive MZM become

$$\phi_{i1} = \theta_i + \cos^{-1}\left(\frac{r_i}{r_{\max}}\right) \tag{2.25a}$$
$$\phi_{i2} = \theta_i - \cos^{-1}\left(\frac{r_i}{r_{\max}} + \pi\right). \tag{2.25b}$$

Thus, with the driving signal given above, any complex signal in polar coordinates can be represented as

$$s_i = \frac{r_{\max}}{2} \left(e^{j\phi_{i1}} - e^{j\phi_{i2}} \right). \tag{2.26}$$

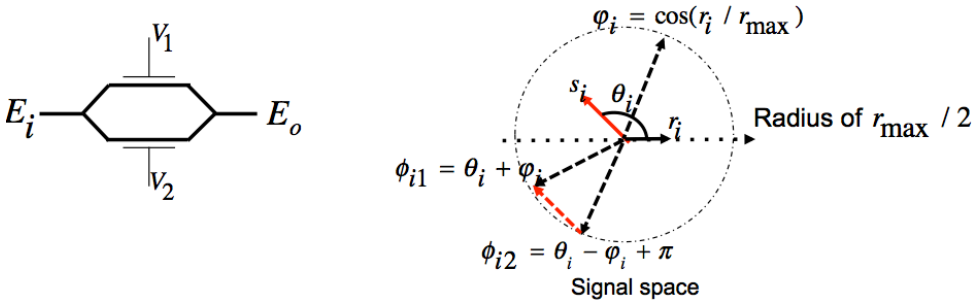

Fig. 2.6: DD-MZM structure (left) with its signal space (right).

The procedure for generating optical quadrature amplitude modulation (QAM) symbols (s_i) using the driving signals ϕ_{i1} and ϕ_{i2} with a radius of $r_{\max/2}$ is illustrated in Fig. 2.6 [18]. This modulator requires an additional digital signal processing (DSP) block at the transmitter that performs a conversion from

Cartesian to polar coordinates which is investigated in [19]. An optimization for driving voltages due to the instantaneous phase jumps is also studied in [20].

Another widely used modulator is IQ-modulator which operates in Cartesian coordinates, as depicted in Fig. 2.7. It is composed of a PM and two single-drive Mach-Zehnder modulators (MZMs). As in the case of dual-drive MZM, the incoming light is split into two paths, called I and Q arms, depending on the modulator's splitting ratio (γ_{sp}).

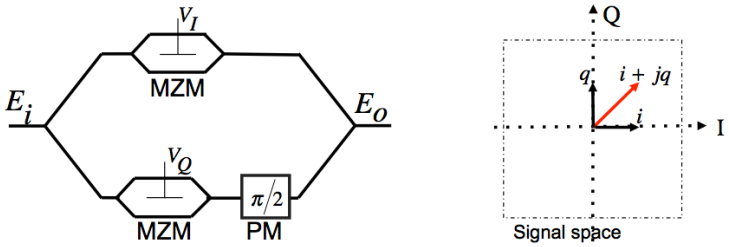

Fig. 2.7: IQ-modulator with its signal space.

In both arms, intensity modulation takes place by using a single-drive MZM in push-pull mode at its minimum transmission (null) point, *i.e.,* the optical carrier is fully suppressed [21]. The transfer function of a single-drive MZM is shown in Fig. 2.8, and given in Eq. 2.27.

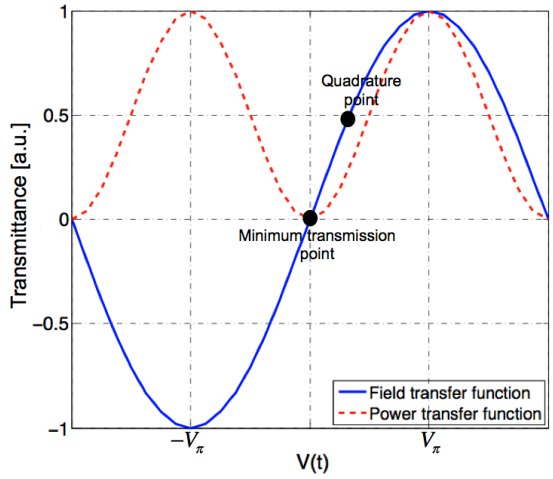

$$E_o(t) = E_i(t)\cos\left(\frac{V(t)}{V_\pi}\pi\right). \tag{2.27}$$

Fig. 2.8: Transfer function of a single-drive MZM.

Additionally, a relative phase-shift of $\pi/2$ is added by a PM in the Q-arm. After combining two single-drive MZMs and a phase shifter to provide $\pi/2$ phase-shift in one arm, the transfer function of an IQ-modulator becomes

$$E_o(t) = E_i(t)\left[\gamma_{sp}\cos\left(\frac{V_I(t)}{V_\pi}\pi\right) + (1-\gamma_{sp})\underbrace{e^{j\pi/2}}_{\mathrm{j}}\cos\left(\frac{V_Q(t)}{V_\pi}\pi\right)\right]. \tag{2.28}$$

The IQ-modulator described above can modulate the phase and amplitude of an optical field in single polarization. Note that to modulate the second polarization which is orthogonal to the first one, two parallel IQ-modulators nested in an interferometric configuration need to be used. Consequently, each polarization can be independently modulated with a decorrelated data. Alternatively, polarization demultiplexing emulator can be used to modulate the second polarization using only two driving signals.

Any arbitrary signal on the complex IQ-plane (Cartesian coordinate) can be obtained at the output of the modulator, as illustrated in Fig. 2.7. If an IQ-modulator is driven by binary signals, *e.g.,* generation

of quadrature phase-shift keying (QPSK) signal, the optical signal is generated using the full $2V_\pi$ swing since the electrical noise can be suppressed due to non-linear transfer function of the modulator whilst converting the electrical signal into an optical signal, as shown in Fig. 2.8 [22, Ch. 2]. To achieve high-order modulation formats using only binary signals is also possible but it requires phase-stabilized fibre interferometer, as demonstrated in [22]. These approaches increase the optical complexity and reduce the robustness of the transmitter. A simpler method, enabled by high-speed digital-to-analogue converters (DACs), is to use multilevel driving signals that are generated by the DACs and drive each modulator at its linear regime (quadrature point), as shown in Fig. 2.8. In this case though, the electrical noise is directly translated into optical noise.

On the other hand, although the linear field modulation is required to generate a subcarrier modulated signal, (direct detection optical OFDM (DDO-OFDM) or Nyquist-subcarrier modulation (SCM)), the modulator should be biased at its linear regime but not necessarily at its quadrature point to achieve a linear transformation between the two domains. The operation point in the linear regime depends on the required optical carrier power value for the transmitted signal. DD-MZM, single and dual polarization IQ-modulators are used experimentally to generate the subcarrier modulated signals and detailed in chapters 4 and 5.

2.3 Detection techniques

Fundamentally, there are three types of optical detection technique, namely direct (square-law) detection, balanced detection and coherent detection. In this section, the principles of these three detection methods, that are utilized to detect the modulation formats implemented in this thesis, are discussed. The output photocurrents generated after the detection are studied theoretically and their applications are briefly discussed.

2.3.1 Direct (square-law) detection

A simple direct detection receiver is a single-ended photodetector (PD), as shown in Fig. 2.9. It detects the envelope of the optical signal. The output photocurrent ($i_s(t)$) is proportional to the responsivity of the photodiode and given by

$$\begin{aligned} i_s(t) &\propto E_s(t)E_s^*(t) \\ &\propto \left[A_s(t)e^{j\omega_s t}e^{j\phi_s}\right]\left[A_s^*(t)e^{-j\omega_s t}e^{-j\phi_s}\right] \\ &\propto |A_s(t)|^2, \end{aligned} \tag{2.29}$$

where $E_s(t)$ is the optical field of a signal, t is the time index and * represents complex conjugate. $A_s(t)$ is the complex amplitude of the optical signal varying in time, $\omega_s(t)$ and $\phi_s(t)$ are the angular frequency and the phase of the signal, respectively. Since the phase information is lost upon detection, the symbol decision is purely based on the received optical power, $|A_s(t)|^2$.

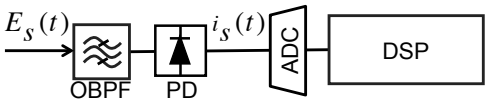

Fig. 2.9: A schematic of a direct detection receiver.

The simplest modulation formats that can be detected using a single-ended PD are on-off keying (OOK), so-called 2-level pulse amplitude modulation (PAM), and duobinary [23]. However, their information spectral densities (ISDs) are limited to 1 bit/s/Hz as only 1 bit-per-symbol is transmitted. To encode more than 1 bit-per-symbol, multiple amplitude levels need to be modulated such as 4-PAM, but it has poor receiver sensitivity performance since it uses only one degree-of-freedom, the amplitude of the optical field [24]. This degradation in receiver sensitivity performance limits the transmission distance. Thus, subcarrier modulation (SCM) becomes attractive since it enables QAM signalling in direct detection links, and consequently, higher ISDs with reasonable receiver sensitivity can be achieved using cost-effective transceiver architectures, described in chapter 3.

In direct-detection SCM systems, an optical carrier $E_c(t)$ is added to the subcarrier modulated signal ($E_{sc}(t)$) at the transmitter and they co-propagate in the fibre. An optical carrier is required to recover the phase and amplitude of the subcarrier modulated QAM symbols in such systems. Considering a noisy channel, the transmitted signal in direct detection links is the sum of $E_c(t)$, $E_{sc}(t)$ and ASE-noise ($E_{ASE}(t)$). After the photodetection, the output photocurrent contains 6 mixing products, as shown in Fig. 2.10 with the corresponding optical spectrum.

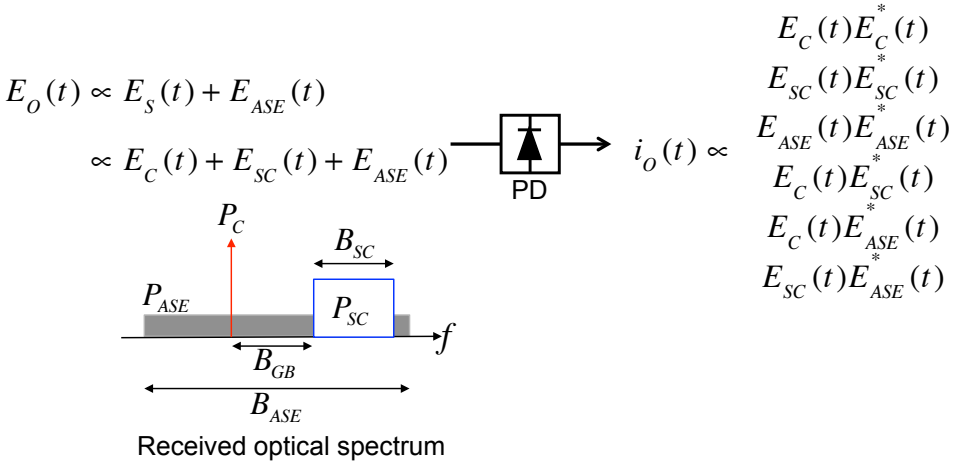

Fig. 2.10: The optical spectrum of a SCM signal in direct detection links and the resultant mixing products after photodetection. P_C, P_{SC}, and P_{ASE} are the optical carrier power, subcarrier modulated signal power and ASE-noise power whereas B_{GB}, B_{SC} and B_{ASE} are the bandwidth of the guard band, subcarrier modulated signal and ASE-noise, respectively.

The ASE-noise is unpolarized and band-limited by an optical band-pass filter (OBPF) before detection in order to filter out-of-band noise, as depicted in Fig. 2.9. The output photocurrent after the detection is analytically represented in Fig. 2.10. Some of these mixing products become electrical noise after the detection and it is not possible to distinguish from the desired signal ($E_c(t) \times E_{sc}(t)$) using a single-ended PD. The explanation of the mixing products in electrical domain are listed below and further discussions can be found in [25, 26].

(i) $E_c^2(t)$: The optical carrier-optical carrier beating which can be simply removed by AC-coupled detection using a DC-block or a pre-amplifier before the analogue-to-digital converter (ADC).

(ii) $E_{sc}^2(t)$: The signal-signal beating that is unwanted tones between the subcarrier signal and optical carrier. In direct detection systems, this causes a penalty which can be avoided through the use of a spectral gap $B_{gap} \geq B_{sc}$ between the optical carrier and subcarrier signal in order to avoid interference with the desired signal. Alternatively, it can be rejected using balanced detection.

(iii) $E_{ASE}^2(t)$: The ASE-ASE-noise beating that mainly falls on the frequencies close to 0 and linearly decreases towards higher frequencies. This component can be removed using a balanced coherent receiver.

(iv) $E_c(t) \times E_{sc}(t)$: The optical carrier-signal beating which is the desired recovered SCM signal. The carrier-to-signal power ratio determines the receiver sensitivity performance at high OSNR levels.

(v) $E_c(t) \times E_{ASE}(t)$: The optical carrier-ASE-noise (at the same polarization as the signal) beating that mixes with the desired signal, determines the receiver sensitivity of the system at low OSNR levels.

(vi) $E_{sc}(t) \times E_{ASE}(t)$: The signal-ASE-noise beating (at the same polarization) that produces some in-band electrical noise. It can be eliminated using a balanced coherent receiver.

2.3.2 Balanced detection

As discussed in the previous section, the desired signal is the beating between the optical carrier and modulated signal. However, other beating terms may distort the signal and degrade the receiver sensitivity performance significantly. To increase the detection quality, balanced detection instead of direct detection can be utilized. In balanced detection, two optical signals are first coupled, and then, detected using two similar photodiodes. The resulting photocurrents are amplified differentially in order to reject the common modes or direct detection terms (i, ii and iii discussed above), offering higher signal-to-noise ratio (SNR) compared to direct detection [7]. The rejection quality is quantified through the common mode rejection ratio (CMRR) [27] and measured in dB. It is defined by

$$\text{CMRR(dB)} = 10\log_{10}\left(\frac{\Delta i(t)}{|i_+(t)| + |i_-(t)|}\right), \tag{2.30}$$

where $\Delta i(t)$ is the output photocurrent when both ports of the balanced photodetector (BPD) are illuminated, and $i_+(t)$ and $i_-(t)$ are the output photocurrents when only one port of the BPD is illuminated, as shown in Fig. 2.11. CMRR indicates the similarity of the photodiodes (responsivity, polarization dependence, frequency response) and is specified as a function of frequency. BPDs can offer up to a 3 dB better receiver sensitivity depending on their CMRR. Typically, 15 dB of CMRR is sufficient to have 3 dB SNR gain in comparison to a single-ended PD. Further discussions can be found in [27, 28].

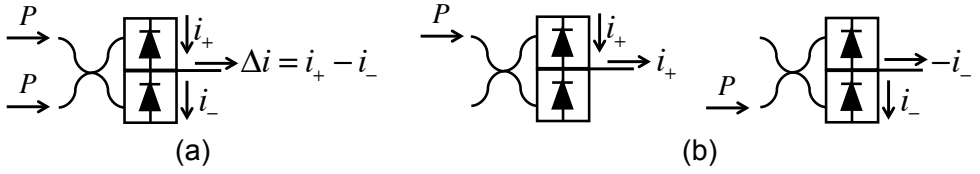

Fig. 2.11: Illumination conditions for determining the CMRR of a BPD. (a) Dual-photodiode and (b) single-ended photodiode illumination).

2.3.2.1 Balanced detection with delay line interferometer

In optical communication links, BPDs are commonly combined with an additional delay-line interferometer (DLI) and used to detect differential phase-shift keying (DPSK) signals that utilize differential encoding/decoding technique [7], as shown in Fig. 2.12.

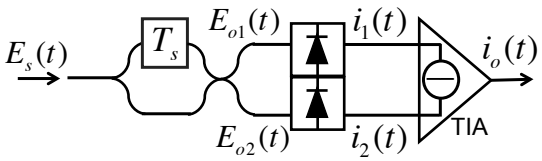

Fig. 2.12: Balanced photodetection using a single BPD with DLI.

The incoming signal $E_s(t)$ is given by

$$E_s(t) = A_s(t)e^{j\omega_s t}e^{j\phi_s}, \tag{2.31}$$

where $A_s(t)$, $\omega_s t$ and ϕ_s are the complex amplitude, angular frequency and the phase of the OPTICAL signal, respectively. It is split into two branches using a 3 dB coupler, and subsequently, one of the branches is delayed using a DLI, as shown in Fig. 2.12. A 3 dB coupler is the simplest optical hybrid to mix two optical signals. It couples two incoming optical fields (E_{i1} and E_{i2}) and its two output ports (E_{o1} and E_{o2}) have a relative π phase difference. It can be expressed in matrix form as follows:

$$\begin{bmatrix} E_{o1} \\ E_{o2} \end{bmatrix} = \begin{bmatrix} 1 & j \\ j & 1 \end{bmatrix} \begin{bmatrix} E_{i1} \\ E_{i2} \end{bmatrix} = \begin{bmatrix} 1 & j \\ j & 1 \end{bmatrix} \begin{bmatrix} E_s(t) \\ E_s(t-T_s) \end{bmatrix} = \begin{bmatrix} E_s(t) + jE_s(t-T_s) \\ jE_s(t) + E_s(t-T_s) \end{bmatrix}, \tag{2.32}$$

The DLI allows detection of differential phase between the symbol of interest and one or more reference symbol(s) by subtracting them from each other. The phase reference is provided by the local oscillator (LO) laser in coherent detection, as explained in the following section. The output photocurrent ($i_s(t)$) is equal to the difference of two photocurrents ($i_1(t)$ and $i_2(t)$) and written as follows:

$$\begin{aligned} i_o(t) &= i_1(t) - i_2(t) \qquad (2.33) \\ &\propto \underbrace{\left\{[E_s(t) + jE_s(t-T_s)]\,[E_s(t) + jE_s(t-T_s)]^*\right\}}_{i_1(t)} - \underbrace{\left\{[jE_s(t) + E_s(t-T_s)]\,[jE_s(t) + E_s(t-T_s)]^*\right\}}_{i_2(t)} \\ &\propto \mathbb{R}\left\{E_s(t)E_s(t-T_s)\right\} \\ &\propto A_s(t)A_s(t-T_s)\cos\left[\omega_s(t-T_s) + \phi_s(t) - \phi_s(t-T_s)\right]. \qquad (2.34) \end{aligned}$$

where $\mathbb{R}$ represents the real part of the complex signal, $A_s(t-T_s)$ and $\phi_s(t-T_s)$ are amplitude and phase of the delayed copy of the original signal $E_s(t)$. T_s is the symbol period and it can be easily adjusted using the DLI. The phase reference is given by $\phi_s(t) - \phi_s(t-T_s)$. This receiver configuration can be used to detect a differential binary phase-shift keying (DBPSK) signal ('1' and '-1' on a Cartesian plane), also known as DBPSK receiver. However, it can only the detect phase different on the real axis (π phase-shift). To detect the modulation schemes like QPSK or M-level phase-shift keying (PSK), an additional DLI with a phase-shift of $\pi/2$ needs to be added (see Fig.2 in [29]). High ISDs ($\geq$2 bits/s/Hz) can be achieved by transmitting high order modulation formats detected utilizing the multiple DPSK receivers. However, the optical complexity of these receivers increases significantly to implement such modulation formats, as further discussed in section 3.

2.3.3 Coherent detection

Unlike direct detection, the coherently detected optical signal can be linearly mapped into an electrical domain (without any loss of information), also referred to as phase-diverse coherent reception. Prior to detection, the incoming optical signal ($E_s(t)$) is mixed with the output of a continuous wave (CW) LO

laser ($E_{LO}(t)$) before the photodetector (photodiode and trans-impedance amplifier (TIA)) using a 3 dB coupler, as shown in Fig. 2.13.

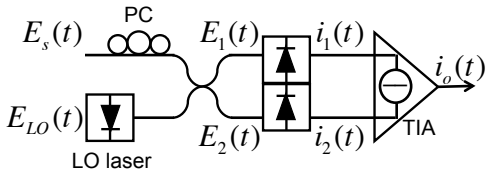

Fig. 2.13: Principle of coherent detection. PC: polarization controller, TIA: trans-impedance amplifier.

$E_{LO}(t)$ can be written as

$$E_{LO}(t) = A_{LO} e^{j\omega_{LO}t} e^{j\phi_{LO}}, \tag{2.35}$$

where A_{LO}, $\omega_{LO}(t)$ and ϕ_{LO} are the constant complex amplitude, angular frequency and the phase of the LO laser, respectively. Typically, balanced detection is used in a coherent receiver to minimize the distortion due to the direct detection terms, as discussed in the previous section 2.3.1. Using a 3 dB coupler adds a 180° phase shift to one of the output ports. To ensure that the state of polarization of the incoming signal and LO laser are aligned, a polarization controller (PC) is used. The output ports of the 3 dB coupler can be written as follows:

$$E_1(t) = \frac{E_s(t) + E_{LO}(t)}{\sqrt{2}} \quad \text{and} \quad E_2(t) = \frac{E_s(t) - E_{LO}(t)}{\sqrt{2}}. \tag{2.36}$$

Hence, the corresponding photocurrents after the photodiodes become

$$\begin{aligned} i_1(t) &\propto E_1(t) E_1^*(t) \\ &\propto \mathbb{R}\left\{ \frac{A_s(t) e^{j\omega_s t} e^{j\phi_s} + A_{LO} e^{j\omega_{LO}t} e^{j\phi_{LO}}}{\sqrt{2}} \right\}^2 \\ &\propto A_s^2(t) + A_{LO}^2 + 2\sqrt{A_s A_{LO}} + \cos(\omega_{IF}(t) + \phi_s(t) - \phi_{LO}(t)) \end{aligned} \tag{2.37a}$$

$$\begin{aligned} i_2(t) &\propto E_2(t) E_2^*(t) \\ &\propto \mathbb{R}\left\{ \frac{A_s(t) e^{j\omega_s t} e^{j\phi_s} - A_{LO} e^{j\omega_{LO}t} e^{j\phi_{LO}}}{\sqrt{2}} \right\}^2 \\ &\propto A_s^2(t) + A_{LO}^2 - 2\sqrt{A_s A_{LO}} + \cos(\omega_{IF}(t) + \phi_s(t) - \phi_{LO}(t)), \end{aligned} \tag{2.37b}$$

where $\mathbb{R}$ represents the real part of the complex signal, $\omega_{IF} = \omega_s - \omega_{LO}$ is the intermediate frequency (IF), so-called frequency offset, and ϕ_s and ϕ_{LO} are the phases of the transmitted signal and LO laser, respectively. Note that the photocurrents $i_1(t)$ and $i_2(t)$ are proportional to the responsivity of the photodiodes but they are not included in Eq.2.37a and Eq.2.37b for simplicity. Finally, the output photocurrent of the BPD is given by

$$i_o(t) \propto i_{1_+}(t) - i_{2_-}(t) \propto \sqrt{A_s A_{LO}} \cos(\omega_{IF}(t) + \phi_s(t) - \phi_{LO}(t)). \tag{2.38}$$

If the transmitter laser has identical frequency to the LO laser, so-called homodyne detection, ω_{IF} becomes (almost) zero and only the in-phase (I) component of an optical signal can be detected. In this case, 90° optical hybrid is required to detect the quadrature (Q) component and the output photocurrent ($i_Q(t)$) can be written as

$$i_Q(t) \propto i_{1_+}(t) - i_{2_-}(t) \propto \sqrt{A_s A_{LO}} \sin(\omega_{IF}(t) + \phi_s(t) - \phi_{LO}(t)). \tag{2.39}$$

In coherent detection with homodyne reception, only phase noise compensation (PNC) needs to be performed in DSP to recover the transmitted symbols. There is no need to perform frequency offset (FO) correction. However, it is not feasible in real systems. Practically, a different laser source is used as a LO and the incoming optical signal is detected at an ω_{IF}, *i.e.,* the signal is centered around ω_{IF}. If the IF is lower than the symbol rate f_s, it is referred to as intradyne detection. This technique also requires a 90^o optical hybrid to recover the Q-component. When the IF is equal or larger than f_s, it is referred to as heterodyne detection. To reconstruct the I- and Q-components of a complex signal in heterodyne detection, down-conversion is performed digitally using two orthogonal RF-carriers.

A SSMF supports two orthogonal polarization modes, as discussed in section 2.1.2. Both polarization states can be detected simultaneously using a pair of single phase-diverse homodyne or heterodyne receiver combined with a PBS [30, Ch.2, pp. 38–40] [2, Ch.3, pp. 56–58] [29], so-called polarization- and phase-diverse receiver. Such receiver architecture has become standard for long-haul systems. However, it is still an open question if coherent technology will be suitable for short and medium links. The complexity of various coherent receivers with homodyne and heterodyne reception is analyzed and compared more in depth in chapter 5.

2.4 References

[1] International Telecommunication Union, "Optical system design and engineering - supplement 39," 2008.

[2] C. Behrens, "Mitigation of nonlinear impairments for advanced optical modulation formats," Ph.D. dissertation, University College London (UCL), 2012.

[3] G. Agrawal, *Applications of nonlinear fiber optics*, Academic press, 2010.

[4] E. Desurvire, D. Bayart, B. Desthieux, and S. Bigo, *Erbium-doped fiber amplifiers: Device and system developments*, Wiley-Interscience, 2002, vol. 2.

[5] G.P. Agrawal, "Applications of nonlinear fiber optics," 3rd edition, Academic press, 2010.

[6] H. Kogelnik, R.M. Jopson, and L.E. Nelson, "Polarization-mode dispersion," in Optical Fiber Telecommunication, I. Kaminow and T. Li, Eds. New York: Academic, 2002, pp. 725–861.

[7] P.J. Winzer and R.-J. Essiambre, "Advanced modulation formats for high-capacity optical transport networks," *J. Lightw. Technol.*, vol. 24, no. 12, pp. 4711–4728, 2006.

[8] S.J. Savory, "Digital filters for coherent optical receivers," *Optics Express*, vol. 16, no. 2, pp. 804–817, 2008.

[9] Z. Wang, C. Xie, and X. Ren, "PMD and PDL impairments in polarization division multiplexing signals with direct detection," *Optics express*, vol. 17, no. 10, pp. 7993–8004, 2009.

[10] C.D. Poole and J. Nagel, "Polarization effects in lightwave systems," *Optical Fiber Telecommunications IIIA*, pp. 114–161, 1997.

[11] R.A. Meyers, *Encyclopedia of physical science and technology*, Academic Press, 1992, vol. 12.

[12] S. J. Savory, "Digital coherent optical receivers: algorithms and subsystems," *J. Selected Topics in Quantum Electron*, vol. 16, no. 5, pp. 1164–1179, 2010.

[13] F. Buchali, R. Dischler, and X. Liu, "Optical OFDM: A promising high-speed optical transport technology," *J. Bell Labs Technical*, vol. 14, no. 1, pp. 125–146, 2009.

[14] R. A. Griffin, S. K. Jones, N. Whitbread, S. C. Heck, and L. N. Langley, "InP Mach–Zehnder modulator platform for 10/40/100/200-Gb/s operation," *J. Selected Topics in Quantum Electron.*, vol. 19, no. 6, pp. 158–166, 2013.

[15] N. Kikuchi, E. Yamada, Y. Shibata, and H. Ishii, "High-speed InP-based Mach–Zehnder modulator for advanced modulation formats," in *Proc. IEEE Compound Semiconductor Integrated Circuit Symp. (CSICS)*, 2012, pp. 1–4.

[16] E. Rouvalis, C. Metzger, A. Charpentier, T. Ayling, S. Schmid, M. Gruner, D. Hoffmann, M. Hamacher, G. Fiol, and M. Schell, "A low insertion loss and low V_π InP IQ modulator for advanced modulation formats," in *Proc. IEEE European Conference on Optical Communication (ECOC)*, 2014, paper Tu.4.4.1.

[17] M. Seimetz, *High-order modulation for optical fiber transmission*, Springer, 2009, vol. 143.

[18] K.-P. Ho and H.-W. Cuei, "Generation of arbitrary quadrature signals using one dual-drive modulator," *J. Lightw. Technol.*, vol. 23, no. 2, pp. 764–780, 2005.

[19] S. Kametani, T. Sugihara, and T. Mizuochi, "16-QAM modulation by polar coordinate transformation with a single dual drive Mach–Zehnder modulator," in *Proc. IEEE/OSA Optical Fiber Communication Conference*, 2009, paper OWG6.

[20] D.J. Fernandes Barros and J.M. Kahn, "Optical modulator optimization for orthogonal frequency-division multiplexing," *J. Lightw. Technol.*, vol. 27, no. 13, pp. 2370–2378, 2009.

[21] E. L. Wooten, K. M. Kissa, A.Y.-Yan, E.J. Murphy, D. Lafaw, P.F. Hallemeier, D. Maack, D.V. Attanasio, D.J. Fritz, G.J. McBrien, "A review of Lithium Niobate modulators for fiber-optic communications systems," *J. Selected Topics in Quantum Electron.*, vol. 6, no. 1, pp. 69–82, 2000.

[22] S. Makovejs, D.S. Millar, V. Mikhailov, G. Gavioli, R.I. Killey, S.J. Savory, and P. Bayvel, "Novel method of generating QAM-16 signals at 21.3 GBaud and transmission over 480 km," *IEEE Photon. Technol. Lett.*, vol. 22, no. 1, pp. 36–38, 2010.

[23] E. Pincemin, C. Gosset, N. Boudrioua, A. Tan, D. Grot, and T. Guillossou, "Experimental performance comparison of duobinary and PSBT modulation formats for long-haul 40 Gb/s transmission on G 0.652 fibre," *Optics Express*, vol. 20, no. 27, pp. 28171–28190, 2012.

[24] J. Wei, J. Ingham, D. Cunningham, R. Penty, and I. White, "Performance and power dissipation comparisons between 28 Gb/s NRZ, PAM, CAP, and optical OFDM systems for data communication applications," *J. Lightw. Technol.*, vol. 30, no. 20, pp. 3273–3280, 2012.

[25] A.J. Lowery, "Amplified-spontaneous noise limit of optical OFDM lightwave systems," *Optics Express*, vol. 16, no. 2, pp. 860–865, 2008.

[26] A.J. Lowery, "Improving sensitivity and spectral efficiency in direct-detection optical OFDM systems," in *Proc. IEEE/OSA Optical Fiber Communication Conference*, 2008, paper OMM4.

[27] H.-G. Bach, "Ultra-broadband photodiodes and balanced detectors towards 100 Gbit/s and beyond," in *Proc. SPIE 6014*, Active and Passive Optical Components for WDM Communications V, 60140B, 2005.

[28] Y. Painchaud, M. Poulin, M. Morin, and M. Tŕtu, "Performance of balanced detection in a coherent receiver," *Optics express*, vol. 17, no. 5, pp. 3659–3672, 2009.

[29] E. Ip, A.P.T. Lau, D.J. Barros, and J.M. Kahn, "Coherent detection in optical fiber systems," *Optics Express*, vol. 16, no. 2, pp. 753–791, 2008.

[30] D. Lavery, "Digital coherent receivers for passive optical networks," Ph.D. dissertation, University College London (UCL), 2013.

Chapter 3

Transceiver Architecture and Literature Review on Non-coherent Modulation Schemes

The purpose of this chapter is to provide an extensive literature review regarding the various modulation formats that can be detected without using a local oscillator (LO) laser (non-coherent detection). The review is presented in section 3.1 focusing on the achieved information spectral densities (ISDs). Following this, the digital signal processing (DSP) subsystems of two spectrally-efficient subcarrier modulation (SCM) formats used in their transceiver architecture are described in section 3.2.

3.1 Literature review on non-coherent modulation schemes

Until recently, most deployed optical transmission systems have been based on non-coherent detection and use binary modulation schemes, namely on-off keying (OOK) or duobinary, operating at a bit rate of 10 or 40 Gb/s per wavelength or channel (λ). The main reason for this is that they can be implemented using a cost-effective optical transceiver architecture. Such modulation schemes can be detected using the simplest optical receiver, that is a single-ended photodiode without a delay-line interferometer (DLI). However, they can only offer ISDs of up to 1 b/s/Hz, encoding 1 bit-per-symbol. Thus, it became challenging to meet rapidly increasing bandwidth demand due to data intensive services such as IP-TV, high-definition video-on-demand and cloud computing in direct detection links over access, metropolitan and regional distances. To utilize the available optical bandwidth more efficiently, by increasing the achievable information spectral density (ISD), higher order modulation schemes encoding $\log_2(M)$ bits-per-symbol, *e.g.,* M-quadrature amplitude modulation (QAM) or M-phase-shift keying (PSK) inherited from digital/wireless communication, needed to be implemented. QAM signalling utilizes multiple amplitude and phase levels of an optical field whereas PSK signalling encodes the signal using only a single amplitude level with phases of $2\pi n/M$ where $0 \leq n \leq M-1$. QAM signalling is preferable to the M-PSK format since it requires lower signal-to-noise ratio (SNR) for the same values of M due to the larger Euclidean symbol spacing [1, Ch.3].

Multi-level and multi-dimensional modulation formats, *e.g.,* QAM with polarization multiplexing, using coherent receivers combined with DSP-based compensation of fibre impairments [2] enable the highest channel bit rates and ISDs [3–5]. However, cost-effectiveness is another essential requirement for short- and medium-haul links, in which direct detection might be more attractive due to its lower

optical complexity, as also discussed in chapter 1. Recently, service providers have started deploying 100 Gb/s metro solutions on a 100 GHz grid (offering a net optical ISD of 1 b/s/Hz) based on 4×28 Gb/s direct detection technology [6]. Thus, transceivers offering ISDs greater than 1 b/s/Hz will be required in the near future.

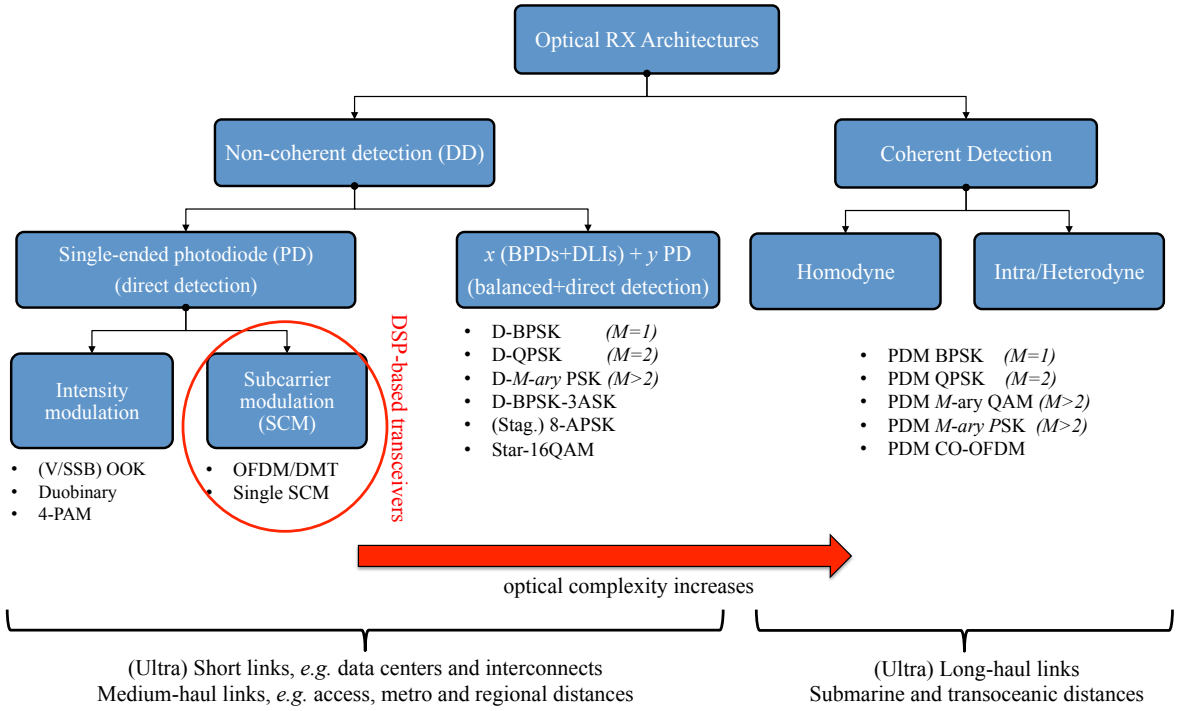

Fig. 3.1: The proposed signal modulation schemes for optical communication links.

As an alternative to binary coding, Nyquist pulse-shaped four-level pulse amplitude modulation (PAM) (Nyquist 4-PAM), a simple and low complexity multi-level format potentially offering an ISD greater than 1 b/s/Hz can be used. However, it suffers from low receiver sensitivity as it uses only one degree-of-freedom. Yet, it is attractive for (ultra) short distances, *e.g.,* interconnects and intra-data centers applications [7]. Moreover, *M*-ary differential phase-shift keying (DPSK) schemes are proposed using one or more balanced photodetectors (BPDs) combined with DLIs, as presented in Fig. 3.1. However, they come at the expense of higher optical receiver complexity.

With the innovations in silicon complementary metal oxide semiconductor (CMOS) technology, particularly high-speed digital-to-analogue converters (DACs)/analogue-to-digital converters (ADCs), the complexity shifts from the optical to electrical domain to achieve high ISD in direct detection systems. Thus, DSP-enabled optical transceivers using direct detection receivers, *i.e.,* consisting of a single-ended photodiode with no DLIs, offer promising and practical solutions for metro and access links. Subcarrier modulation which enables QAM signalling, becomes the most promising and practical format, and therefore, is starting to be implemented using DSP-based optical transceiver architectures, as discussed in section 3.1.4.

In this section, the modulation techniques used in optical fibre communications links are divided into three categories, focusing on their bits-per-symbol capacity. First, intensity modulation formats, and then, differential *M*-ary phase-shift keying schemes are discussed including their transceiver architecture. Finally, SCM formats are described. Among the published studies, the notable single polarization wavelength division multiplexing (WDM) direct detection demonstrations using such techniques are

also summarized in tables, listing the modulation format, achieved ISD, line-rate, capacity, reach, and the optical components used in transceiver architecture with fibre type(s). Only single polarization transmissions are considered in this discussion since a polarization-multiplexed signal requires much higher optical receiver complexity and a fast optical polarization mode dispersion (PMD) controller, which increases the cost in direct detection links.

3.1.1 Intensity modulation formats

3.1.1.1 On-off keying (OOK)

On-off keying is the simplest modulation scheme for optical data transmission links. The transmitter sends a high or low optical power to encode a '1' or a '0', respectively. A single bit of information is modulated onto the amplitude (intensity) of an optical carrier using a single-drive modulator or a directly modulated laser and detected by a single-ended photodetector (PD). Following the detection, the analogue signal is converted into a digital signal after sampling and quantization by a 1-bit ADC. Finally, the transmitted bits are recovered by the decoder, as shown in Fig. 3.2.

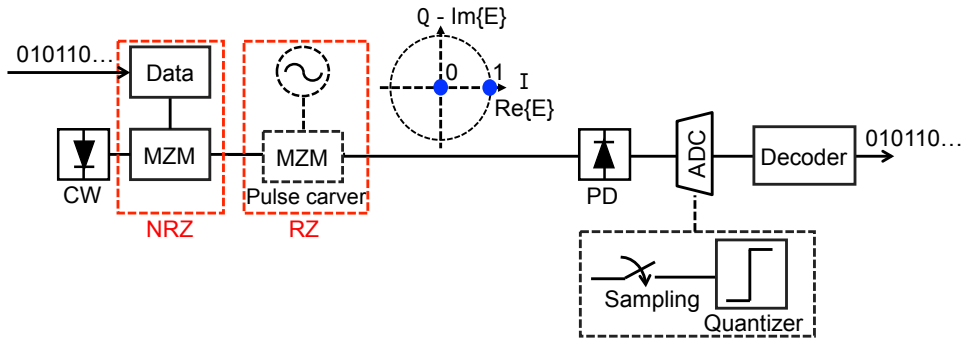

Fig. 3.2: Transceiver design for NRZ- and RZ-OOK signal generation and detection.

On-off keying can be divided into two groups, called NRZ if the power level stays constant between the consecutive '1's and RZ if the power level returns to the '0' level in the same time slot. Moreover, RZ-OOK pulses with duty cycles of 33%, 50%, and 67%, so-called carrier-suppressed RZ (CS-RZ), can be generated using a pulse carver, typically an additional single-drive Mach-Zehnder modulator (MZM) driven sinusoidally after optical modulation [8]. These different duty-cycle signals are dependent on the amplitude and biasing point of the sinusoidal driving signal. Further discussions regarding the generation of RZ-formats using a pulse carver and different modulator technologies can be found in [8, 9].

The duration of a RZ pulse occupies a part of the bit slot which gives more transition points from '1' to '0' as opposed to NRZ. Fourier transform theory indicates that if the duration of a pulse in time is shorter, the frequency spectrum gets wider [9]. Therefore, the optical spectra of RZ formats are broader than NRZ. Although this characteristic provides an increased robustness to fibre nonlinearities due to reduced power spectral density [10] that is essential for (ultra) long-haul transmission over more than 1000 km, it is not desirable for metro and regional applications since it offers a reduced chromatic dispersion tolerance and lower ISD (typically less than 0.5 b/s/Hz) [11, 12]. Among the RZ formats, 33% RZ pulse has the highest resilience to fibre nonlinearities, as it has the widest spectrum [8, 9, 42].

Several NRZ-OOK experiments at ISDs of less than 0.5 b/s/Hz without the use of optical filtering at the transmitter have been demonstrated for submarine links [13, 14]. To increase the achievable ISD and improve the dispersion tolerance, one of the sidebands can be partially suppressed, referred to as vestigial sideband (VSB) signalling, or fully removed, referred to as single sideband (SSB) signalling, using an

optical filter. Since the spectrum of a real-valued baseband signal is symmetric around zero frequency, theoretically, one of the side-bands can be filtered out whilst preserving the full information content and square-law detectability. The difference between these two signal formats is that in SSB signalling, one of the sidebands is completely suppressed by modulating the optical field with its $\pi/2$ phase-shifted Hilbert transform (HT) and the signal itself. In VSB signalling, part of one of the sideband is suppressed using an optical filter with a defined roll-off and offset from the optical carrier frequency. Therefore, a real-valued double sideband signal is converted into a complex-valued (chirped) VSB or SSB signal. SSB signalling is hard to implement using an optical filter in practice since it requires a very steep profile for the optical filter and the implementation of broadband HT is problematic [15, 16]. Using VSB-OOK signalling, the experimental demonstrations with ISDs of from 0.64 to 1 b/s/Hz have been reported at 40 and 100 Gb/s [17–21]. To increase the dispersion resilience of CS-RZ, VSB can be also performed. It has been successfully demonstrated at 40 Gb/s per channel achieving an ISD of 0.8 b/s/Hz over transoceanic links [22] and 1 b/s/Hz over metro distances [23, 24]. The details for the experimental setups of these demonstrations are given in Tab. 3.1.

3.1.1.2 Duobinary

NRZ- and RZ-OOK formats have been used for decades at up to 10 Gb/s in optical communication. However, beyond 10 Gb/s, increasing the bit rate per channel to 40 Gb/s or 100 Gb/s using OOK, significant penalties are observed incurred due to chromatic dispersion and PMD. Hence, as an alternative to VSB or SSB filtering, the optical spectrum of a modulated signal can be compressed by correlative coding [25]. The most widely used one is called duobinary. It is a 3-level format which can be generated using different approaches, *e.g.,* electrical or optical low-pass filtering methods, referred to as electrical or optical phase-shaped binary transmission (PSBT) [26, 27], or optical delay-and-add method, called optical duobinary [28].

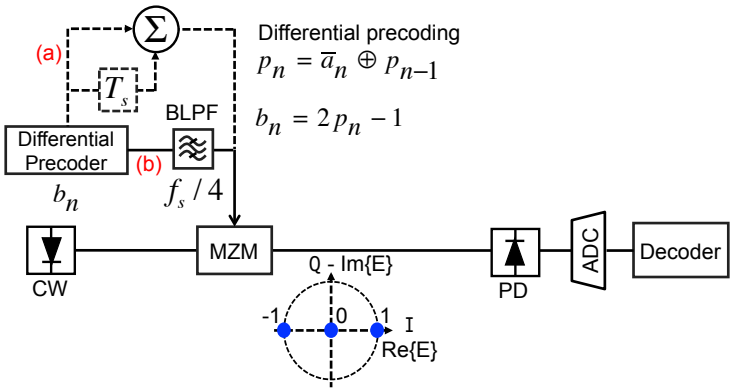

Fig. 3.3: Transceiver design for duobinary signal generation and detection using (a) a delay-and-add circuit or (b) Bessel LPF with a bandwidth of $f_s/4$.

To generate a duobinary signal, precoded data (b_n) is generated applying differential precoding on the binary data-stream (a_n) using an XOR-gate. It combines the bit with its predecessor (p_{n-1}). Subsequently, p_n is passed through a delay-and-add circuit or a Bessel LPF with a 3 dB bandwidth of 25% of the symbol rate ($f_s/4$), as shown in Fig. 3.3. A relative π phase-shift occurs when the number of '0's is odd between two '1's. Hence, it is a phase modulation in addition to an intensity modulation. Finally, the 3-level signal is used to drive a push-pull MZM around its minimum transmission (null) point (for different duobinary transmitter configurations, see [29]). This type of correlative coding does not increase

the system throughput since the phase modulation is lost upon detection, *i.e.,* '-1' levels overlaps with '1' levels after square-law detection. However, it gives an ability to combat chromatic dispersion more effectively compared to NRZ. The reason is that '0' levels are preserved better due to the destructive interference of '+1' and '-1' levels [30, 31]. The spectral compression of duobinary results from smoother transitions between '+1', '0' and '-1' compared to the sharper transitions between '+1', '0' and '+1' in OOK.

Besides an increased dispersion tolerance, the narrow optical spectrum offers a higher ISD than OOK (typically $\leq$ 0.8 b/s/Hz, *i.e.,* 42.7 Gb/s in 50 GHz WDM channel spacing assuming a 7% hard-decision forward error correction (HD-FEC) overhead), and better receiver sensitivity due to no optical carrier being required. Such abilities make duobinary signalling favorable for dense wavelength-division multiplexing (DWDM) metro and core applications. Today, duobinary formats are considered as being the most promising cost-effective solutions for the deployment of 40 Gb/s technology on existing 10 Gb/s WDM long-haul transmission infrastructures [27]. Duobinary signalling has been demonstrated for 40 Gb/s per channel links at an ISD of 0.6 b/s/Hz [32], 0.8 b/s/Hz [20, 33], and 1 b/s/Hz [34], as presented in Tab. 3.1.

Tab. 3.1: Notable experimental demonstrations of single polarization WDM OOK and duobinary (PSBT) signal.

Mod. scheme	net ISD (b/s/Hz)	Line rate (Gb/s)	Reach (km)	Fibre type	# of ch.	TX	RX	Year/Ref.
Duobinary	1	112	580	SSMF+DCF	4	DFB+MZM	PD	2015 / [34]
VSB-NRZ	1	107	510	NZ-DSF+DCF	80	DFB+MZM+OF	PD	2009 / [35]
VSB-NRZ	1	107	480	SSMF+DCF	8	DFB+MZM+OF	PD	2007 / [21]
CS-RZ	1	42.7	320	SSMF+DCF	25	DFB+2 MZMs	PD	2002 / [23]
CS-RZ	0.8	42.7	1280	SSMF+DCF	128	DFB+2 MZMs	PD	2002 / [22]
PSBT	0.8	42.7	2700	NZ-DSF+DCF	158	DFB+MZM	PD	2003 / [36]
PSBT	0.8	42.7	1700	SSMF+DCF	158	DFB+MZM	PD	2002 / [20]
PSBT	0.8	42.7	300	SSMF+DCF	80	DFB+MZM	PD	2001 / [33]
PSBT	0.6	20	120	SSMF+DCF	132	DFB+MZM	PD	1998 / [32]
VSB-NRZ	0.8	42.66	300	LEAF+DCF	80	DFB+MZM+OF	PD	2002 / [19]
NRZ	0.7	107	1000	NZDF+DCF	10	DFB+MZM	PD	2007 / [37]
VSB-NRZ	0.64	42.7	1200	LEAF+DCF	125	DFB+MZM+OF	PD	2001 / [17]
NRZ	0.45	11.6	6850	SSMF+DCF	365	DFB+MZM	PD	2001 / [14]
RZ	0.4	11.6	7000	SSMF+DCF	180	DFB+2 MZMs	PD	2000 / [13]
RZ	0.25	10	11000	SSMF+DCF	256	DFB+2 MZMs	PD	2002 / [38]
standard single-mode fibre (SSMF) non-zero dispersion fibre (NZDF)			non-zero dispersion shifted fibre (NZ-DSF) dispersion compensating fibre (DCF)			large effective area fibre (LEAF) optical filter (OF)		

3.1.2 Differential phase modulation formats

The intensity modulation formats encode the data onto the amplitude of the optical field alone, since the absolute phase is lost due to square-law detection principle, as discussed in section 2.3.1. Therefore, the phase cannot be recovered. To increase the ISD, differential encoding scheme, in which each bit behaves as a phase reference for the subsequent bits, is introduced to enable data transmission using phase information in balanced-detected systems [39].

3.1.2.1 Differential binary (M =2) phase-shift keying (DBPSK)

The data is encoded on the binary phase changes between adjacent bits with some differential precoding, similar to duobinary. '1' is encoded onto a π phase change whereas '0' is represented by no phase

change. It is worth noting that, in experiments, if a pseudo-random binary sequence (PRBS) is used as the test bit-sequence, differential precoding can be bypassed since it has no effect on PRBS [40].

The same transmitter architecture for RZ- or NRZ-OOK can be used to generate differential binary phase-shift keying (DBPSK). Compared to OOK signalling, the symbol spacing for DBPSK on the in-phase and quadrature (IQ)-plane increases by a factor of $\sqrt{2}$ at a fixed average optical power. In order to recover the phase information of an optical signal without using a LO, it needs to be converted to intensity modulation before detection. To achieve this, a single BPD with a DLI and a 3 dB couplers are required to detect the DBPSK signal, as shown in Fig. 3.4 and discussed theoretically in section 2.3.2. The incoming light is first split into two branches using a 3 dB coupler. Using a DLI, one of the branches is delayed by one symbol period, *i.e.,* 25 ps for a 40 Gb/s signal. Consequently, two adjacent bits interfere either constructively or destructively so that the preceding bit in DBPSK bit stream can be used as a phase reference during demodulation. It is worth noting that this phase reference is provided by the LO laser in coherent detection. In principle, a single-ended photodetector (direct detection) is sufficient to detect a DBPSK signal [39]. However, commonly, a BPD is used to achieve ∼3 dB optical signal-to-noise ratio (OSNR) gain over OOK signalling at a given bit error rate (BER) due to the increased symbol spacing [41].

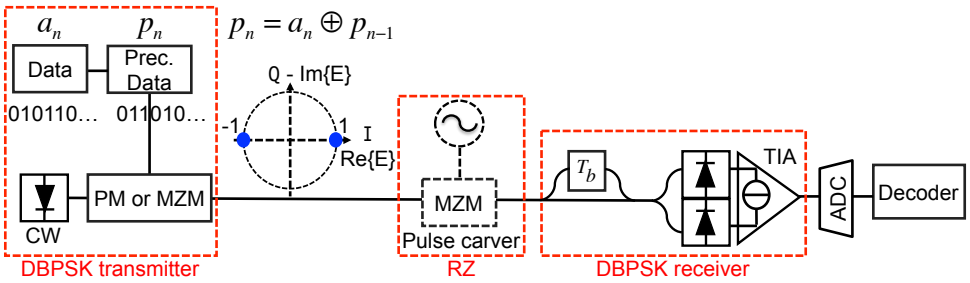

Fig. 3.4: Transceiver design for DBPSK signal generation and detection.

The maximum achievable ISD using DBPSK is 1 b/s/Hz per polarization regardless of signal generation/detection technique since it uses binary modulation, similar to OOK or duobinary. Thus, beyond 40 Gb/s, binary modulation scheme is not practical due to the bandwidth limitations of optical and electrical components. Moreover, DBPSK is not very attractive for metropolitan or regional applications due to its optical receiver complexity. Nevertheless, there have been several experimental demonstrations, field trials for (ultra) long-haul transmission to evaluate its tolerance against fibre nonlinearity, as summarized in Tab. 3.2 focusing on the achieved ISD, and commercial exploitation of the technology. In a field trial over 13,100 km of installed submarine fibre at 10 Gb/s with an ISD of 0.3 bits/s/Hz, the nonlinear transmission performance of RZ-DBPSK was found to be similar to OOK in terms of the optimum launch power levels [42]. The same group reported another field trial at 40 Gb/s with an ISD of 0.8 bits/s/Hz over a transoceanic distance [43]. In this case, RZ-DBPSK performed slightly better than RZ-OOK.

3.1.2.2 Differential quadrature (M =4) phase-shift keying (DQPSK)

To increase the ISD beyond 1 b/s/Hz, more than 1 bit-per-symbol should be encoded onto the optical field. One of the first multi-level modulation formats was differential quadrature phase-shift keying (DQPSK), first proposed by Griffin and Carter [44], that makes use of four optical phase shifts $\{0, +\pi/2, +\pi, -\pi/2\}$ for the symbol encoding of {'00', '01', '11', '01'} at a symbol rate (f_s) of half the aggregate bit rate ($f_b = 2f_s$).

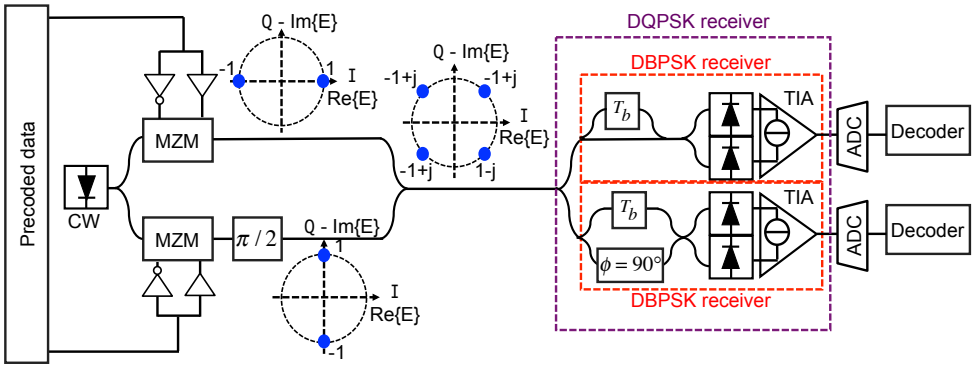

Fig. 3.5: Transceiver design for DQPSK signal generation and detection.

The DQPSK transmitter design requires an IQ-modulator, that consists of 2 nested single-drive MZMs operating as amplitude modulators for in-phase (I) and quadrature (Q) components, and a $\pi/2$ optical phase shifter in one of the paths, as depicted with the corresponding constellations in Fig. 3.5. It requires two binary electrical signals driving the IQ-modulator. A pulse carver can be added to generate a RZ-DQPSK signal [45–47] in order to increase the nonlinear tolerance for (ultra) long-haul transmission. The optical bandwidth of a DQPSK signal is the same as that of a DBPSK signal. Hence, it can potentially double the achievable ISD per polarization compared to the aforementioned modulation schemes. However, this high achievable ISD comes at the expense of optical complexity in the transceiver design. Particularly, the receiver architecture to detect a DQPSK signal requires a complexity twice as high as that used for DBPSK signal detection. The transmitted DQPSK signal is first split into two branches, and subsequently, two DBPSK receivers are used to detect the I- and Q-components, as illustrated in Fig. 3.5. Note that a 90° phase shifter needs to be used to recover the Q-component.

Further discussion about DQPSK signalling can be found in [39]. Several successful DQPSK experiments have been demonstrated so far, using bit rates of 12.5 Gb/s [48], 20 Gb/s [49], 40 Gb/s [50], 80 Gb/s [51], and 100 Gb/s [52] with ISDs of up to 1.6 bits/s/Hz. Some of the notable experimental demonstrations using such modulation schemes are listed in Tab. 3.2.

Tab. 3.2: Notable experimental demonstrations of single polarization WDM DPSK and DQPSK signal.

Mod. scheme	net ISD (b/s/Hz)	Line rate (Gb/s)	Reach (km)	Fiber type	# of ch.	TX	RX	Year/Ref.
CS-RZ-DQPSK	1.14	85.4	300	NZ-DSF+DCF	50	DFB+PM+ DD-MZM	2(BPDs+DLIs)	2005/ [51]
NRZ-DQPSK (FIELD)	1	112	450	SSMF+DCF	16	DFB+IQ-mod.	2(BPDs+DLIs)	2010/ [53]
NRZ-DQPSK	1	107	1,200	NZDF+DCF	10	DFB+IQ-mod.	2(BPDs+DLIs)	2008/ [54]
RZ-DQPSK	0.8	10	1,000	SSMF+DCF	64	DFB+IQ-mod.+ MZM	2(BPDs+DLIs)	2003/ [55]
RZ-DPSK (FIELD)	0.8	40	6,550	NZ-DSF+NDSF	64	DFB+2 MZMs	BPD+DLI	2004/ [43]
NRZ-DPSK	0.8	42.7	4,400	ULLS+DCF	28	DFB+MZM	BPD+DLI	2009/ [56]
CS-RZ-DPSK	0.8	42.7	8,200	LEAF+DCF	64	DFB+2 MZMs	BPD+DLI	2003/ [57]
NRZ-DPSK	0.65	10.7	10,270	LEAF+DCF	301	DFB+MZM	BPD+DLI	2003/ [58]
CS-RZ-DPSK	0.4	42.7	10,000	UW-DMF+DCF	40	DFB+2 MZMs	BPD+DLI	2003/ [59]
RZ-DPSK	0.4	12.3	11,000	LEAF+DCF	373	DFB+2 MZMs	BPD+DLI	2003/ [60]
RZ-DPSK (FIELD)	0.3	12.3	13,100	NZ-DSF+NDSF	96	DFB+2 MZMs	BPD+DLI	2005/ [42]
RZ-DQPSK	0.2	12.5	6,500	LEAF+DCF	64	DFB+IQ-mod.+ MZM	2(BPDs+DLIs)	2004/ [48]
non-dispersion shifted fibre (NDSF)			ultra-low loss fibre (ULLS)			UltraWave dispersion-managed fibre (UW-DMF)		

DPSK modulation schemes have attractive OSNR requirements and very good tolerance against non-linearities [54] as it is a constant amplitude format. However, the distance between the symbols decreases drastically for higher numbers of phase levels (M$>$ 4), and thus, significant reduction of transmission margins is observed through the higher required OSNR values and lower tolerances toward nonlinear impairments [39].

3.1.3 Multi-level ($>$2 bits-per-symbol) modulation formats

Numerous multi-level modulation formats using various combinations of amplitude-shift keying (ASK) and DPSK have been proposed as an alternative to polarization-multiplexing to increase the achievable ISD. Since the receiver design depends on delay detection performed by DLIs to detect phase modulation, there is no need to use 90° optical hybrids and a LO laser unlike a polarization- and phase-diverse coherent receiver.

Although several transceiver configurations for optical 16- and 32-level signal generation have been presented in [61–65], the constellations having $\geq$16 symbols encounter serious challenges in fibre transmission (typically over $\geq$100 km) such as maintaining the stability between the cascaded modulators, unacceptable required OSNR degradation due to very dense symbol spacing, intrinsic low noise tolerance of multi-level ASK and the cost-ineffective optical transceiver configuration due to high optical complexity [66, 67]. Thus, the focus of the discussion is the modulation techniques encoding 2.5, 3 and 4 bits-per-symbol (6-, 8- and 16-level signalling).

DBPSK-3ASK (2.5 bits-per-symbol) signal has three symbol pairs at different amplitude levels. The symbols at each pair have a π differential phase difference between two consecutive symbols. The constellation is shown in Fig. 3.6. The transmitter consists of a splitter and a MZM, driven differentially with the data delayed by N and $N+2$ symbol periods where N is approximately 200 [68]. The modulator is biased at its quadrature point with a peak-to-peak driving amplitude of V_π to generate 3-ASK signalling. Following this, 3-ASK optical signal is passed through the second MZM that is driven by a PRBS signal with a peak-to-peak amplitude of $2V_\pi$ and biased at its minimum transmission (null) point, as shown in Fig. 3.6. A third MZM can be added as a pulse carver to apply RZ pulse-shaping to increase nonlinear resilience, and consequently, improve the long-haul transmission performance. To detect the signal, a DBPSK receiver module needs to be combined with an OOK receiver, as illustrated in Fig.3.6. Experimental demonstration of WDM DBPSK-3ASK signal transmission over 335 km of standard single mode fibre (SSMF) and dispersion compensating fibre (DCF) operating at a bit rate of 100 Gb/s has been reported at an ISD of 1.2 b/s/Hz [68]. The system details are summarized in Tab. 3.3.

Another 6-level modulation scheme is differential 6-ary phase-shift keying (D6PSK) in which the symbols are modulated with a phase difference of $\pi/3$ at a constant amplitude level. First, the DBPSK signal, $[0, \pi]$ phase modulated symbols, is generated using a MZM. Then, a phase modulator in tandem is driven by the optical DBPSK signal and electrical signal with phases of $[-\pi/3, 0, +\pi/3]$, as depicted in Fig. 3.7. The detection can be achieved by using a DQPSK receiver with the corresponding DSP to decode D6PSK symbols. D6PSK signal has a shorter symbol duration, *i.e.,* occupies more bandwidth, than DQPSK signal. Thus, its tolerance to cross-phase modulation (XPM)-induced nonlinear effects caused by the neighboring channels in WDM transmission is higher than DQPSK signal, as demonstrated in [69] over 320 km of both SSMF with in-line dispersion compensation and dispersion shifted fibre (DSF) operating at a bit rate of 100 Gb/s with an ISD of 0.5 bits/s/Hz. However, poor receiver

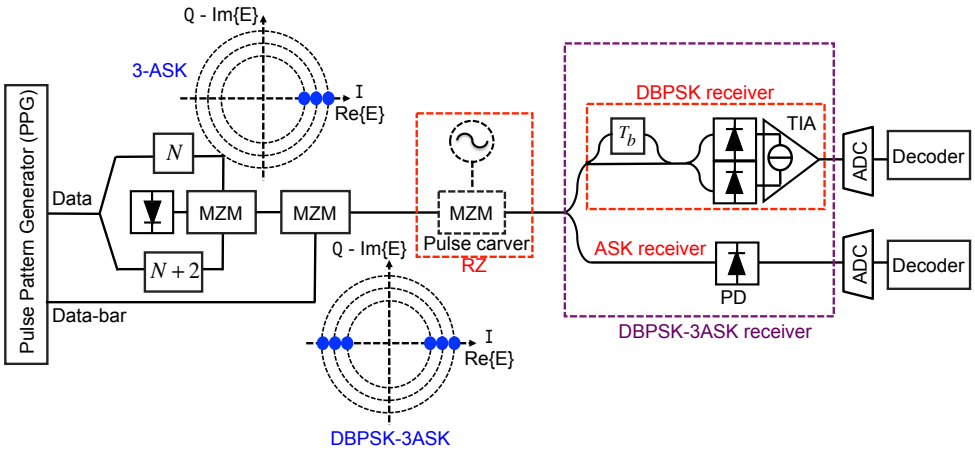

Fig. 3.6: Transceiver design for 3-DBPSK-ASK signal generation and detection.

sensitivity due to dense symbol spacing (utilizing only one amplitude level) reduces the transmission distance significantly compared to DBPSK or DQPSK signal formats.

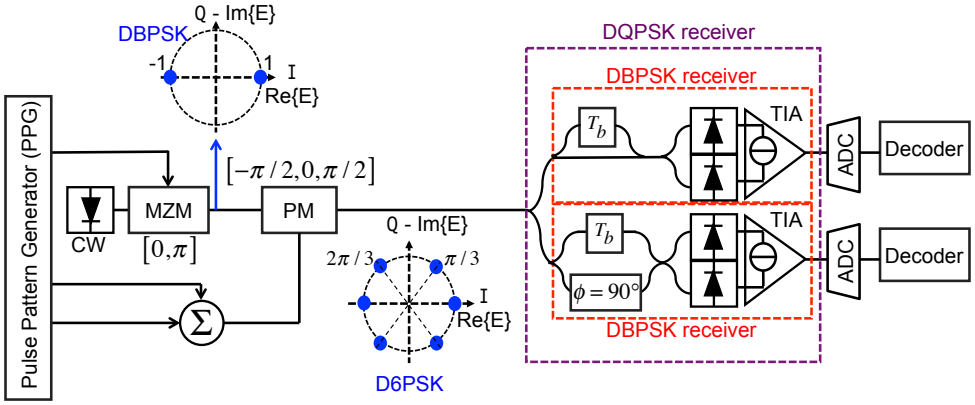

Fig. 3.7: Transceiver design for D6PSK signal generation and detection.

There are two commonly used 8-ary signal formats encoding 3 bits-per-symbol, namely differential quadrature phase (DQP)-ASK and differential 8-ary phase-shift keying (D8PSK). The most common method to generate a D8PSK signal is to combine a quadrature phase-shift keying (QPSK)-transmitter with a phase modulator with $\pi/4$ phase-shift, as shown in Fig. 3.8. It encodes three bits in the phase difference between two consecutive symbols which belong to the set of $\{\pi/8, 3\pi/8, \cdots (2M-1)\pi/8\}$ where $M = 8$. Alternative D8PSK signal generation techniques can be found in [70]. If the QPSK transmitter is combined with the MZM rather than a phase modulator, a DQP-ASK signal, which has two amplitude levels with four different phase modulated symbols at each level, can be generated [71]. Different receiver designs are demonstrated to detect D8PSK signal [72]. A common one is depicted in Fig. 3.8 in which the signal is first split into two branches using a 3 dB coupler. One branch is detected using a single-ended photodiode (ASK receiver) for intensity detection and the other branch is detected using a DBPSK receiver (a BPD combined with the DLI) for differential phase detection.

The notable experimental demonstrations of WDM transmission using 8-level signalling are summarized in Tab. 3.3. It has been shown that the required OSNR for DQP-ASK signal is 2 dB less than the D8PSK signal. Therefore, DQP-ASK signal outperforms D8PSK in WDM transmission up to 400 km. However, beyond 400 km, since D8PSK is more resilient to fibre nonlinearities than DQP-ASK due to its constant amplitude, its BER performance is better at higher launch power values [71]. The first experimental demonstration of 30 Gb/s per channel WDM D8PSK signal transmission over 1040 km

of SSMF and DCF has been reported at an ISD of 1.2 b/s/Hz [73]. Following this, WDM RZ-D8PSK signal transmission over 320 km of SSMF and DCF operating at a bit rate of 120 Gb/s per channel has been demonstrated at the same ISD [74].

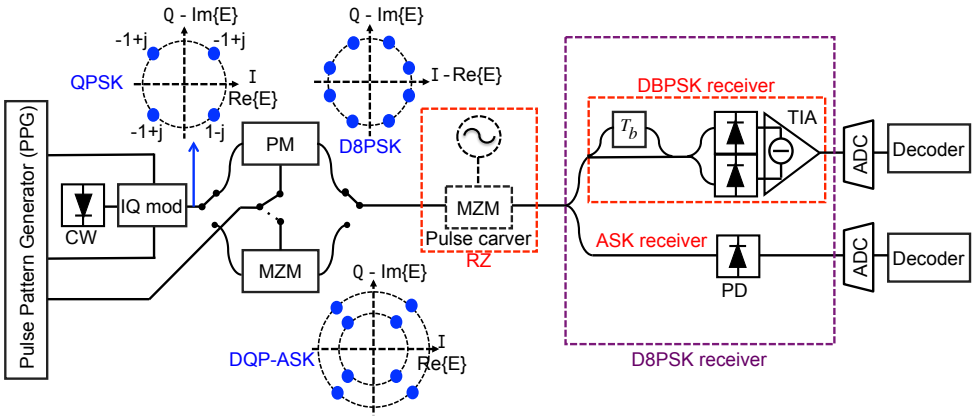

Fig. 3.8: Transceiver design for 8-DPSK signal generation and detection.

As an alternative, 8-level staggered amplitude- and phase-shift keying (APSK) has been proposed and provides better receiver sensitivity than D8PSK due to the difference in symbol spacing [63], as depicted in Fig. 3.9(b). The reason is that the spacing in 8-sAPSK between the symbols are not even which comes at the expense of an additional tandem $\pi/4$-phase modulator compared to a DQPSK modulator and higher computational complexity in the DSP [63]. The transmission experiment over 140 km of DSF has been reported in [63].

To increase the achievable ISD further, ASK signalling can be superimposed on a D8PSK signal [75], referred to as 16-amplitude DPSK (ADPSK) or star 16-QAM, as shown in Fig. 3.9(c). It has been demonstrated in [75] with an ISD of 2 b/s/Hz over 80 km long dispersion managed link operating at a bit rate of 100 Gb/s. Although star 16-QAM has better receiver sensitivity than differential 16-ary phase-shift keying (D16PSK), its self-phase modulation (SPM) performance is very poor due to unequal nonlinear phase shifts, occurring on different amplitude rings [64]. Another approach to generate a 16-ary signal is to superimpose a DQPSK signal on a quaternary ASK (QASK) signal. It has been demonstrated for a net bit rate of 40 Gb/s in [76] and 100 Gb/s [77]. However, such 16-level signalling formats suffer from low receiver sensitivity, and consequently, a significant reduction in maximum transmission distances since their symbol spacing is not the minimum Euclidean distance in the signal space.

Digital phase pre-integration using DSP-based transceivers enables to generate 8- and 16-QAM signals with minimum Euclidean symbol spacing which offers lower required OSNR compared to other possible 8- or 16-QAM constellations [62, 78, 79]. 8- and 16-QAM signal constellations with minimum Euclidean symbol spacing are shown in Fig. 3.9(c) and Fig. 3.9(e). Using DACs with sampling speed of 20 GSa/s, single channel 8- and 16-QAM transmission over 400 km and 160 km of SSMF with no DCF operating at a symbol rate of 10 GBaud/s have been demonstrated in [62]. However, although their OSNR performance is reasonably good, a DQPSK and an ASK receiver is required to detect these signals which is not favorable in metropolitan links. In addition, the required DSP for decoding is computationally expensive (see Fig.1 in [62]), and thus, there is no reported WDM transmission experiment using such transceiver architectures. Detailed discussion regarding the optical generation of star 16-QAM and DQPSK-QASK signalling can be found in [67] and [76], respectively.

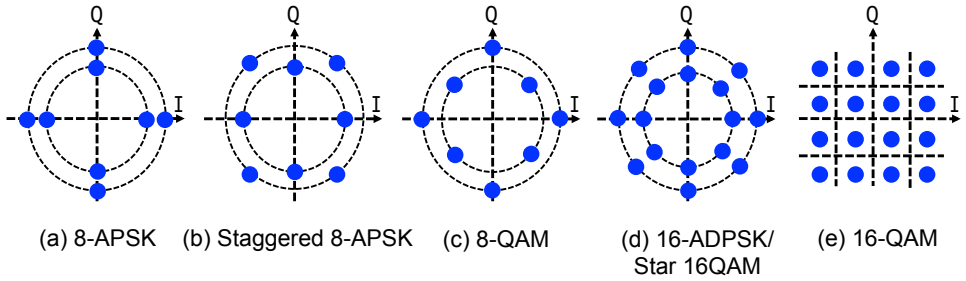

Fig. 3.9: Various constellation diagrams for 8- and 16-level signalling.

Tab. 3.3: Notable transmission experiments using multi-level modulation formats and non-coherent detection receivers, particularly focusing on spectral efficiency and reach.

Mod. scheme	net ISD (b/s/Hz)	Line rate (Gb/s)	Reach (km)	Fiber type	# of ch.	TX	RX	Year/Ref.
RZ-DQP-ASK	1.2	120	480	SSMF+DCF	1	DFB+2 MZMs+ IQ-mod.	BPD+DLI+PD	2011/ [71]
DPSK-3ASK	1.2	107	335	SSMF+DCF	1	DFB+DD-MZM+ MZM	BPD+DLI+PD	2010/ [68]
D6PSK	0.5	53.5	320	SSMF/DSF+DCF	21	DFB+MZM+PM	2(BPDs+DLIs)	2012/ [69]
RZ-D8PSK	0.6	30	320	SSMF+DCF	9	DFB+MZM+ IQ-mod+PM	BPD+DLI+PD	2005/ [80]

3.1.4 Subcarrier modulation (SCM) formats

The implementation of high order modulation schemes generated using cascaded modulators with BPDs and DLIs increases the cost of the transceiver architecture. In addition, employing dispersion compensating fibres (DCFs) to compensate the chromatic dispersion can increase the cost of a transmission link, and therefore, might not be preferable in direct detection links. Without DSP being used in such transmitters, it is not possible to apply pre-compensation, equalization or pre-distortion to mitigate the dispersion or any other effect causing degradation in signal quality. Although there are some receiver-based DSP equalization methods, also referred to as post-compensation, significant penalties are observed due to square-law detection and the complexity of nonlinear equalization[1], such as maximum likelihood sequence estimation (MLSE), increases exponentially with the dispersion accumulated along the fibre [81–86]. In addition to the cost issue, the stability of the cascaded modulators needs to be managed. Typically, a feedback control circuit is required to stabilize the modulators. Finally, the symbol spacing is not ideal in the sense of minimum Euclidean distance which causes degradation in receiver sensitivity, and hence, reduction in transmission margins.

To overcome these problems, DSP-based optical transceivers have started to be utilized in order to generate and detect high order modulation formats, superseding the transceiver architectures consisting of cascaded modulators with BPDs and DLIs in direct detection links over metropolitan, core and regional distances. It is expected that the use of high sampling rate DACs and ADCs will be acceptable in future low-cost systems, as the performance of silicon complementary metal oxide semiconductor technology continues to increase, and the cost and power consumption reduce. These transceivers allow to encode the symbols with minimum Euclidean spacing, pre-equalize the electrical signal, and hence, realize dispersion pre-compensation without the need for any optical dispersion compensation (ODC)

[1]Chromatic dispersion is translated from a linear distortion in the optical domain to a nonlinear distortion in the electrical domain due to square-law detection. Therefore, nonlinear equalization technique are more effective than the linear ones to mitigate the dispersion.

unit or DCFs along the fibre [87, 88].

SCM, which is enabled by DSP-based transceivers, has been proposed for optical communication in the last few years to increase the spectral efficiency and dispersion tolerance for access and metropolitan applications[2]. Using the SCM technique, QAM signals with minimum Euclidean symbol spacing can be generated and detected in direct detection links over access and metropolitan distances. This is due to the fact that the amplitude and phase recovery can be achieved by beating the subcarrier with the optical carrier within the bandwidth of the single-ended photodetector (PD). In addition to this, chromatic dispersion can be mitigated digitally using such transceivers. Thus, much of the complexity in the transceiver design is shifted from optical to the electrical domain which potentially reduces the transceiver cost.

The number of subcarriers can vary from one to many depending on the system architecture and parameters such as required receiver sensitivity, targeted distance and system budget. The use of multiple subcarriers is referred to as orthogonal frequency division multiplexing (OFDM) if the subcarriers are orthogonal to each other and spaced in frequency by the sampling rate divided by the fast Fourier transform (FFT) size. Among the various direct detection optical OFDM (DDO-OFDM) signal formats, the most promising is single sideband OFDM (SSB-OFDM) for direct detection links over metropolitan distances ($\geq$100 km) due to its spectral efficiency and dispersion tolerance [89, 90] [91, Ch.7].

Alternatively, single subcarrier combined with single sideband signalling and digital pulse shaping, so-called SSB Nyquist-SCM, can be used to realize QAM formats in direct detection links. The transceiver DSP subsystems for DDO-OFDM and Nyquist-SCM are described in section 3.2. Therefore, in the following section, their signal generation schemes are briefly discussed and the focus of the review given below is placed on their signal characteristic and previous experimental demonstrations.

3.1.4.1 Direct detection optical orthogonal frequency division multiplexing (DDO-OFDM)

OFDM is a spectrally-efficient example of multiple subcarrier modulation (MSM) technique. The main difference compared to the previous modulation techniques is the inverse fast Fourier transform (IFFT) and FFT blocks which take place at the transmitter and receiver, respectively. The high-speed serial data is converted into a number of low-speed parallel data, and subsequently, mapped to the frequency domain via an inverse discrete Fourier transform (IDFT), referred to as subcarriers. The orthogonal subcarriers, carrying low-speed parallel data, are multiplexed to form the serial OFDM signal. If an OFDM signal satisfies the Hermitian symmetry (a real-valued OFDM signal), it is referred to as discrete multi-tone (DMT). In the frequency domain, the total signal frequency band is divided into a number of non-overlapping or overlapping orthogonal frequency subcarriers N_{sc} to increase the spectral efficiency, as shown in Fig. 3.10. Each subcarrier frequency band is much narrower than the total frequency band. However, overlapping subcarriers should satisfy the orthogonality condition to minimize the inter-channel interference (ICI) between the subcarriers [92]. To satisfy the condition, the subcarrier frequencies should be spaced at integer multiples (n) of the symbol rate ($f_s = 1/T_s$) on each subcarrier, $f_k - f_i = n/T_s$ where f_k and f_i are any different subcarrier frequencies. Consequently, each subcarrier has a sinc-function, $(sin(x)/x)^2$, spectrum [91, Ch.2-p.39]. The spectrum of a single subcarrier intercepts with the other sinc spectra at their null points enabled by the orthogonality condition so that

[2]OFDM has been also proposed for (ultra) long-haul applications using coherent detection. However, such applications are out of the scope of this work.

no ICI occurs between the subcarriers. However, this condition comes at the price of strict time alignment/synchronization requirements between the modulated OFDM symbols at the demultiplexing stage. Besides the time alignment, OFDM is highly susceptible to timing and sampling frequency offset between the transmitter and receiver, and thus, they need to be managed properly. Otherwise, the system suffers from a significant receiver sensitivity penalty due to the crosstalk. The required DSP for the DDO-OFDM signal is described in section 3.2.2.

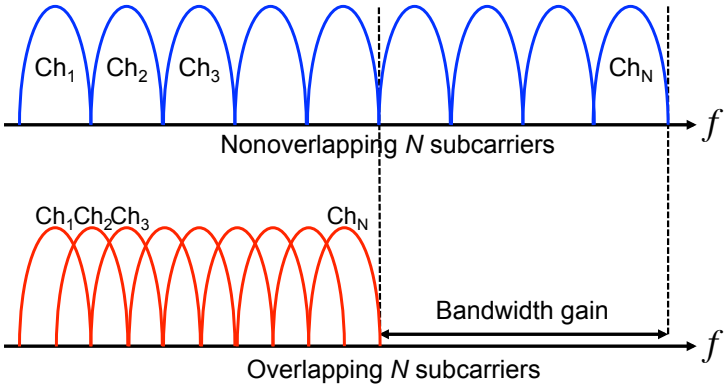

Fig. 3.10: MSM spectrum: Non-overlapping (non-orthogonal) (top) and overlapping (orthogonal) N subcarriers (bottom).

The null-to-null bandwidth of an OFDM spectrum ($BW_{null-to-null}$) is given by

$$BW_{null-to-null} = \frac{N_{sc}+1}{T_s} = (N_{sc}+1)f_s. \tag{3.1}$$

where N_{sc} is the number of subcarriers, $T_s = 1/f_s$ is the symbol period. As N_{sc} approaches infinity, the normalized $BW_{null-to-null}$ approaches 1, implying no out-of-band spectral components. However, higher N_{sc} means higher complexity at DACs/ADCs due to larger IFFT/FFT size. N_{sc} is chosen depending on the system requirements, such as the desired bit rate, distance or total number of users *etc.* In optical communication, typically N_{sc} is chosen at least 128 to obtain a sufficiently narrow spectrum. Each subcarrier can be modulated with a separate signalling format, *e.g.,* PSK or QAM [93]. This feature of adaptively changing the modulation format of the subcarriers, referred to as adaptively modulated optical OFDM (AMO-OFDM), gives OFDM signals the ability to cope with some linear distortions caused by non-ideal frequency responses of the optical and electrical components [94–96], as briefly described in section 3.2.2.1. Although using a high number of subcarriers gives more flexibility for link adaptation and less out-of-band spectral power, it increases not only the DSP complexity but also the peak-to-average-power ratio (PAPR) significantly. This is caused by the high peaks in an OFDM signal waveform due to the constructive addition of the subcarriers resulting from their phase alignments [97]. High PAPR results in an increase in the required optimum optical carrier-to-signal power ratio (CSPR) for direct detection links and dynamic range of the signals being converted by the DACs/ADCs used in the transceiver, causing increased converter quantization noise. Clipping is a practical low complexity solution to reduce the PAPR of OFDM driving signals and its value is chosen depending on the given DACs/ADCs resolution [98, 99]. However, it comes at the expense of nonlinear distortion and penalties [93, 97, 99].

In dispersive channels such as an optical link, a time delay is introduced mainly by the chromatic dispersion. This time delay leads to interference between OFDM symbols, so-called inter-symbol interference (ISI). Furthermore, since the FFT window fails to include all the samples of an OFDM symbol

due to the ISI, the orthogonality condition cannot be satisfied, resulting in ICI. One solution to eliminate the channel dispersion-induced ISI and ICI is to add a cyclic prefix (CP), also referred to as a guard interval [100]. The first N_{CP} subcarriers of the OFDM frame are copied and added to its end or vice versa. A CP is also necessary to compensate for timing offset during OFDM frame/symbol synchronization. A CP-added OFDM symbol can combat the phase changes (time-shifts) due to any channel dispersion up to the duration of the CP (no ISI), and all the samples of an OFDM symbol can be included in the FFT window at the receiver (no ICI) [91]. However, CP introduces some redundancy so that there is a trade-off between the net data rate and ISI robustness. The minimum required number of samples (CP duration or guard interval length) is mainly determined by the targeted transmission distance and is selected proportional to the FFT window size ($N_{sc}+N_{CP}$) [101, 102]. The overhead resulting from the CP (OH_{CP}) is given by

$$OH_{CP} = \frac{N_{CP}}{N_{sc}+N_{CP}}. \tag{3.2}$$

Despite the overhead introduced by the CP, its usage is the key for simple equalization in OFDM systems.

There are two forms of DDO-OFDM signal formats, namely intensity modulated (IM) OFDM and SSB-OFDM. Intensity modulated OFDM signals are preferable for (ultra) short-haul communication links due to their lower complexity [103–105] whereas SSB-OFDM is more practical for medium and long-haul transmission links (>80 km) due to its robustness to chromatic dispersion and higher receiver sensitivity [89, 106]. If a signal is double-sided such as IM-OFDM, chromatic dispersion accumulated along the fibre causes a phase rotation on the two sidebands, converting intensity modulation into phase modulation which produces nulls at certain frequencies in the optical carrier-signal mixing product after photodetection [107]. Therefore, the discussion from this point is focused on SSB-OFDM signal in this section.

Single sideband orthogonal frequency division multiplexing (SSB-OFDM)

In optical fibre communications, each discrete subcarrier frequency in an OFDM baseband signal should be linearly mapped into a single discrete optical frequency. This is achieved using linear field modulation [89, 97]. The optical carrier is added using the modulator and transmitted along with the OFDM signal [89, 93, 106]. To achieve this, there are three transceiver configurations which are studied in [89]. Their optical complexity at the transmitter varies, but they all make use of a direct detection receiver consisting of a single-ended PD without any DLIs. In this thesis, the second transmitter design in [89] using an IQ-modulator with a digital sideband filter is considered, as discussed in section 4.1.1.2.

In direct detection links, the baseband OFDM signal is up-converted to a subcarrier frequency, with a spectral gap (a guard band) being used between the optical carrier and sideband. The signal-signal mixing products interfere with the carrier-signal mixing products "desired signal" after photodetection, called signal-signal beating interference (SSBI) and cause distortion, as explained in section 2.3.1 [108]. Therefore, the use of the guard band is essential to avoid distortion due to SSBI. To avoid SSBI completely, a guard band with the same bandwidth as the OFDM signal should be used. However, this halves the ISD, and also wastes approximately 50% of the bandwidth of the electrical and optical components used in the transmitter, *e.g.,* optical modulator(s), photodiode(s), DACs/ADCs *etc*. Hence, the bandwidth requirements for such components are nearly doubled.

There are some proposed optical or DSP-based methods to mitigate/cancel the SSBI, allowing the

width of the guard band to be reduced. One approach is to modulate the envelope of the optical signal instead of the field, a technique called compatible SSB (cSSB)-OFDM, using an IQ-modulator [109] or a dual-drive Mach-Zehnder modulator (dual-drive MZM) [110]. However, it causes a significant degradation in OSNR performance due to the high required optical carrier power to avoid clipping at the receiver. Another approach is to estimate the signal-signal mixing products applying an iterative estimation technique. It reconstructs the signal-signal mixing products using the detected signal, and then, the estimated signal is subtracted from the detected signal to cancel the SSBI [111, 112]. However, this technique increases the DSP complexity significantly due to the need for multiple iterations, since each iteration includes FFT/IFFT operations. If the need for multiple iterations, *i.e.,* single iteration to reconstruct the signal-signal mixing products, can be eliminated, this technique would be very effective from SSBI mitigation. Another DSP-based cancellation technique is to use an interleaver combined with turbo codes, which requires approximately 30% overhead [113]. Alternatively, a BPD and a 4^{th}- or higher-order super-Gaussian optical filter with a very sharp edge gradient can be used to filter the optical carrier, enabling the detection of the signal with and without the carrier [114, 115]. Although this method offers an OSNR gain, it increases the optical complexity of the receiver, which is not desirable for cost-effective applications. Another scheme is proposed in [116] to eliminate the impact of SSBI by modulating only the odd subcarriers, called interleaved OFDM. This scheme enables to utilize the bandwidth of the components more efficiently. However, the achievable ISD does not change. Although the aforementioned techniques have been shown to be effective in various aspects, they come at the price of either a significant degradation in OSNR performance, increased optical complexity, digital complexity or overheads. Alternatively, the subcarriers can be adaptively modulated to deal with the frequency dependent SNR due to SSBI. This is discussed in chapter 4.

High PAPR due to the constructive interference of the subcarriers, leading to high peaks in the signal waveform, is another drawback for OFDM signals. This leads to the requirement to use high optical carrier power in order to maintain a unipolar signal waveform. The use of high carrier power increases the required OSNR, causing a reduction in transmission margin. It also necessitates a higher resolution in the required dynamic range of the DACs/ADCs. Signal clipping can be used to reduce the PAPR, although this results in nonlinear distortion and penalties. Clipping and other techniques for reducing the PAPR for OFDM have been discussed, though all have increased complexity or overheads [93,97,99].

Nevertheless, DDO-OFDM has attracted much research interest for access, metro and regional applications. It offers a promising solution for such applications due to its resilience to chromatic dispersion [93], and the ability to modulate the subcarriers adaptively to tackle the non-ideal frequency response of practical links [96, 117]. High capacity, long reach and ISDs greater than 1 b/s/Hz can be achieved using DDO-OFDM superchannel transceivers, first proposed in [118] and modified in [119]. They utilize multiple closely spaced OFDM sub-bands with two or multiple pilot-carriers. Each pilot-carrier beats with half of the total sub-bands so that the spectral guard band is shared among the sub-bands, eliminating the guard band requirement for each sub-band. This is enabled by using a double pass-band filter to demultiplex one of the pilot-carriers and the desired sub-band simultaneously before the photodiode [118, 119]. However, the required optical filter is very challenging to implement so that it increases the complexity of the receiver.

Although no WDM transmission experiment using DDO-OFDM superchannel configuration has been demonstrated at an ISD greater than 1 b/s/Hz, there are notable reports of single polarization WDM

DDO-OFDM transmission experiments, which are listed in Tab. 3.4. Recently, WDM DDO-OFDM experiments have been demonstrated with an ISD of 0.6 b/s/Hz over 3040 km [119] and 1 b/s/Hz over 320 km of SSMF [120]. A real-valued OFDM signal, so-called discrete multi-tone (DMT), has also been demonstrated over 240 km of SSMF with an ISD of 1.12 b/s/Hz [121].

Tab. 3.4: Notable single polarization WDM DDO-OFDM transmission experiments, focusing on spectral efficiency and reach.

Mod. scheme	net ISD (b/s/Hz)	Line rate (Gb/s)	Reach (km)	Fiber type	# of ch.	TX	RX	Year/Ref.
SSB DDO-OFDM (16-QAM)	2	20	320	SSMF	8	ECL+IQ-mod.	PD	2007/ [122]
VSB DMT (bit-loading)	1.12	56	240	SSMF	8	ECL+MZM	PD	2014/ [121]
SSB DDO-OFDM (QPSK) superchannel	0.6	11.36	3,040	SSMF	38	ECL+IQ-mod.	PD	2013/ [119]
SSB DDO-OFDM (QPSK)	0.4	10	4,000	SSMF	32	DFB+MZM+OF	PD	2006/ [106]

3.1.4.2 Single sideband Nyquist-subcarrier modulation

Single SCM, introduced in wireless infrared communication [123, Ch. 5] [124], has been recently utilized to realize high order modulation formats [125]. The baseband QAM signal is first electrically modulated onto a single (RF) subcarrier [126], in contrast to the multiple subcarriers used in OFDM. Subsequently, a DC bias is added, and then, converted to an optical signal using either a single-drive MZM combined with an optical filter or a dual-input vector modulator, *e.g.,* IQ-modulator or dual-drive MZM, as described in chapter 4. It encodes the QAM symbols through the amplitude and phase of the subcarrier, which can be recovered during direct detection through beating with the optical carrier. This is sometimes referred to as self-coherent modulation [125, 127]. Since this format utilizes only one subcarrier, it has a lower PAPR than OFDM which enables to reduce the quantization noise from the DACs/ADC, or use lower resolution converters. This potentially improves the OSNR performance compared to the OFDM signal format [128].

The mathematical expression for a SCM-QAM signal is given by

$$s(t) = 1/\sqrt{2}\,[m_I(t)\cos(2\pi f_{sc}t) - m_Q(t)\sin(2\pi f_{sc}t)] \quad \text{where} \quad f_{sc} = 1/T_s \quad \text{and} \quad 0 \le t < T_s, \tag{3.3}$$

where $m_I(t)$ and $m_Q(t)$ are the bi-polar pulses (baseband signals) that represent I- and Q-components of the signal, f_{sc} is the subcarrier frequency, and T_s is the symbol period. The subcarrier frequency (f_{sc}) should be selected as close as possible to the optical carrier to maximize the ISD. Conventionally, it is selected proportional to the symbol rate (f_s). Following this, Eq.3.3 can be re-written as:

$$s(t) = 1/\sqrt{2}\,[m_I(t)\cos(2\pi c f_s t) - m_Q(t)\sin(2\pi c f_s t)] \quad \text{where} \quad c = f_{sc}/f_s. \tag{3.4}$$

The block diagrams of single-cycle subcarrier modulation (SC-SCM) and half-cycle subcarrier modulation (HC-SCM) QAM signal generation are presented with their signal spectra in Fig. 3.11. The choice of the subcarrier frequency determines the ISD. Its value should be selected as close as possible to the optical carrier to maximize the spectral efficiency. If c is equal to 1, which implies f_{sc} is equal to f_s, it is called SC-SCM in which the optical carrier and f_{sc} are placed by a relative frequency difference of f_s [125]. Hence, the ISD becomes $\log_2(M)/4$ for a SC-SCM M-QAM signal. The electrical eye diagram

of 10 GBaud/s SC-SCM QPSK, 8-QAM and 16-QAM signals are also shown in Fig. 3.12. In a single symbol period, a single-cycle of a subcarrier (sine wave) signal with its four equally spaced phases (0°, 90°, 180° and 270°) and the symbol decision levels can be clearly observed. After detection, the subcarrier modulated signal is down-converted to a baseband signal by the receiver DSP. Chromatic dispersion compensation can be achieved utilizing electronic pre-distortion (EPD), as discussed in section 3.2.1.3. SC-SCM was demonstrated using QPSK in [125], RZ-DQPSK in [129] and 16-QAM in [126] over a transmission distance of 80 km.

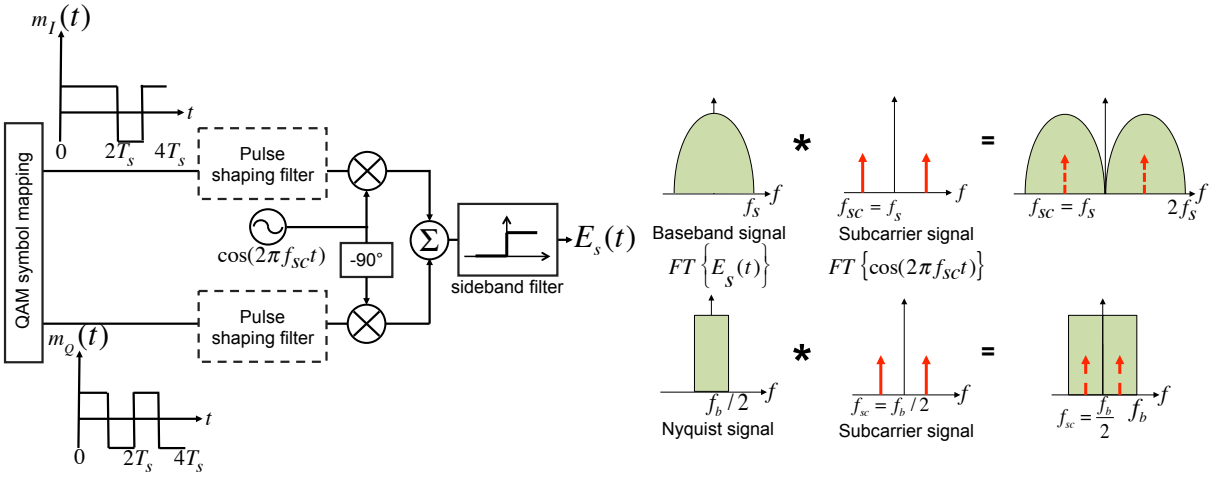

Fig. 3.11: (a) SC-SCM and HC-SCM QAM signal generation (left) and the schematic of their signal spectra (right).

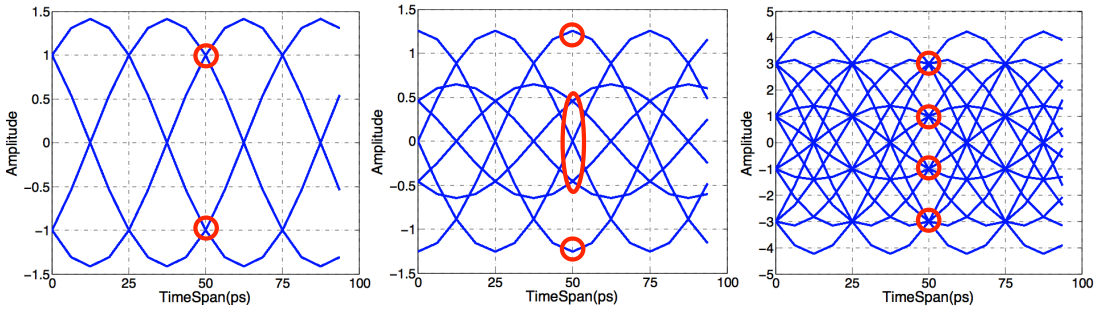

Fig. 3.12: Optical intensity waveforms for SC-SCM QPSK (left), 8-QAM (middle) and 16-QAM (right) with the symbol decision levels shown with red circles.

When c is equal to 0.5, the difference halves so that the ISD increases to $\log_2(M)/2$, called HC-SCM, as depicted in Fig. 3.11. However, HC-SCM signalling requires a pulse-shaping filter at the transmitter DSP and a matched filter at the receiver DSP with a roll-off factor close to zero to avoid any overlapping between the sidebands, as described in section 3.2.1.1. HC-SCM with Nyquist pulse shaping was demonstrated in transmission over short optical links in [130, 131]. Moreover, 16-QAM SCM signalling combined with pulse shaping has been utilized for passive optical networks (PONs) experiments in [132, 133]. A further increase in ISD or optical spectral efficiency by a factor of 2, approaching $\log_2(M)$, can be achieved using a sideband filter, referred to as SSB signalling which is also discussed in the DSP section (see section 3.2.1.2).

As with SSB-OFDM, SSB Nyquist-SCM suffers from SSBI as well, but it has a higher tolerance compared to OFDM signaling, as discussed in chapter 4. There was no previously reported experimen-

tal WDM demonstration of SSB single-SCM signalling with or without pulse shaping over access and metropolitan distances. However, an ISD higher than 1 b/s/Hz over transmission distances of more than 100 km have been achieved using SSB Nyquist-pulse shaped SCM QAM signalling in the work described in this thesis [134–136]. The results presented in chapter 4 exhibit the highest achieved ISDs at given distances among the reported experimental single polarization WDM demonstrations in direct detection links.

3.2 Digital signal processing (DSP) for SCM formats

In this section, the DSP algorithms used in SSB Nyquist-SCM and SSB-OFDM signal generation and detection are outlined. Pulse shaping, Hilbert transform for SSB signalling and electronic pre-distortion (EPD) techniques used in the single SCM transmitter DSP, and digital equalization for symbol re-timing used in the receiver DSP are described in section 3.2.1. Following the description of Nyquist-SCM transceiver DSP, SSB-OFDM signal waveform/frame generation at the transmitter, and OFDM symbol synchronization and channel estimation at the receiver are explained in section 3.2.2.

3.2.1 DSP for Nyquist-SCM

3.2.1.1 Nyquist pulse shaping

The term Nyquist filtering is inherited from digital communication. When consecutive symbols are transmitted over a linear channel, the channel distorts the signal and these distorted symbols start interfering with each other, referred to as inter-symbol interference (ISI). These distortions fall on the position of zero-crossing points (symbol sampling points) between the consecutive symbols, and hence, cause a reduction in the eye opening where the sampling takes place before the symbol-to-bit mapping. This phenomenon causes the system to be more sensitive to any channel impairments and reduces the receiver sensitivity [1].

To avoid ISI and increase the ISD, a pulse shaping method can be applied to obtain a band-limited signal in such a way that meets the Nyquist criterion, *i.e.,* the peak of a pulse of interest coincides with the zeros of neighboring pulses. The Nyquist sampling theorem states that any analogue band-limited signal $x(t)$ with a bandwidth interval of $[-B, B]$ can be perfectly reconstructed from its samples provided that the sampling frequency of an ADC is $\geq 2B$ [137]. Pulses that satisfy zero ISI condition as well as having a bandwidth limited to the Nyquist frequency ($f_s = 1/T_s$ where T_s is the symbol period) are referred as Nyquist pulses. A well known pulse shape is the "sinc" pulse which has the narrowest bandwidth among all the possible Nyquist pulses. However, it is impractical to design such a filter since it is an infinite and non-causal pulse in the time domain. A practical pulse spectrum which almost satisfies the Nyquist criterion $T = 1/2f_s$ is the raised cosine (RC) spectrum $H_{RC}(f)$. Since transmitter and receiver filters should be jointly designed to achieve zero ISI, the pulse shaping is applied both at the transmitter $H_T(f)$, and receiver $H_R(f)$. Thus, the RC filter is split into two parts and applied at the transmitter, referred to as root raised cosine (RRC) or square-root raised cosine (SRRC) filter $H_{RRC}(f)$, and at the receiver, referred to as matched filter $H_{MF}(f) = H_{RRC}(f)$.

$$H_{RC}(f) = \sqrt{H_{RC}(f)}\sqrt{H_{RC}(f)} = H_T(f)H_R(f) \\ = H_{RRC}(f)H_{MF}(f) \tag{3.5}$$

The frequency response of the RRC filter is the square-root of the RC filter and defined by

$$H_{RRC}(f) = \begin{cases} \sqrt{T_s} & , \quad 0 \leq |f| \leq \frac{1-\beta}{2T_s} \\ \sqrt{\frac{T_s}{2}\left(1+\cos\left[\frac{\pi T_s}{\beta}\left(|f|-\frac{1-\beta}{2T_s}\right)\right]\right)} & , \quad \frac{1-\beta}{2T_s} \leq |f| \leq \frac{1+\beta}{2T_s} \\ 0 & , \quad |f| \geq \frac{1+\beta}{2T_s} \end{cases} \tag{3.6}$$

where f is the frequency space and β is the roll-off factor which takes values in the range $0 \leq \beta \leq 1$. It determines the excess bandwidth occupied beyond the Nyquist frequency and it is usually expressed as a percentage of the Nyquist frequency, *e.g.,* the excess bandwidth is 10% when $\beta = 0.1$.

The impulse response of RRC filters and their corresponding spectra are plotted in Fig. 3.13. When the value of β gets closer to 0, the amplitude of the side lobes increase in the time domain, as shown in Fig. 3.13. This causes an increase in PAPR, which becomes an important parameter in system design due to its impact on the receiver sensitivity. Therefore, the roll-off factor needs to be optimized for the given DACs/ADCs resolution. The change in PAPR with respect to the roll-off factor of a RRC filter for a SCM signal is discussed in detail in section 4.3. Note that the oscillation when $\beta = 0$ in Fig. 3.13(b) is due to the use of finite taps for the pulse-shaping filter.

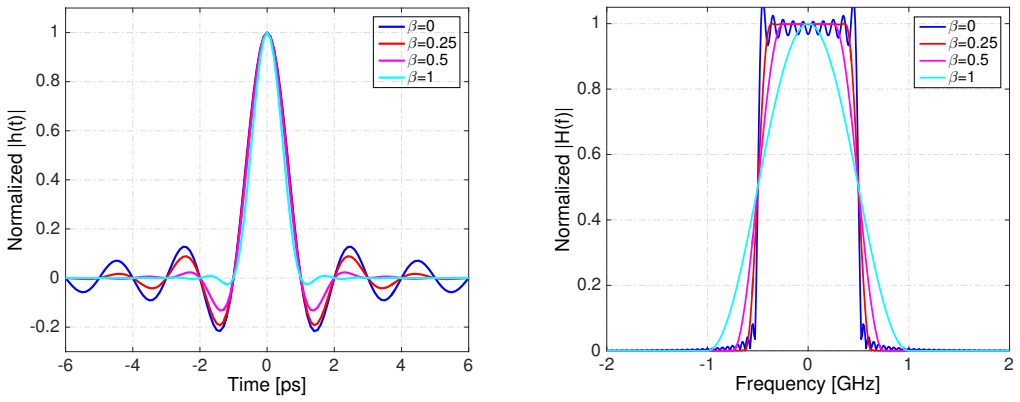

(a) (b)

Fig. 3.13: (a) Impulse and (b) frequency response of the RRC filter

3.2.1.2 Discrete Hilbert transform (HT) to generate SSB signal

The subcarrier modulation technique generates a double sideband (DSB) signal due to the Fourier transform (FT) of (co)/sine wave, as illustrated in Fig. 3.11. However, this halves the spectral efficiency.[3] Therefore, SSB signalling is essential in order to double the ISD without any loss of information (both sidebands carry the same information). This can be achieved by applying a discrete HT to the signal.

[3] Additionally, a double-sided optical signal suffers from a walk-off in the relative phase of the sidebands due to the square-law detection. This limits the capacity-distance product when the dispersion is not mitigated in the transmitter [93].

The Hilbert transform is a process in which all negative frequency components of a signal are phase-advanced by 90° whereas all positive frequency components are phase-delayed by 90°. The amplitude of the spectrum remains unchanged. In other words, it introduces a 180° phase difference between the negative and positive frequency components of an input signal [139, Ch.2, pp.47–55] [107, 138]. The frequency response of a HT $G_{HT}(\omega)$ can be expressed as follows:

$$G_{HT}(\omega) = \begin{cases} e^{-j\pi/2} & \text{, if } \omega > \omega_c \\ 0 & \text{, if } \omega = \omega_c \\ e^{j\pi/2} & \text{, if } \omega < \omega_c \end{cases} \tag{3.7}$$

where ω is the angular frequency and ω_c is the angular frequency of the optical carrier. The output of the HT is added to the signal itself after multiplying with a phase shift, $e^{j\theta}$. This operation creates a complex SSB signal without any loss of information, as shown in Fig. 3.14.

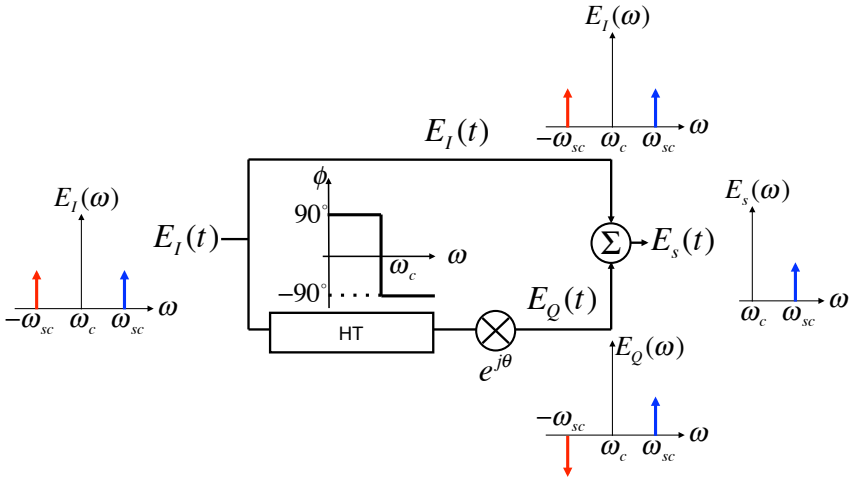

Fig. 3.14: SSB signal generation using Hilbert transform.

Analytically, the in-phase $E_I(t)$ and quadrature $E_Q(t)$ components of an optical field $E_s(t)$ can be expressed as follows:

$$E_I(t) = Ae^{j\omega_c t}[1 + \delta\cos(\omega_{sc}t)] \tag{3.8a}$$

$$E_Q(t) = Ae^{(j\omega_c t + j\theta)}[1 + \delta\cos(\omega_{sc}t - \phi)], \tag{3.8b}$$

where A and $e^{j\omega_c t}$ are the amplitude and phase of the optical field, δ is the modulation index and ω_{sc} is the angular frequency of the subcarrier modulated (up-converted) signal. Using Euler's formula, $\cos(\omega_{sc}t)$ can be rewritten as $0.5[e^{j\omega_{sc}t} + e^{-j\omega_{sc}t}]$. Following this, the output optical signal $E_S(t)$, that is the sum of $E_I(t)$ and $E_Q(t)$, can be expressed

$$\begin{aligned} E_S(t) &= E_I(t) + E_Q(t) \\ E_S(t) &= E_I(t) + jH\{E_I(t)\} \\ &= Ae^{(j\omega_c t)} \left\{ \begin{array}{r} 1 + e^{j\theta} + \frac{\delta}{2}e^{j\omega_{sc}t}[1 + e^{j(\theta-\phi)}] \\ + \frac{\delta}{2}e^{-j\omega_{sc}t}[1 + e^{j(\theta+\phi)}] \end{array} \right\}, \end{aligned} \tag{3.9}$$

where $H\{\cdot\}$ denotes the Hilbert transform. In Eq. 3.9, if the value of ϕ is chosen as $\pi/2$, the upper/lower sideband shown with the red/blue arrow in Fig. 3.14 is suppressed when the value of θ is chosen as $\pi/2/-\pi/2$.

Alternatively, the SSB signal can be generated optically using an optical filter [140–142] or an optical HT based on a fibre Bragg grating (FBG) [143–145]. However, the main drawback of performing the SSB signalling using an optical filter is the need for optical filters with very steep profile (transition bandwidth) and precise wavelength control of the laser and filter. Otherwise, a spectral gap is required between the optical carrier and sideband which significantly reduces ISD. On the other hand, optical HT based on FBG suffers from worse receiver sensitivity due to the reflectivity [146] and relatively poor stability due to the wavelength drift of the FBG [143].

3.2.1.3 Electronic pre-distortion (EPD)

Although electronic dispersion compensation (EDC) gained attention in early '90s, it became practical in 2000s with the innovation of high-speed electronic circuits in the range of 10-40 GHz. The main advantage of using EDC that it is a cost-effective solution for chromatic dispersion compensation in optical communication systems by eliminating the need of using any optical dispersion compensation (ODC) unit or dispersion compensating fibre (DCF) along the transmission link.

In simple direct detection optical links (a single-ended photodiode without any DLI), chromatic dispersion is transformed from a linear distortion in the optical domain to a non-linear distortion in the electrical domain since the optical phase is lost upon square-law detection. Although receiver-based equalization in the receiver DSP, referred to as electronic dispersion post-compensation, is applied, significant receiver sensitivity degradation is observed. Besides the performance degradation, the complexity of nonlinear equalization such as maximum likelihood sequence estimation (MLSE) increases exponentially with the dispersion accumulated along the fibre [81, 82, 84, 86]. Thus, electronic pre-distortion (EPD), pre-dispersing the signal with transmitter-based DSP to mitigate the chromatic dispersion, is proposed and demonstrated in [87, 147, 148] as an alternative method.

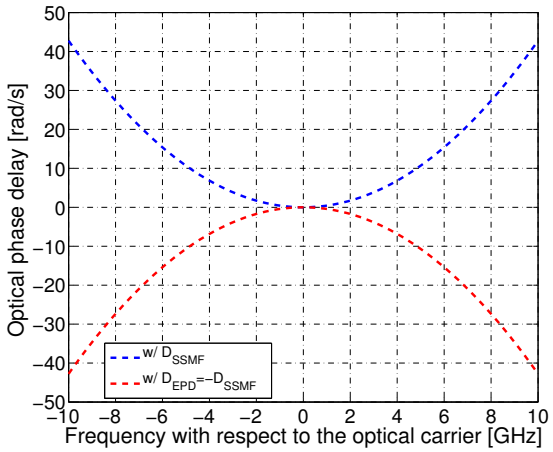

Fig. 3.15: The optical phase delay with respect to the frequency.

The optical phase delay (shift) in standard single mode fibre (SSMF) and its inversion as a function of frequency are given in Fig. 3.15. The phase shift varies quadratically with respect to the frequency (frequency dependent phase-shift), as shown in Fig. 3.15. The subcarrier modulated signal is pre-dispersed with the inverse of the linear lossless channel response ($H^{-1}(L,\omega)$) in the frequency domain, as described in [87]. This can be achieved by simply inverting the sign of the dispersion parameter of a SSMF, denoted as D_{SMF} in Eq.2.8, and putting it into Eq.2.9. Hence, $H^{-1}(L,\omega)$ can be defined as follows:

$$H^{-1}(L,\omega) = \exp\left(-jL\frac{D_{EPD}\lambda_0^2}{4\pi c_0}\omega^2\right) = \exp\left(-jL\frac{-D_{SMF}\lambda_0^2}{4\pi c_0}\omega^2\right), \tag{3.10}$$

where D_{EPD} is equal to $-D_{SMF}$. The digital filter with this transfer function can be implemented in the frequency domain, using IFFT/FFT operations or with a time domain finite impulse response (FIR) filter design whose impulse response is essentially the inverse of the channel response given in Eq.3.10, as proposed in [2]. A closed form solution for tap weights of the FIR filter with the bounds on the number of taps required for a given amount of dispersion is also presented in [2]. The amount of dispersion to be compensated determines the complexity of frequency/time domain implementation, *i.e.,* the FFT size/number of taps used.

3.2.1.4 Digital equalization for Nyquist-SCM symbol re-timing

Digital equalization is required due to the sampling rate difference between the transmitter and receiver. It is performed for symbol re-timing to recover the transmitted symbols after demodulation (down-conversion and matched filtering), as shown in Fig. 3.16. In this thesis, blind equalizers (non data-aided) are applied, in which the tap weights, denoted as **h**, are adaptively updated based on the received signal, denoted as **x**. Note that the variables, denoted in bold, correspond to vectors. The tap weights of the equalizer are updated based on the error signal (e) at each iteration. Commonly, the least mean squares (LMS) algorithm, as opposed to a Kalman filter or recursive least squares algorithm, is used to update the filter taps due to its stability, fast convergence rate and lower computational complexity [149]. In the LMS algorithm, the tap weights are adapted using the method of steepest-descent algorithm, based on the derivate of the error signal, the so-called cost function, with respect to the filter coefficients. For a single-input, single-output complex channel, the filter taps are adapted as follows:

$$\mathbf{h(n+1)} = \mathbf{h(n)} - \mu\hat{\nabla}J(n), \tag{3.11}$$

where $\mathbf{h(n)}$ is the tap vector at instant n, μ is the step-size and $\hat{\nabla}J(n)$ is the estimated gradient of the cost surface with respect to $\mathbf{h(n)}$. The adaptation of a filter is often formulated in terms of an error signal $e(n)$ given by

$$e(n) = -\frac{\mathbf{x(n)}y(n)^*}{\hat{\nabla}J(n)}, \qquad \text{and} \qquad y(n) = \mathbf{h(n)}^H\mathbf{x(n)}, \tag{3.12}$$

where $\mathbf{x(n)}$ is the input vector at instant n, $y(n)$ is the instantaneous output of the equalizer at instant n, * and H represent the complex conjugate and the Hermitian conjugate, respectively. From Eq. 3.12, $\hat{\nabla}J(n)$ can be found as follows:

$$\hat{\nabla}J(n) = e(n)y^*(n)\mathbf{x(n)}. \tag{3.13}$$

So that, Eq. 3.11 can be re-written as

$$\mathbf{h(n+1)} = \mathbf{h(n)} + \mu e(n)y^*(n)\mathbf{x(n)}. \tag{3.14}$$

The error signal or cost function given in Eq. 3.12 indicates the deviation of the instantaneous symbol from the desired symbol. The constant modulus algorithm (CMA), proposed by Godard [150], and the

decision-directed algorithm are the two main cost functions used whilst computing the error signal, and subsequently, updating the filter tap weights. The CMA assumes that all the symbols of the input signal have a constant modulus (power) such as M-PSK signals and computes the error signal accordingly as given by

$$e(n) = R - |x(n)|^2, \tag{3.15}$$

where R is the modulus that the equalizer attempts to approach (desired modulus), as shown in Fig. 3.16(b). If the received signal has more than one modulus such as M-QAM where $M > 2$, the CMA can be modified by simply adding decision boundaries between the modulus rings before the cost function computation and tap weights adaptation, a technique called radius directed equalization (RDE) [151], [152, Ch. 2.4.2], as shown in Fig. 3.16(b). Although CMA usage is limited by the modulation formats having a constant power, it converges very rapidly and is highly robust. Therefore, it is used for pre-convergence at the equalization stage, *i.e.,* for the purpose of initialization before the next equalizer stage, and then, switched to decision-directed mode to minimize the error function, yielding a better SNR tolerance.

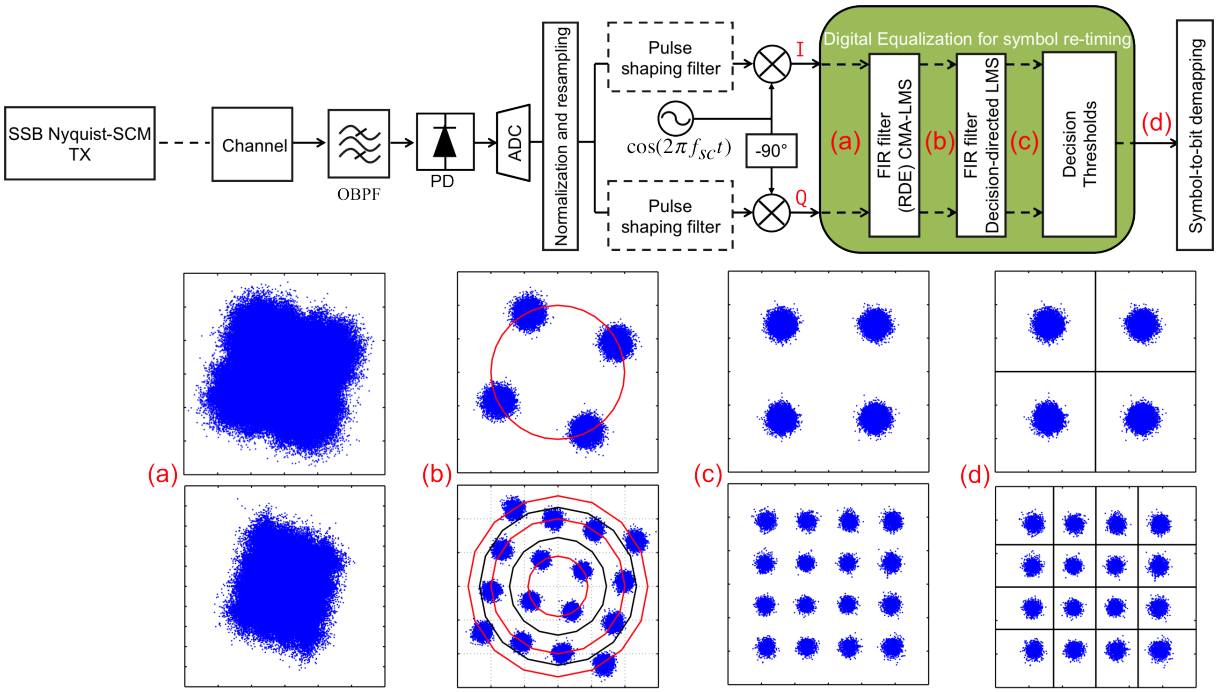

Fig. 3.16: Digital equalization for Nyquist-SCM signal. Received constellation (a) before digital equalization, (b) after FIR filter with CMA-LMS algorithm, (c) after FIR filter with DD-LMS algorithm and (d) with decision thresholds. The red and black circles in (b) represent the desired modulus that the equalizer attempts to approach and the decision boundaries between modulus rings in RDE CMA-LMS case, respectively. Black lines in (d) correspond to decision threshold levels.

In decision-directed equalization, the error signal is computed by subtracting the instantaneous output of the equalizer at instant n, denoted as $y(n)$, from the output of the hard decision function ($D[.]$). It is given by

$$e(n) = D[y(n)] - y(n). \tag{3.16}$$

Assuming $y(n)$ is a QPSK symbol, $D[y_{QPSK}(n)]$ is written as

$$D[y_{QPSK}(n)]\frac{1}{\sqrt{2}}[\text{sgn}\{\text{Re}[y(n)]\}+j\text{sgn}\{\text{Im}[y(n)]\}] \tag{3.17}$$

where sgn{.} is the signum function. Using this equalization method as a second stage, the received symbols converge to their hard decision levels, as shown in Fig. 3.16(c) and Fig. 3.16(d). After applying the FIR filter with the decision-directed LMS algorithm, the symbol decision process becomes simple. The drawback of this equalization technique is that the convergence of the algorithm depends on making a series of successive correct decisions for symbols. Otherwise, false decisions slow down the convergence process and even sometimes prevent convergence. Thus, decision-directed equalizers are often started with the CMA to initialize the filter coefficients [153].

3.2.2 DSP for DDO-OFDM

3.2.2.1 OFDM frame generation

A typical OFDM frame is depicted in Fig. 3.17, in which the y-axis depicts frequency and the x-axis represents time. Each row in an OFDM frame is referred to as a subcarrier (SC_1,...,$SC_{N/2}$,...,SC_N) whereas each column is referred to as an OFDM symbol ($S_1, S_2, ..., S_M$). Depending on the transmission link, each subcarrier can be modulated adaptively using a different constellation, *i.e.,* treating each subcarrier as a different channel. The adaptive modulation feature is the main advantage of OFDM signalling over single carrier modulation scheme, such as Nyquist-SCM. When all the subcarriers are modulated with the same constellation, the total error probability is dominated by the subcarriers with the highest distortion. To overcome this issue, and consequently, optimize the system performance, each subcarrier can be modulated with an optimally chosen format cardinality (also termed bit loading) so that similar bit error probabilities are experienced by all the subchannels. Bit loading is applied depending on the SNR of each subcarrier [94].

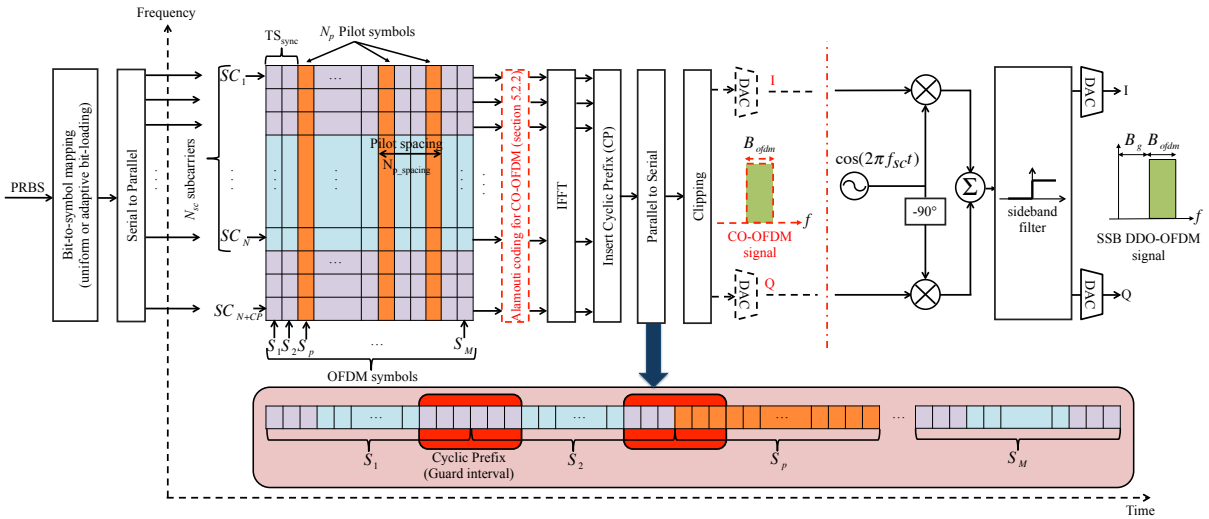

Fig. 3.17: DDO-OFDM transmitter DSP for signal generation. B_g and B_{ofdm} correspond to the bandwidth of spectral gap and OFDM signal. The schematics drawn in red dashed lines are used for CO-OFDM signal waveform generation and excluded in this section for simplicity. The discussion regarding CO-OFDM can be found in chapter 5.

For the bit loading, the Levin-Campello (LC) algorithm was utilized since it provides an optimum discrete bit distribution (finite granularity) assuming the information granularity is the same for all sub-channels which is usually the case [94]. It is chosen over other algorithms such as Chow's algorithm [154] since it converges on a discrete efficient bit distribution without violating the total allowable energy constraint. Assuming a granularity of $\beta = 1$, each subcarrier (subchannel) energy for M–QAM is given by

$$\varepsilon_n(b_n) = 2\frac{\Gamma}{g_n}(2^{b_n} - 1), \tag{3.18}$$

where $1 \leq n \leq N_{sc}$ is the subcarrier index, g_n is the received SNR of the subcarrier n, b_n is the number of bits-per-symbol carried by the subcarrier n. Γ is the gap–to–capacity for uncoded M–QAM signal, given by

$$\Gamma = \frac{Q^{-1}(P_e)}{3}, \tag{3.19}$$

where $Q^{-1}(P_e)$ is the inverse Q function of target symbol-error probability. The optimum bit distribution is obtained for a desired BER that is taken to be the HD-FEC threshold BER of 3.8×10^{-3} in this thesis. After total subcarrier energies are computed, the incremental energies $e_n(b_n)$ for all subcarriers for all levels of modulation are calculated as follows:

$$e_n(b_n) = \varepsilon_n(b_n) - \varepsilon_n(b_n - \beta), \tag{3.20}$$

where $\beta = 1$. Following this, the index of the minimum incremental energy required to add an extra bit-per-symbol to a subcarrier to variable m is assigned as follows:

$$m \leftarrow arg \min_{1 \leq i \leq N} e_i(b_i + 1). \tag{3.21}$$

and the index of the maximum incremental energy, which would be saved by subtracting 1 bit-per-symbol from a subcarrier to variable n, is assigned as follows:

$$n \leftarrow arg \max_{1 \leq j \leq N} e_j(b_j). \tag{3.22}$$

After the initialization stage, the next step is to load the bits efficiently until the minimum increase in energy required becomes less than the maximum energy. The efficient bit distribution is obtained as follows:

while $e_m(b_m + 1) < e_n(b_n)$; `// while min. increase in energy < max. energy`

- $b_m \leftarrow b_m + 1$; `// add 1 bit-per-symbol`
- $b_n \leftarrow b_n - 1$; `// subtract 1 bit-per-symbol`
- $m \leftarrow arg \min_{1 \leq i \leq N} e_i(b_i + 1)$; `// update index`
- $n \leftarrow arg \min_{1 \leq j \leq N} e_j(b_j)$; `// update index`

end

Algorithm: Efficient bit distribution with no energy constraint.

After the efficient bit distribution is found considering no energy constraint, the bit distribution needs to be updated under the constraint of total allowable energy which is as follows:

$S \leftarrow \sum_{n=1}^{N} \varepsilon_n(b_n)$; // calculate total allowable energy
$\varepsilon_T \leftarrow S$;
while $(\varepsilon_T - S) < 0$ *or* $(\varepsilon_T - S) \geq \min_{1 \leq i \leq N} e_i(b_i + 1)$
  if $(\varepsilon_T - S) < 0$; // if energy limit is exceeded
    $n \leftarrow arg \min_{1 \leq j \leq N} e_j(b_j)$; // assign index of maximum energy saving
    $S \leftarrow S - e_n(b_n)$; // update the energy value
    $b_n \leftarrow b_n - 1$; // decrease the assigned bits-per-symbol by 1
  else
    $m \leftarrow arg \min_{1 \leq i \leq N} e_i(b_i + 1)$; // update index
    $S \leftarrow S + e_m(b_m + 1)$; // update the energy value
    $b_m \leftarrow b_m + 1$; // increase the assigned bits-per-symbol by 1
  endif
end

Algorithm: Update the efficient bit distribution with subject to total energy.

In this thesis, the bit loading is applied to assess the tolerance of OFDM signals to signal-signal beating interference (SSBI). It is further discussed in section 4.4. The power was kept uniform across the subcarriers. The bit loading algorithm stopped when the desired bit rate was achieved, *i.e.,* if the symbol rate is set to 7 GBaud, the average bits-per-symbol across all the subcarriers needs to be 2 to transmit 14 Gb/s. Although bit loading significantly increases the receiver sensitivity compared to uniform modulation, it requires a feedback from the receiver to the transmitter to obtain the SNR values of each subcarrier [94, Ch.4, pp. 317-323] [155].

After bit-to-symbol mapping and serial to parallel conversion, training symbols for FFT window synchronization are inserted. Following this, the location of pilot tones for channel estimation are determined with a certain amount of symbol spacing, as illustrated in Fig. 3.17. After the IFFT is applied, a CP is inserted to minimize the ISI and ICI, as discussed previously in section 3.1.4.1. In OFDM demodulation, the FFT window used at the receiver has to match its corresponding IFFT window used at the transmitter to demodulate the transmitted signal. The IFFT/FFT window size is equal to the total number of subcarriers or the single OFDM symbol duration, as shown Fig. 3.17. The frame is converted from parallel to serial, followed by the up-conversion and sideband filtering to obtain SSB-OFDM signal waveform.

3.2.2.2 OFDM symbol synchronization

The received OFDM symbols after the ADC is converted from serial to parallel, and subsequently, the CP is removed. There is always a symbol timing offset between a transmitter and receiver in a real system. To demodulate the OFDM symbols, the start of the OFDM waveform needs to be located. This is critical to avoid any ISI and ICI since the timing offset destroys the orthogonality between the subcarriers, and thus, causes severe BER degradation, as discussed earlier in this chapter.

The most popular method to determine the start of the discrete Fourier transform (DFT) window was

proposed by Schmidl & Cox [156]. In this method, two highly-correlated training symbols are inserted at the start of an OFDM frame, whose first half is identical to its second half. An autocorrelation between its first and second half is performed to locate the start of the OFDM frame. Assuming there are $N_{sc}/2$ complex samples in the first half of the training symbol excluding the CP, its auto correlation can be written as

$$R(d) = \sum_{m=0}^{N_{sc}/2-1} r^*_{d+m} r_{d+m+N_{sc}/2}, \tag{3.23}$$

where d is a time index corresponding to the first sample in a window of $2N_{sc}$ samples. The received energy for the second half-symbol is defined by

$$R(d) = \sum_{m=0}^{N_{sc}/2-1} |r_{d+m+N_{sc}/2}|^2. \tag{3.24}$$

Then, a timing metric can be defined as

$$M(d) = \frac{|P(d)|}{(R(d))^2}. \tag{3.25}$$

When d is equal to 0, the auto correlation function, and consequently, timing metric ($M(d)$) reach their maximum and draws a plateau with a length equal to the length of the guard interval (N_{CP}) minus the length of the channel impulse response, as shown in Fig. 3.18. This is due to the fact that the second half of r_m is identical to its first half except for a phase shift. There is no ISI within this plateau to distort the signal so that the start of the OFDM frame can be chosen any point within this plateau with no SNR degradation [156].

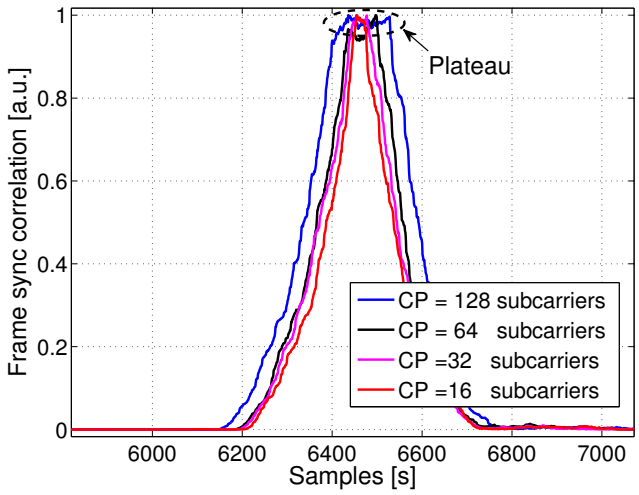

Fig. 3.18: The timing metric function with different CP lengths (25%, 12.5%, 6.25% and 3.125% of the FFT size).

3.2.2.3 Channel estimation

After the signal is transmitted through the dispersive channel, the symbol constellation at the receiver is rotated due to the chromatic dispersion and DFT sampling timing offset, referred to as common phase

error. They generate a linear phase term across the subcarriers. Note that phase noise also causes a phase rotation. However, there is no need for frequency offset (FO) correction and phase noise compensation (PNC) in direct detection links in contrast to coherent detection systems, which are discussed in section 5.

Since the data is transmitted on a number of different frequencies unlike conventional modulation formats such OOK or M-QAM, each OFDM symbol period is much longer than single symbol period in a serial systems. Therefore, only one symbol at most is affected by ISI which can be equalized using a frequency domain single-tap equalizer, enabled by the CP insertion [91, 104, 108]. To mitigate the chromatic dispersion and linear phase term due to the timing offset, the channel impulse response needs to be estimated using pilot tones, and subsequently, the received signal should be equalized before measuring the system performance. There are two types of pilot-based channel estimation techniques, namely block-type and comb-type. Comb-type channel estimation, that uses subcarriers as pilots, is suitable for fast-fading channels such as wireless communication whereas block-type channel estimation, that uses OFDM symbols as pilots, is suitable for slow-fading (considered as stationary within a certain period of OFDM symbols) frequency-selective channels such as those in optical fibre communication [89, 157]. Therefore, the block-type method is utilized for pilot-based channel estimation in this thesis.

In block-type pilot-based channel estimation, the pilot symbols (S_p) are inserted periodically at all subcarriers in time to keep track of the time-varying channel characteristics [158], as shown in Fig. 3.17. Pilot symbols have the same data sequence with other OFDM symbols. The pilot spacing ($N_{p\_spacing}$ - the number of OFDM symbols between each pilot symbol) depends on the channel. Large spacing is preferable as this reduces the overhead OH_p where short spacing may not track the fast changes in the optical channel causing performance degradation. OH_p is given by

$$OH_p = \frac{N_p}{N_{p\_spacing}}. \tag{3.26}$$

After OFDM symbol synchronization and taking the IFFT of the received OFDM signal, the pilot symbols are removed from the received signal for channel estimation. The channel coefficients are found through the use of a zero-forcing criterion, comparing the received symbols with the transmitted ones [158]. The number of coefficients that represents the channel response is equal to the number of pilot symbols (N_p). A polynomial fit (interpolating the derived coefficients from the pilot symbols to the number of OFDM symbols) is applied to improve the channel estimation/equalization performance. Finally, the received signal is multiplied with the inverse of the estimated channel response to cancel the common phase error and distortions incurred along the transmission path and restore the transmitted OFDM symbols, as shown in Fig. 3.19.

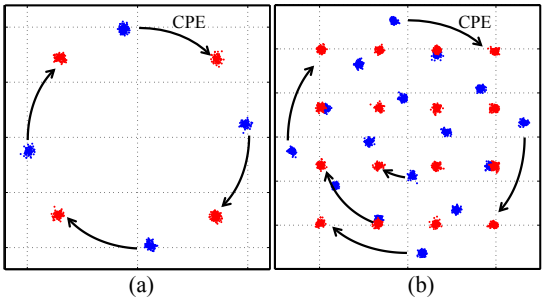

Fig. 3.19: Received (a)QPSK and (b)16-QAM symbols before/after channel estimation (blue/red markers). CPE: common phase error due to timing offset.

3.3 References

[1] J.G. Proakis and M. Salehi, *Digital communications*, 4th edition, McGraw-Hill, 2008.

[2] S.J. Savory, "Digital filters for coherent optical receivers," *Optics Express*, vol. 16, no. 2, pp. 804–817, 2008.

[3] M. Mazurczyk, "Spectral shaping in long haul optical coherent systems with high spectral efficiency," *J. Lightw. Technol.*, vol. 32, no. 16, pp. 2915–2924, 2014.

[4] J.-X. Cai, "100G transmission over transoceanic distance with high spectral efficiency and large capacity," *J. Lightw. Technol.*, vol. 30, no. 24, pp. 3845–3856, 2012.

[5] P. J. Winzer, "High-spectral-efficiency optical modulation formats," *J. Lightw. Technol.*, vol. 30, no. 24, pp. 3824–3835, 2012.

[6] ADVA, "Efficient 100G transport," 2015, [Online]. Available:http://www.advaoptical.com/en/innovation/100g-transport.aspx (retrieved on August 15th 2015).

[7] J. Wei, J. Ingham, D. Cunningham, R. Penty, and I. White, "Performance and power dissipation comparisons between 28 Gb/s NRZ, PAM, CAP, and optical OFDM systems for data communication applications," *J. Lightw. Technol.*, vol. 30, no. 20, pp. 3273–3280, 2012.

[8] P.J. Winzer and R.-J. Essiambre, "Advanced modulation formats for high-capacity optical transport networks," *J. Lightw. Technol.*, vol. 24, no. 12, pp. 4711–4728, 2006.

[9] E. Ip and J.M. Kahn, "Power spectra of return-to-zero optical signals," *J. Lightw. Technol.*, vol. 24, no. 3, pp. 1610–1618, 2006.

[10] D. Breuer and K. Petermann, "Comparison of NRZ and RZ modulation format for 40 Gb/s TDM standard fiber systems," *IEEE Photon. Technol. Lett.*, vol. 9, no. 3, pp. 398–400, 1997.

[11] M. Hayee and A. Willner, "NRZ versus RZ in 10-40-Gb/s dispersion-managed WDM transmission systems," *IEEE Photon. Technol. Lett.*, vol. 11, no. 8, pp. 991–993, 1999.

[12] Y. Frignac, S. Bigo, and J.-P. Hamaide, "NRZ versus RZ format in N×40 Gbit/s WDM terrestrial transmission systems with high spectral efficiency of 0.4 bit/(s.Hz)," in *Proc. IEEE European Conference on Optical Communication (ECOC)*, 2001, paper Th.B.1.1.

[13] C. Davidson, C. Chen, M. Nissov, A. Pilipetskii, N. Ramanujam, H. Kidorf, B. Pedersen, M. Mills, C. Lin, M. Hayee, J.X. Cai, A.B. Puc, P.C. Corbett, R. Menges, H. Li, A. Elyamani, C. Rivers, and N.S. Bergano, "1800 Gb/s transmission of one hundred and eighty 10 Gb/s WDM channels over 7,000 km using the full EDFA C-band," in *Proc. IEEE/OSA Optical Fiber Communication Conference (OFC)*, 2000, paper PD25.

[14] G. Vareille, B. Julien, F. Pitel, and J.-F. Marcerou, "3.65 Tbit/s (365×11.6 Gbit/s) transmission experiment over 6850 km using 22.2 GHz channel spacing in NRZ format," in *Proc. IEEE European Conference on Optical Communication (ECOC)*, 2001, pp. 14–15.

[15] S. Shimotsu, S. Oikawa, T. Saitou, N. Mitsugi, K. Kubodera, T. Kawanishi, and M. Izutsu, "Single side-band modulation performance of a $LiNbO_3$ integrated modulator consisting of four-phase modulator waveguides," *IEEE Photon. Technol. Lett.*, vol. 13, no. 4, pp. 364–366, 2001.

[16] P. Watts, V. Mikhailov, M. Glick, P. Bayvel, and R. Killey, "Single sideband optical signal generation and chromatic dispersion compensation using digital filters," *Electronics Letters*, vol. 40, no. 15, pp. 958–960, 2004.

[17] S. Bigo, Y. Frignac, G. Charlet, W. Idler, S. Borne, H. Gross, R. Dischler, W. Poehlmann, P. Tran, C. Simonneau, D. Bayart, G. Veith, A. Jourdan, and J.-P. Hamaide, "10.2 Tbit/s (256×42.7 Gbit/s PDM/WDM) transmission over 100 km Teralight fiber with 1.28 bit/s/Hz spectral efficiency," in *Proc. IEEE/OSA Optical Fiber Communication Conference (OFC)*, 2001, paper PD25.

[18] W. Idler, S. Bigo, Y. Frignac, B. Franz, and G. Veith, "Vestigial sideband demultiplexing for ultra high capacity (0.64 bit/s/Hz) transmission of 128×40 Gb/s channels," in *Proc. IEEE/OSA Optical Fiber Communication Conference (OFC)*, 2001, paper MM3.

[19] W. Idler, G. Charlet, R. Dischler, Y. Frignac, and S. Bigo, "0.8 bit/s/Hz of information spectral density by vestigial sideband filtering of 42.66 Gb/s NRZ," in *Proc. IEEE European Conference on Optical Communication (ECOC)*, 2002, paper 8.1.5.

[20] G. Charlet, S. Lanne, L. Pierre, C. Simonneau, P. Tran, H. Mardoyan, P. Brindel, M. Gorlier, J.-C. Antona, M. Molina, P. Sillard, J. Godin, W. Idler, and S. Bigo, "Cost-optimized 6.3 Tbit/s-capacity terrestrial link over 17×100 km using phase-shaped binary transmission in a conventional all-EDFA SMF-based system," in *Proc. IEEE/OSA Optical Fiber Communication Conference (OFC)*, 2003, paper PDP25.

[21] K. Schuh, E. Lach, B. Junginger, A. Klekamp, and G. Veith, "8×107 Gbit/s serial binary NRZ/VSB transmission over 480 km SSMF with 1 bit/s/Hz spectral efficiency and without optical equalizer," in *Proc. IEEE European Conference on Optical Communication (ECOC)*, 2007, pp. 1–2.

[22] D. Grosz, A. Agarwal, S. Banerjee, A. Kung, D. Maywar, A. Gurevich, T. Wood, C. Lima, B. Faer, J. Black, and C. Hwu, "5.12 Tb/s (128×42.7 Gb/s) transmission with 0.8 bit/s/Hz spectral efficiency over 1280 km of standard single-mode fiber using all-Raman amplification and strong signal filtering," in *Proc. IEEE European Conference on Optical Communication (ECOC)*, 2002, paper PD4.3.

[23] I. Morita, T. Tsuritani, N. Yoshikane, A. Agata, K. Imai, and N. Edagawa, "100% spectral-efficient 25×42.7 Gbit/s transmission using asymmetrically filtered CS-RZ signal and a novel crosstalk suppressor," in *Proc. IEEE European Conference on Optical Communication (ECOC)*, 2002, paper PD4.7.

[24] S.L. Jansen, R.H. Derksen, C. Schubert, X. Zhou, M. Birk, C.-J. Weiske, M. Bohn, D. van den Borne, P.M. Krummrich, M. Möller, F. Horst, B.J. Offrein, H. de Waardt, G.D. Khoe, A. Kirstädter, "107-Gb/s full-ETDM transmission over field installed fiber using vestigial sideband modulation," *Proc. IEEE/OSA Optical Fiber Communication Conference (OFC)*, 2007, paper OWE3.

[25] A. Lender, "The duobinary technique for high-speed data transmission," *Trans. of American Institute of Electrical Engineers, part I: Communication and Electronics*, vol. 82, no. 2, pp. 214–218, 1963.

[26] D. Penninckx, M. Chbat, L. Pierre, and J.-P. Thiery, "The phase-shaped binary transmission (PSBT): A new technique to transmit far beyond the chromatic dispersion limit," *IEEE Photon. Technol. Lett.*, vol. 9, no. 2, pp. 259–261, 1997.

[27] E. Pincemin, C. Gosset, N. Boudrioua, A. Tan, D. Grot, and T. Guillossou, "Experimental performance comparison of duobinary and PSBT modulation formats for long-haul 40 Gb/s transmission on G 0.652 fibre," *Optics Express*, vol. 20, no. 27, pp. 28171–28190, 2012.

[28] K. Yonenaga, S. Kuwano, S. Norimatsu, and N. Shibata, "Optical duobinary transmission system with no receiver sensitivity degradation," *Electronics Letters*, vol. 31, no. 4, pp. 302–304, 1995.

[29] C. Gosset, L. Dupont, A. Tan, A. Bezard, and E. Pincemin, "Experimental performance comparison of duobinary formats for 40 Gb/s long-haul transmission," in *Proc. IEEE/OSA Optical Fiber Communication Conference (OFC)*, 2008, paper JThA55.

[30] D. Penninckx, L. Pierre, J.-P. Thiery, B. Clesca, M. Chbat, and J. Beylat,"Relation between spectrum bandwidth and the effects of chromatic dispersion in optical transmissions," *Electronics Letters*, vol. 32, no. 11, pp. 1023–1024, 1996.

[31] J.B. Stark, J. Mazo, and R. Laroia, "Phased amplitude-shift signaling (PASS) codes: Increasing the spectral efficiency of DWDM transmission," in *Proc. IEEE European Conference on Optical Communication (ECOC)*, 1998, pp. 373–374.

[32] T. Ono, Y. Yano, K. Fukuchi, T. Ito, H. Yamazaki, M. Yamaguchi, and K. Emura, "Characteristics of optical duobinary signals in Terabit/s capacity, high-spectral efficiency WDM systems," *J. Lightw. Technol.*, vol. 16, no. 5, p. 788, 1998.

[33] H. Bissessur, G. Charlet, C. Simonneau, S. Borne, L. Pierre, C. De Barros, P. Tran, W. Idler, and R. Dischler, "3.2 Tb/s (80×40 Gb/s) C-band transmission over 3×100 km with 0.8 bit/s/Hz efficiency," in *Proc. IEEE European Conference on Optical Communication (ECOC)*, 2001, paper PD.M.1.11.

[34] M. Alfiad and S. Tibuleac, "100G superchannel transmission using 4×28 Gb/s subcarriers on a 25-GHz grid," *IEEE Photon. Technol. Lett.*, vol. 27, no. 2, pp. 157–160, 2015.

[35] K. Schuh, E. Lach, B. Junginger, G. Veith, J. Renaudier, G. Charlet, and P. Tran, "8 Tb/s (80×107 Gb/s) DWDM NRZ-VSB transmission over 510 km NZ-DSF with 1 bit/s/Hz spectral efficiency," *J. Bell Labs Technical*, vol. 14, no. 1, pp. 89–104, 2009.

[36] G. Charlet, J.-C. Antona, S. Lanne, and S. Bigo, "From 2,100 km to 2,700 km distance using phase-shaped binary transmission at 6.3 Tbit/s capacity," in *Proc. IEEE/OSA Optical Fiber Communication Conference (OFC)*, 2003, paper WE3.

[37] G. Raybon, P. J. Winzer, and C. R. Doerr, "1-Tb/s (10×107 Gb/s) electronically multiplexed optical signal generation and WDM transmission," *J. Lightw. Technol.*, vol. 25, no. 1, pp. 233–238, 2007.

[38] D. Foursa, C. Davidson, M. Nissov, M. Mills, L. Xu, J. Cai, A. Pilipetskii, Y. Cai, C. Breverman, R. Cordell, T.J. Carvelli, P.C. Corbett, H.D. Kidorf, and N.S. Bergano, "2.56 Tb/s (256×10 Gb/s) transmission over 11,000 km using hybrid Raman/EDFAs with 80 nm of continuous bandwidth," in *Proc. IEEE/OSA Optical Fiber Communication Conference (OFC)*, 2002, paper FC3–1.

[39] A.H. Gnauck and P.J. Winzer, "Optical phase-shift-keyed transmission," *J. Lightw. Technol.*, vol. 23, no. 1, pp. 115–130, 2005.

[40] M. Rice, S. Tretter, and P. Mathys, "On differentially encoded M-sequences," *IEEE Transactions on Communications*, vol. 49, no. 3, pp. 421–424, 2001.

[41] P.A. Humblet and M. Azizoglu, "On the bit error rate of lightwave systems with optical amplifiers," *J. Lightw. Technol.*, vol. 9, no. 11, pp. 1576–1582, 1991.

[42] J.-X. Cai, D. Foursa, L. Liu, C. Davidson, Y. Cai, W. Patterson, A. Lucero, B. Bakhshi, G. Mohs, P. Corbett, V. Gupta, W. Anderson, M. Vaa, G. Domagala, M. Mazurczyk, H. Li, S. Jiang, M. Nissov, A.N. Pilipetskii, and N.S. Bergano, "RZ-DPSK field trial over 13,100 km of installed non-slope-matched submarine fibers," *J. Lightw. Technol.*, vol. 23, no. 1, pp. 95–103, 2005.

[43] J.-X. Cai, A. Turukhin, B. Anderson, W. Patterson, G. Berkowitz, J. Figueiredo, W. Kellner, M. Mazurczyk, T. Marino, G. Valvo, B. Li, G. Mohs, A.N. Pilipetskii, and N.S. Bergano, "40G field trial with 0.8 bits/s/Hz spectral efficiency over 6,550 km of installed undersea cable," in *Proc. IEEE/OSA Optical Fiber Communication Conference (OFC)*, 2011, paper NThB6.

[44] R. Griffin and A. Carter, "Optical differential quadrature phase-shift key (oDQPSK) for high capacity optical transmission," in *Proc. IEEE/OSA Optical Fiber Communication Conference (OFC)*, 2002, paper WX6.

[45] A. Gnauck, P. Winzer, S. Chandrasekhar, and C. Doerr, "Spectrally efficient (0.8 b/s/Hz) 1-Tb/s (25×42.7 Gb/s) RZ-DQPSK transmission over 28 100-km SSMF spans with 7 optical add/drops," in *Proc. IEEE European Conference on Optical Communication (ECOC)*, 2004, paper Th4.4.1.

[46] G. Charlet, P. Tran, H. Mardoyan, M. Lefrancois, T. Fauconnier, F. Jorge, and S. Bigo, "151×43 Gb/s transmission over 4080 km based on return-to-zero-differential quadrature phase-shift keying," in *Proc. IEEE European Conference on Optical Communication (ECOC)*, 2005, paper Th4.1.3.

[47] D. van den Borne, S. L. Jansen, G.-D. Khoe, H. de Waardt, and E. Gottwald, "Line optimization in long-haul transmission systems with 42.8 Gbit/s RZ-DQPSK modulation," in *Proc. IEEE/OSA Optical Fiber Communication Conference (OFC)*, 2006, paper OFD2.

[48] T. Tokle, C. Davidson, M. Nissov, J.-X. Cai, D. Foursa, and A. Pilipetskii, "6500 km transmission of RZ-DQPSK WDM signals," *Electronics Letters*, vol. 40, no. 7, pp. 444–445, 2004.

[49] K. Ishida, D.-S. Ly-Gagnon, K. Shimizu, T. Mizuochi, K. Motoshima, and K. Kikuchi, "Transmission of 20×20 Gb/s RZ-DQPSK signals over 5090 km with 0.53 b/s/Hz spectral efficiency," in *Proc. IEEE/OSA Optical Fiber Communication Conference (OFC)*, 2004, p. 3.

[50] S. Susskind and E.A. de Souza, "40 Gb/s RZ-DQPSK transmission with SPM and ASE suppression by dispersion management," in *SBMO/IEEE MTT-S Int.'l Microwave and Optoelectronics Conference (IMOC)*, 2009, pp. 106–109.

[51] N. Yoshikane and I. Morita, "1.14 b/s/Hz spectrally efficient 50×85.4 Gb/s transmission over 300 km using copolarized RZ-DQPSK signals," *J. Lightw. Technol.*, vol. 23, no. 1, pp. 108–114, 2005.

[52] X. Zhou, J. Yu, M. Du, and G. Zhang, "2 Tb/s (20×107 Gb/s) RZ-DQPSK straight-line transmission over 1005 km of standard single mode fiber (SSMF) without Raman amplification," in *Proc. IEEE/OSA Optical Fiber Communication Conference (OFC)*, 2008, paper OMQ3.

[53] W. Idler, E. Lach, W. Kuebart, B. Junginger, K. Schuh, A. Klekamp, D. Werner, A. Steffan, A. Schippel, M. Schneiders, S. Vorbeck, and R.-P. Braun, "16×112 Gb/s NRZ-DQPSK lab experiments and WDM field trial over ultimate metro distances including high PMD fibers," *J. Lightw. Technol.*, vol. 29, no. 15, pp. 2195–2203, 2011.

[54] P. J. Winzer, G. Raybon, H. Song, A. Adamiecki, S. Corteselli, A. H. Gnauck, D. A. Fishman, C. R. Doerr, S. Chandrasekhar, L. L. Buhl, T.J. Xia, G. Wellbrock, W. Lee, B. Basch, T. Kawanishi, K. Higuma, and Y. Painchaud, "100 Gb/s

DQPSK transmission: From laboratory experiments to field trials," *J. Lightw. Technol.*, vol. 26, no. 20, pp. 3388–3402, 2008.

[55] P.S. Cho, V.S. Grigoryan, Y.A. Godin, A. Salamon, and Y. Achiam, "Transmission of 25 Gb/s RZ-DQPSK signals with 25-GHz channel spacing over 1000 km of SMF-28 fiber," *IEEE Photon. Technol. Lett.*, vol. 15, no. 3, pp. 473–475, 2003.

[56] E. Pincemin, T. Guillossou, N. Evanno, S. Lobanov, and S. Ten, "Record transmission distances over ultra low loss G.652 fibre with NRZ-OOK or NRZ-DPSK 40 Gbps WDM systems," in *Proc. IEEE/OSA Optical Fiber Communication Conference (OFC)*, 2009, paper OThC2.

[57] I. Morita, "50 GHz-spaced 64×42.7 Gbit/s transmission over 8200 km using pre-filtered CS-RZ DPSK signal and EDFA repeaters," *Proc. IEEE European Conference on Optical Communication (ECOC)*, 2003, paper Mo4.3.1.

[58] P.P.L. Becouarn, G. Vareille and J. Marcerou, "3 Tbit/s transmission (301 DPSK channels at 10.709 Gb/s) over 10,270 km with a record efficiency of 0.65(bit/s)/Hz," in *Proc. IEEE European Conference on Optical Communication (ECOC)*, 2003, post-deadline paper Th4.3.2.

[59] C. Rasmussen, T. Fjelde, J. Bennike, L. Fenghai, S. Dey, B. Mikkelsen, P. Mamyshev, P. Serbe, P. van der Wagt, Y. Akasaka, D. Harris, D. Gapontsev, V. Ivshin, and P. Reeves-Hall, "DWDM 40 G transmission over trans-pacific distance (10,000 km) using CSRZ-DPSK, enhanced FEC, and all-Raman-amplified 100-km ultrawave fiber spans," in *Proc. IEEE/OSA Optical Fiber Communication Conference (OFC)*, 2003, paper PD18–P1.

[60] J.-X. Cai, D.G. Foursa, C.R. Davidson, Y. Cai, G. Domagala, H. Li, L. Liu, W.W. Patterson, A.N. Pilipetskii, M. Nissov, and N.S. Bergano, "A DWDM demonstration of 3.73 Tb/s over 11,000 km using 373 RZ-DPSK channels at 10 Gb/s," in *Proc. IEEE/OSA Optical Fiber Communication Conference (OFC)*, 2003, paper PD22.

[61] N. Kikuchi, K. Mandai, K. Sekine, and S. Sasaki, "First experimental demonstration of single-polarization 50-Gbit/s 32-level (QASK and 8-DPSK) incoherent optical multilevel transmission," in *Proc. IEEE/OSA Optical Fiber Communication Conference (OFC)*, 2007, paper PDP21.

[62] N. Kikuchi and S. Sasaki, "Highly sensitive optical multilevel transmission of arbitrary quadrature-amplitude modulation (QAM) signals with direct detection," *J. Lightw. Technol.*, vol. 28, no. 1, pp. 123–130, 2010.

[63] N. Kikuchi, K. Mandai, and S. Sasaki, "Experimental demonstration of incoherent optical multilevel staggered-APSK (amplitude-and phase-shift keying) signaling," in *Proc. IEEE/OSA Optical Fiber Communication Conference (OFC)*, 2008, paper OMI3.

[64] M. Seimetz, M. Noelle, and E. Patzak, "Optical systems with high-order DPSK and star QAM modulation based on interferometric direct detection," *J. Lightw. Technol.*, vol. 25, no. 6, pp. 1515–1530, 2007.

[65] N. Kikuchi, K. Mandai, K. Sekine, and S. Sasaki, "Incoherent 32-level optical multilevel signaling technologies," *J. Lightw. Technol.*, vol. 26, no. 1, pp. 150–157, 2008.

[66] H. S. Chung, S. H. Chang, J. Lee, and K. Kim, "Transmission performance comparison of direction detection-based 100-Gb/s modulation formats for metro area optical networks," *Electronics and Telecommunications Research Institute Journal*, vol. 34, no. 6, 2012.

[67] N. Sotiropoulos, T. Koonen, and H. de Waardt, "Advanced differential modulation formats for optical access networks," *J. Lightw. Technol.*, vol. 31, no. 17, pp. 2829–2843, 2013.

[68] B.T. Teipen and M.H. Eiselt, "107Gb/s DPSK-3ASK optical transmission over SSMF," in *Proc. IEEE/OSA Optical Fiber Communication Conference (OFC)*, 2010, paper NMB1.

[69] H.Y. Choi and I. Morita, "Nonlinear tolerance of 53.5-Gb/s differential 6-ary PSK surrounded by 10.7-Gb/s NRZ-OOK neighbors in SMF and DSF transmission links," *IEEE Photon. Technol. Lett.*, vol. 24, no. 10, pp. 806–808, 2012.

[70] C. Kim and G. Li, "Direct-detection optical differential 8-level phase-shift keying (OD8PSK) for spectrally efficient transmission," *Optics Express*, vol. 12, no. 15, pp. 3415–3421, 2004.

[71] E. Tipsuwannakul, M. Karlsson, E. Agrell, and P. Andrekson, "Performance comparison between 120 Gbit/s RZ-DQP-ASK and RZ-D8PSK over a 480 km link," in *Proc. IEEE/OSA Optical Fiber Communication Conference (OFC)*, 2011, paper OMI5.

[72] H. Yoon, D. Lee, and N. Park, "Performance comparison of optical 8-ary differential phase-shift keying systems with different electrical decision schemes," *Optics Express*, vol. 13, no. 2, pp. 371–376, 2005.

[73] K, Mandai, N. Kikuchi, and S. Sasaki, "First long distance (1040-km) WDM transmission of 16-channels 30-Gbit/s (480-Gbit/s) 8-ary differential phase-shift-keying (8-DPSK) signals," *Proc. OptoElectronics and Communication Conference*, 2007, paper PD1-2.

[74] E. Tipsuwannakul, M. Sköld, M. Karlsson, and P. Andrekson, "Transmission of 240 Gb/s PM-RZ-D8PSK over 320 km in 10 Gb/s NRZ-OOK WDM system," in *Proc. IEEE/OSA Optical Fiber Communication Conference (OFC)*, 2010, paper OMJ2.

[75] Y. Takushima, H. Choi, and Y. Chung, "Transmission of 108-Gb/s PDM 16ADPSK signal on 25-GHz grid using non-coherent receivers," *Optics Express*, vol. 17, no. 16, pp. 13458–13466, 2009.

[76] M. Serbay, T. Tokle, P. Jeppesen, and W. Rosenkranz, "42.8 Gbit/s, 4 bits per symbol 16-ary inverse-RZ-QASK-DQPSK transmission experiment without polmux," in *Proc. IEEE/OSA Optical Fiber Communication Conference (OFC)*, 2007, paper OThL2.

[77] R. Hirai, N. Kikuchi, and S. Sasaki, "Experimental demonstration of single polarization direct-detection 107-Gbit/s 16APSK modulation," in *OptoElectronics and Communications Conference (OECC)*, 2010, paper 8B1-2.

[78] N. Kikuchi and S. Sasaki, "Incoherent 40-Gbit/s 16QAM and 30-Gbit/s staggered 8APSK (amplitude-and phase-shift keying) signaling with digital phase pre-integration technique," in *IEEE/LEOS Summer Topical Meetings*, 2008, pp. 251–252.

[79] N. Kikuchi and S. Sasaki, "Optical dispersion-compensation free incoherent multilevel signal transmission over standard single-mode fiber with digital pre-distortion and phase pre-integration techniques," in *Proc. IEEE European Conference on Optical Communication (ECOC)*, 2008, paper Tu.1.E.2.

[80] C. Kim, G. Goldfarb, Y. Han, Z. Li, X. Li, and G. Li, "WDM transmission over 320 km EDFA-amplified SSMF using 30 Gb/s return-to-zero optical differential 8-level phase-shift keying (OD8PSK)," *Optics Express*, vol. 13, no. 11, pp. 4044–4049, 2005.

[81] W. Rosenkranz and C. Xia, "Electrical equalization for advanced optical communication systems," *AEU-Int.'l J. Electronics and Communication*, vol. 61, no. 3, pp. 153–157, 2007.

[82] H. Bulow, F. Buchali, and A. Klekamp, "Electronic dispersion compensation," *J. Lightw. Technol.*, vol. 26, no. 1, pp. 158–167, 2008.

[83] G. Katz and D. Sadot, "A nonlinear electrical equalizer with decision feedback for OOK optical communication systems," *IEEE Transactions on Communications*, vol. 56, no. 12, pp. 2002–2006, 2008.

[84] J. Yu, Z. Jia, T. Wang, and G. K. Chang, "Centralized lightwave radio-over-fiber system with photonic frequency quadrupling for high-frequency millimeter-wave generation," *IEEE Photon. Technol. Lett.*, vol. 19, no. 19, pp. 1499–1501, 2007.

[85] M. Cavallari, C. Fludger, and P. Anslow, "Electronic signal processing for differential phase modulation formats," in *Proc. IEEE/OSA Optical Fiber Communication Conference (OFC)*, 2004, paper TuG2.

[86] O.E. Agazzi, M.R. Hueda, H.S. Carrer, and D.E. Crivelli, "Maximum-likelihood sequence estimation in dispersive optical channels," *J. Lightw. Technol.*, vol. 23, no. 2, pp. 749–763, 2005.

[87] R. I. Killey, P. M. Watts, V. Mikhailov, M. Glick, and P. Bayvel, "Electronic dispersion compensation by signal predistortion using digital processing and a dual-drive Mach–Zehnder modulator," *IEEE Photon. Technol. Lett.*, vol. 17, no. 3, pp. 714–716, 2005.

[88] D. McGhan, C. Laperle, A. Savchenko, C. Li, G. Mak, and M. O'Sullivan, "5120 km RZ-DPSK transmission over G.652 fiber at 10 Gb/s with no optical dispersion compensation," in *Proc. IEEE/OSA Optical Fiber Communication Conference (OFC)*, 2005, paper PDP27.

[89] B.J. Schmidt, A.J. Lowery, and J. Armstrong, "Experimental demonstrations of electronic dispersion compensation for long-haul transmission using direct-detection optical OFDM," *J. Lightw. Technol.*, vol. 26, no. 1, pp. 196–203, 2008.

[90] D.J. Barros and J.M. Kahn, "Comparison of orthogonal frequency-division multiplexing and on-off keying in amplified direct-detection single-mode fiber systems," *J. Lightw. Technol.*, vol. 28, no. 12, pp. 1811–1820, 2010.

[91] W. Shieh and I. Djordjevic, *OFDM for optical communications*, Academic Press, 2009.

[92] B. Saltzberg, "Performance of an efficient parallel data transmission system," *IEEE Transactions on Communication Technology*, vol. 15, no. 6, pp. 805–811, 1967.

[93] A.J. Lowery and L.B. Du, "Optical orthogonal division multiplexing for long haul optical communications: A review of the first five years," *Optical Fiber Technology*, vol. 17, no. 5, pp. 421–438, 2011.

[94] J. Cioffi, *"Course notes:Ch.4"*, 1995 [Online]. Available: http://www.stanford.edu/group/cioffi/book.

[95] R. Giddings, X. Jin, E.H.-Salas, E. Giacoumidis, J. Wei, and J. Tang, "Experimental demonstration of a record high 11.25 Gb/s real-time optical OFDM transceiver supporting 25km SMF end-to-end transmission in simple IMDD systems," *Optics Express*, vol. 18, no. 6, pp. 5541–5555, 2010.

[96] E. Giacoumidis, A. Kavatzikidis, A. Tsokanos, J. Tang, and I. Tomkos,"Adaptive loading algorithms for IMDD optical OFDM PON systems using directly modulated lasers," *Journal of Optical Communications and Networking*, vol. 4, no. 10, pp. 769–778, 2012.

[97] J. Armstrong, "OFDM for optical communications," *J. Lightw. Technol.*, vol. 27, no. 3, pp. 189–204, 2009.

[98] T. Jiang and Y. Wu, "An overview: Peak-to-average power ratio reduction techniques for OFDM signals," *IEEE Transactions on Broadcasting*, vol. 54, no. 2, pp. 257–268, 2008.

[99] C.R. Berger, Y. Benlachtar, R.I. Killey, and P.A. Milder, "Theoretical and experimental evaluation of clipping and quantization noise for optical OFDM," *Optics express*, vol. 19, no. 18, pp. 17713–17728, 2011.

[100] S. Hara and R. Prasad, *Multicarrier techniques for 4G mobile communications*, Artech House, 2003.

[101] D.J. Barros and J.M. Kahn, "Optimized dispersion compensation using orthogonal frequency-division multiplexing," *J. Lightw. Technol.*, vol. 26, no. 16, pp. 2889–2898, 2008.

[102] W. Shieh and C. Athaudage, "Coherent optical orthogonal frequency division multiplexing," *Electronics Letters*, vol. 42, no. 10, pp. 587–589, 2006.

[103] D.J. Barros and J.M. Kahn, "Comparison of orthogonal frequency-division multiplexing and on-off keying in amplified direct-detection single-mode fiber systems," *J. Lightw. Technol.*, vol. 28, no. 12, pp. 1811–1820, 2010.

[104] J. Armstrong and B.J. Schmidt, "Comparison of asymmetrically clipped optical OFDM and DC-biased optical OFDM in AWGN," *IEEE Communications Letters*, vol. 12, no. 5, pp. 343–345, 2008.

[105] S.D. Dissanayake and J. Armstrong, "Comparison of ACO-OFDM, DCO-OFDM and ADO-OFDM in IM/DD systems," *J. Lightw. Technol.*, vol. 31, no. 7, pp. 1063–1072, 2013.

[106] A. Lowery and J. Armstrong, "Orthogonal-frequency-division multiplexing for dispersion compensation of long-haul optical systems," *Optics Express*, vol. 14, no. 6, pp. 2079–2084, 2006.

[107] M. Sieben, J. Conradi, and D.E. Dodds, "Optical single sideband transmission at 10 Gb/s using only electrical dispersion compensation," *J. Lightw. Technol.*, vol. 17, no. 10, pp. 1742–1749, 1999.

[108] A.J. Lowery, "Improving sensitivity and spectral efficiency in direct-detection optical OFDM systems," in *Proc. IEEE/OSA Optical Fiber Communication Conference (OFC)*, 2008, paper OMM4.

[109] M. Schuster, S. Randel, C.A. Bunge, S.C.J. Lee, F. Breyer, B. Spinnler, and K. Petermann, "Spectrally efficient compatible single-sideband modulation for OFDM transmission with direct detection," *IEEE Photon. Technol. Lett.*, vol. 20, no. 9, pp. 670–672, 2008.

[110] J. Zhang, X. Yuan, M. Lin, Y. Zhang, M. Zhang, and X. Zhang, "112Gb/s Pol-Mux RZ-DQPSK transmission over 960km SMF with high-speed polarization controller," in *OptoElectronics and Communications Conference (OECC)*, 2010, paper 9B1-3.

[111] W.-R. Peng, X. Wu, K.-M. Feng, V. R. Arbab, B. Shamee, J.-Y. Yang, L.C. Christen, A.E. Willner, and S. Chi, "Spectrally efficient direct-detected OFDM transmission employing an iterative estimation and cancellation technique," *Optics express*, vol. 17, no. 11, pp. 9099–9111, 2009.

[112] W.-R. Peng, B. Zhang, K.-M. Feng, X. Wu, A.E. Willner, and S. Chi, "Spectrally efficient direct-detected OFDM transmission incorporating a tunable frequency gap and an iterative detection techniques," *J. Lightw. Technol.*, vol. 27, no. 24, pp. 5723–5735, 2009.

[113] Z. Cao, J. Yu, W. Wang, L. Chen, and Z. Dong, "Direct-detection optical OFDM transmission system without frequency guard band," *IEEE Photon. Technol. Lett.*, vol. 22, no. 11, pp. 736–738, 2010.

[114] S.A. Nezamalhosseini, L.R. Chen, Q. Zhuge, M. Malekiha, F. Marvasti, and D.V. Plant, "Theoretical and experimental investigation of direct detection optical OFDM transmission using beat interference cancellation receiver," *Optics Express*, vol. 21, no. 13, pp. 15237–15246, 2013.

[115] W.-R. Peng, I. Morita, and H. Tanaka, "Enabling high capacity direct-detection optical OFDM transmissions using beat interference cancellation receiver," in *Proc. IEEE European Conference on Optical Communication (ECOC)*, 2010, paper Tu.4.A.2.

[116] W.-R. Peng, X. Wu, V.R. Arbab, K.-M. Feng, B. Shamee, L.C. Christen, J.-Y. Yang, A.E. Willner, and S. Chi, "Theoretical and experimental investigations of direct-detected RF-tone-assisted optical OFDM systems," *J. Lightw. Technol.*, vol. 27, no. 10, pp. 1332–1339, 2009.

[117] X. Jin, J. Wei, R. Giddings, T. Quinlan, S. Walker, and J. Tang, "Experimental demonstrations and extensive comparisons of end-to-end real-time optical OFDM transceivers with adaptive bit and/or power loading," *IEEE Photon. Technol. Lett.*, vol. 3, no. 3, pp. 500–511, 2011.

[118] W.-R. Peng, I. Morita, H. Takahashi, and T. Tsuritani, "Transmission of high-speed (> 100 Gb/s) direct-detection optical OFDM superchannel," *J. Lightw. Technol.*, vol. 30, no. 12, pp. 2025–2034, 2012.

[119] Z. Li, X. Xiao, T. Gui, Q. Yang, R. Hu, Z. He, M. Luo, C. Li, X. Zhang, D. Xue, S. You, and S. Yu, "432-Gb/s direct-detection optical OFDM superchannel transmission over 3040-km SSMF," *IEEE Photon. Technol. Lett.*, vol. 25, no. 15, pp. 1524–1526, 2013.

[120] X. Zhang, Z. Li, C. Li, M. Luo, H. Li, C. Li, Q. Yang, and S. Yu, "Transmission of 100-Gb/s DDO-OFDM/OQAM over 320-km SSMF with a single photodiode," *Optics Express*, vol. 22, no. 10, pp. 12079–12086, 2014.

[121] A. Dochhan, H. Grieser, M. Eiselt, and J.-P. Elbers, "Flexible bandwidth 448 Gb/s DMT transmission for next generation data center inter-connects," in *Proc. IEEE European Conference on Optical Communication (ECOC)*, 2014, paper P.4.10.

[122] B.J. Schmidt, A.J. Lowery, and J. Armstrong, "Experimental demonstrations of 20 Gbit/s direct-detection optical OFDM and 12 Gbit/s with a colorless transmitter," in *Proc. IEEE/OSA Optical Fiber Communication Conference (OFC)*, 2007, pp. 1–3.

[123] J. Barry, *Wireless infrared communications*, Kluwer Academic Publishers, Norwell, MA, USA, 1994.

[124] J. Kahn and J. Barry, "Wireless infrared communications," *Proc. of the IEEE*, vol. 85, no. 2, pp. 265–298, 1997.

[125] A.O. Wiberg, B.-E. Olsson, and P.A. Andrekson, "Single-cycle subcarrier modulation," in *Proc. IEEE/OSA Optical Fiber Communication Conference (OFC)*, 2009, paper OTuE1.

[126] B.-E. Olsson and A. Alping, "Electro-optical subcarrier modulation transmitter for 100 GbE DWDM transport," in *Asia Optical Fiber Communication Conference (ACP)*, 2008, paper SaF3.

[127] E. Ip, A.P.T. Lau, D.J. Barros, and J.M. Kahn, "Coherent detection in optical fiber systems," *Optics Express*, vol. 16, no. 2, pp. 753–791, 2008.

[128] N. Liu, X. Chen, C. Ju, and R. Hui, "40-Gbps vestigial sideband half-cycle Nyquist subcarrier modulation transmission experiment and its comparison with orthogonal frequency division multiplexing," *Optical Engineering*, vol. 53, no. 9, pp. 096114–096114, 2014.

[129] B.-E. Olsson and M. Sköld, "QPSK transmitter based on optical amplitude modulation of electrically generated QPSK signal," in *Asia Optical Fiber Communication Conference (ACP)*, 2008, paper SaA3.

[130] T.-T. Pham, R. Rodes, J.B. Jensen, C.J. Chang-Hasnain, and I.T. Monroy, "Sub-cycle QAM modulation for VCSEL-based optical fiber links," *Optics Express*, vol. 21, no. 2, pp. 1830–1839, 2013.

[131] A.S. Karar and J.C. Cartledge, "Generation and detection of a 56 Gb/s signal using a DML and half-cycle 16-QAM Nyquist-SCM," *IEEE Photon. Technol. Lett.*, vol. 25, no. 8, pp. 757–760, 2013.

[132] J.M. Buset, Z. El-Sahn, and D.V. Plant, "Experimental demonstration of a 10 Gb/s subcarrier multiplexed WDM PON," *IEEE Photon. Technol. Lett.*, vol. 25, no. 15, pp. 1435–1438, 2013.

[133] J.M. Buset, Z.A. El-Sahn, and D.V. Plant, "Experimental demonstration of a 10 Gb/s RSOA-based 16-QAM subcarrier multiplexed WDM PON," *Optics Express*, vol. 22, no. 1, pp. 1–8, 2014.

[134] M. Erkılınç, S. Kilmurray, R. Maher, M. Paskov, R. Bouziane, S. Pachnicke, H. Griesser, B. Thomsen, P. Bayvel, and R. Killey, "Nyquist-shaped dispersion-precompensated subcarrier modulation with direct detection for spectrally-efficient WDM transmission," *Optics Express*, vol. 22, no. 8, pp. 9420–9431, 2014.

[135] S. Erkilinc, S. Pachnicke, H. Griesser, B. Thomsen, P. Bayvel, and R. Killey, "Performance comparison of single sideband direct-detection Nyquist-subcarrier modulation and OFDM," *J. Lightw. Technol.*, vol. 33, no. 10, pp. 2038–2046, 2015.

[136] M. Erkilinc, M. P. Thakur, S. Pachnicke, H. Griesser, J. Mitchell, B. Thomsen, P. Bayvel, and R. Killey, "Spectrally-efficient WDM Nyquist pulse-shaped subcarrier modulation using a dual-drive Mach–Zehnder modulator and direct detection," *J. Lightw. Technol.*, vol. 33, no. 15, pp. 3147–3155, 2015.

[137] J. Proakis and D. Manolakis, *Digital signal processing*, 4th edition, Upper Saddle River, NJ, 2006.

[138] V. Čižek, "Discrete Hilbert transform," *IEEE Transactions on Audio and Electroacoustics*, vol. 18, no. 4, pp. 340–343, 1970.

[139] O.O. Omomukuyo, "Orthogonal frequency division multiplexing for optical access networks," Ph.D. dissertation, University College London (UCL), 2013.

[140] J. Park, W. Sorin, and K. Lau, "Elimination of the fibre chromatic dispersion penalty on 1550 nm millimetre-wave optical transmission," *Electronics Letters*, vol. 33, no. 6, pp. 512–513, 1997.

[141] J. Yu, M.-F. Huang, Z. Jia, T. Wang, and G.-K. Chang, "A novel scheme to generate single-sideband millimeter-wave signals by using low-frequency local oscillator signal," *IEEE Photon. Technol. Lett.*, vol. 20, no. 7, pp. 478–480, 2008.

[142] Z. Tang, S. Pan, and J. Yao, "A high resolution optical vector network analyzer based on a wideband and wavelength-tunable optical single-sideband modulator," *Optics Express*, vol. 20, no. 6, pp. 6555–6560, 2012.

[143] Z. Li, H. Chi, X. Zhang, and J. Yao, "Optical single-sideband modulation using a fiber-Bragg-grating-based optical Hilbert transformer," *IEEE Photon. Technol. Lett.*, vol. 23, no. 9, pp. 558–560, 2011.

[144] Y. Ogiso, Y. Tsuchiya, S. Shinada, S. Nakajima, T. Kawanishi, and H. Nakajima, "High extinction-ratio integrated Mach–Zehnder modulator with active y-branch for optical SSB signal generation," *IEEE Photon. Technol. Lett.*, vol. 22, no. 12, pp. 941–943, 2010.

[145] K. Takano, N. Hanzawa, S. Tanji, and K. Nakagawa, "Experimental demonstration of optically phase-shifted SSB modulation with fiber-based optical Hilbert transformers," in *Proc. IEEE/OSA Optical Fiber Communication Conference (OFC)*, 2007, paper JThA48.

[146] M. Attygalle, C. Lim, G. Pendock, A. Nirmalathas, and G. Edvell, "Transmission improvement in fiber wireless links using fiber Bragg gratings," *IEEE Photon. Technol. Lett.*, vol. 17, no. 1, pp. 190–192, 2005.

[147] J. McNicol, M. O'Sullivan, K. Roberts, A. Comeau, D. McGhan, and L. Strawczynski, "Electrical domain compensation of optical dispersion [optical fibre communication applications]," in *Proc. IEEE/OSA Optical Fiber Communication Conference (OFC)*, 2005, paper OThJ3.

[148] M.M.E. Said, J. Sitch, and M.I. Elmasry, "An electrically pre-equalized 10-Gb/s duobinary transmission system," *J. Lightw. Technol.*, vol. 23, no. 1, pp. 388–400, 2005.

[149] S.S. Haykin, *Adaptive Filter Theory*, 4th edition, Pearson Education India, 2005.

[150] D. Godard, "Self-recovering equalization and carrier tracking in two-dimensional data communication systems," *IEEE Transactions on Communications*, vol. 28, no. 11, pp. 1867–1875, 1980.

[151] I. Fatadin, D. Ives, and S. J. Savory, "Blind equalization and carrier phase recovery in a 16-QAM optical coherent system," *J. Lightw. Technol.*, vol. 27, no. 15, pp. 3042–3049, 2009.

[152] D. Lavery, "Digital coherent receivers for passive optical networks," Ph.D. dissertation, University College London (UCL), 2013.

[153] G. Picchi and G. Prati, "Blind equalization and carrier recovery using a stop-and-go decision-directed algorithm" *IEEE Transactions on Communications*, vol. 35, no. 9, pp. 877–887, 1987.

[154] P.S. Chow, J.M. Cioffi, J.A.C Bingham, "A practical discrete multitone transceiver loading algorithm for data transmission over spectrally shaped channels," *IEEE Transactions on Communications*, vol. 43, no. 234, pp. 773–775, 1995.

[155] D. Bykhovsky and S. Arnon, "An experimental comparison of different bit-and-power-allocation algorithms for DCO-OFDM," *J. Lightw. Technol.*, vol. 32, no. 8, pp. 1559–1564, 2014.

[156] T.M. Schmidl and D.C. Cox, "Robust frequency and timing synchronization for OFDM," *IEEE Transactions on Communications*, vol. 45, no. 12, pp. 1613–1621, 1997.

[157] X. Yi, W. Shieh, and Y. Tang, "Phase estimation for coherent optical OFDM," *IEEE Photon. Technol. Lett.*, vol. 19, no. 12, pp. 919–921, 2007.

[158] J.-J.V. De Beek, O. Edfors, M. Sandell, S.K. Wilson, and P.O. Borjesson, "On channel estimation in OFDM systems," in *IEEE Vehicular Technology Conference*, 1995, vol.2, pp. 815–819.

Chapter 4

Spectrally-Efficient WDM Transmission of Subcarrier Modulation Schemes

Next generation optical transceivers designs are needed to achieve higher information spectral densities (ISDs) in direct detection links over access and metropolitan distances to meet the increasing data demand in the upcoming years, as discussed in chapter 1. In this chapter, numerical simulations and experimental demonstrations achieving an information spectral density (ISD) greater than 1 b/s/Hz are presented using a variety of modulators. The direct detection system architecture considered throughout the chapter is shown in Fig. 4.1. Subcarrier modulation schemes, a single or multiple subcarrier(s), are used to transmit data over a fibre link. High order modulation schemes, *e.g.,* quadrature amplitude modulation (QAM), can be realized using a single or multiple subcarrier(s) and using linear optical field modulation. At the receiver, the channel of interest is optically demultiplexed by an optical band-pass filter (OBPF) and optical-to-electrical conversion is achieved by a single-ended photodiode, beating between the optical carrier and the sideband during the square-law photodetection. Then, the electrical signal is digitized using a single analogue-to-digital converter (ADC), as depicted in Fig. 4.1.

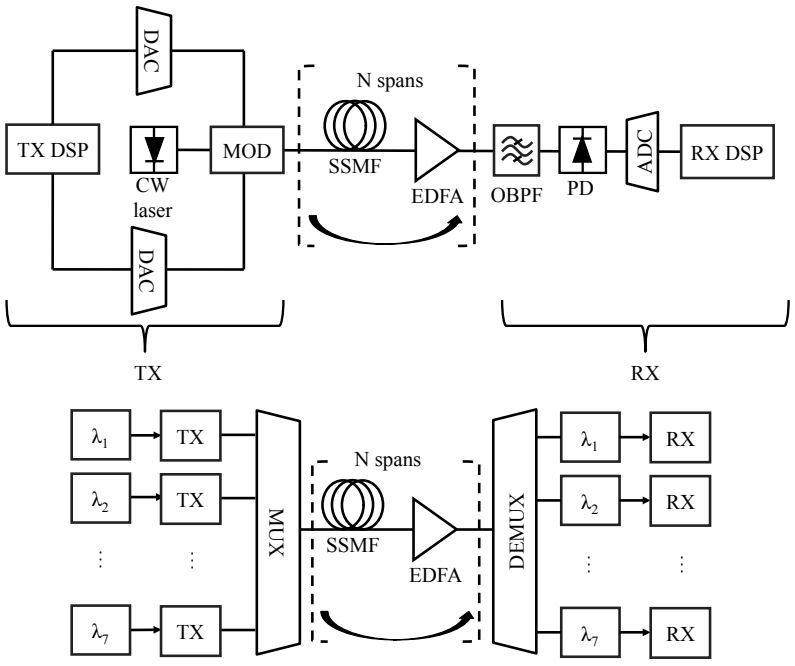

Fig. 4.1: System architecture for single channel (top) and WDM system (bottom) considered throughout the chapter.

Initially, the numerical simulation model to investigate the fundamental limits of the subcarrier modulation (SCM) formats offering the highest achievable ISDs are described in section 4.1. The same simulation model is used to verify the experimental results by taking into account the practical parameters. The experimental setup using different optical modulators that emulates the transmission performance of wavelength division multiplexed (WDM) single sideband (SSB) Nyquist-SCM QAM signalling are outlined in section 4.2. Following the description of numerical simulations and experimental setups, SSB Nyquist-SCM transceiver characterization in simulations, that determines the subcarrier frequency and roll-off factor of the pulse shaping filter exhibiting a good compromise point between spectral efficiency and required optical signal-to-noise ratio (OSNR), is presented in section 4.3. Additionally, in section 4.3.2, clipping is investigated to ascertain whether it offers any significant performance gain for dispersion-precompensated SSB Nyquist-SCM signal.

The back-to-back and transmission performance of two spectrally-efficient SCM schemes, SSB Nyquist-SCM and single sideband orthogonal frequency division multiplexing (OFDM) (SSB-OFDM), are compared, for the first time, by means of simulations for a range of wavelength division multiplexing (WDM) at net optical ISDs up to 2.0 b/s/Hz in section 4.4. Furthermore, ideal numerical simulations and experimental results (with their verification in simulations) for the spectrally-efficient WDM back-to-back and transmission performance of dispersion-precompensated SSB Nyquist pulse-shaped SCM 16-QAM signal are discussed in section 4.5. In this discussion, the performance of the in-phase and quadrature (IQ)-modulator, Lithium Niobate ($LiNbO_3$) and Indium Phosphide (InP) dual-drive Mach-Zehnder modulators (dual-drive MZMs) are compared. Finally, the findings and key results are summarized in section 4.6.

4.1 Simulation model

Based on the literature review in section 3.1, two spectrally-efficient and dispersion tolerant SCM signal formats, namely SSB Nyquist-SCM and SSB-OFDM with QAM signalling, are studied in this thesis as potential modulation techniques for cost-effective direct detection WDM systems over metropolitan distances. Their transceiver architectures were first investigated in numerical simulations to demonstrate their fundamental limits and compare their transmission performance. These simulations were performed assuming ideal components, referred to as ideal simulations throughout the chapter. Moreover, to verify the experimental results, further simulations using the same transceiver models but with practical (non-ideal) parameters, replicating the experimental setups, were carried out. These are referred to as practical simulations.

The simulation software was developed in MATLAB. 40% of the MATLAB code used in simulations, *e.g.,* the fibre link model using split-step Fourier method and the optical amplification using Erbium-doped fibre amplifiers (EDFAs), has been taken from the Optical Networks Group MATLAB toolbox with small modifications. The rest, in particular, the code for i) transceiver modeling such as SSB Nyquist-SCM and OFDM signal de/modulation, ii) offline waveform generation for the field programmable gate arrays (FPGAs) and the offline processing after the real-time sampling scope, and iii) the simulation code, which takes into account the practical limitations such as the frequency response and limited resolution of the digital-to-analogue converters (DACs)/ADCs, limited extinction ratio of the modulators, and non-ideal optical band-pass filters, has been specifically developed for the study presented in this thesis.

The transmitter models for SSB Nyquist-SCM and SSB-OFDM signal formats are outlined in section 4.1.1. Following this, the recirculating loop and direct detection receiver models are described in sections 4.1.2 and 4.1.3, respectively. The digital signal processing (DSP) blocks of SSB Nyquist-SCM and SSB-OFDM in the transceiver models are already discussed in sections 3.2.1 and 3.2.2, respectively.

4.1.1 Transmitter models

4.1.1.1 Nyquist-SCM transmitter model

First, a 7 GBaud conventional quadrature phase-shift keying (QPSK)/16-QAM signal was generated. Subsequently, a pair of 256-tap root raised cosine (RRC) filters with a stop-band attenuation of 40 dB were applied to the in-phase (I)- and quadrature (Q)-components separately to achieve Nyquist pulse shaping. Then, the Nyquist pulse-shaped signals were up-converted to the subcarrier frequency and added to each other to obtain a (real-valued) double sideband Nyquist-SCM QAM signal (x_r). Following this, digital electronic pre-distortion (EPD) was applied to mitigate the chromatic dispersion accumulated at the targeted distance with a minimum penalty, as described in section 3.2.1.3 and in [1, 2]. Finally, the digital Hilbert transform (HT) was applied to the real (x'_r) and imaginary parts of the signal (x'_i) to obtain the SSB signal, as discussed in section 3.2.1.2, as shown in Fig. 4.2.

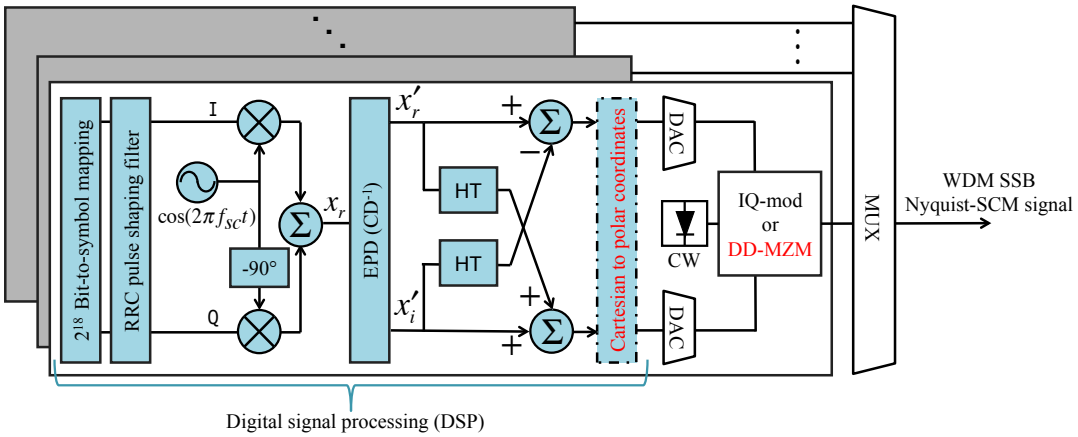

Fig. 4.2: Transmitter model for WDM SSB Nyquist-SCM signal in simulations. The DSP blocks are also used for the SSB Nyquist-SCM signal waveform generation in the experiment, as described in section 3.2.1. Note that the conversion from Cartesian to polar coordinates is only applied when dual-drive MZM is used.

4.1.1.2 OFDM transmitter model

Similar to the Nyquist-SCM signal generation, first, a 7 GBaud conventional QPSK/16-QAM signal was generated using two/four decorrelated 2^{18} de Bruijn bit sequences. 128 subcarriers were first modulated, and multiplexed using a 256-point inverse fast Fourier transform (IFFT), as shown in Fig. 4.3. The subcarriers were modulated adaptively if necessary, as discussed in section 4.4. Two training symbols were inserted at the start of an OFDM frame for frame synchronization. Moreover, the pilot symbols were inserted periodically, every 64 data symbols leading to approximately 1.5% overhead, as discussed in section 3.2.2. Then, a 2% cyclic prefix (CP) was added as a guard band to avoid inter-symbol interference (ISI) due to filter delays introduced by the electrical and optical filters in the system. Clipping (1^{st}-stage) was applied to the back-to-back OFDM signal waveform (prior to EPD). After clipping, the signal waveform was pre-distorted/dispersed to mitigate the dispersion with a minimum penalty (rather than using a longer CP), in order to operate at the same ISD as the Nyquist-SCM signal. Finally, clipping

(2^{nd}-stage) was applied to optimize its OSNR performance.

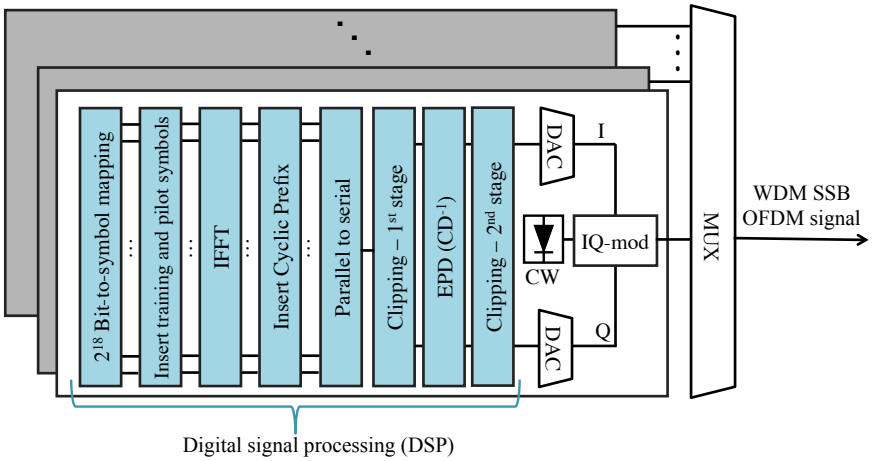

Fig. 4.3: Transmitter model for the WDM SSB-OFDM signal in simulations. The DSP blocks are discussed in section 3.2.2.

After SSB Nyquist-SCM and SSB-OFDM electrical signals were generated for the IQ-modulator, the quantization was applied. Note that in the case of the dual-drive MZM being used, prior to quantization, the waveforms need to be converted from Cartesian to polar coordinates to generate the modulator driving signals, as given in Eqs.2.25a and 2.25b and discussed in section 2.2. In ideal simulations, the resolution of the DACs operating at 28 GSa/s was assumed to be 5 bits, which was sufficient to avoid significant penalties due to the quantization noise. To prevent crosstalk between the WDM channels due to the images generated by the DACs, electrical anti-imaging filters, 5^{th}-order Bessel low-pass filters (LPFs) with an optimized bandwidth of $0.8f_s$, were used. The total penalty due to the quantization noise and LPFs were kept within $\leq$0.5 dB in ideal simulations. In practical simulations though, the nominal resolution of the DACs was set to 6 bits. Its assumed effective number of bits (ENOB) was 3.8 bits at 10 GHz which was modeled by adding additive white Gaussian noise (AWGN) to the 6-bit quantized signal waveforms. Moreover, the bandwidth of the 5^{th}-order Bessel LPFs was set to 7 GHz.

The experimental and simulated (with practical parameters) optical intensity waveforms after the IQ- and dual-drive MZ (DD-MZ) modulators are shown side by side in Fig. 4.7 and Fig. 4.9, respectively. The optical carrier for the single channel signal was added using the modulators whose transfer functions are given in Eqs.2.23 and 2.28, respectively. The modulators were biased close to their quadrature points to achieve linear mapping from the electrical to the optical domain, with the bias voltages adjusted to achieve the desired optical carrier power. The optical carrier-to-signal power ratio (CSPR) optimization is discussed in the results section 4.4. In practical simulations, the OSNR of the optical signal was set to 34 dB per channel after the modulators to emulate the experimental setup. The practical limitation on the signal OSNR was the extinction ratio of a modulator and amplified spontaneous emission (ASE)-noise added by the EDFAs used in the experimental setup (see Fig. 4.6).

In modeling WDM transmission, all WDM channels each carrying either SSB Nyquist-SCM QPSK/16-QAM or the equivalent adaptively modulated OFDM signal were decorrelated by approximately 1000 samples compared to the immediate neighboring channels.

4.1.2 Fibre link model

The fibre transmission link considered in the simulations was uncompensated standard single mode fibre (SSMF) and the fibre parameters (loss α, chromatic dispersion D, and nonlinear coefficient γ), the EDFA noise figure and span length were chosen as 0.2 dB/km, 16.8 ps/(nm.km), 1.2 $W^{-1}km^{-1}$, 5 dB and 80 km, respectively. A single EDFA with a noise figure of 5 dB was used to compensate the fibre loss over each span which had 16 dB attenuation in ideal simulations. However, in addition to the span loss, the total insertion loss of the loop components were approximately 15 dB in the experiments, as explained in section 4.2.2. Therefore, the signal was attenuated by 15 dB, and then, amplified by a second EDFA with the same noise figure to mimic this effect in practical simulations. All ASE-noise generated by the EDFAs was added inline to model nonlinear signal-ASE beating noise interaction. The transmission in the fibre was modeled using the symmetric split-step Fourier method [3] in which the step sizes were empirically chosen as 1 km and 0.4 km for single channel and WDM signals, respectively. Since an OBPF with a 3 dB bandwidth of 200 GHz and a filter edge gradient of 500 dB/nm (corresponding to the frequency response of a 3rd-order super-Gaussian optical filter) was used to filter the out-of-band ASE-noise in the transmission experiments, the simulation bandwidth was chosen as approximately 200 GHz to simulate this filtering effect.

4.1.3 Receiver model

Before detecting the transmitted signal using a single-ended photodiode with a responsivity of 1/0.8 A/W in ideal/practical simulations, a rectangular "brick-wall"/4th-order super-Gaussian OBPF filter was applied to demultiplex the channel of interest and remove out-of-band ASE-noise. Following the quantization of the detected analogue signal by a single ADC with an ENOB of 5-bit at 10 GHz and a sampling rate of 50 GSa/s in both simulations, a 5th-order Bessel LPF with a bandwidth of 16 GHz was used to emulate the frequency response of the real-time sampling scope used in the experiment in practical simulations. The normalized and resampled (to 2 samples-per-symbol) Nyquist-SCM signal was first split into two branches, and then, down-converted to generate the I- and Q-baseband signals, as shown in Fig. 4.4. A pair of matched RRC filters with $\beta = 0.3$ were used, as described in section 3.2.1.1, followed by a 5-tap finite impulse response (FIR) filter for symbol re-timing and prior to the bit error rate (BER) counter. Initially, the constant modulus algorithm (CMA) was chosen as a cost function for fast convergence, and then, switched to decision-directed least mean squares (LMS), as discussed in section 3.2.1.4. Finally, the BER was computed by error counting over 2^{20} bits.

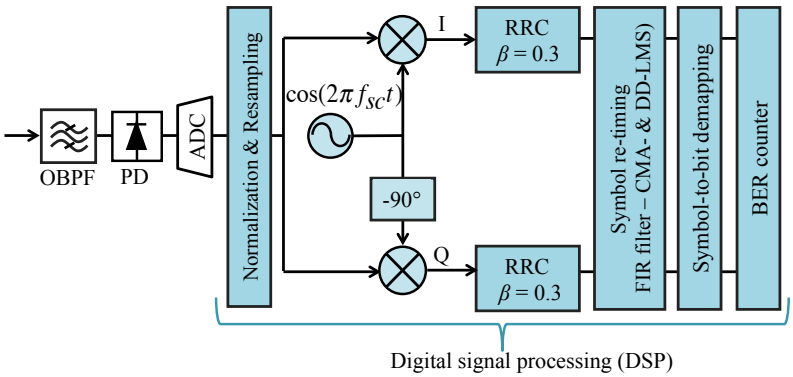

Fig. 4.4: Receiver model for Nyquist-SCM signal in simulations. The DSP blocks are also used for the SSB Nyquist-SCM signal demodulation in the experiment, as outlined in section 3.2.1.

In the OFDM case, after photodetection, the frame window synchronization was achieved by applying the Schmidl and Cox algorithm, as described in section 3.2.2.2. Then, the received signal was first converted from serial to parallel, and subsequently, the CP was removed from the OFDM frame, as shown in Fig. 4.5. Following this, a 256-point fast Fourier transform (FFT) was applied and block-type channel estimation was performed using a single-tap equalizer with zero-forcing criterion to cancel the phase errors and distortions incurred along the transmission path, as discussed in 3.2.2.3. Finally, the received signal was multiplied with the inverse of the estimated channel response to restore the transmitted signal. After equalization, symbol-to-bit demapping was performed and BER for each subcarrier was calculated by counting the errors over 2^{20} bits.

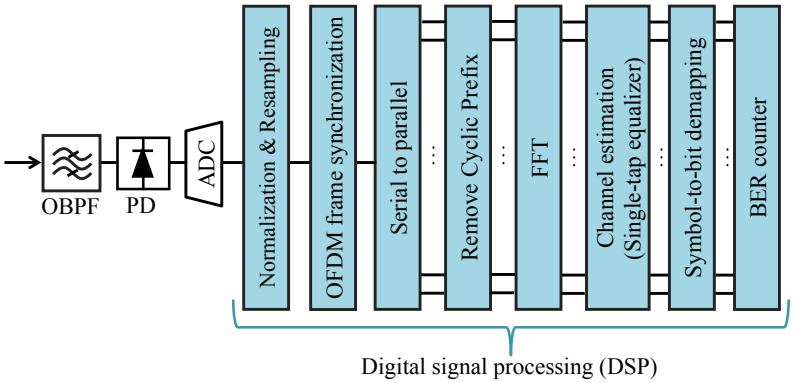

Fig. 4.5: Receiver model for OFDM signal in simulations. The DSP blocks are also used for the SSB-OFDM signal demodulation in the experiment, as described in section 3.2.2.

4.2 Experimental transmission setups

This section focuses on the details of the experimental transmission setup for SSB Nyquist-SCM QPSK and 16-QAM using the $LiNbO_3$ IQ-modulator (Oclaro Avanex 79200054), $LiNbO_3$ dual-drive MZM (Fujitsu FTM7921ER) and InP dual-drive MZM (Oclaro tunable transmitter assembly (TTA) D00081-AN). The optical transmission test-bed for each modulator consists of a WDM SSB Nyquist-SCM transmitter, an optical fibre recirculating loop and a direct detection receiver. The transmitter design for each modulator is outlined in section 4.2.1. The recirculating loop and receiver designs were kept the same for all three transmitter setups, as described in sections 4.2.2 and 4.2.3, respectively.

4.2.1 Transmitter setups

The SSB Nyquist-SCM signal waveforms for all three transmitter designs were generated offline using DSP in MATLAB, as outlined in section 4.1.1.1 with the block diagram shown in Fig. 4.2. Following the generation of signal waveforms (I and Q waveforms for each modulator), they were quantized to 6 bits and uploaded to the random-access memory (RAM) blocks of a pair of Xilinx Virtex-5 FPGAs, interfaced with a pair of the DACs (Micram VEGA DACII). Each DAC has two output ports, named as negative ('n') and positive ('p'), as shown in Figs. 4.6, 4.8, and 4.10. The modulators were driven by two electrical signals (the output pair of 'p' and 'n') generated using the DACs with a nominal resolution of 6-bits (ENOB of 3.8 bits at 10 GHz) and a maximum sampling rate of 28 GSa/s. The waveforms uploaded to the memory of the FPGAs consisted of 4 samples-per-symbol. Since the experiments were proof-of-concept and they were the first experimental demonstrations in the literature, the fundamental

limits of the proposed systems were the priority. Although the tone at the subcarrier frequency could be generated using an RF-signal generator (analog approach) or using 2 samples-per-symbol, they provided a clean tone of 20 dB whereas a clean tone of approximately 30 dB was obtained using 4 samples-per-symbol. Therefore, the symbol rate of 7 GBaud using 4 samples-per-symbol (instead of 14 GBaud using 2 samples-per-symbol) was chosen for the SSB Nyquist-SCM QPSK experiments. For 16-QAM experiments, the symbol rate was reduced to 6.25 GBaud, as the DACs were not running stable at a sampling rate of 28 GSa/s at that time. Note that having a waveform with 4 samples-per-symbol is not a theoretical limitation. The approaches utilizing 2 samples-per-symbol will be assessed in the future, as discussed in section 6.2.

The two electrical paths connecting the DACs to the modulator inputs were substantially the same. After the DACs, first, the signals were aligned in time using electrical phase shifters. It is worth noting that the alignment process is crucial since any relative time delay (phase-shift) between the driving signals reduces the sideband power and optical sideband suppression, causing linear crosstalk between neighboring channels. Following the time alignment of the driving signals, they were amplified using RF-amplifiers (40 GHz SHF 803P) to boost the signal power. To prevent crosstalk between WDM channels due to the images generated by the DACs, Anritsu electrical filters with a frequency response of 5^{th}-order Bessel LPFs and a 3 dB bandwidth of 7 GHz were used as anti-imaging filters. The appropriate peak-to-peak voltage levels of the electrical signals for each modulator are indicated in their corresponding sections.

Due to the limited number of $LiNbO_3$ and InP dual-drive MZMs available, the main difference between the transmitter setups is in the generation of the multiple wavelength channels needed for WDM transmission experiments, which is described for each modulator below. Note that the non-conventional channel spacing values for the WDM experiments described below are chosen in order to maximize the achieved net optical ISD with the available DACs, RF-amplifiers and modulators.

4.2.1.1 Using $LiNbO_3$ IQ-modulator

An external cavity laser (ECL) with a linewidth of 100 kHz at 1550 nm was used as the seed for the optical comb generator (OCG) based on cascaded amplitude and phase modulators to generate seven equally spaced unmodulated optical channels. Although a laser source with higher linewidth could be used in direct detection SCM (since carrier phase recovery is not so challenging), an ECL was used due to its availability. The number of comb lines was limited to seven in order to maintain the power variation across the channels to within 1 dB. The channel spacing was chosen to ensure the penalty caused by linear crosstalk due to the neighboring channels was within 1 dB. Odd ($\lambda_{1,3,5,7}$) and even ($\lambda_{2,4,6}$) channels were demultiplexed using three cascaded Kylia micro-interferometer interleavers with a suppression of 40 dB to allow independent modulation with uncorrelated bit sequences, as shown in the inset (a) of Fig. 4.6. Note that the optical spectra shown in Fig. 4.6 are taken from the optical spectrum analyzer (OSA) at a resolution of 0.01 nm. The optical carrier was added to the modulated signal by biasing the modulator. The IQ-modulators had a 3 dB bandwidth of 40 GHz and a switching voltage (V_π) of 3.5 V. The modulators were driven by the electrical signals with a peak-to-peak voltage (V_{p-p}) of 3.4 V. They were biased close to their quadrature points to achieve approximately linear mapping from the electrical to the optical domain with the bias voltages, adjusted to achieve the desired CSPR. The CSPR is the optical carrier power P_c divided by the sideband power P_s and defined as follows:

$$\text{CSPR[dB]} = 10\log10\left(\frac{P_c}{P_s}\right). \tag{4.1}$$

The discussion dedicated to the CSPR optimization can be found in the results section. The odd and even channels were first amplified, and then, combined using a 3 dB coupler. The odd channels were decorrelated using a fibre with a length of approximately 3.4 m (17 ns delay - 495 samples) before launching into the recirculating loop. The WDM SSB Nyquist pulse-shaped SCM signal with an OSNR of approximately 34 dB per channel at a resolution of 0.1 nm was generated and shown in the inset (b) of Fig. 4.6. Note that only the central channel (λ_4) was transmitted over the fibre in the single channel case. For QPSK transmission, the symbol rate and channel spacing were set to 7 GBaud and 11 GHz, respectively whereas a symbol rate of 6.25 GBaud and a channel spacing of 12 GHz were chosen for 16-QAM transmission. The corresponding results are discussed in section 4.5.

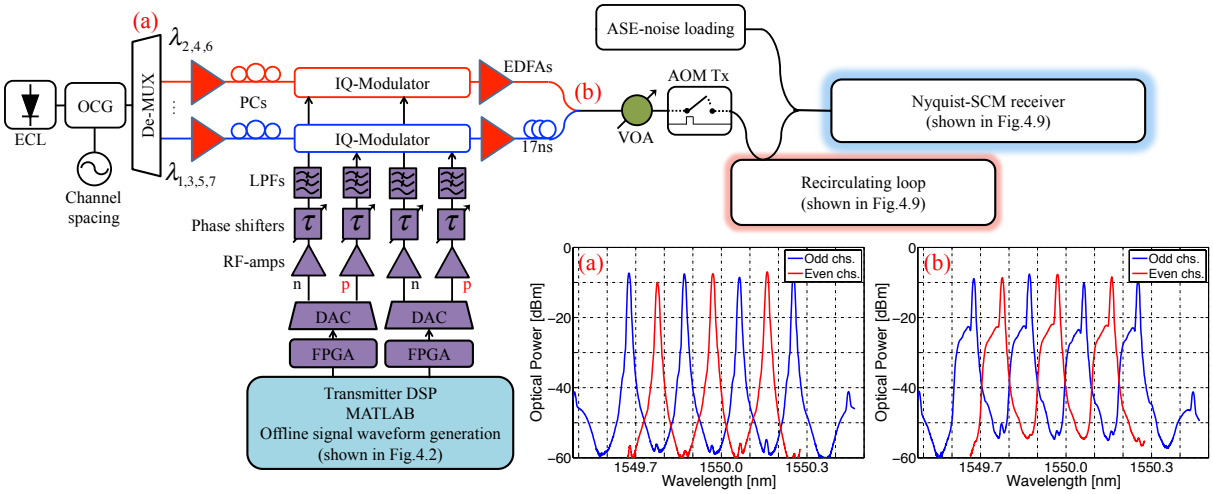

Fig. 4.6: Transmitter setup for Nyquist-SCM signal using the $LiNbO_3$ IQ-modulator. Inset: The optical spectrum of (a) unmodulated seven channels and (b) WDM SSB Nyquist pulse-shaped 16-QAM SCM at a resolution bandwidth of 0.01 nm. The offline signal waveform generation in MATLAB is described in section 4.1.1.1. Recirculating loop and receiver setups are described in the section 4.2.2 and section 4.2.3.

The experimental and simulated single channel back-to-back optical intensity waveforms with practical parameters are shown side by side in Fig. 4.7. It indicates that there is a good agreement between the practical simulations and experiment. In one symbol period (approximately 1/7GBaud≈143 ps), three-quarters of the subcarrier (sine wave) with its four phases can be observed.

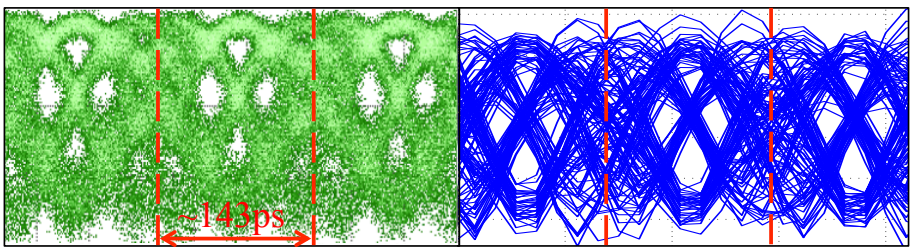

Fig. 4.7: (a) Experimental and (b) simulated optical intensity waveforms for back-to-back case.

4.2.1.2 Using $LiNbO_3$ dual-drive MZM

The OCG used in the transmitter setup with the IQ-modulator could not be used since there was only one available $LiNbO_3$ dual-drive MZM. Therefore, the setup was modified, as described below to generate the WDM SSB Nyquist pulse-shaped SCM signal using the dual-drive MZM.

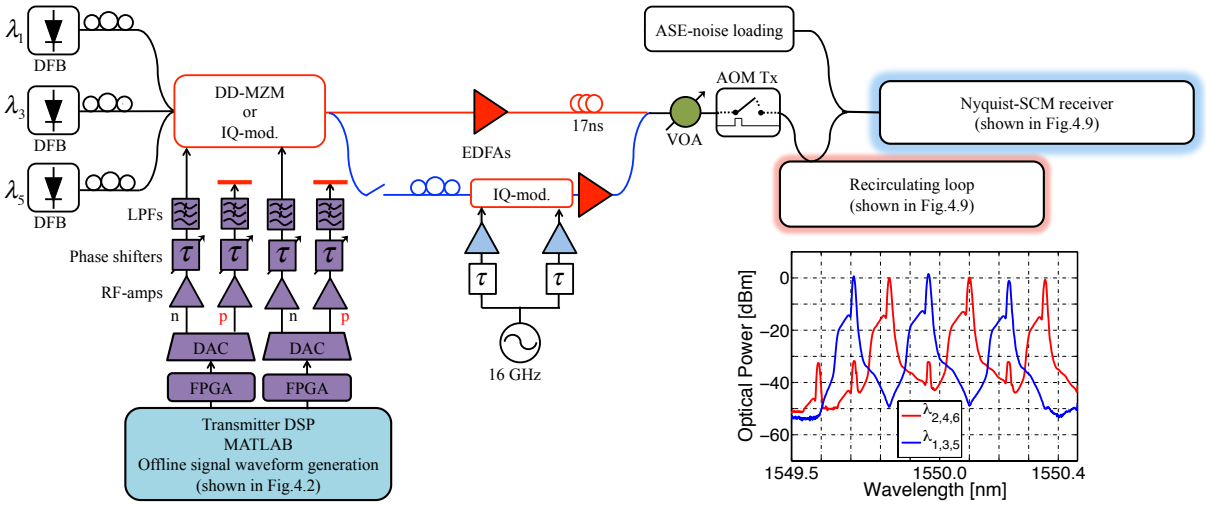

Fig. 4.8: Transmitter setup for Nyquist-SCM signal using the $LiNbO_3$ dual-drive MZM with the optical spectrum of WDM SSB Nyquist pulse-shaped 16-QAM SCM at a resolution bandwidth of 0.01 nm. The offline signal waveform generation in MATLAB is described in section 4.1.1.1. Recirculating loop and receiver setups are described in the section 4.2.2 and section 4.2.3.

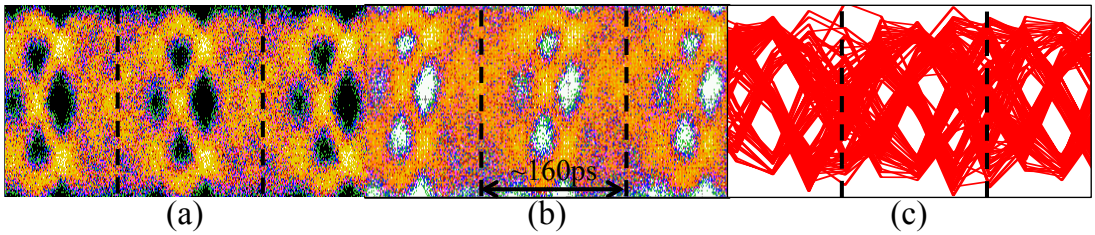

Fig. 4.9: Experimental back-to-back optical intensity waveforms (a) using $LiNbO_3$ and (b) InP dual-drive MZM (Oclaro TTA). (c) Simulated optical intensity waveforms using dual-drive MZM model and taking into account the practical parameters.

Distributed feedback lasers ($\lambda_{1,3,5}$) with a linewidth of approximately 1 MHz centered at 1549.60 nm (λ_3), separated by twice the channel spacing, were used as an optical source for the dual-drive MZM with a V_π of 2.6 V, a 3 dB bandwidth of 9 GHz and a DC extinction ratio of 18 dB. The peak-to-peak voltage levels of the electrical signals were set to 2.5 V. The odd channels ($\lambda_{1,3,5}$) were frequency shifted by the value of the channel spacing using a separate IQ-modulator (the same modulator used above - Oclaro Avanex 79200054) to generate the even channels ($\lambda_{2,4,6}$). As shown in Fig. 4.8, both arms of the IQ-modulator were driven by a signal generator with a tone at the frequency corresponding to the WDM channel spacing. The amplitudes and phase shifters on both arms were adjusted such that a 90° phase difference with equal power levels was obtained between two arms to suppress one of the side tones by approximately 30 dB. The IQ-modulator was biased at its null point to suppress the carrier at the original frequency. The odd channels were delayed using a fibre with a length of 3.4 m (delay of 17 ns corresponding to 429 samples) to achieve bit sequence decorrelation between odd and even channels. Finally, the odd and even channels were combined using a 3 dB coupler to generate the WDM SSB Nyquist pulse-shaped 16-QAM SCM signal, as depicted in Fig. 4.8 with its optical spectrum. The optical

carrier was added by biasing the dual-drive MZM close to its quadrature point to achieve approximately linear mapping from the electrical to the optical domain, with the bias voltages adjusted to achieve the desired CSPR (similar to the IQ-modulator case, as explained above). Note that only the distributed feedback (DFB) laser operating at λ_3 was turned on in single channel transmission. Similar to the IQ-modulator transmitter, the experimental optical intensity waveforms using the $LiNbO_3$ dual-drive MZM matches well with the one simulated using practical parameters, as shown in Fig. 4.9(a) and Fig. 4.9(c).

4.2.1.3 Using InP dual-drive MZM

The same signal waveforms generated for the $LiNbO_3$ dual-drive MZM were used for the InP dual-drive MZM. It was not possible to use the OCG, or any other external optical source, with the Oclaro TTA which contained the InP-dual-drive MZM, since it had its own integrated laser.

The Oclaro TTA comprised a digital supermode distributed Bragg reflector (DS-DBR) laser source (tunable over the C-band from 1528 to 1563 nm) operating at 1550.4 nm, and an InP dual-drive MZM (with a V_π of 1.9 V, a 3 dB bandwidth of 10 GHz and a DC extinction ratio of 17 dB). The inner three channels ($\lambda_{2,3,4}$) were generated from the output of the TTA, followed by an IQ-modulator (same modulator used in the transmitter setup with IQ modulator - see section 4.2.1.1) which was driven with a tone from a signal generator at a frequency of channel spacing (16 GHz). The IQ modulator was operated at its null point to suppress the carrier. A fibre with a length of 3.4 m providing a delay of 17 ns was used to decorrelate the channels before they were coupled. The outer channels ($\lambda_{1,5}$) were generated using a pair of discrete DFB lasers and the $LiNbO_3$ dual-drive MZM (same modulator used in the dual-drive MZM transmitter setup - see section 4.2.1.2). The peak-to-peak voltage levels of the electrical driving signals for the InP and $LiNbO_3$ dual-drive MZM were set to 2.0 V and 2.5 V, respectively. The optical spectrum of the WDM signal (taken from an OSA operating at a resolution bandwidth of 0.01 nm) is shown in the inset of Fig.4.10. The transmission characteristic of the InP dual-drive MZM is shown in Fig. 4.10(b). It can be seen that the maximum applied bias voltage could be approximately -3 V to achieve maximum transmission (causing no attenuation on the optical signal) for the InP dual-drive MZM whereas this value is typically around approximately 6 V for the $LiNbO_3$ dual-drive MZM. The applied voltage bias behaves nonlinearly with respect to the phase of the optical signal. On the other hand, the phase of the optical signal changes linearly with the applied voltage for the $LiNbO_3$ dual-drive MZM [4]. This nonlinear phase-shift effect can be also observed from the optical intensity waveforms shown in Fig. 4.9(a) and Fig. 4.9(b). The dual-drive MZMs were biased close to their quadrature points to generate the WDM SSB Nyquist pulse-shaped 16-QAM SCM signal to achieve the desired CSPR. In single channel transmission, only the central channel (λ_3) was transmitted.

4.2.2 Recirculating loop setup

The transmission experiment was performed using an optical recirculating loop with a single span of 80.7 km of SSMF. The fibre parameters, α, D, γ EDFA noise figure and span length were 0.2 dB/km, 16.8 ps/(nm.km), 1.2 $W^{-1}km^{-1}$, approximately 4.5 dB and 80 km, respectively. The loop was gated with two acousto-optical modulators (AOMs) to switch between 'signal loading from transmitter' and 'signal recirculation' stage, as shown in Fig. 4.11. An OBPF (Yenista Optics XTM50-Wide) with a bandwidth of 200 GHz and a filter edge gradient of 500 dB/nm was used to filter the out-of-band ASE-noise during the transmission. A loop synchronous polarization scrambler (PS) was utilized to randomize the state

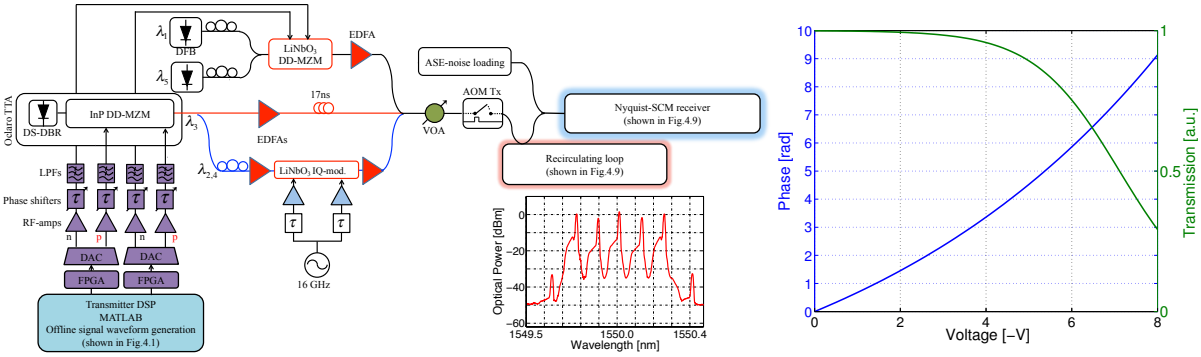

Fig. 4.10: Transmitter setup for Nyquist-SCM signal using the InP dual-drive MZM with the optical spectrum of WDM SSB Nyquist pulse-shaped 16-QAM SCM at a resolution bandwidth of 0.01 nm. Offline signal waveform generation in MATLAB is described in section 4.1.1.1. Recirculating loop and receiver setups are described in the section 4.2.2 and section 4.2.3. (b) Dependence of phase shift and normalized transmission with respect to applied voltages for InP dual-drive MZM.

of polarization of the signal at each circulation. The launch power into the span was controlled by a variable optical attenuator (VOA). The fibre loss (16 dB) plus the insertion loss of the loop components (approximately 15 dB from VOA, PS, AOMs and OBPF) resulted in a total loss of 31 dB per recirculation. This loss was compensated by two EDFAs with a noise figure of approximately 4.5 dB operating at their saturation point (18 dBm output power).

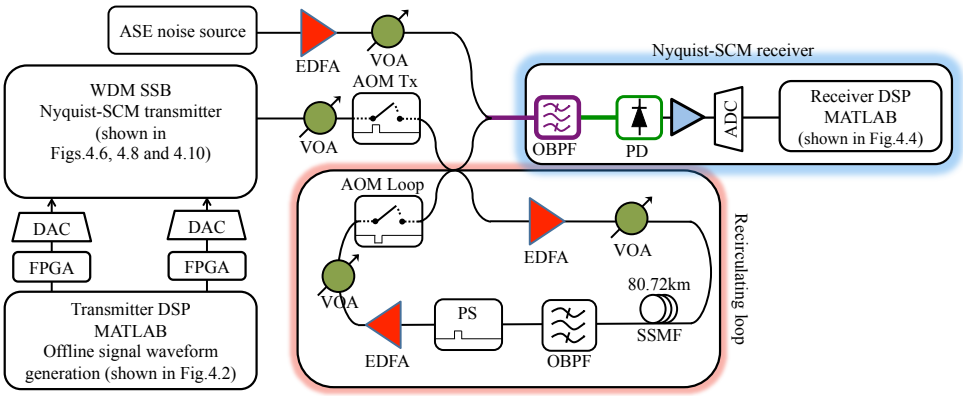

Fig. 4.11: Optical transmission test-bed setup for WDM SSB Nyquist-SCM signal.

4.2.3 Receiver setup

At the receiver, the channel of interest was demultiplexed using a manually tunable OBPF (Yenista Optics XTM50- Ultrafine) with a 3 dB bandwidth set to 2 GHz less than the channel spacing and a filter edge gradient of 800 dB/nm. ASE-noise loading was carried out at the receiver to test the back-to-back performance of the Nyquist-SCM QPSK and 16-QAM signal formats, and the transmission performance of only Nyquist-SCM QPSK signal. Note that the transmission performance of Nyquist-SCM 16-QAM signals was evaluated without noise loading. A single-ended PIN Discovery photodiode (DSC10H) was used to detect the filtered optical signal, followed by an SHF 806P RF-amplifier. The received electrical signal was digitized using a single ADC (Tektronix DPO 72004 oscilloscope), operating at 50 GSa/s with an electrical 3 dB bandwidth of 16 GHz and a nominal resolution of 8 bits (ENOB of 5 bits at 10 GHz).

The same receiver DSP used in the simulation model was also used in the experiments, as described in section 4.1.3 with the block diagram presented in Fig. 4.4. The BER was computed by error counting over 2^{20} bits. BER measurement precision from 10^{-2} to 10^{-4} is found to be within 0.2 dB. To further enhance this precision, the data points at a given BER have been measured 5 to 10 times and the average values have been reported. To calculate the upper bounds on the net bit rate and net optical ISD, the hard decision decoding bound for the binary symmetric channel was utilized resulting in a maximum code rate (r) of [5]

$$r = 1 + p_b \log_2 p_b + (1 - p_b)\log_2(1 - p_b). \tag{4.2}$$

where p_b is the BER. Using Eq.4.2, r was found to be 0.96 at a p_b of 3.8×10^{-3}.

4.3 Transmitter characterization

4.3.1 Subcarrier frequency and roll-off factor of the pulse shaping filter selection

A high spectral efficiency, (approaching $\log_2(M)$ b/s/Hz for M-QAM signalling), can be achieved by using SSB SCM with Nyquist pulse-shaping using RRC filters with a roll-off factor (β) of 0. However, this roll-off factor causes high peak-to-average-power ratio (PAPR) which leads to a degradation in receiver sensitivity, caused by DAC quantization noise, and the requirement for high optical carrier power to maintain a unipolar signal at the receiver (essential for direct detection). The PAPR of a real-valued signal is commonly given in dB values and defined as follows:

$$\text{PAPR} = \frac{\max[E_s(t)E_s^*(t)]}{E[E_s(t)E_s^*(t)]} \quad \text{and} \quad \text{PAPR}_{\text{dB}} = 10\log_{10}(\text{PAPR}) \tag{4.3}$$

where $E_s(t)$ is a real-valued signal, t is the time index, $E[E_s(t)E_s^*(t)]$ is the expected value of the signal power and * represents the complex conjugate. Besides the PAPR issue, signal-signal beating interference (SSBI) degrades the system performance which is discussed in detail while comparing the two spectrally-efficient SCM formats in section 4.4. Therefore, a value of β greater than zero and a corresponding increased subcarrier frequency can be used to achieve a trade-off between the achieved ISD and the required OSNR.

In order to choose the value of β and subcarrier frequency f_{sc}, the proposed SSB Nyquist-SCM QPSK system at a bit rate of 14 Gb/s (a symbol rate f_s of 7 GBaud) was first studied by means of numerical simulations. The signal was generated using DACs operating at 28 GSa/s with 6-bit nominal resolution and an ENOB of 3.8 bits at 10 GHz. The variations of the PAPR, signal bandwidth BW and the required OSNR versus β for a variety of cycle values c, defined as the ratio of the subcarrier frequency f_{sc} to the symbol rate f_s, are plotted in Fig. 4.12(a)-(c), respectively. The signal bandwidth BW, that was taken as the bandwidth between the optical carrier and the frequency at which the signal power drops to zero, is given by

$$\begin{aligned} BW &= f_{sc} + f_s\left(\frac{1+\beta}{2}\right) \\ &= f_s\left(c + \frac{1+\beta}{2}\right), \qquad \text{where} \qquad c = \frac{f_{sc}}{f_s}. \end{aligned} \tag{4.4}$$

It can be seen from Figs. 4.12(b), (c) and (d) that both the PAPR and required OSNR decrease with

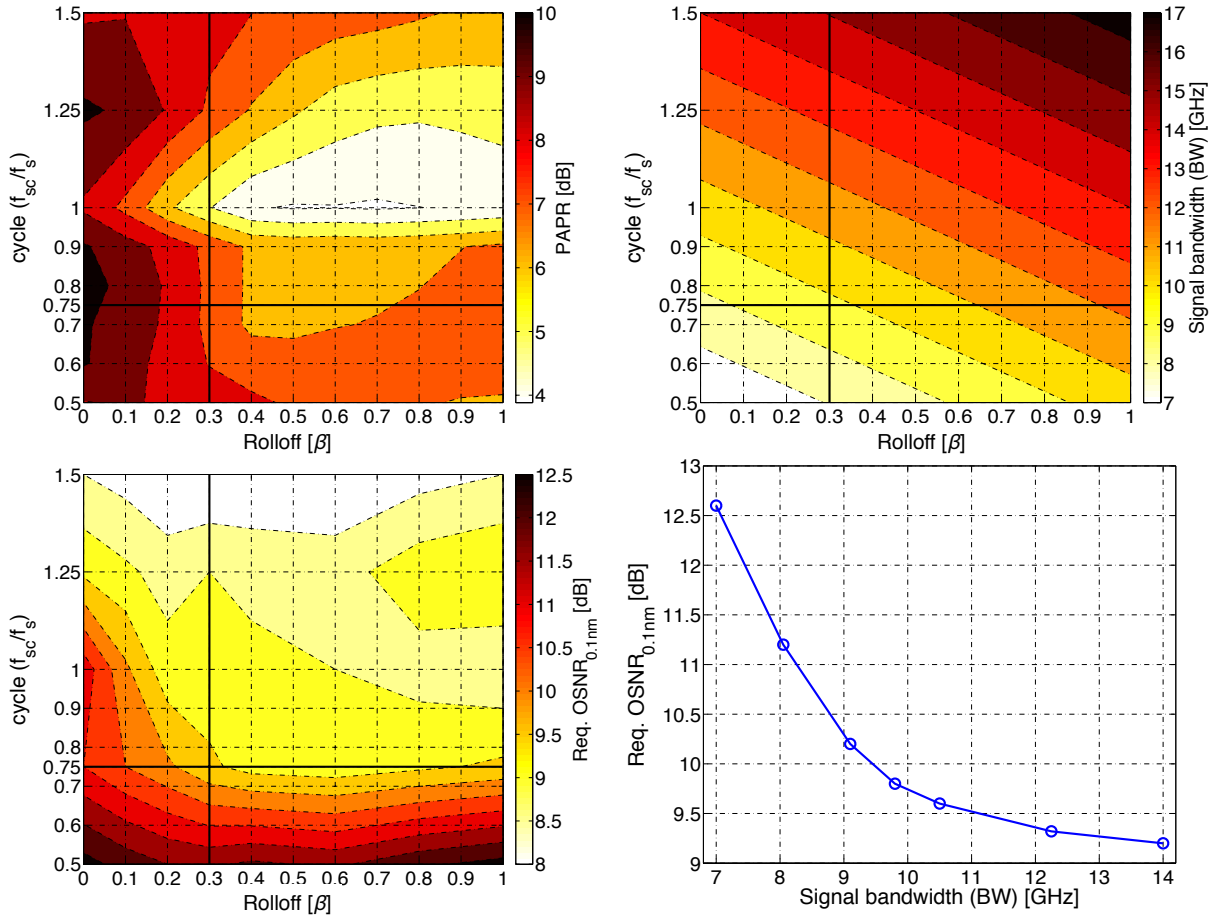

Fig. 4.12: The change in (a) PAPR values of the complex SSB Nyquist-SCM signal (average of I and Q waveforms), (b)the signal bandwidth and (c) the required OSNR with respect to the roll-off factor (β) of the RRC filter and cycle (f_{sc}/f_s). (d) The required OSNR versus the signal bandwidth which is calculated using Eq.4.4 with the given c and β (a slice through Fig. 4.12(c)).

increasing β from 0 to 0.4 whereas BW increases with increasing β and f_{sc}. A slice through Fig. 4.12(c) is shown in Fig.4.12(d) in which the x-axis is calculated using Eq.4.4. The required OSNR decreases 3 dB (from 12.5 to 9.5 dB) when β increases from 0 to 0.3. Beyond $\beta = 0.4$, the change in PAPR is not significant and the required OSNR decreases only approximately 1 dB. Thus, based on these simulation results, a roll-off factor of 0.3 with a subcarrier frequency f_{sc} =0.75f_s is a 'sweet spot' to achieve a good trade-off between the spectral efficiency and the required OSNR for the numerical simulations and experimental demonstrations of SSB Nyquist-SCM QPSK/16-QAM signal. The chosen β and f_{sc} yield a PAPR value of 7.8 dB and a signal bandwidth of 9.8/8.75 GHz at a symbol rate of 7/6.25 GBaud.

4.3.2 Effect of clipping on the transmission performance of dispersion-precompensated Nyquist-SCM

As discussed in section 2.1.1.2, chromatic dispersion is the linear channel impairment that distorts the signal severely. Therefore, it needs to be compensated when transmitting a signal over long-reach access, metro or regional links. It can be effectively compensated by applying EPD, as described in section 3.2.1.3. However, applying EPD causes an increase in the PAPR of the transmitted signal, and hence, the required dynamic range of the DAC. Note that the PAPR of a real-valued signal is defined in Eq.4.3.

It is worth noting that the PAPR value was found to be almost the same for both SSB Nyquist-SCM QPSK and 16-QAM formats. Therefore, for simplicity, QPSK was used as a symbol mapping scheme throughout the following discussion. Following the back-to-back signal waveform generation as shown in Fig 4.2, digital EPD was performed to mitigate the chromatic dispersion accumulated at the targeted distance. Subsequently, hard clipping was applied to reduce the required dynamic range of the DACs. The clipped signal can be formalized as

$$E_{s_{\text{clipped}}(t)} = \begin{cases} E_s(t) & \text{if} \quad |E_s(t)| \leq ClipTh \\ A_s(t)e^{j\omega_s t} & \text{if} \quad |E_s(t)| > ClipTh \end{cases} \tag{4.5}$$

where $E_s(t)$ and $E_{s_{\text{clipped}}}(t)$ represents the electrical signal before and after clipping, $A_s(t)$ and ω_s are the amplitude and the angular frequency of $E_s(t)$. $ClipTh$ is the clipping threshold which becomes the maximum allowable normalized amplitude value after clipping, *i.e.,* a $ClipTh$ of 1 corresponds to no clipping.

In simulations, the sample probability distributions of the 6-bit quantized dispersion-precompensated (EPD applied) signals at the output of the DACs (driving the IQ-modulator) for a range of transmission distances are plotted in Fig. 4.13(a). The back-to-back SSB Nyquist-SCM QPSK signal is fairly uniform over the range of quantization levels. The PAPR gradually increases from 7.8 dB to 11.2 dB as the signal is pre-dispersed up to 10 spans (800 km). Beyond this point, the change in probability distribution and the increase in corresponding PAPR is less significant, as plotted in Fig. 4.13(b).

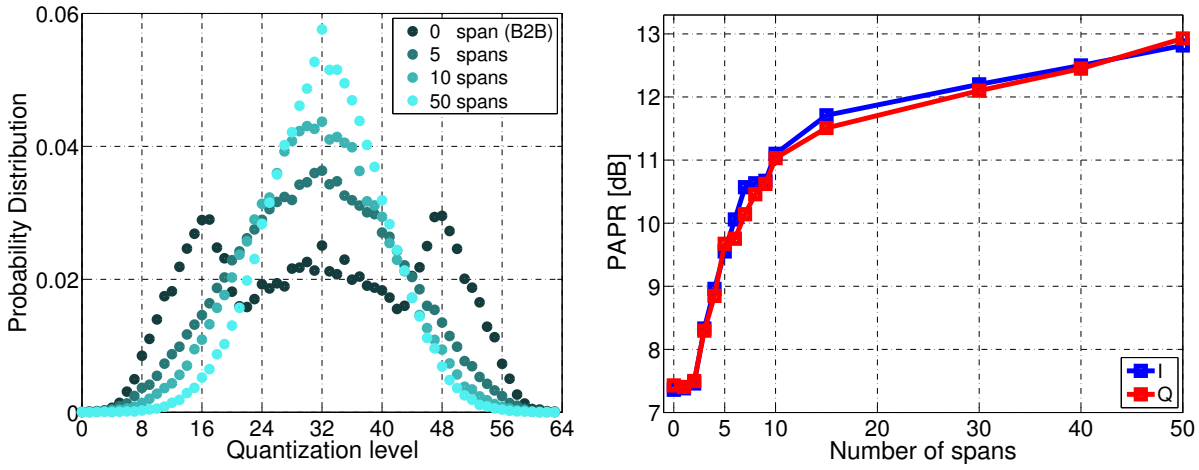

Fig. 4.13: (a) The probability distribution of the pre-dispersed signals at various distances without any clipping versus quantization levels. (b) The change in PAPR with respect to the transmission distance [6].

The probability distribution of the pre-dispersed signals at 800 km with various clipping threshold values and their corresponding simulated and experimental optical spectra, monitored after the transmitter, are presented in Fig. 4.14. It can be observed from Fig. 4.14(b) and (c) that the spectrum broadens due to clipping below a $ClipTh$ value of 0.7. Excessive spectral broadening would lead to additional penalties in the case of spectrally-efficient WDM transmission. The optical spectra in simulations and experiment match fairly well.

Fig. 4.15(a) shows the results of simulations quantifying the improvement in the required OSNR value that can be obtained by clipping the pre-dispersed signal, assuming ENOB values of between 3

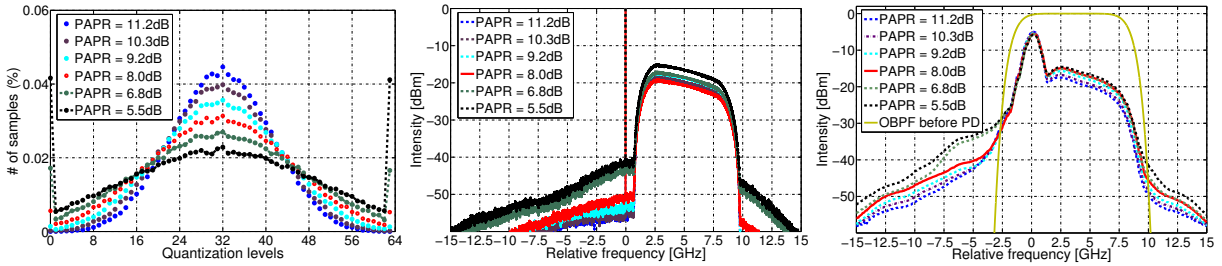

(a) (b) (c)

Fig. 4.14: (a) The probability distribution of the pre-dispersed signals at 800 km with various clipping threshold values (from 1 to 0.5) and the corresponding (b) simulated and (c) experimental optical spectra. Note that frequency scales in (b) and (c) are relative to the optical carrier frequency of the channel [6].

and 6 bits. The highest gain is obtained when the ENOB is 3 bits, as expected whereas the ENOB of 4, 5 and 6 bits give similar OSNR gains for the single channel transmission over 400 and 800 km of SSMF. Although the highest gain can be obtained at an ENOB of 3 bits, it exhibits the lowest OSNR performance due to the DAC quantization noise in general. Note that the difference in the required OSNR value between 400 and 800 km is due to the self-phase modulation (SPM).

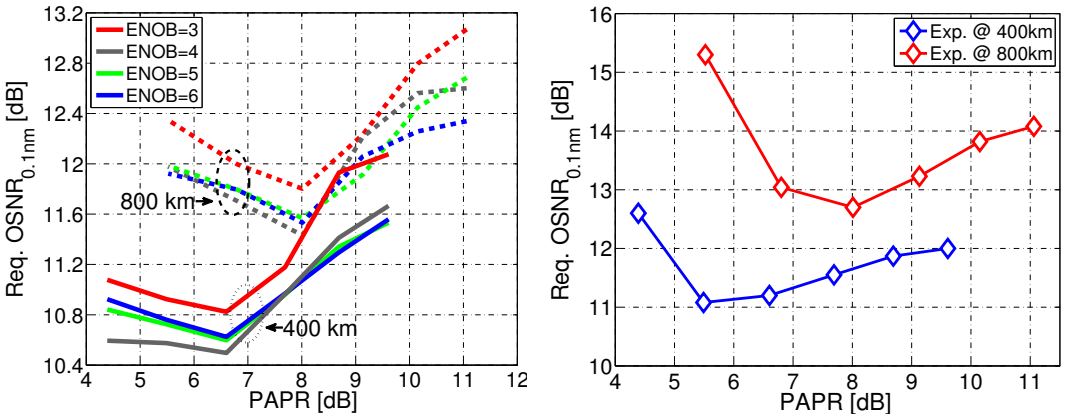

(a) (b)

Fig. 4.15: The required OSNR values for the dispersion-precompensated SSB Nyquist-SCM QPSK signal with respect to the PAPR with (a) various ENOB values in simulations and (b) an ENOB of 3.8 bits in experiments at 400 and 800 km [6].

Following the simulations, the experiments were performed to evaluate the effect of clipping on the system performance. The targeted transmission distances in the experiment were chosen to be 5 and 10 spans (400 and 800 km) to investigate the clipping effect on the transmission performance of the dispersion pre-compensated SSB Nyquist-SCM QPSK signal. Such distances can be considered as typical reaches for metropolitan links. The DACs utilized in the transmitter had a 6-bit nominal resolution and measured ENOB of 3.8 bits at 10 GHz. Initially, the *ClipTh* was varied from 1 to 0.5, yielding a PAPR of 11 to 5 dB. The required OSNR values for the transmission distances of 400 and 800 km at the hard-decision forward error correction (HD-FEC) threshold (assumed to be BER$= 3.8 \times 10^{-3}$) are plotted in Fig. 4.15(b). Both in simulations and experiments, the optimum performance was obtained at PAPR values of 6.8 and 8 dB at 400 and 800 km, respectively, as shown in Fig. 4.15 whilst the spectrum preserves its shape (see Fig. 4.14(b)-(c)).

At optimum PAPR values, the OSNR performance of single channel transmission for back-to-back,

400 and 800 km were assessed, as presented in Fig. 4.16. The implementation penalty at the HD-FEC threshold for the back-to-back case was found to be 0.7 dB compared to the ideal simulations due to the DAC quantization noise and non-ideal rectangular (brick-wall shape) optical filtering to reject out-of-band ASE noise before photodetection. In transmission over 400 km of SSMF, a 0.7 dB improvement was obtained at a PAPR of 6.8 dB compared to the non-clipped pre-dispersed signal with a PAPR of 9 dB. Furthermore, the required OSNR was reduced by 1.2 dB at a PAPR of 8 dB compared to the PAPR of 11.2 dB in single channel transmission over 800 km, as shown in Fig. 4.16. The OSNR performance of the single channel system degrades due to SPM as the transmission distance increases (see next section for further discussions).

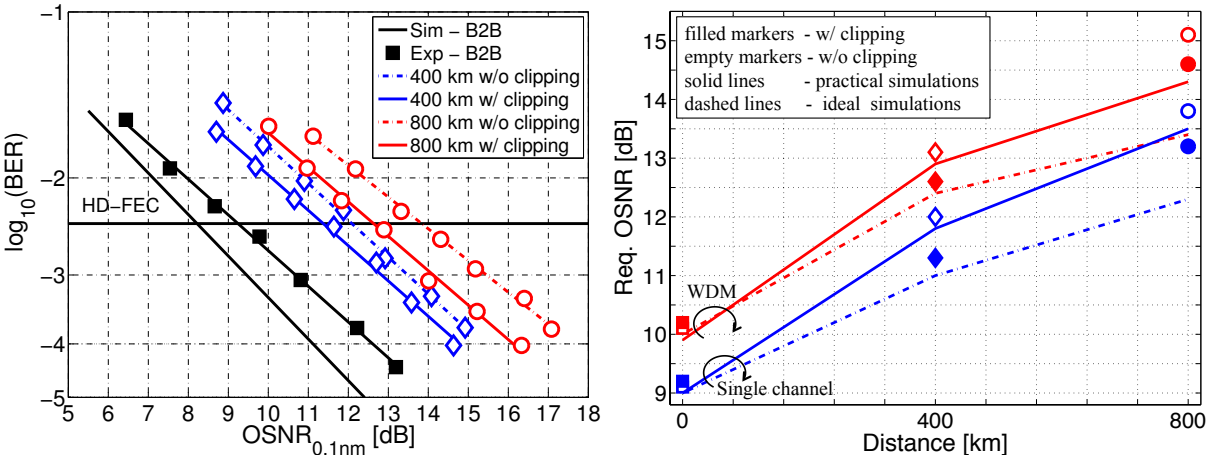

Fig. 4.16: (a) BER versus OSNR performance at various distances. (b) Required OSNR with respect to transmission distance with and without clipping for single channel and WDM system.

Following the single channel transmission, the clipped signal waveforms were evaluated for WDM transmission. In practical simulations, the OSNR gains at 400 and 800 km were found to be approximately 0.5 and 1 dB, as shown in Fig. 4.16(b). However, the gains become negligible (0.2 and 0.4 dB) in the experimental demonstrations due to the frequency drift of the DFB lasers and crosstalk between the neighboring channels. Hence, no clipping is applied whilst EPD is performed in the rest of the thesis.

4.4 Performance comparison of SSB Nyquist-SCM and SSB OFDM (tolerance to signal-signal beating interference)

As discussed in section 3.1, a variety of formats have been proposed to achieve high ISDs in non-coherent detection links. Among these formats, cost-effective DSP-based transceiver architectures using the SCM technique enable QAM signalling, yielding an optical ISD greater than 1 b/s/Hz, in direct detection links (a single-ended photodiode with no delay-line interferometer (DLI)). However, the receiver sensitivity performance of direct detection SCM formats, namely SSB Nyquist-SCM and SSB-OFDM, degrades due to the nonlinear square-law detection resulting in signal-signal beating interference (SSBI), as described in section 2.3.1. One approach to reduce the associated performance degradation is the use of SSBI estimation/cancellation. There are some proposed estimation/cancellation techniques to reduce this interference. However, they result in degradation in receiver sensitivity due to high CSPR [7, 8],

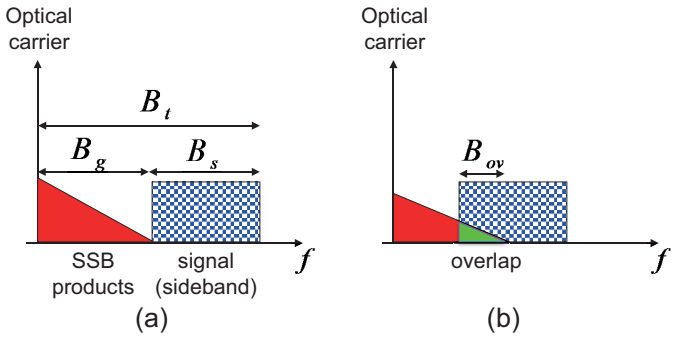

Fig. 4.17: The spectrum of detected SCM signals (a) non-overlapping and (b) overlapping case. Total bandwidth (B_t) is equal to $2B_s - B_{ov}$ where the spectral guard band between the optical carrier and sideband (B_g) is equal to the signal bandwidth B_s, and B_{ov} is the overlapping bandwidth between the signal and signal-signal beating products [15].

increased DSP complexity [9,10], optical complexity [11,12] or overheads [10], as discussed in detail in section 3.1.4.1.

An alternative approach is to use a spectral guard band between the sideband and the optical carrier with bandwidth B_g (see Fig. 4.17). Since the bandwidth of signal-signal beating products is equal to the signal bandwidth B_s, the guard band bandwidth must be set such that $B_g \geq B_s$ to avoid any spectral overlap between the carrier-signal and signal-signal beating products. However, in comparison to the case without a guard band, this results in a reduction of the ISD by a factor of two and inefficient use of the available bandwidth of RF-components used in the system [13]. Alternatively, the bandwidth of the guard band may be set to a lower value, *i.e.*, $B_g < B_s$, to achieve the desired ISD/OSNR penalty trade-off depending on the overlap between the sideband and signal-signal mixing products [14]. In the following, to quantify the amount of overlap between the sideband and signal-signal beating, the overlap ratio (in percentages) parameter, defined as the ratio of the overlapping bandwidth (B_{ov}) and B_s, was used, as depicted in Fig. 4.17(b).

In the study described in this section, which was carried out by simulations, the performance of SSB-OFDM and SSB Nyquist-SCM formats with equivalent ISDs were compared; the symbol rate of the signals was kept constant at 7 GBaud, with two gross bit-rates per channel considered: 14 and 28 Gb/s. The ISD was varied by adjusting the guard band B_g between the optical carrier and the sideband (hence changing the overlapping ratio parameter), and the WDM channel spacing $\Delta\nu_{ch}$. The performance of the signal formats was compared in terms of the required OSNR in back-to-back operation, and the maximum transmission distance over SSMF links (including the effects of EDFA noise, fibre dispersion and nonlinearities). No digital or optical SSBI estimation/cancellation was carried out to avoid significant additional transceiver complexity.

The total bandwidth of a single channel (B_t) is the sum of B_g and B_s, as shown in Fig. 4.17. To compare the ISD of modulation techniques fairly, B_t was kept the same for both techniques. When the overlap ratio was equal to 0, B_s was set to 7 GHz at 7 GBaud, as can be seen in Fig. 4.18(1a), (1b), (3a) and (3b). No bit-loading was applied for the SSB-OFDM signal and, in the case of SSB Nyquist-SCM signal, the RRC filter roll-off parameter β was set to 0. However, with B_t set to between 7 and 14 GHz by varying the guard bandwidth, the roll-off factor of pulse shaping filter β for the Nyquist-SCM signal was relaxed from 0 to 0.3 to optimize its OSNR performance. Moreover, the subcarrier frequency was adjusted to maintain B_t and the ISD at values identical to those of the equivalent adaptively modulated OFDM signal, as shown in Fig. 4.18(2a) and (4a).

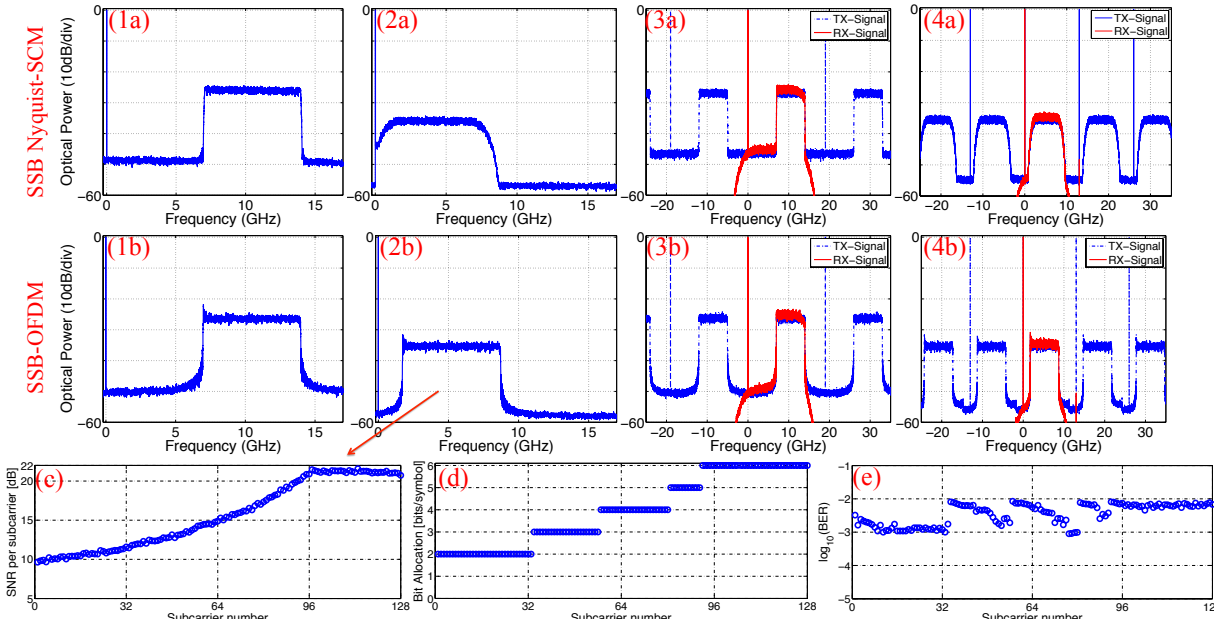

Fig. 4.18: Single channel optical spectra for the SSB (1a) Nyquist-SCM and (1b) OFDM signals, and WDM spectra before and after the OBPF for (3a) Nyquist-SCM and (3b) OFDM signals with a B_t of 14 GHz and a Δv_{ch} of 19 GHz (non-overlapping case). Single channel optical spectra for (2a) Nyquist-SCM and (2b) OFDM signals, and WDM spectra after the OBPF for (4a) Nyquist-SCM and (4b) OFDM signals with a B_t of 8.75 GHz and a Δv_{ch} of 13 GHz (overlapping case). Note that frequency scales in optical spectra are relative to the optical carrier frequency of the central channel. (c) SNR in dB per subcarrier, (d) bit allocation per subcarrier to achieve 28 Gb/s and (e) BER values per subcarrier for the SSB-OFDM signal while bit loading is performed at a CSPR of 13 dB, an OSNR of 26 dB, and a B_t of 8.75 GHz at the HD-FEC limit.

For the OFDM signals, in the case of non-zero overlap ratios ($B_{ov} > 0$ GHz so $B_t < 14$ GHz), the SSBI decreases towards higher frequencies, so that the subcarriers close to the optical carrier are more significantly distorted than those further away from the carrier. Therefore, bit-loading using the Levin-Campello algorithm was applied so that similar bit error probabilities were experienced by all the sub-channels, as explained in section 3.2.2.1. The bits were allocated to the subcarriers by comparing the signal-to-noise ratio (SNR) threshold values for conventional modulation formats, *e.g.,* BPSK, QPSK *etc.*, and their received SNR values which were obtained from the receiver. The threshold values for the conventional modulation formats can be found in [16, Ch.2]. Since their received SNR values also depend on the CSPR, the optimum bit allocation was found by applying an exhaustive search for the CSPR value to achieve the best OSNR performance. For instance, to achieve the bit-rate of 28 Gb/s (requiring an average number of bits/symbol of 4), the sub-carriers overlapping the signal-signal beating products, and hence, suffering from lower SNR were allocated lower numbers of bits-per-symbol (0, 1, 2 or 3 bits-per-symbol), as shown in Fig. 4.18(c) and (d). On the other hand, the subcarriers that did not overlap with the beating products were allocated higher bits/symbol (4, 5 or 6 bits-per-symbol, depending on their SNR values).

SNR, bit allocation and BER values per subcarrier at an OSNR of 26 dB, a CSPR of 13 dB and B_t of 8.75 GHz are shown in Fig. 4.18(c)-(e). At this value of B_t, 97 subcarriers overlapped with the signal-signal beating products. The BER for each subcarrier varied between approximately 1×10^{-3} and 8×10^{-3}. For the best receiver sensitivity performance, the BER should be approximately equal across the subcarriers. To equalize BER on each subcarrier, power loading in addition to the bit loading can be also applied instead of allocating the power equally across subcarriers. Nevertheless, it has been shown

that the system performance that utilizes power-and-bit loading is not significantly different than systems utilizing only bit loading [17–19]. Table 4.1 shows the optical bandwidth and ISD values considered in the simulations. In both cases, Δv_{ch} was chosen such that there was negligible linear crosstalk penalty between the channels and net ISD is calculated assuming a 7% HD-FEC overhead.

Tab. 4.1: Optical bandwidth and ISD values used in the simulations

B_t (GHz)	B_s (GHz)	B_g (GHz)	B_{ov} (GHz)	Δv_{ch} (GHz)	Net ISD (b/s/Hz)
14	7	7	0	19	1.37
8.75	7	1.75	5.25	13	2.0

4.4.1 Back-to-back results

SSB Nyquist-SCM QPSK/16-QAM and the equivalent adaptively modulated SSB-OFDM signals were simulated in back-to-back operation to determine their OSNR performance, as shown in Fig. 4.19. In the case of SSB Nyquist-SCM QPSK with a B_t of 14 GHz, the required OSNR values are very similar for both formats. It was found that the performance difference between SSB Nyquist-SCM and OFDM signals at $B_t \geq 8.75$ GHz does not differ significantly. However, when B_t was reduced below 8.75 GHz, the required OSNR values for the two signal formats diverged significantly. The Nyquist-SCM QPSK format required an OSNR of 12.0 dB at $B_t = 7$ GHz, while the corresponding value for the OFDM signal was found to be 16.1 dB, 4 dB higher than Nyquist-SCM signal (see Fig. 4.19(a) and Fig. 4.20(a)). When the Nyquist-SCM modulation format was switched from QPSK to 16-QAM (and the bit distribution on the OFDM subcarriers also increased to achieve equivalent ISD values), they had similar OSNR requirements for $B_t \geq 10.5$ GHz. However, at $B_t = 8.75$ GHz, the required OSNR difference between Nyquist-SCM and OFDM signals became again approximately 4 dB. With B_t set to 7 GHz, at which point the gross ISD approaches $\log_2(M)$, 4 b/s/Hz, neither system was able to achieve the HD-FEC threshold BER of 3.8×10^{-3}.

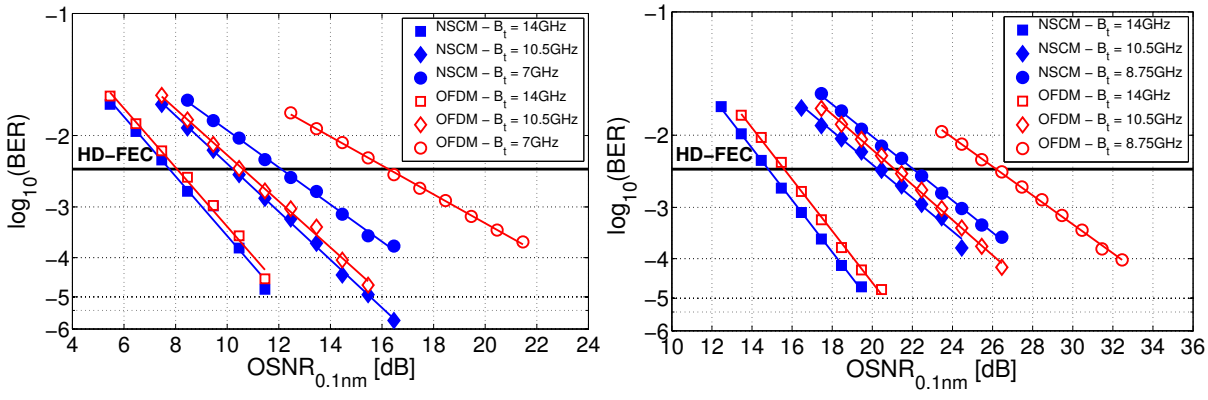

(a) (b)

Fig. 4.19: Back-to-back BER with respect to OSNR with different values of signal bandwidth (B_t) for SSB (a) Nyquist-SCM QPSK and the equivalent adaptively modulated OFDM signals at 14 Gb/s and SSB (b) Nyquist-SCM 16-QAM and the equivalent adaptively modulated OFDM signals at 28 Gb/s [15].

The performance difference between these two formats can be explained by two reasons: 1) the Nyquist-SCM signal averages the distortion due to the SSBI across the entire signal bandwidth whereas

the subcarriers in OFDM signal overlapping with the beating interference are severely affected even though they are modulated adaptively. 2) Although the PAPR of the OFDM signal was optimized (by clipping and minimizing the required OSNR) for the 5-bit DAC resolution, its value is still 3.3 dB higher that of the Nyquist-SCM signal. This PAPR difference reduces the required CSPR value for the Nyquist-SCM signal, and hence, the required OSNR for the optimum detection, as can be seen in Fig. 4.20. Better performance of Nyquist-SCM at high ISD was also observed in [20], in which the single channel vestigial sideband (VSB) Nyquist-SCM signal was compared with OFDM signal in back-to-back and transmission performance over 100 km, although without considering any adaptive bit-loading for the OFDM signal or EPD to mitigate the chromatic dispersion. It is worth noting that the slope of the BER versus OSNR curves for QPSK/16-QAM case in Fig. 4.19 changes when B_t is less than 8.75/10.5 GHz due to the SSBI.

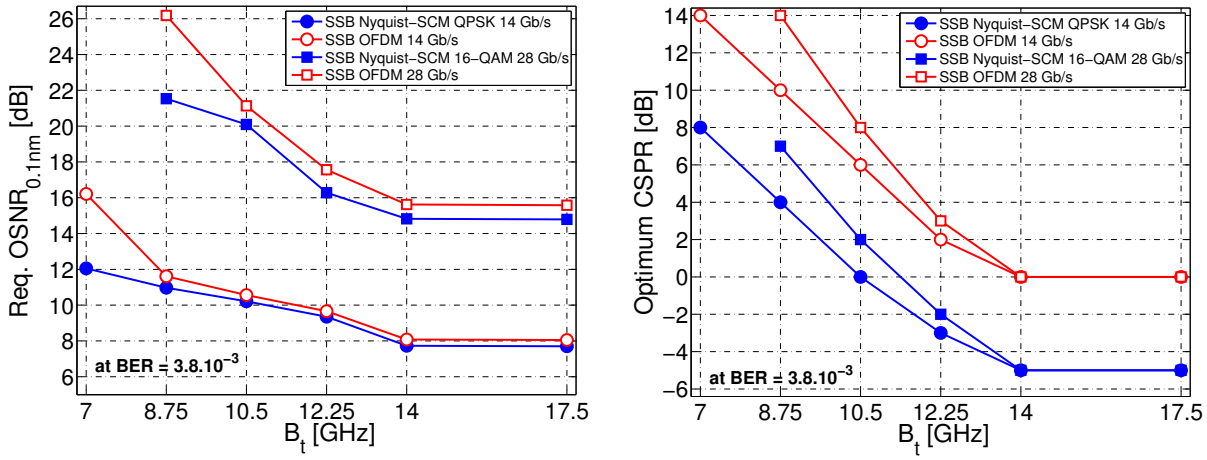

Fig. 4.20: (a) Required OSNR and (b) optimum CSPR with respect to B_t at the HD-FEC threshold for SSB Nyquist-SCM QPSK/16-QAM and the equivalent adaptively modulated SSB OFDM signals [15].

In direct detection systems, optimizing the CSPR is essential to achieve the best trade-off between signal-ASE beating noise and SSBI. When $B_t = 14$ GHz, at the OSNR values required to reach the HD-FEC threshold BER of 3.8×10^{-3}, the optimum CSPR values for the SSB Nyquist-SCM and OFDM signal formats were found to be -5 dB and 0 dB, respectively, for both QPSK and 16-QAM signalling. The difference in CSPR values is explained by the difference in PAPR of the signals after clipping. On the other hand, when the signal overlaps with the signal-signal beating products, *i.e.*, $B_t < 14$ GHz, the carrier-signal beating products have to be large enough compared to the SSBI to be recovered. Thus, the optimum CSPR value increases with reducing B_t. At $B_t = 8.75$ GHz, it was found that the optimum CSPR value for QPSK/16-QAM signal increases to 4 dB/7 dB and 10 dB/14 dB for the Nyquist-SCM and OFDM signals at the HD-FEC threshold. Since 16-QAM is more sensitive to distortions due to its denser symbol spacing, the increase in the optimum CSPR with reducing B_t is more rapid than QPSK. This increase in CSPR directly translates into OSNR penalties, as can be seen in Figs. 4.19 and 4.20(a).

4.4.2 Transmission results

Following the back-to-back assessment described above, both single channel and 7-channel WDM transmission simulations at 28 Gb/s per channel were carried out. In each case, the WDM channel spacing $\Delta\nu_{ch}$ was chosen such that a negligible penalty (≤ 0.5 dB) resulted due to linear inter-channel crosstalk.

Initially, the signal bandwidth B_t was set to 14 GHz ($B_s = B_g = 7$ GHz so that $B_{ov} = 0$ GHz) and a Δv_{ch} of 19 GHz was chosen (resulting in a net ISD of 1.37 b/s/Hz assuming 7% HD-FEC overhead). Fig. 4.21(a) shows the range of launch powers at which the HD-FEC threshold BER (3.8×10^{-3}) was achieved. Due to the low crosstalk between channels, the transmission performance of single channel and WDM are very similar in the linear regime. However, in the non-linear regime in single channel transmission, the lower maximum launch powers indicate that SSB OFDM is more sensitive to SPM due to its higher PAPR. SSB Nyquist-SCM exhibits a 2 dB greater margin compared to the OFDM signal. This margin was reduced to 0.8 dB in WDM transmission. At $B_{ov} = 0$ GHz or $B_t = 14$ GHz, the maximum transmission distance of Nyquist-SCM and OFDM signal formats were quite similar, (1880 km vs 1720 km, respectively) which was expected from the result, shown in Fig. 4.20(a).

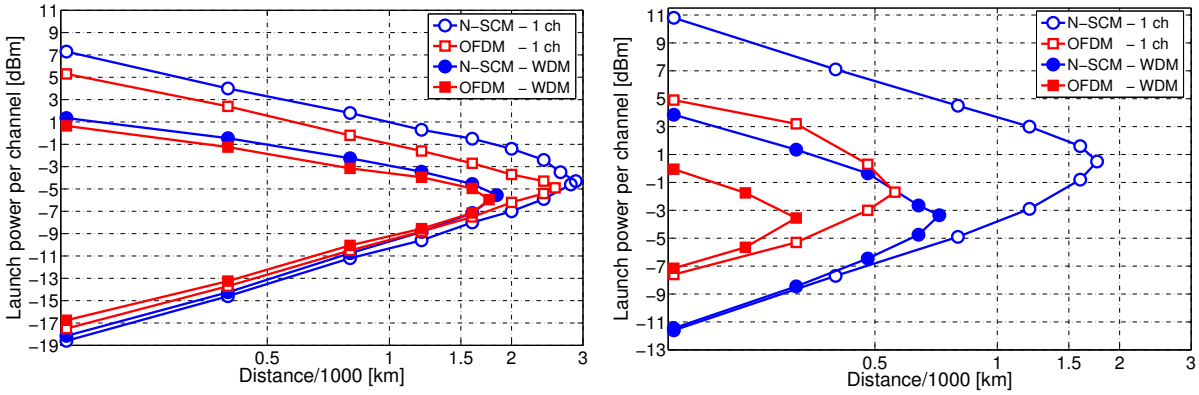

Fig. 4.21: At BER= 3.8×10^{-3}, single channel and WDM transmission performance of 28 Gb/s Nyquist-SCM 16-QAM and the equivalent adaptively modulated OFDM signals at net ISD of (a) 1.37 b/s/Hz ($B_t = 14$ GHz and $\Delta v_{ch} = 19$ GHz) and (b) 2.0 b/s/Hz ($B_t = 8.75$ GHz and $\Delta v_{ch} = 13$ GHz) [15].

Next, B_t was reduced from 14 to 8.75 GHz, and consequently, it was possible to reduce Δv_{ch} from 19 to 13 GHz, resulting in an increase in the net ISD from 1.37 to 2.0 b/s/Hz. The transmission results are presented in Fig. 4.21(b); in both single channel and WDM transmission cases, Nyquist-SCM offers a maximum transmission distance approximately two times larger than the OFDM signal. This difference is mainly due to the approximately 4 dB difference in the required OSNR observed in back-to-back operation between the Nyquist-SCM and the OFDM formats, as shown in Fig. 4.19(b) and Fig. 4.20(a). Accordingly, the WDM Nyquist-SCM signal could be transmitted over distances of up to 720 km of SSMF whereas WDM OFDM transmission is limited to just 320 km. The maximum transmission distances of single channel and WDM systems for the Nyquist-SCM 16-QAM and the equivalent adaptively modulated OFDM signals are summarized in Fig. 4.22.

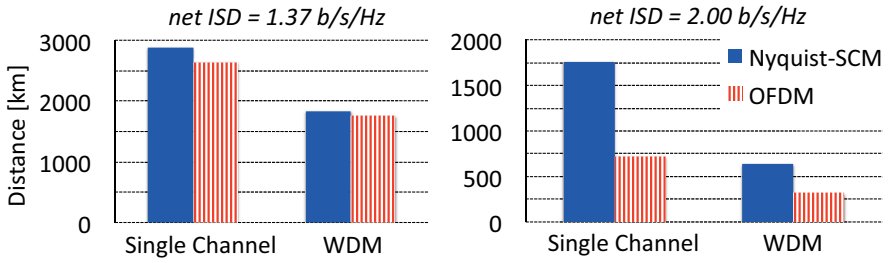

Fig. 4.22: Maximum transmission distances of single channel and WDM systems for 28 Gb/s Nyquist-SCM and OFDM signals at net ISD of 1.37 b/s/Hz (left) and 2 b/s/Hz (right) [15].

4.5 SSB Nyquist-SCM transmission experiments achieving ISDs >1b/s/Hz

In this section, the experimental results for the single channel and WDM SSB Nyquist-SCM transmission are presented. Measurements of the BER versus the received OSNR values for the central WDM channel were carried out to test the back-to-back and transmission performance of the system. ASE-noise loading was performed at the receiver. As the central WDM channel is expected to have the worst transmission performance due to the fibre nonlinearities compared to the other channels, the results for the central channel are mainly presented and discussed. The experimental setups are explained in section 4.2 above. The results that were obtained using three transmitter setups are divided in two sections, namely using IQ-modulator and dual-drive MZMs in sections 4.5.1 and 4.5.2, respectively. The back-to-back and transmission performance of the modulators is also compared in section 4.5.2.

4.5.1 Using $LiNbO_3$ IQ-modulator

4.5.1.1 Back-to-back results for SSB Nyquist-SCM QPSK and 16-QAM

In the back-to-back single channel case, the implementation penalty at the HD-FEC threshold for QPSK was found to be 0.7 dB compared to the ideal simulations, as shown in Fig. 4.23. This is due to the DAC quantization noise and non-ideal optical filtering (4^{th}-order super-Gaussian optical filter rather than ideal rectangular 'brick-wall' shape optical filter), *i.e.,* some out-of-band ASE-noise was detected by the photodiode due to non-ideal optical filtering. The penalty for the 16-QAM signal increased to 2 dB since it is more sensitive to distortions. When the practical parameters are taken into account, the simulations match well with the experiments, as can be seen in Fig. 4.23.

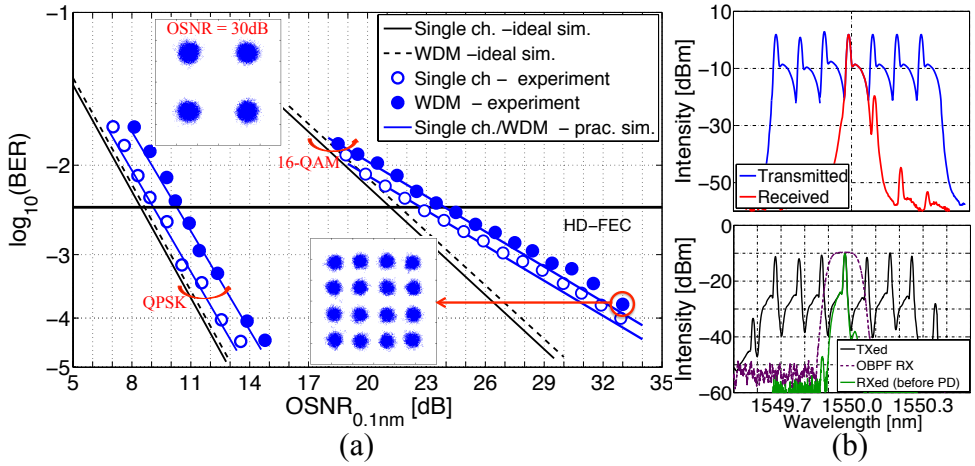

Fig. 4.23: (a) BER versus OSNR for single and 7 channel in back-to-back operation with the received QPSK and 16-QAM constellations at an OSNR of 30 dB and 34 dB, respectively (left). (b) The corresponding transmitted and received optical spectra (right).

Following this, the back-to-back OSNR performance of WDM SSB Nyquist-SCM QPSK and 16-QAM was assessed. The received QPSK and 16-QAM constellations at an OSNR of 30 dB and 34 dB are shown in the inset of Fig. 4.23(a). As expected, the required OSNR difference at the HD-FEC threshold is negligible between the single channel and WDM system in ideal simulations since rectangular optical filter with a bandwidth equal to the signal bandwidth was used, *i.e.,* no out-of-band ASE-noise. The required OSNR penalties for WDM QPSK and 16-QAM signals are approximately 1 dB compared to the single channel case due to the linear crosstalk caused by the neighboring channels. To keep the penalties within 1 dB, the channel spacing values were chosen as 11 and 12 GHz for 7 GBaud QPSK and

6.25 GBaud 16-QAM signals, respectively (hence, the signal bandwidths were 9.8 GHz and 8.75 GHz, as calculated using Eq.4.4).

At the demultiplexing stage in the receiver, this approximately 2 GHz relaxation in the grid translates into the suppression of approximately 20 and 30 dB for the SSB Nyquist-SCM QPSK and 16-QAM signals, respectively, as shown in Fig. 4.23(b). A required OSNR difference of approximately 12 dB is observed between the SSB Nyquist-SCM QPSK and 16-QAM. This is due to the reduction in Euclidean distance between the symbols (which differ by a factor of 4, causing a 6 dB increase in the required OSNR) and the susceptibility to SSBI. Since 16-QAM has lower tolerance to SSBI than QPSK signalling [15], the optimum CSPR increases significantly to achieve the HD-FEC threshold BER, leading to an increase in the required OSNR, as can be observed in Fig. 4.20(b).

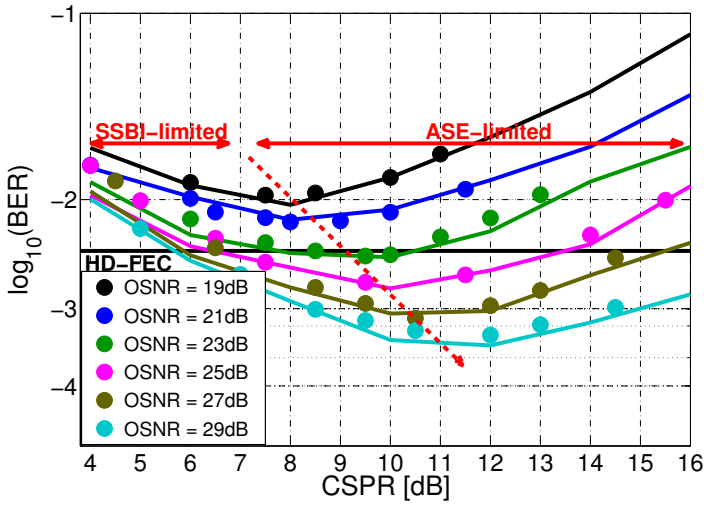

Fig. 4.24: Simulated (solid lines) and experimental (markers) BER with respect to CSPR at different OSNR levels in back-to-back operation. The dashed red arrow indicates the shift in the optimum CSPR value [21].

In subcarrier modulation-based direct detection systems, it is crucial to optimize the CSPR to achieve the minimum BER at a given OSNR. Thus, we investigated the system sensitivity to CSPR variation, both in practical simulations and experimentally. To measure the CSPR value at a given OSNR accurately, two different methods were assessed. First, the transmitted signal was split into two arms and, one arm was detected using a coherent receiver whilst the other arm was detected with a direct detection receiver for BER counting. After the full optical field was recovered using the coherent receiver, two brickwall-shaped digital filters were used to filter out the optical carrier and sideband. The corresponding power values for the carrier (P_C) and sideband (P_s) were computed and the resulting CSPR value was determined using Eq.4.1. Since the measurement was carried out at a very high resolution (approximately 100 kHz), it is the most accurate method to measure the CSPR. In a simpler alternative approach, the CSPR was measured at a given OSNR using the corresponding optical spectrum taken from the OSA at a resolution of 0.01 nm. After the spectrum was acquired, the carrier and sideband power were measured using two 5^{th}-order super-Gaussian-shaped filters in MATLAB, similar to the first method. Finally, the measured CSPR values using the two different methods were compared and a discrepancy of approximately 10% was found. Since the second, simpler method was sufficiently accurate for the demonstrations, the majority of the CSPR values were measured using the second method.

The BER as functions of CSPR at six different OSNR values are shown in Fig. 4.24 for 16-QAM Nyquist-SCM. The dashed red arrow indicates how the optimum CSPR shifts towards higher values as the OSNR is increased. At low CSPR values, the system is SSBI-limited since the signal-signal

mixing products distort the desired signal (carrier-signal mixing products) severely. On the other hand, in the high CSPR regime, signal-ASE beating noise limits the system performance. The simulation results shown with the solid lines closely match with the experimental results shown with the markers in Fig. 4.24. It was found that optimum CSPR values were similar for single channel and WDM systems in back-to-back operation.

4.5.1.2 Transmission results

11 GHz-spaced 7×14 Gb/s SSB Nyquist-SCM QPSK transmission

The performance of the single channel and WDM systems were investigated in transmission experiments over 400 km and 800 km (5 and 10 spans) of SSMF, which are typical distances for metropolitan, regional and long-haul applications. The optimum launch power was found to be approximately 0 dBm per channel except for WDM transmission over 800 km in which case it was found to be approximately -1 dBm.

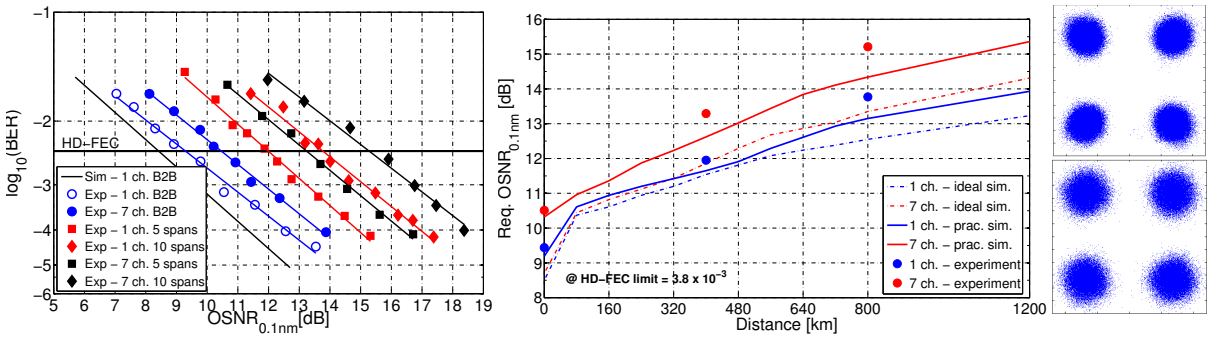

(a) (b) (c)

Fig. 4.25: (a) BER vs OSNR for back-to-back, 400 and 800 km for single and 7 channel transmission. (b) Required OSNR values (at 0.1 nm resolution) versus transmission distances for the ideal and practical simulations, and the experimental results. (c) The received constellations for single (top) and 7 channel transmission (bottom) over 800 km in experiments [22].

After the optimum launch power into the fibre was found, single channel and WDM transmission for targeted distances was performed. Fibre nonlinearities cause gradual degradation in OSNR performance, as shown in Fig. 4.25(a). To demonstrate the fundamental limits of the system, simulations under ideal conditions were performed and the results are presented in Fig. 4.25(b). Additionally, to validate the experimental results, practical simulations that incorporate the experimental parameters (*e.g.,* ENOB of DACs/ADC, limited bandwidth of electrical components at the transceiver, and non-ideal optical filtering) were also carried out. The experimental results for both single channel and the WDM system matched fairly well with the practical simulation results, as shown in Fig. 4.25(b). The required OSNR values at the HD-FEC threshold for single channel transmission after 400 km of SSMF were 11.4 dB, 11.8 dB and 12 dB for the ideal simulation, practical simulation and experiment, respectively. At 800 km, the corresponding OSNR values were 12.5 dB, 13.2 dB and 13.8 dB. Similar to the results presented in section 4.3.2, the penalty in single channel case between 400 and 800 km is due, firstly, to the increase in PAPR resulted from EPD, and secondly, from fibre nonlinearity (SPM). The penalty can be improved through the use of higher resolution DACs.

Furthermore, in WDM transmission over 400 km of SSMF, the corresponding required OSNR values were measured to be 11.9 dB, 12.5 dB and 13.3 dB (see Fig. 4.25(a)). When the transmission distance increased to 800 km, the values at the HD-FEC threshold also increased to 13.4 dB, 14.3 dB and 15.3 dB.

This increase is due to four-wave mixing (FWM) caused by neighboring channels. During the single channel transmission, only SPM distorts the signal (the distortion exhibits a non-Gaussian distribution around symbols) whereas FWM (Gaussian distribution around the symbol points) between the closely spaced WDM channels degrades the system performance, as shown in Fig. 4.25(c). Therefore, over longer transmission distances, the required OSNR increases more rapidly in WDM transmission relative to the single channel transmission case. The optimum CSPR at the HD-FEC threshold was found to be 2 dB both in back-to-back and single channel transmission. However, it decreases to approximately 0 dB in WDM transmission.

To sum up, the transceiver that uses SSB Nyquist-SCM QPSK signalling and operates at 14 Gb/s per channel with a channel spacing of 11 GHz, achieved a BER below a HD-FEC threshold of 3.8×10^{-3} in transmission over SSMF links of up to 800 km. The achieved net optical ISD of 1.2 b/s/Hz was demonstrated, taking into account a 7% HD-FEC overhead.

12 GHz-spaced 7×25 Gb/s SSB Nyquist-SCM 16-QAM transmission

Single channel 16-QAM transmission was carried out for distances from 242 km up to 727 km (up to 9 spans) using the recirculating fibre loop. The experimental and simulated BER values for single channel transmission distances of up to 727 km with respect to the launch power per channel are shown in Fig. 4.26(a). In single channel transmission, the optimum launch power was found to be approximately 1 dBm. BER values below the HD-FEC threshold were obtained for launch powers over the range from -4.0 dBm to $+4$ dBm at 242 km. This range decreased when the transmission distance increased as expected. The maximum achieved transmission distance was 727 km at a launch power of 1 dBm with the measured BER of 3.5×10^{-3}, just achieving the HD-FEC threshold. The optimum CSPR value was found to be approximately 9 dB at 727 km.

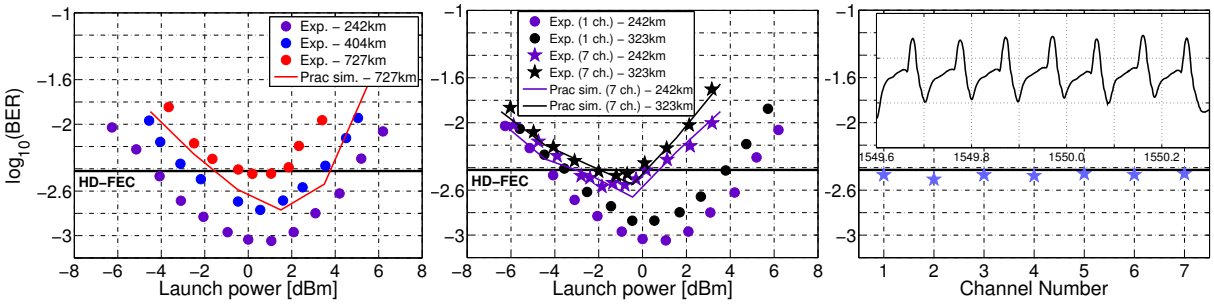

(a) (b) (c)

Fig. 4.26: BER versus launch power per channel for (a) single channel and (b) WDM systems with practical simulations. BER for each received channel at 323 km. Inset: Transmitted optical spectrum (zoomed version of 16-QAM spectrum shown in Fig. 4.23) [21].

7-channel WDM transmission distances of 242 and 323 km were achieved with minimum BER of 3.2 and 3.4×10^{-3}, respectively, at a launch power of -1.6 dBm per channel, as shown in Fig. 4.26(b). In the linear regime, WDM achieves the same BER value at a slightly higher launch power per channel compared to the single channel transmission. This is due to the linear crosstalk caused by the neighboring channels which was also observed in the back-to-back operation (see Fig. 4.23(a)). Due to the additional inter-channel nonlinear effects during WDM transmission compared to single channel transmission, the maximum transmission distance was reduced from 727 to 323 km. There is a very good agreement between the transmission experiments and simulations. The optimum CSPR value was found to be approximately 7 dB in WDM transmission at 323 km, slightly lower than the single channel transmission

at 727 km. This small change in the optimum CSPR value is due to the trade-off between the SSBI and fibre nonlinearities, and, as expected, the optimum CSPR value is lower in WDM transmission because of the fibre nonlinearities.

All 7 channels operating at a net bit rate of 24 Gb/s (a gross bit rate of 25 Gb/s) achieved a BER $< 3.8 \times 10^{-3}$ at the optimum launch power of -1.6 dBm per channel, as shown in Fig. 4.26(c). Hence, a total net bit rate of 168 Gb/s (7ch.$\times$25 Gb/s$\times r$ where r is given in Eq.4.2) with a net ISD of 2.0 b/s/Hz (a gross optical ISD of 2.08 b/s/Hz) was achieved over 323 km of SSMF.

4.5.2 Using $LiNbO_3$ and InP dual-drive MZMs

4.5.2.1 Single channel back-to-back performance

The BER versus OSNR values for the single channel case, the transmitted optical spectra and constellations are shown in Fig. 4.27, comparing the IQ-modulator and dual-drive MZM. In ideal simulations, the dual-drive MZM requires 2 dB higher OSNR to achieve the HD-FEC threshold since the optimum CSPR at the HD-FEC threshold is higher than with the IQ-modulator. This is due to the combination of higher PAPR of the driving signals and their lower voltage levels. The required OSNR for the $LiNbO_3$ dual-drive MZM was found to be 11.6 dB in the experiment. The implementation penalty for the dual-drive MZM increases from 0.7 to 1.5 dB. Besides the DACs/ADC quantization noise, and the effects of the LPF and OBPF, dual-drive MZMs were not able to achieve CSPR values lower than 5 dB. This experimental limitation prevents operation at the optimum CSPR values for the OSNR values over the range of 8.5 dB to 13 dB. This can be observed from the slope difference between two modulators' OSNR curve in Fig. 4.27(a), *i.e.,* the curves are converging at higher OSNR values which is unusual. An IQ-modulator requires 2.5 dB lower OSNR compared to the dual-drive MZMs due to its ability to operate at the optimum CSPR values for each OSNR level and the low PAPR value of the modulator driving signals. No significant performance difference was observed between the $LiNbO_3$ and InP dual-drive MZMs.

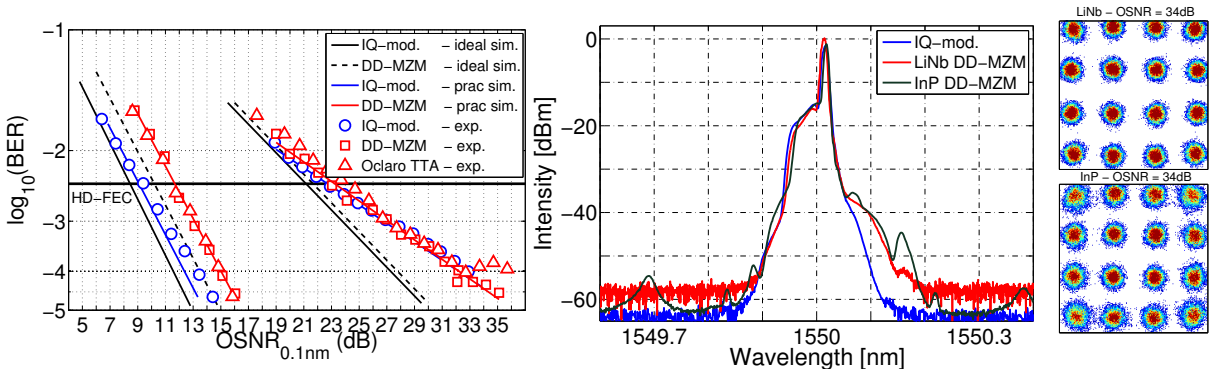

(a) (b) (c)

Fig. 4.27: (a) BER versus OSNR performance and (b) transmitted optical spectrum of the IQ-modulator, $LiNbO_3$ and InP dual-drive MZMs for the single channel case in back-to-back operation. (c) The received constellations using the dual-drive MZM at an OSNR of 34 dB.

On the other hand, the OSNR performance of 16-QAM signalling experiment showed a similar behavior compared to the simulation results since the optimum CSPR values are high enough to be realized in practice by the dual-drive MZMs. Similar to the IQ-modulator, the required OSNR values at the HD-FEC threshold were found to be 23 and 23.5 dB for the $LiNbO_3$ and InP dual-drive MZMs. The optimum CSPR values at the HD-FEC threshold were found to be approximately 10 dB. The lowest

achieved BER value was found to be 1×10^{-4} for both dual-drive MZMs. The outer-most symbols in InP dual-drive MZM constellation are more distorted than the symbols in $LiNbO_3$ dual-drive MZM constellation, as shown in Fig. 4.27(c). This is because the peak-to-peak voltage levels of the driving signals V_{p-p} for the InP dual-drive MZM were higher than the optimum value.

4.5.2.2 Optimum channel spacing for the DD-MZMs

The extinction ratio (ER) of an optical modulator is crucial in the generation of an optical SSB signal. If the input optical field E_i is not equally split (*i.e.,* if the optical splitting ratio γ_{sp} in Eqs.2.22 and 2.28 is not equal to 0.5), the unwanted sideband is not fully suppressed, causing spectral broadening. Hence, linear crosstalk between the neighboring WDM channels is observed (assuming no optical filtering is used when the WDM channels are combined), and consequently, causing penalties at channel spacing values of less than twice the SSB signal bandwidth. The ER of an optical modulator in dB, which is related to γ_{sp}, is given by

$$\mathrm{ER(dB)} = -20\log_{10}(2\gamma_{sp} - 1) \approx \mathrm{OSSR(dB)}. \tag{4.6}$$

where the optical sideband suppression ratio (OSSR) is defined as the power of the desired sideband divided by the power of the suppressed sideband. If the SSB signal is generated utilizing the Hilbert transform, the OSSR is approximately equal to the ER, assuming the attenuation and the phase on both arms are optimized. The change in OSSR and ER with respect to γ_{sp} are shown in Fig. 4.28 along with the simulated optical spectra at certain ER values. For instance, if the incoming light is split with a ratio of 0.55 ($0.55E_i$ to one arm and $0.45E_i$ to the other arm), this implies that the ER of the modulator is 20 dB, meaning that the unwanted sideband can be suppressed by up to approximately 20 dB, as can be seen in Fig. 4.28.

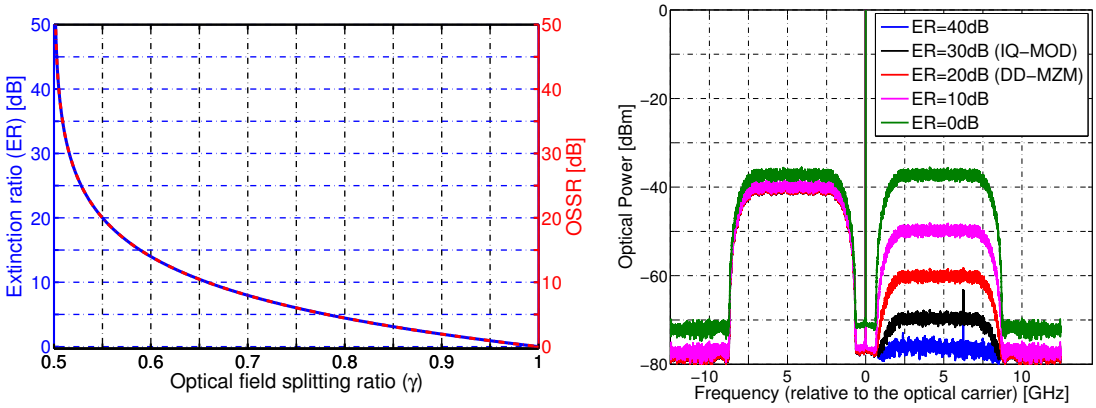

Fig. 4.28: ER and OSSR with respect to γ_{sp} of the optical modulator (left). Simulated optical spectrum at a resolution of 10 MHz for different extinction ratio value (right) [136].

Following the single channel measurements, the channel spacing was varied from 20 to 12 GHz (a net optical ISD of from 1.2 to 2.0 b/s/Hz) to determine a reasonable compromise between the spectral efficiency and the required OSNR performance, and hence, transmission performance. Using the IQ-modulator and $LiNbO_3$ dual-drive MZM, the back-to-back required OSNR with respect to the channel spacing values for WDM system were assessed experimentally and in practical simulations using different values of the ER. As discussed above, the OSSR is directly proportional to the ER of a modulator. The simulation model and experimental setup are described in sections 4.1.1 and 4.2.1.

One of the central channels (λ_3) was selected as the channel of interest during these measurements. In the practical system simulations with an ER of 40 dB, no significant OSNR degradation was observed with channel spacing above 12 GHz. The OSNR penalty at a channel spacing of 12 GHz is due to the non-ideal demultiplexing before the photodiode. In the experiment, using the $LiNbO_3$ dual-drive MZM, the required OSNR values were found to be 34 dB and 26 dB (the OSNR penalties of 11 dB and 3 dB compared to the single channel case) at channel spacing values of 12 GHz and 14 GHz, respectively. The values for the IQ-modulator at the same channel spacing values were measured to be 24.4 dB and 24.1 dB (OSNR penalties of only 1.4 dB and 1.1 dB compared to the single channel case), respectively. The greater OSNR penalties observed with the dual-drive MZM are due to the lower suppression of the unwanted sideband compared to the IQ-modulator, resulting in higher linear crosstalk between the neighboring channels. The spectral broadening, that causes higher linear crosstalk for the dual-drive MZMs, can be clearly observed from the optical spectra, plotted in Fig. 4.27(b). The sideband suppression ratio, typically limited to 20 dB for a dual-drive MZM, can be increased to 45 dB by cascading the dual-drive MZM with a phase modulator, as experimentally demonstrated in [24]. At a channel spacing of 16 GHz or more, the measured required OSNR penalties were found to be within 1 dB compared to the single channel performance. The experimental results for the WDM system match the practical simulations fairly well, as can be seen in Fig. 4.29. As a result, we chose 16 GHz as the channel spacing value $\Delta\nu$ for the WDM demonstration using the dual-drive MZMs.

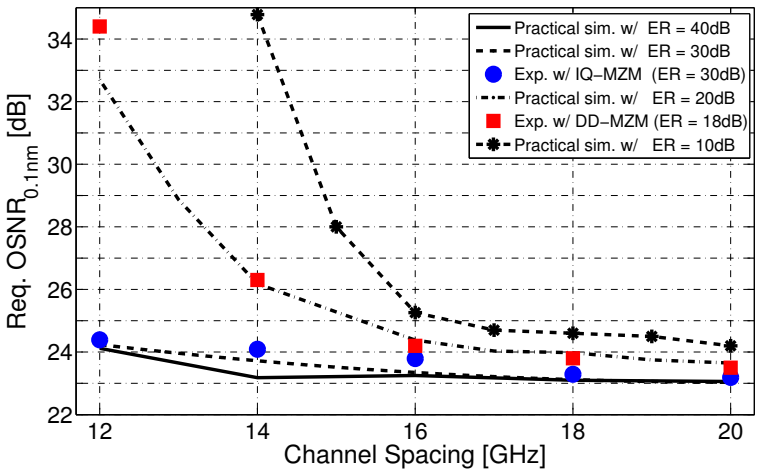

Fig. 4.29: Simulated and experimental required OSNR values with respect to the channel spacing $\Delta\nu$ using the IQ-modulator and dual-drive MZM [136].

4.5.2.3 WDM performance

Once the optimum channel spacing had been determined, the back-to-back and transmission performance of 16 GHz-spaced WDM SSB Nyquist pulse-shaped 16-QAM SCM signal generated by the $LiNbO_3$ and InP dual-drive MZMs was assessed. In back-to-back operation, no OSNR degradation was observed between the single channel and WDM systems operating at a bit rate of 25 Gb/s per channel, as shown in Fig. 4.30(a).

Following the back-to-back performance assessment, single channel and WDM signal transmission experiments were carried out. Note that the experimental setups using the dual-drive MZMs are described in sections 4.2.1.2 and 4.2.1.3. The experimental measured BER values with respect to the launch power per channel for both modulators are shown in Fig. 4.30(b). The maximum transmission

distance for the $LiNbO_3$ and InP dual-drive MZMs were 565 and 484 km, respectively. The optimum launch power values per channel for both modulators were found to be 2.5-3 dB, operating at an optimum CSPR of approximately 10 dB at the HD-FEC threshold (similar to the back-to-back operation). Due to the additional inter-channel nonlinear effects during the WDM transmission, the distance reduced to 242 km of SSMF at an optimum launch power per channel of -2.5 dBm. The received constellations after the transmission over 242 km of SSMF are shown in Fig. 4.30(b). Since no significant penalty was observed between the single channel and WDM back-to-back performance (see Fig. 4.30(a)), their transmission performances at a given distance (242 km) was very similar in the linear regime, as can be observed in Fig. 4.30(b). The optimum CSPR value in WDM transmission was found to be approximately 9 dB at 242 km, slightly lower than the single channel transmission at 565 km, due to the trade-off between the SSBI and fibre nonlinearities.

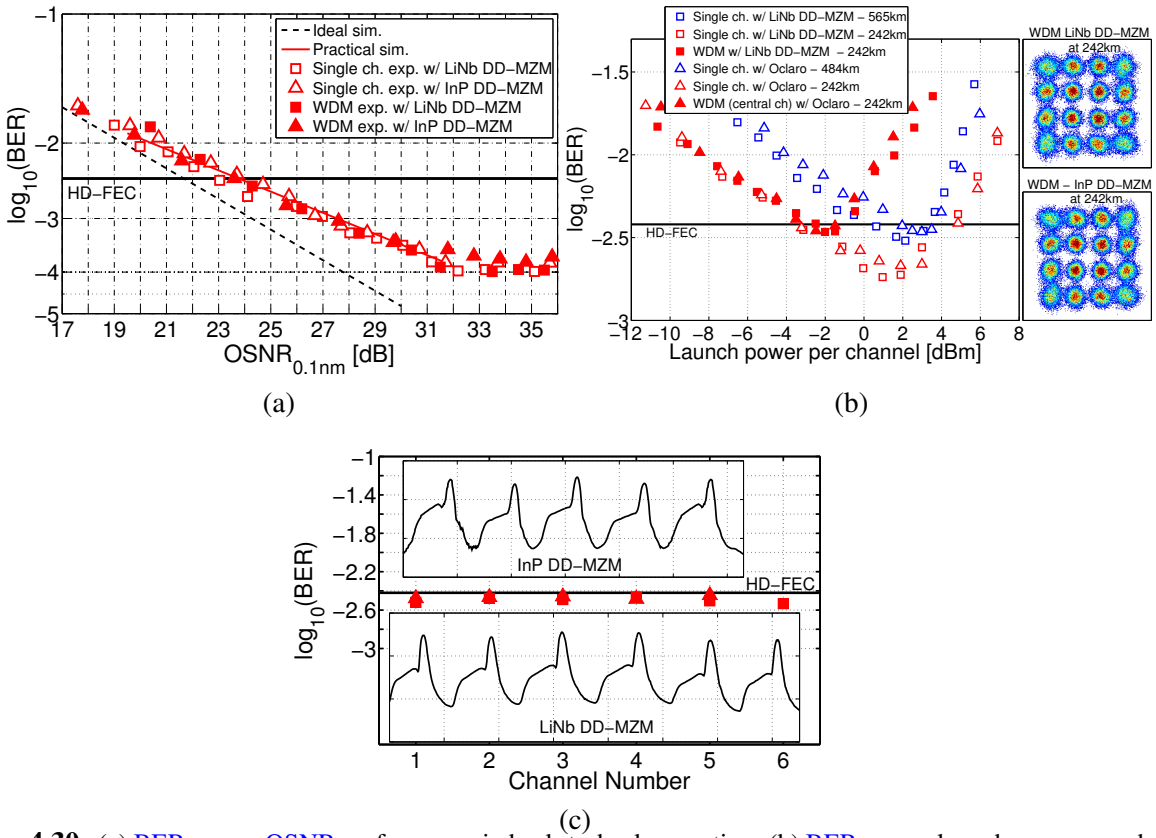

Fig. 4.30: (a) BER versus OSNR performance in back-to-back operation. (b) BER versus launch power per channel during single channel and WDM transmission. Insets: The received constellations for $LiNbO_3$ dual-drive MZM (top) and InP dual-drive MZM (bottom) at the HD-FEC threshold. (c) BER for each received channel at 242 km using dual-drive MZMs. Insets: Transmitted optical spectra for $LiNbO_3$ dual-drive MZM (bottom) and InP dual-drive MZM (top) (the zoomed version of 16-QAM spectra, shown in Figs.4.8 and 4.10)

Furthermore, all six/five transmitted channels generated by the $LiNbO_3$/InP dual-drive MZM, carrying SSB Nyquist pulse-shaped 16-QAM SCM signals and operating at a bit rate of 25 Gb/s per channel, achieved the HD-FEC threshold BER just below 3.8×10^{-3} at the optimum launch power per channel, as shown in Fig. 4.30(c) with their transmitted optical spectra. A net optical ISD of 1.5 b/s/Hz was achieved over 242 km of SSMF.

4.6 Summary

The increasing bandwidth and data demand in access and metropolitan networks in the upcoming years indicate that the available optical spectrum needs to be used more efficiently, *i.e.,* exceeding an ISD of 1 b/s/Hz, whilst requiring no higher optical complexity in the transceiver configuration. This can be achieved using DSP-based optical transmitters and direct detection receivers. Such transceivers potentially offer cost-effective solutions achieving high spectral efficiency (high optical ISD), dispersion tolerance and energy efficiency. Therefore, SCM formats realized by such transceivers were investigated in numerical simulations and experimentally demonstrated in WDM configuration. These WDM demonstrations are plotted in Fig. 4.31 along with previous demonstrations using other signal formats, as mentioned in section 3. Relative to the previous experiments, some of the experimental results presented in this thesis, associated journal and conference publications [21, 22, 25, 136], demonstrated the highest achieved optical ISDs reported for single polarization WDM direct detection systems at the given transmission distances.

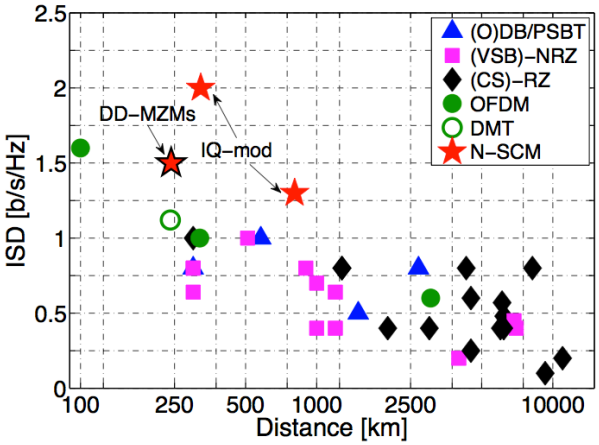

Fig. 4.31: Reported experimental demonstrations of WDM single polarization direct detection systems in terms of achieved net optical ISD versus distance. Formats: (VSB)-NRZ [26–33], (CS)-RZ [34–37], (O)DB [32, 38–40], OFDM [41, 42], DMT [43] and Nyquist-SCM [this thesis].

The key results of the work described in this chapter are as follows:

- SSB Nyquist-SCM signal format has higher tolerance to SSBI. Thus, it exhibits more than two-fold longer transmission distance compared to the SSB-OFDM signal at a net optical ISD of 2 b/s/Hz.

- SSB Nyquist-SCM QPSK/16-QAM signal was transmitted up to 800/323 km at net optical ISDs of 1.2/2 b/s/Hz using the transmitter design with IQ-modulator. The chromatic dispersion can be effectively mitigated using EPD technique. These demonstrations exhibit the record (highest) achieved ISDs at these transmission distances among the reported experimental WDM demonstrations in direct detection links using a single-ended photodiode and a single ADC.

- Nyquist-SCM can also be realized using low-cost optical modulators, such as $LiNbO_3$ or InP dual-drive MZM, and low-cost laser such as DFB lasers. No significant performance difference is observed between the dual-drive MZMs. However, compared to the IQ-modulator, the ISD and transmission performance decrease by 25% (from 2 b/s/Hz over 343 km to 1.5 b/s/Hz over 242 km of SSMF). Nevertheless, these are the record (highest) achieved ISDs using a dual-drive MZM-based transmitter in direct detection links over such transmission distances.

- SSB Nyquist-SCM offers high spectral efficiency using cost-effective optical transceiver architectures. Thus, it can be an attractive approach and practical for metro, access and back-haul applications.

4.7 References

[1] R. I. Killey, P. M. Watts, V. Mikhailov, M. Glick, and P. Bayvel, "Electronic dispersion compensation by signal predistortion using digital processing and a dual-drive Mach–Zehnder modulator," *IEEE Photon. Technol. Lett.*, vol. 17, no. 3, pp. 714–716, 2005.

[2] D. McGhan, C. Laperle, A. Savchenko, C. Li, G. Mak, and M. O'Sullivan, "5120 km RZ-DPSK transmission over G.652 fiber at 10 Gb/s with no optical dispersion compensation," in *Proc. IEEE/OSA Optical Fiber Communication Conference (OFC)*, 2005, paper PDP27.

[3] G. Agrawal, *Applications of nonlinear fiber optics*, Academic press, 2010.

[4] Y. Jiang, X. Tang, J. Cartledge, M. Poirier, M. Boudreau, K. Roberts, and A. Atieh, "Electronic dispersion precompensation for 10.709 Gbit/s NRZ-OOK using InP and $LiNbO_3$ Mach–Zehnder modulators," *Electronics letters*, vol. 47, no. 15, pp. 865–867, 2011.

[5] C. Shannon, "A mathematical theory of communication," *J. Bell Syst. Tech.*, vol. 27, no. 3, pp. 379-–423, 1943.

[6] M. S. Erkilinc, S. Pachnicke, H. Griesser, B.C. Thomsen, P. Bayvel, and R. Killey, "Effect of clipping on the performance of Nyquist-shaped dispersion-precompensated subcarrier modulation transmission with direct detection," *Proc. IEEE European Conference on Optical Communication (ECOC)*, 2014, paper Tu.3.3.1.

[7] M. Schuster, S. Randel, C.A. Bunge, S.C.J. Lee, F. Breyer, B. Spinnler, and K. Petermann, "Spectrally efficient compatible single-sideband modulation for OFDM transmission with direct detection," *IEEE Photon. Technol. Lett.*, vol. 20, no. 9, pp. 670–672, 2008.

[8] J. Zhang, X. Yuan, M. Lin, Y. Zhang, M. Zhang, and X. Zhang, "112Gb/s Pol-Mux RZ-DQPSK transmission over 960km SMF with high-speed polarization controller," in *OptoElectronics and Communications Conference (OECC)*, 2010, paper 9B1-3.

[9] W.-R. Peng, X. Wu, K.-M. Feng, V. R. Arbab, B. Shamee, J.-Y. Yang, L.C. Christen, A.E. Willner, and S. Chi, "Spectrally efficient direct-detected OFDM transmission employing an iterative estimation and cancellation technique," *Optics express*, vol. 17, no. 11, pp. 9099–9111, 2009.

[10] Z. Cao, J. Yu, W. Wang, L. Chen, and Z. Dong, "Direct-detection optical OFDM transmission system without frequency guard band," *IEEE Photon. Technol. Lett.*, vol. 22, no. 11, pp. 736–738, 2010.

[11] S.A. Nezamalhosseini, L.R. Chen, Q. Zhuge, M. Malekiha, F. Marvasti, and D.V. Plant, "Theoretical and experimental investigation of direct detection optical OFDM transmission using beat interference cancellation receiver," *Optics Express*, vol. 21, no. 13, pp. 15237–15246, 2013.

[12] W.-R. Peng, I. Morita, and H. Tanaka, "Enabling high capacity direct-detection optical OFDM transmissions using beat interference cancellation receiver," in *Proc. IEEE European Conference on Optical Communication (ECOC)*, 2010, paper Tu.4.A.2.

[13] A.J. Lowery, "Improving sensitivity and spectral efficiency in direct-detection optical OFDM systems," in *Proc. IEEE/OSA Optical Fiber Communication Conference (OFC)*, 2008, paper OMM4.

[14] W.-R. Peng, B. Zhang, K.-M. Feng, X. Wu, A.E. Willner, and S. Chi, "Spectrally efficient direct-detected OFDM transmission incorporating a tunable frequency gap and an iterative detection techniques," *J. Lightw. Technol.*, vol. 27, no. 24, pp. 5723–5735, 2009.

[15] M.S. Erkılınç, S. Pachnicke, H. Griesser, B.C. Thomsen, P. Bayvel, and R. Killey, "Performance comparison of single sideband direct detection Nyquist-subcarrier modulation and OFDM," in *J. Lightw. Technol.*, vol. 33, no. 10, pp. 2038–2046, 2015.

[16] J.G. Proakis and M. Salehi, *Digital communications*, 4^{th} edition, McGraw-Hill, 2008.

[17] D. Bykhovsky and S. Arnon, "An experimental comparison of different bit-and-power-allocation algorithms for DCO-OFDM," *J. Lightw. Technol.*, vol. 32, no. 8, pp. 1559–1564, 2014.

[18] E. Giacoumidis, A. Kavatzikidis, A. Tsokanos, J. Tang, and I. Tomkos, "Adaptive loading algorithms for IMDD optical OFDM PON systems using directly modulated lasers," *J. Optical Communications and Networking*, vol. 4, no. 10, pp. 769–778, 2012.

[19] X. Jin, J. Wei, R. Giddings, T. Quinlan, S. Walker, and J. Tang, "Experimental demonstrations and extensive comparisons of end-to-end real-time optical OFDM transceivers with adaptive bit and/or power loading," *IEEE Photon. Technol. Lett.*, vol. 3, no. 3, pp. 500–511, 2011.

[20] N. Liu, X. Chen, C. Ju, and R. Hui, "40-Gbps vestigial sideband half-cycle Nyquist subcarrier modulation transmission experiment and its comparison with orthogonal frequency division multiplexing," *Optical Engineering*, vol. 53, no. 9, pp. 096114–096114, 2014.

[21] M.S. Erkılınç, Z. Li, S. Pachnicke, H. Griesser, B.C. Thomsen, P. Bayvel, and R. Killey, "Spectrally-efficient WDM Nyquist-pulse-shaped 16-QAM subcarrier modulation transmission with direct detection," in *J. Lightw. Technol.*, vol. 33, no. 15, pp. 3147–3155, 2015.

[22] M. Erkılınç, S. Kilmurray, R. Maher, M. Paskov, R. Bouziane, S. Pachnicke, H. Griesser, B. Thomsen, P. Bayvel, and R. Killey, "Nyquist-shaped dispersion-precompensated subcarrier modulation with direct detection for spectrally-efficient WDM transmission," *Optics express*, vol. 22, no. 8, pp. 9420–9431, 2014.

[23] M.S. Erkılınç, M.P. Thakur, J. Mitchell, S. Pachnicke, H. Griesser, B.C. Thomsen, P. Bayvel, and R.I. Killey, "Spectrally-efficient WDM Nyquist-pulse-shaped subcarrier modulation using a dual-drive Mach-Zehnder modulator and direct detection," in *J. Lightw. Technol.*, pre-print, 2015.

[24] M. P. Thakur, M. C. Medeiros, P. Laurêncio, and J. E. Mitchell, "Optical frequency tripling with improved suppression and sideband selection," *Optics express*, vol. 19, no. 26, pp. B459–B470, 2011.

[25] M.S. Erkılınç, S. Pachnicke, H. Griesser, B.C. Thomsen, P. Bayvel, and R.I. Killey, "Spectrally-efficient single sideband 16-QAM Nyquist-subcarrier modulation-based WDM transmission using an InP dual-drive Mach-Zehnder modulator and direct-detection," in *Proc. IEEE European Conference on Optical Communication (ECOC)*, 2015, paper PA5.2.

[26] C. Davidson, C. Chen, M. Nissov, A. Pilipetskii, N. Ramanujam, H. Kidorf, B. Pedersen, M. Mills, C. Lin, M. Hayee, J.X. Cai, A.B. Puc, P.C. Corbett, R. Menges, H. Li, A. Elyamani, C. Rivers, and N.S. Bergano, "1800 Gb/s transmission of one hundred and eighty 10 Gb/s WDM channels over 7,000 km using the full EDFA C-band," in *Proc. IEEE/OSA Optical Fiber Communication Conference (OFC)*, 2000, paper PD25.

[27] G. Vareille, B. Julien, F. Pitel, and J.-F. Marcerou, "3.65 Tbit/s (365×11.6 Gbit/s) transmission experiment over 6850 km using 22.2 GHz channel spacing in NRZ format," in *Proc. IEEE European Conference on Optical Communication (ECOC)*, 2001, pp. 14–15.

[28] S. Bigo, Y. Frignac, G. Charlet, W. Idler, S. Borne, H. Gross, R. Dischler, W. Poehlmann, P. Tran, C. Simonneau, D. Bayart, G. Veith, A. Jourdan, and J.-P. Hamaide, "10.2 Tbit/s (256×42.7 Gbit/s PDM/WDM) transmission over 100 km Teralight fiber with 1.28 bit/s/Hz spectral efficiency," in *Proc. IEEE/OSA Optical Fiber Communication Conference (OFC)*, 2001, paper PD25.

[29] W. Idler, S. Bigo, Y. Frignac, B. Franz, and G. Veith, "Vestigial sideband demultiplexing for ultra high capacity (0.64 bit/s/Hz) transmission of 128×40 Gb/s channels," in *Proc. IEEE/OSA Optical Fiber Communication Conference (OFC)*, 2001, paper MM3.

[30] S. Bigo, A. Bertaina, Y. Frignac, S. Borne, L. Lorcy, D. Hamoir, D. Bayart, J.-P. Hamaide, W. Idler, E. Lach, B. Franz, G. Veith, P. Sillard, L. Fleury, P. Guénot, and P. Nouchi, "5.12 Tbit/s (128×40 Gbit/s WDM) transmission over 3×100 km of TeraLight fiber," in *Proc. IEEE European Conference on Optical Communication (ECOC)*, 2000, paper PD1.2.

[31] W. Idler, G. Charlet, R. Dischler, Y. Frignac, and S. Bigo, "0.8 bit/s/Hz of information spectral density by vestigial sideband filtering of 42.66 Gb/s NRZ," in *Proc. IEEE European Conference on Optical Communication (ECOC)*, 2002, paper 8.1.5.

[32] G. Charlet, S. Lanne, L. Pierre, C. Simonneau, P. Tran, H. Mardoyan, P. Brindel, M. Gorlier, J.-C. Antona, M. Molina, P. Sillard, J. Godin, W. Idler, and S. Bigo, "Cost-optimized 6.3 Tbit/s-capacity terrestrial link over 17×100 km using phase-shaped binary transmission in a conventional all-EDFA SMF-based system," in *Proc. IEEE/OSA Optical Fiber Communication Conference (OFC)*, 2003, paper PDP25.

[33] K. Schuh, E. Lach, B. Junginger, A. Klekamp, and G. Veith, "8×107 Gbit/s serial binary NRZ/VSB transmission over 480 km SSMF with 1 bit/s/Hz spectral efficiency and without optical equalizer," in *Proc. IEEE European Conference on Optical Communication (ECOC)*, 2007, pp. 1–2.

[34] J.-X. Cai, M. Nissov, C. Davidson, Y. Cai, A. Pilipetskii, H. Li, M. Mills, R.-M. Mu, U. Feiste, L. Xu, A.J. Lucero, D.G. Foursa, and N.S. Bergano, "Transmission of thirty-eight 40 Gb/s channels (> 1.5 Tb/s) over transoceanic distance," in *Proc. IEEE/OSA Optical Fiber Communication Conference (OFC)*, 2002, paper FC4-1.

[35] Y. Frignac, G. Charlet, W. Idler, R. Dischler, P. Tran, S. Lanne, S. Borne, C. Martinelli, G. Veith, A. Jourdan, J.-P. Hamaide, and S. Bigo, "Transmission of 256 wavelength-division and polarization-division-multiplexed channels at 42.7 Gb/s (10.2 Tb/s capacity) over 3x100km of Teralight fiber," in *Proc. IEEE/OSA Optical Fiber Communication Conference (OFC)*, 2002, paper FC5-1.

[36] D. Grosz, A. Agarwal, S. Banerjee, A. Kung, D. Maywar, A. Gurevich, T. Wood, C. Lima, B. Faer, J. Black, and C. Hwu, "5.12 Tb/s (128×42.7 Gb/s) transmission with 0.8 bit/s/Hz spectral efficiency over 1280 km of standard single-mode fiber using all-Raman amplification and strong signal filtering," in *Proc. IEEE European Conference on Optical Communication (ECOC)*, 2002, paper PD4.3.

[37] I. Morita, T. Tsuritani, N. Yoshikane, A. Agata, K. Imai, and N. Edagawa, "100% spectral-efficient 25×42.7 Gbit/s transmission using asymmetrically filtered CS-RZ signal and a novel crosstalk suppressor," in *Proc. IEEE European Conference on Optical Communication (ECOC)*, 2002, paper PD4.7.

[38] T. Ono, Y. Yano, K. Fukuchi, T. Ito, H. Yamazaki, M. Yamaguchi, and K. Emura, "Characteristics of optical duobinary signals in Terabit/s capacity, high-spectral efficiency WDM systems," *J. Lightw. Technol.*, vol. 16, no. 5, p. 788, 1998.

[39] H. Bissessur, G. Charlet, C. Simonneau, S. Borne, L. Pierre, C. De Barros, P. Tran, W. Idler, and R. Dischler, "3.2 Tb/s (80×40 Gb/s) C-band transmission over 3×100 km with 0.8 bit/s/Hz efficiency," in *Proc. IEEE European Conference on Optical Communication (ECOC)*, 2001, paper PD.M.1.11.

[40] M. Alfiad and S. Tibuleac, "100G superchannel transmission using 4×28 Gb/s subcarriers on a 25-GHz grid," *IEEE Photon. Technol. Lett.*, vol. 27, no. 2, pp. 157–160, 2015.

[41] Z. Li, X. Xiao, T. Gui, Q. Yang, R. Hu, Z. He, M. Luo, C. Li, X. Zhang, D. Xue, S. You, and S. Yu, "432-Gb/s direct-detection optical OFDM superchannel transmission over 3040-km SSMF," *IEEE Photon. Technol. Lett.*, vol. 25, no. 15, pp. 1524–1526, 2013.

[42] H. Chen, M. Chen, F. Yin, M. Xin, and S. Xie, "100Gb/s Polmux-NRZ-AOS-OFDM transmission system," *Optics Express*, vol. 17, no. 21, pp. 18768–18773, 2009.

[43] A. Dochhan, H. Grieser, M. Eiselt, and J.-P. Elbers, "Flexible bandwidth 448 Gb/s DMT transmission for next generation data center inter-connects," in *Proc. IEEE European Conference on Optical Communication (ECOC)*, 2014, paper P.4.10.

Chapter 5

The Implementation of Simplified (Polarization-Insensitive Single Balanced Photodetector) Coherent Receiver

The digital signal processing (DSP) based transmitters combined with direct detection receivers, shifting the complexity from optical to electrical domain, can be considered as the cost-effective optical transceiver architectures over access and metropolitan distances, as discussed in chapters 3 and 4. On the other hand, the highest channel bit rates and information spectral densities are achievable using the most advanced receiver type, a polarization- and phase-diverse coherent receiver. However, they are far from meeting the strict cost requirements of access and metro links, as discussed in chapter 1.

On the other hand, coherent receivers have several advantages compared to the direct detection receivers: (1) Multi-level modulation formats such as quadrature amplitude modulation (QAM) can be realized with lower required optical signal-to-noise ratio (OSNR) [1, Ch.3]. (2) In wavelength division multiplexed transmission, to select the channel of interest, arrayed waveguide grating (AWG) or Fabry-Perot filter is used in direct detection systems whereas a local oscillator (LO) laser and digital filter can be used to select the wavelength with high resolution. (3) It can convert an optical signal into an electrical signal without any loss of information. The optical amplitude and phase information can be linearly mapped into the electrical domain, which gives the ability to mitigate the channel impairments digitally at the receiver.

A single polarization direct detection (DD) receiver and a polarization- and phase-diverse coherent receiver with homodyne/intradyne reception are shown side by side in Fig. 5.1. It is not convenient to have no middle solution between these two receiver architectures since the complexity difference is vast, *i.e.,* a single-ended photodiode with a single analogue-to-digital converter (ADC) as opposed to a polarization beam splitter (PBS), two 90^{o} optical hybrids and 4 balanced photodetectors (BPDs) with 4 ADCs (see Fig. 5.1). To meet the increasing bandwidth demand, the spectral efficiency, receiver sensitivity and/or transmission distance offered by the DD receivers might be insufficient. On the other hand, the implementation of the coherent receiver with homodyne/intradyne reception is challenging in cost-effective applications. Therefore, alternative simplified coherent receiver designs, that are more cost-effective than the conventional coherent receivers offering better receiver sensitivities than a DD receiver, need to be investigated.

The simplification process of a coherent receiver from polarization- and phase-diverse to polarization-insensitive phase-diverse single BPD (simplified and cost-effective) coherent receiver is discussed in section 5.1. Following the discussion, the transceiver DSP stages to implement the simplified coherent

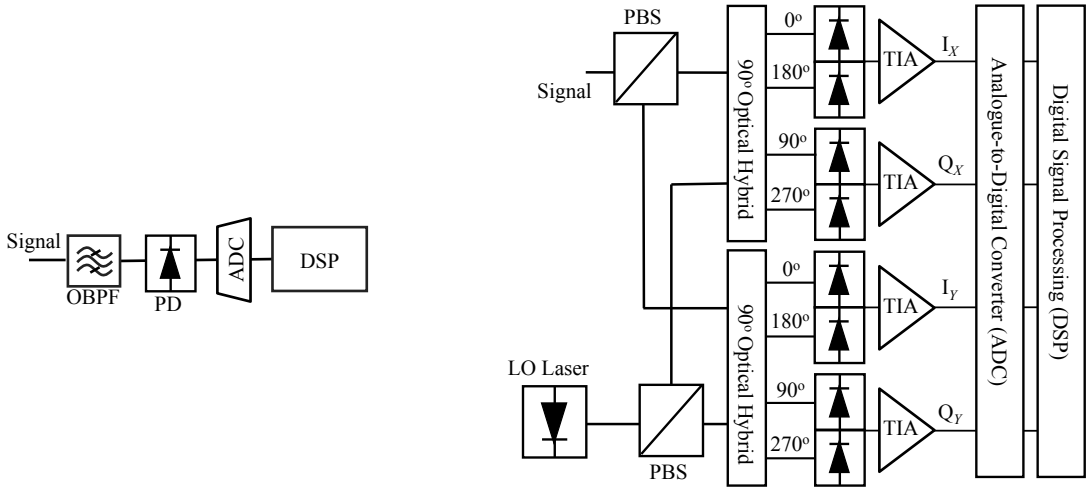

(a) (b)

Fig. 5.1: (a) Direct detection receiver. (b) Polarization- and phase-diverse coherent receiver with homodyne/intradyne reception.

receiver is explained in section 5.2. The experimental setup for the demonstration of the proposed coherent receiver is outlined in section 5.3. Finally, the numerical simulation and experimental results, including a performance comparison with the DD receiver, are presented in section 5.4.

5.1 Coherent receivers: From conventional homodyne to single balanced photodiode

The 90° optical hybrids can be removed from a coherent receiver utilizing heterodyne reception [2]. The in-phase (I) and quadrature (Q) components for both polarization states can be recovered digitally instead of using the optical hybrids, as shown in Fig. 5.2(a). Hence, heterodyne detection, as opposed to homodyne/intradyne detection, simplifies the coherent receiver architecture by enabling the use of 3dB couplers (180° optical hybrids) instead of 90° optical hybrids combined with two BPDs instead of four BPDs. Further discussions can be found in chapter 2.

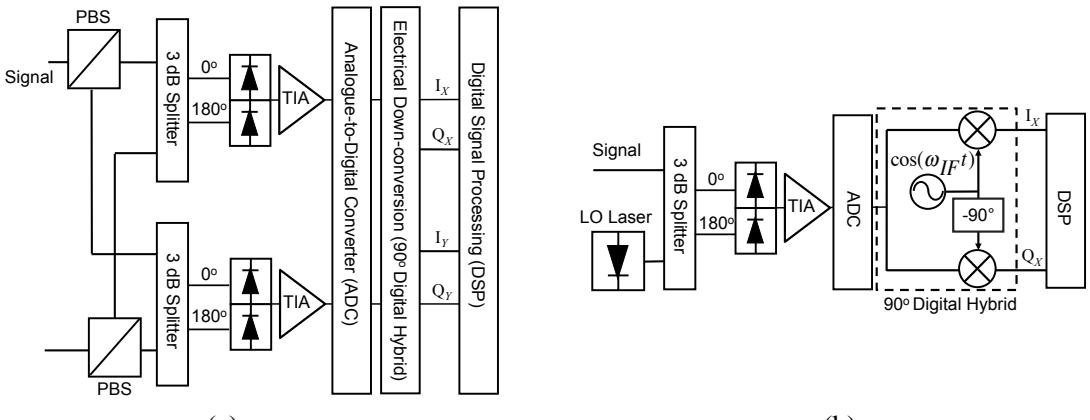

(a) (b)

Fig. 5.2: (a) Polarization- and phase-diverse coherent receiver and (b) polarization-insensitive phase-diverse (simplified) coherent receiver with heterodyne detection.

Unfortunately, this simplification comes at the price that the photodetectors and RF-components in the heterodyne case should have a bandwidth of at least twice the symbol rate ($2f_s$) [2]. Furthermore, homodyne/intradyne detection offers a 3 dB higher receiver sensitivity compared to the heterodyne detection. The reason is that the Q-component is detected in the optical domain in the homodyne case which provides 3 dB higher signal power gain compared to the LO shot-noise power [3]. A comparison for the polarization- and phase-diverse coherent receivers based on their detection technique is summarized in Tab. 5.1.

Tab. 5.1: Comparison of the pol.- and phase-diverse coherent receivers based on detection technique.

Coherent Detection Type	IF (GHz)	Minimum BPD bandwidth (GHz)	No. of BPDs and optical hybrid required
Homodyne	0	f_s	4 BPDs with 2×90° optical hybrids
Intradyne	±0.2	f_s	4 BPDs with 2×90° optical hybrids
Heterodyne	$> f_s$	$2f_s$	2 BPDs with 2×180° optical hybrids (3dB couplers)

From a cost and packaging point of view, the high optical complexity of a polarization diversity intradyne coherent receiver makes its full monolithic integration challenging, mainly due to the PBS integration. Thus, hybrid implementations (typically using free-space discrete optical components) are commonly employed [4–6]. To date, although there are few reported studies regarding the fully monolithically integrated polarization- and phase-diverse intradyne coherent receiver [7–9], they are not sufficiently mature and cost-effective for volume production. To remove the PBS from the coherent receiver, the detection needs to be independent from the state of polarization of the received signal, so-called polarization insensitive (PI). Otherwise, the system performance degrades significantly due to polarization rotation, *i.e.,* LO is not co-polarized, and hence, fails to recover the transmitted signal. If somehow polarization-insensitiveness is achieved for a phase-diverse coherent receiver, then the structure shown in Fig. 5.2(b) can be implemented. It can be achieved optically, which requires high complexity in the form of feedback loops for endless optical polarization tracking.

Previously demonstrated PI receivers have either incorporated a PBS in the receiver [10] or incorporated polarization scrambling at the transmitter [11]. The former solution, analytically investigated in [10], proposes a PI coherent receiver, consisting of a PBS, symmetric 3×3 optical coupler (a 120° optical hybrid) and three single-ended photodiodes with analog processing. A LO laser enters at 45° to a PBS, splitting it into two orthogonal components with the same amplitude, and the incoming signal is sent directly to one of the photodiodes. It has been experimentally demonstrated for 1.25 and 10 Gb/s long-reach wavelength division multiplexing (WDM) passive optical networks (PONs) using amplitude-shift keying (ASK) signalling over a transmission distance of 66 km of standard single mode fibre (SSMF) in [12] and [13], respectively. The main advantage of this low-cost receiver is that the signal can be demodulated using basic analogue processing requiring no DSP or ADC. However, the detection scheme is currently limited to ASK signalling. The latter scheme suggests employing a centralized polarization scrambling method in the transmitter that enables the PI coherent detection (requiring no polarization controller or PBS at the receiver). It requires a dual-polarization (DP) transmitter, where the symbol time slot is divided into two or more pairs and alternated states of polarization are transmitted in every bit [11]. Using a 3 dB coupler and a single BPD in the receiver, it has been demonstrated using a

1.25 Gb/s differential phase-shift keying (DPSK) signal, and transmitted over 50 km of SSMF at a channel spacing of 7.5 GHz [11]. Using the same technique with a 120^{o} optical hybrid and three single-ended photodiodes instead, the achieved bit rate at the same transmission distance was increased to 5 Gb/s using a differential quadrature phase-shift keying (DQPSK) signal at a 6.25 GHz channel spacing [14]. The polarization scrambling method successfully achieves the polarization-independent detection without requiring a PBS in the receiver, however, causes an intrinsic 6 dB sensitivity penalty in comparison to a DP signal.

Alternatively, polarization-time block coding (PTBC) can be applied to a DP orthogonal frequency division multiplexing (OFDM) signal at the transmitter side to gain resilience against polarization rotation as well as polarization dependent loss (PDL) [15]. Thus, by combining a PTBC scheme with the well-established principle of heterodyne coherent reception, a **PT!** (**PT!**) coherent receiver (shown in Fig. 5.2(b)) can be implemented while maintaining its frequency selectivity and linearity. It only consists of a 3 dB coupler and a single BPD, *i.e.,* no need for 90° optical hybrids and PBS at the optical front-end. Although only a single polarization can be detected using this receiver (halving the achievable bit rate compared to a dual-polarization signalling), a significant reduction in optical complexity (approximately 75%), whilst maintaining a high OSNR performance, potentially makes this coherent receiver design attractive. The next section describes the transceiver DSP of the PI (simplified and cost-effective) coherent receiver that is immune to polarization rotation without the requirement for polarization-diversity or optical polarization tracking unit at the receiver.

5.2 CO-OFDM (2×1 MISO) transceiver DSP

To achieve polarization diversity using a single BPD without tracking the state of polarization of the optical signal, two OFDM transmitters are required. Therefore, this transceiver architecture is also referred to as 2×1 *multi-input-single-output* (MISO) coherent OFDM (CO-OFDM), as it employs two transmitters and a single polarization receiver [16]. The transceiver DSP for the proposed system is described in sections 5.2.1 and 5.2.2 including the frequency offset (FO) correction and phase noise compensation (PNC), respectively.

5.2.1 CO-OFDM (2×1 MISO) transmitter DSP

Single-polarization direct detection optical OFDM (DDO-OFDM) signal waveform/frame generation was outlined previously in section 3.2.2 (see Fig. 3.17). To convert from single polarization (SP) to DP-OFDM, Alamouti coding which facilitates the PI simplified coherent receiver is incorporated, as shown in Fig. 3.17. The DP-OFDM signal was generated offline in MATLAB using a 512-point inverse fast Fourier transform (IFFT). 316 subcarriers were encoded using quadrature phase-shift keying (QPSK)/16-QAM symbols. Around the DC-component, 18 subcarriers were dropped to enable the FO correction and RF-aided PNC [17], which is discussed further in section 5.2.2. For OFDM frame synchronization, two highly-correlated OFDM symbols were inserted on the X-polarization to utilize the Schmidl and Cox algorithm [18], similar to the DDO-OFDM signal. However, when the Alamouti PTBC was applied, the synchronization symbols were also inserted on the Y-polarization to mitigate the possible fading on the X-polarization. 20 pair-wise training symbols after the synchronization symbols and four pair-wise periodic (every 34 data symbols) training symbols were used for channel estimation using the

zero-forcing method [15, 19]. Following the subcarrier mapping and upsampling with zero padding, the PTBC was applied to the orthogonal polarization states in the time domain, as explained in the following section. A cyclic prefix (CP) with 30 samples per symbol (5.18% overhead) was appended as a guard band to mitigate the chromatic dispersion. To utilize the DACs/ADC resolution efficiently, and consequently, optimize the OSNR performance, the OFDM waveforms were clipped down to various peak-to-average-power ratio (PAPR) values depending on the effective number of bits (ENOB) of the digital-to-analogue converters (DACs) (see section 5.4 for exact PAPRs). After removing the OFDM overheads, the total net bit rate was chosen to be 10.7 and 21.4 Gb/s for QPSK and 16-QAM signalling, assuming a 7% overhead allowing for a hard-decision forward error correction (HD-FEC) correcting a bit error rate (BER) of 4×10^{-3} to below 10^{-15}.

Compared to the DDO-OFDM signal waveform, there is no need to up-convert the baseband OFDM signal (no optical guard band required between the optical carrier and sideband) in coherent reception since the signal-signal mixing products are removed by the balanced detection, as discussed in section 2.3.2. Additionally, high power optical carrier, that enables recovery of the OFDM signal in direct detection links, is not required either since a LO laser is mixed with the transmitted signal at the receiver. Therefore, the modulator is commonly biased (almost) at its null point unlike DDO-OFDM. However, coherent reception is sensitive to FO [20] changes and laser phase noise [17, 21], and thus, they need to be managed.

As discussed in section 2.3.3, the state of polarization of the transmitted signal and LO laser should be co-polarized for optimum receiver sensitivity performance in coherent detection. Otherwise, polarization rotation severely degrades the performance in an optical link. To achieve PI coherent detection with heterodyne reception using a single BPD without any optical polarization tracking unit or PBS, the OFDM symbols need to be encoded in such a way that they can be detected regardless of the state of polarization of the transmitted signal. This is achieved through Alamouti PTBC.

5.2.1.1 Alamouti polarization-time block coding (PTBC)

In wireless communications, using two-transmit/one receive antenna architecture has been shown possible through a space-time block coding, known as Alamouti coding [22]. This half-rate, orthogonal block coding scheme (two time-slots in two spatial dimensions) replicates the transmitted symbols exactly once, in such a way to enable the recovery of both symbols from a block of transmitted symbols.

Drawing an analogue between the two polarization modes and two transmit antennae, referred to as polarization-time block coding (PTBC), it has been adapted to optical communication to compensate PDL in (ultra) long-haul coherent optical systems using 2×2 *multi-input-multi-output* (MIMO)-OFDM [23, 24] systems. Alamouti PTBC can be also utilized in a 2×1 MISO system to simplify the polarization- and phase-diverse coherent receiver structure.

To realize the Alamouti PTBC, two transmitters, one for each polarization, are required. In a conventional DP system, the OFDM symbols on X- ($E_x = [s_{x1}, s_{x2}, \cdots, s_{xM}]$) and Y-polarization modes ($E_y = [s_{y1}, s_{y2}, \cdots, s_{yM}]$), are decorrelated. However, the key idea of Alamouti PTBC is to use the channel twice during two symbol duration. Therefore, the OFDM symbols are grouped into pairs. In the first time slot t, s_{x1} and $s_{y1} = s_{x2}$ are sent whereas in the second time slot $2t$, $-s_{x2}^*$ and $s_{y2} = s_{x1}^*$ are sent on X- and Y-polarization modes, respectively, as shown in Fig. 5.3. On two orthogonal polarization modes ($[E_x \quad E_y]^T$ where T is the transpose of a vector), the two consecutive OFDM symbol pairs ($[s_{x1} \quad s_{x2}]^T$

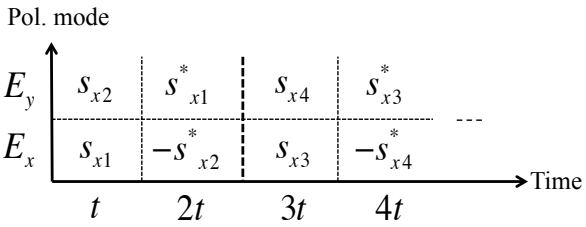

Fig. 5.3: Illustration of Alamouti coding for a DP-OFDM signal.

and $[-s^*_{x2} \quad s^*_{x1}]^T$) are mutually orthogonal as can be seen from their inner product, given by

$$[s_{x1} \quad s_{x2}][-s^*_{x2} \quad s^*_{x1}]^H = -s_{x1}s_{x2} + s_{x2}s_{x1} = 0, \tag{5.1}$$

where H represents the Hermitian transpose. For simplicity, assuming only one symbol pair is sent, the received symbols on X- and Y-polarization modes ($[E^{'}_x \quad E^{'}_y]^T$) can be written as follows:

$$\begin{bmatrix} E^{'}_x \\ E^{'}_y \end{bmatrix} = \mathbf{H} \begin{bmatrix} E_x \\ E_y \end{bmatrix} = \begin{bmatrix} h_{xx} & h_{xy} \\ h_{yx} & h_{yy} \end{bmatrix} \begin{bmatrix} s_{x1} & -s^*_{x2} \\ s_{x2} & s^*_{x1} \end{bmatrix}, \tag{5.2}$$

where $\mathbf{H}$ is the transfer function of linear and noiseless channel response describing the polarization effects. Since only one polarization of the received signal, say $E^{'}_x$, can be co-polarized with the LO laser using the PI coherent receiver, the received symbol pairs can be written as follows:

$$s^{'}_{x1} = h_{xx}s_{x1} + h_{xy}s_{x2} \tag{5.3a}$$

$$s^{'}_{x2} = -h_{xx}s^*_{x2} + h_{xy}s^*_{x1}. \tag{5.3b}$$

To recover the two transmitted consecutive OFDM symbols on the X-polarization (s_{x1} and s_{x2}), both sides of Eq.5.3b are conjugated (Eq.5.3a remains unchanged) and can be re-written in matrix form as follows:

$$\begin{bmatrix} s^{'}_{x1} \\ s^{'*}_{x2} \end{bmatrix} = \begin{bmatrix} h_{xx} & h_{xy} \\ h^*_{xy} & -h^*_{xx} \end{bmatrix} \begin{bmatrix} s_{x1} \\ s_{x2} \end{bmatrix} \tag{5.4}$$

Using zero-forcing criteria, the transmitted symbols can be written as follows:

$$\begin{bmatrix} s_{x1} \\ s_{x2} \end{bmatrix} = \begin{bmatrix} h_{xx} & h_{xy} \\ h^*_{xy} & -h^*_{xx} \end{bmatrix}^{-1} \begin{bmatrix} s^{'}_{x1} \\ s^{'*}_{x2} \end{bmatrix}. \tag{5.5}$$

Due to the orthogonality of $[h_{xx}\, h_{xy}]$ and $[h^*_{xy} \; -h^*_{xx}]$ as shown in Eq.5.5, $\mathbf{H}^H\mathbf{H}$ =-det($\mathbf{H}$)$\mathbf{I}$ where det($\mathbf{H}$) is equal to the determinant of a 2-by-2 matrix $\mathbf{H}$ and $\mathbf{I}$ is the identity matrix. Therefore, even though a single polarization is detected, the system performance is independent of any polarization rotation [15] so that there is no need for polarization tracking. Same method can also be used to mitigate PDL, as demonstrated in [24,25]. However, since the Alamouti coding is a half-rate coding scheme (sending two uncorrelated symbols $[s_{x1} \quad s_{x2}]^T$ and their Alamouti-coded pairs $[-s^*_{x2} \quad s^*_{x1}]^T$ instead of transmitting four uncorrelated symbols on X- and Y-polarization modes, as illustrated in Fig. 5.3), it comes at the cost of at least 3 dB sensitivity penalty compared to a DP-OFDM signal operating at the same bit rate.

5.2.2 CO-OFDM (2×1 MISO) receiver DSP

The receiver DSP of the CO-OFDM signal for 2×1 MISO system is shown in Fig. 5.4. As discussed before, the received signal is down-converted digitally to obtain I- and Q-components in this scheme. Since the desired signal is the signal-LO beating, the FO correction, and subsequently, PNC needs to be applied after OFDM frame synchronization, as discussed in section 2.3.3. Following this stage, the receiver DSP blocks for the Alamouti-coded OFDM signal are almost the same for the DDO-OFDM signal, as described in 3.2.2. The only difference is that the received Alamouti-coded OFDM symbols should be decoded in the same manner that they are encoded (see section 5.2.1.1 for Alamouti encoding) at the channel estimation stage.

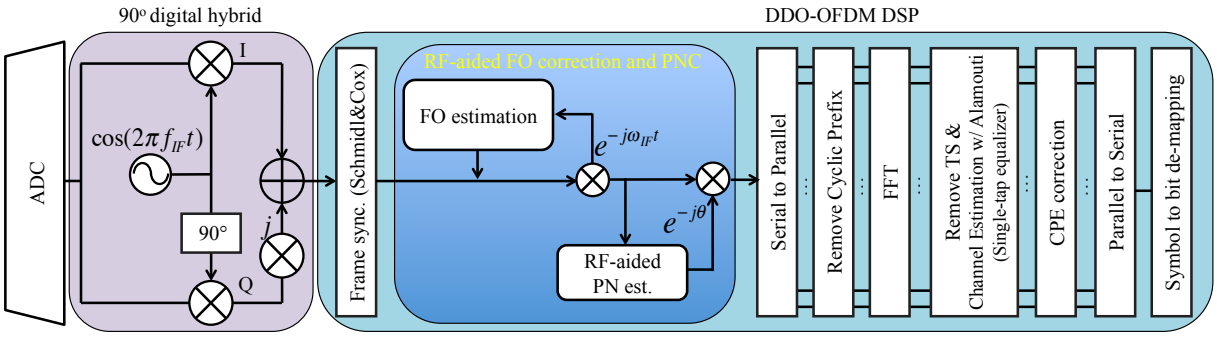

Fig. 5.4: The offline receiver DSP for the CO-OFDM (2×1 MISO) signal. RF-aided FO correction and PNC are discussed in section 5.2.2.1. DDO-OFDM DSP is explained in section 3.2.2.

5.2.2.1 Frequency offset (FO) correction and phase noise compensation (PNC)

In intradyne and heterodyne reception, the wavelength difference between the transmitter and LO laser causes a frequency offset upon photodetection. If the offset is not corrected, the required RF bandwidth of the electrical components increases by the amount of the offset and the subcarriers overlapping with the LO have poorer performance due to direct down-conversion DC leakage. In addition to the frequency offset, the combined linewidth of the transmitter and LO laser is translated into phase noise after detection. The phase noise of the lasers used in coherent optical systems has a big impact on the performance [26], and hence, needs to be compensated.

Generally speaking, lasers are assumed to have Lorentzian power spectral density [27]. Therefore, the phase noise is assumed to be a Wiener process, implying that it is a Gaussian process [28]. Phase noise adds uncertainty in phase, leading to a time varying phase component which causes a symbol rotation and inter-channel interference (ICI), as can be seen in the inset (d) of Fig. 5.5 (blue points). In CO-OFDM systems, it has been shown that data-aided PNC results in poor performance [29] and, frequency domain pilot-assisted PNC still requires a very low linewidth, *e.g.,* 20 kHz. Thus, in this thesis, RF-pilot aided phase noise compensation (PNC) is utilized [17].

An RF-pilot tone is inserted where the null subcarriers are placed by biasing the modulator with the required optical carrier-to-signal power ratio (CSPR), as shown in the inset (a) of Fig. 5.5. There is no extra optical bandwidth or hardware required for RF-pilot tone insertion. However, a few subcarriers around the DC value should be dropped at the bit-to-symbol mapping stage, referred to as null subcarriers, as discussed in section 5.2.1. The number of null subcarriers depends on the linewidth of the transmitter and LO laser, *i.e.,* 8 subcarriers for a total linewidth of 200 kHz (approximately equal to the

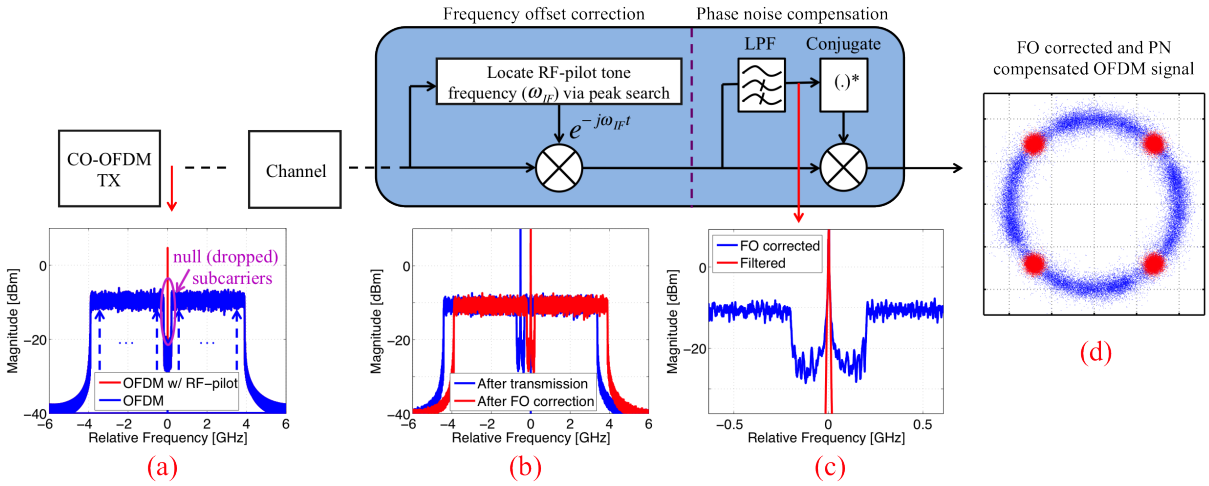

Fig. 5.5: The implementation of RF-pilot tone aided FO correction and PNC. The electrical spectrum of the (a) transmitted signal with RF-pilot tone, (b) received and FO corrected signal, (c) low-pass filtered signal for PNC (zoomed version). (d) The received constellations with and without PNC. Note that the frequency values are relative to the optical carrier frequency.

sum of transmitter and LO linewidth). Since the RF-pilot-tone is distorted by the phase noise in exactly the same way as the CO-OFDM signal, it can be used to invert the phase distortions.

The RF pilot-tone appears as an intermediate frequency (IF) due to the frequency difference between the transmitter and LO laser, *i.e.,* 500 MHz as shown in the inset (b) of Fig. 5.5. First, the tone at a frequency of ω_{IF} is located via a peak search, and subsequently, used for FO correction by multiplying the signal with $e^{-j\omega_{IF}t}$. The FO corrected signal is then filtered out using a low-pass filter (LPF) to separate the tone from the received signal, as shown in the inset (c) of Fig. 5.5. The bandwidth of the LPF depends on the linewidth of the laser, *i.e.,* 5^{th}-order Butterworth LPF with a bandwidth of 1 MHz for a linewidth of 200 kHz. To mitigate the random phase rotations due to phase noise, the filtered signal is first conjugated, and then, multiplied with the received signal. The received constellation with and without PNC are shown in the inset (d) of Fig. 5.5.

5.3 Experimental setup and simulation model for CO-OFDM (2×1 MISO) system

The experimental configuration is shown in Fig. 5.6 along with the transmitted optical spectrum (an optical bandwidth of 8 GHz for a single channel) and received electrical spectrum. Note that the received electrical signal is real-valued in heterodyne detection, and thus, it is a double sideband signal. This results in the requirement to have a channel spacing of at least twice the signal bandwidth, which is further discussed in section 5.4.2. The signal waveforms were generated offline in MATLAB and uploaded to two 12 GSa/s arbitrary waveform generators (AWGs). The identical waveforms were also used in numerical simulations as well. In the experiment, four electrical signals (X_I, X_Q, Y_I and Y_Q), generated by the AWGs with 8-bit nominal resolution (ENOB of 5-bit at 6 GHz and a 3 dB bandwidth of 6 GHz), were filtered by the LPFs with a bandwidth of 5.5 GHz, and then used to drive the modulator. The Y-polarization was ignored in SP-OFDM case. In ideal simulations, the nominal and ENOB of the DACs were both assumed to be 8 bits, whereas in practical simulations, the actual ENOB of the DACs was modeled by adding additive white Gaussian noise (AWGN) to the 8-bit quantized electrical waveforms

to obtain the experimental signal-to-noise ratio (SNR). Moreover, the LPFs were modeled as 8th-order Bessel LPFs at the same bandwidth.

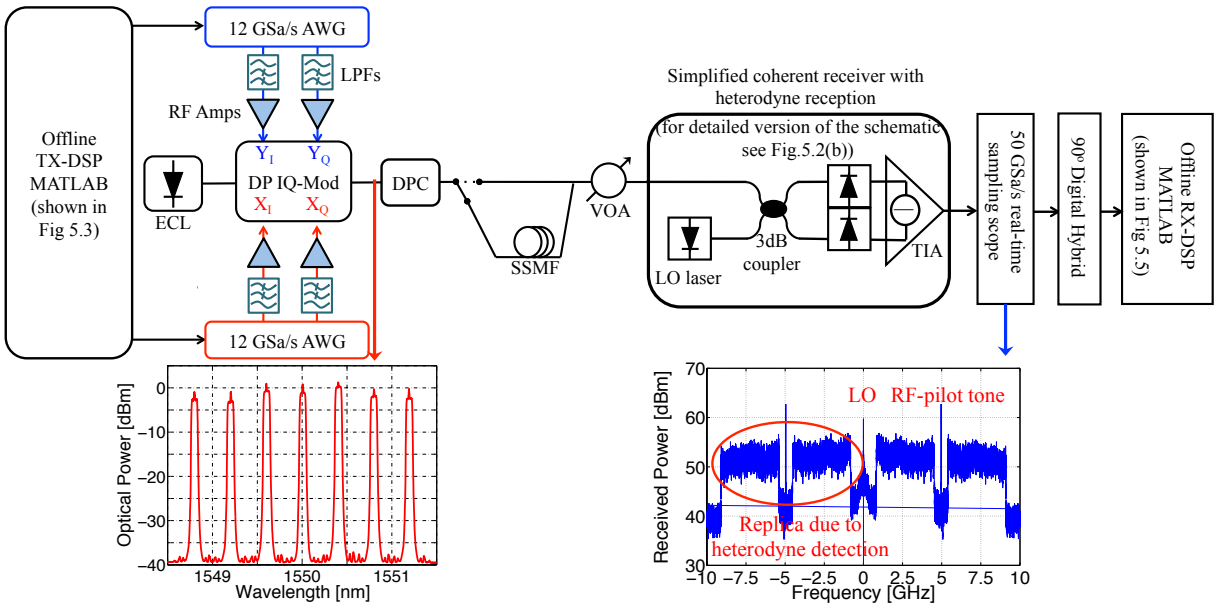

Fig. 5.6: The experimental setup for the CO-OFDM signal. Insets: Transmitted Alamouti-coded OFDM signal spectrum with a channel spacing of 50 GHz at a resolution of 0.01 nm (left) and received electrical spectrum (right). The offline transmitter and receiver DSP are described in sections 5.2.1 and 5.2.2. DPC: Digital polarization controller.

An external cavity laser (ECL) at 1550 nm (100 kHz linewidth) was used as an optical source for the integrated DP IQ-modulator. The optical carrier (used as a RF-pilot tone) for the DP-OFDM signal was added on only the X-polarization (linearly polarized RF-pilot tone) by biasing the modulator just above its null point to obtain a CSPR of approximately -10 dB. However, it was added to both polarization states (circularly polarized RF-pilot tone) when Alamouti PTBC was applied, maintaining the total CSPR $\leq$-9 dB. Otherwise, the pilot tone could not be detected due to 90^{o} polarization rotation (when the polarization states are completely swapped), and hence, both FO correction and PNC fail. In numerical simulations, the DP IQ-modulator was assumed to be linear. The impact of different CSPR values on the BER performance of the system and its optimization is discussed in section 5.4.

To evaluate and compare the resilience of the DP, SP and Alamouti-coded OFDM signals to polarization rotation, a digitally-operated polarization controller (DPC) was used to rotate the signal over the full Poincaré sphere. The back-to-back performance assessment for the DP, SP and Alamouti-coded OFDM signals was carried out using heterodyne reception. The transmitted DP-OFDM signal was detected using the heterodyne receiver configuration shown in the inset (a) of Fig. 5.2 whereas SP- and Alamouti-coded OFDM signals were detected using the receiver architecture depicted in Fig. 5.6.

The LO laser wavelength was set to 1549.95 nm, yielding an IF of 5.1 GHz. After the signal was digitized using a single ADC (50 GSa/s sample rate, 23 GHz 3 dB bandwidth, 5-bit ENOB at 10 GHz), the received electrical signal was down-converted to obtain I- and Q-baseband signals. After fast Fourier transform (FFT) window synchronization using the Schmidl and Cox algorithm, the FO was estimated and corrected via a peak search utilizing the RF-pilot tone method, as discussed in section 5.2.2.1. Subsequently, PNC was also achieved via the RF-pilot tone using a 5th-order Butterworth LPF with a bandwidth of 500 kHz [17]. Following the CP removal and applying an FFT, the channel estimation for SP- and

DP-OFDM signal was achieved using a zero-forcing equalizer with training symbols. In the Alamouti coding case, the received and transmitted training symbols were first divided into 2 space-time blocks, similar to the encoding stage before applying the equalizer. The BER was computed by error counting over 2^{19} bits.

5.4 Results and discussion

5.4.1 CSPR optimization for phase noise compensation in simulations

As discussed earlier, FO correction and PNC were achieved utilizing the RF-pilot tone method. To determine the optimum optical carrier-to-signal power ratio (CSPR), the back-to-back BER performance of a DP-OFDM signal operating at net bit rate of 21.4 Gb/s was assessed using a polarization- and phase-diverse coherent receiver with heterodyne reception. Firstly, to quantify the penalty due to the overheads (CP and training symbols), ideal simulations were carried out considering no quantization noise, no electrical/optical filtering effect and no phase noise. An OSNR penalty of 0.3 dB was observed at the HD-FEC threshold BER of 4×10^{-3} (assuming a 7% overhead), as shown in Fig. 5.7.

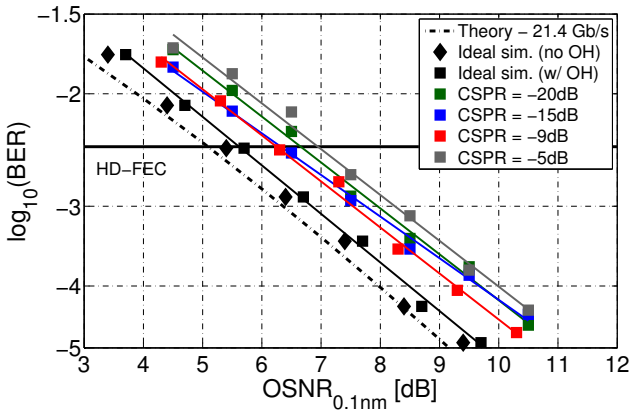

Fig. 5.7: BER vs OSNR for DP-OFDM signal operation at 10.7 Gb/s. OH: overhead.

Following this, FO and phase noise were taken into account to determine the optimum CSPR value. CSPR is defined in Eq.4.1. For low CSPR values, amplified spontaneous emission (ASE) noise limits the amount of mitigated phase noise whereas the OSNR of the OFDM signal becomes too low at high CSPR values. Therefore, there exists an optimum CSPR value, which gives the lowest possible BER at each OSNR level. The penalty due to phase noise decreases from a CSPR of -20 to -15 dB. However, the system is not able to achieve the optimum performance at high OSNR levels (blue curve in Fig. 5.7). Moreover, when the CSPR is increased to -5 dB, significant penalty is observed. Based on these results, the optimum CSPR value was found to be -9 dB. Phase noise was successfully compensated with an approximately 0.7 dB OSNR penalty when QPSK signalling is considered, which was also observed in [30].

5.4.2 Back-to-back assessment of Alamouti-coded OFDM signal with simplified coherent receiver

The back-to-back performance of Alamouti-coded OFDM QPSK/16-QAM signal formats operating at 10.7 Gb/s and 21.4 Gb/s was assessed using the simplified PI coherent receiver, as shown in Fig. 5.6. The results are presented in Fig. 5.8. To quantify the OSNR penalty due to only Alamouti coding, DP-OFDM back-to-back performance, simulated using a polarization- and phase-diverse coherent receiver

with heterodyne reception, was also shown in the same figure. As indicated in the previous section, the OSNR penalties due to the overheads and PNC were found to be 0.3 dB and 0.7 dB for the QPSK signal, respectively. The penalty due to PNC increased to 1.6 dB for 16-QAM signal. Note that the optimum CSPR value for 16-QAM was found to be -9 dB as well. Such a penalty is expected since 16-QAM signalling is more susceptible to phase noise, as its constellation has denser symbol spacing than QPSK. The required OSNR values were found to be 7.5 dB and 14 dB for QPSK and 16-QAM formats in ideal simulations, as shown with red solid lines in Fig. 5.8. The additional 0.5 dB OSNR penalty was observed due to Alamouti-coding since an extra ∼3 dB carrier power needs to be inserted on Y-polarization to achieve PNC successfully in the case of 90^o polarization rotation.

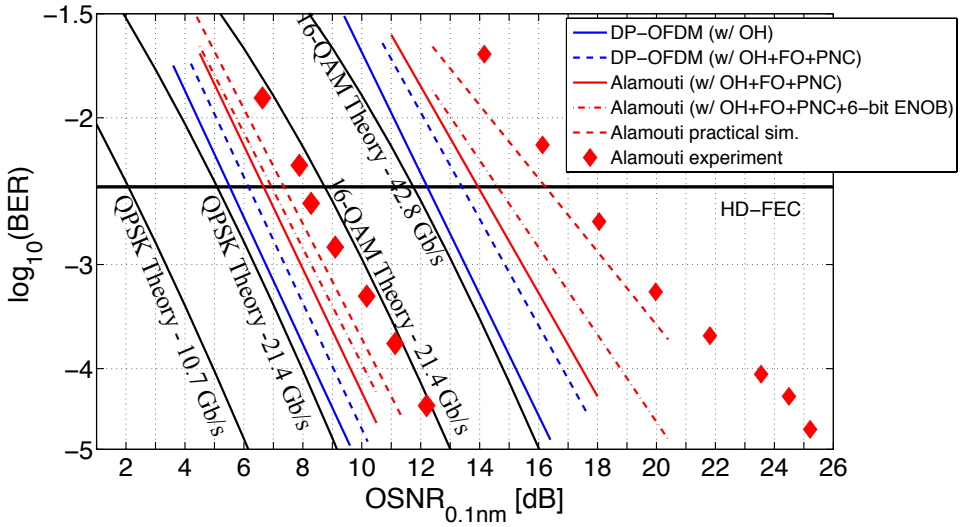

Fig. 5.8: BER vs OSNR performance of single channel DP- and Alamouti-coded OFDM signals using QPSK and 16-QAM formats.

Furthermore, practical simulations were carried out to determine the OSNR penalty due to the DACs' quantization noise. To utilize the DACs' resolution efficiently, and consequently, achieve the optimum performance at an ENOB of 5 and 6 bits resolution, the Alamouti-coded OFDM QPSK signal waveforms were clipped from approximately 15 dB to 7 dB and 9 dB, while, for 16-QAM signal, these values were set to be 9 dB and 11 dB, respectively. No significant penalty was seen for the QPSK format at an ENOB of 6 bit whereas 0.5 dB OSNR penalty was observed for the 16-QAM format, as can be seen from Fig. 5.8. At an ENOB of 5-bit, the ENOB of the DACs used in the experiment, OSNR penalties of 0.4 dB and 1.3 dB were observed. Finally, the simulated system was demonstrated experimentally, in which the required OSNR values for QPSK and 16-QAM formats were measured to be approximately 8 dB and 17 dB. Compared to the theory, the total penalties for the Alamouti-coded OFDM QPSK and 16-QAM signal formats were measured to be approximately 6 dB and 8 dB due to the aforementioned penalties plus 3 dB penalty due to the Alamouti half-rate coding. However, the simplified coherent receiver has 7 dB lower loss than a polarization- and phase-diverse coherent receiver due to the removal of the 90^o optical hybrids and PBS. This provides a 7 dB higher receiver sensitivity gain, as demonstrated in [31] which is crucial if this receiver architecture is considered for long-reach passive optical networks (LR-PONs).

Following the back-to-back characterization, the WDM performance of the proposed simplified coherent receiver was assessed. The channel spacing was varied from 100 GHz to 18 GHz. No significant OSNR penalty was observed at a channel spacing of 20 GHz or above, as shown in Fig. 5.9(a). The

penalties increased to 0.5 dB and 2.5 dB at a channel spacing values of 19 GHz and 18 GHz, respectively. From 18 GHz and below, the received channels start overlapping with each other, causing severe performance degradation. The BERs with respect to OSNR for single channel and 19 GHz-spaced WDM system are also shown in Fig. 5.9(b) in which no performance difference is observed, as expected. It is worth noting that the LO laser and a digital filter were used to select the channel of interest with high resolution, to be detected by the coherent receiver, whereas an optical band-pass filter (OBPF) was required in the direct detection case.

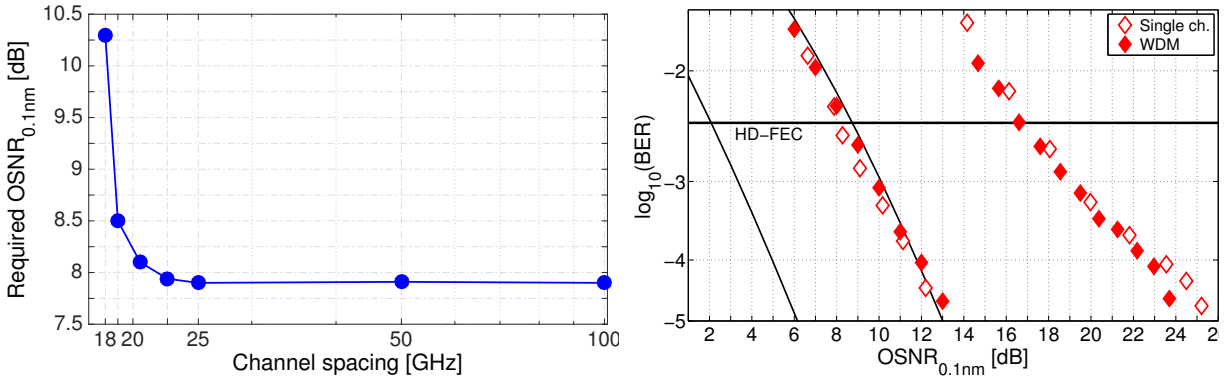

(a) (b)

Fig. 5.9: (a) The required OSNR with respect to channel spacing. (b) Single channel and WDM BER vs OSNR performance of Alamouti-coded OFDM signal using QPSK and 16-QAM formats.

5.4.3 The resilience to polarization rotation

To assess the SP-, DP- and Alamouti-coded OFDM signals' tolerance to polarization rotation, 625 equally-spaced polarization states over the Poincaré sphere were measured and the BER distribution is plotted in Fig. 5.10. Note that the DP-OFDM signal measurements were taken using the coherent receiver shown in Fig. 5.2(a) whereas SP- and Alamouti-coded OFDM signal performance was assessed using the experimental setup, as shown Fig. 5.6.

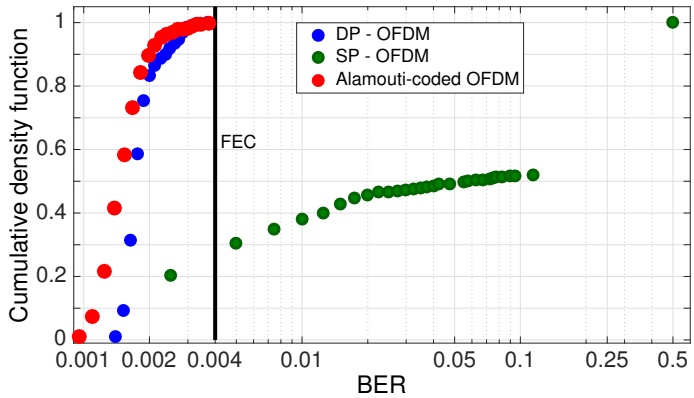

Fig. 5.10: The error probability density of SP-, DP- and Alamouti-coded OFDM signals versus BER.

The DP-OFDM signal achieved an average BER of 1.8×10^{-3} at an OSNR of 8.5 dB. The Alamouti-coded OFDM signal also successfully achieved an average BER of 1.6×10^{-3} at an OSNR of 9 dB. In contrast, 50% of the received SP-OFDM signals failed to achieve a BER below the HD-FEC threshold using the proposed PI coherent receiver. In other words, the state of polarization of the signal and LO were not sufficiently aligned 50% of the time, as expected. On the other hand, the Alamouti-coded

OFDM signal can be completely recovered regardless of any polarization rotation on Poincaré sphere due to the transmission of two consecutive OFDM symbols on orthogonal polarization states, as discussed in section 5.2.1.1.

Tab. 5.2: BERs in 625 polarization states, rotated over the full Poincaré sphere. The OSNR values for the SP-, DP-, and Alamouti-coded OFDM signal formats were chosen as 5.3 dB, 8.6 dB, and 9.2 dB, respectively.

Signal / BER	DP-OFDM	SP-OFDM	Alamouti-coded OFDM
worst case	3.6×10^{-3}	0.5	4×10^{-3}
best case	1×10^{-3}	1.5×10^{-3}	1×10^{-3}
mean	1.8×10^{-3}	0.22	1.6×10^{-3}

5.5 Performance comparison of direct detection and PI (simplified) coherent receiver

In this section, the Alamouti-coded OFDM signal measurements presented in this chapter and the single sideband (SSB) Nyquist-subcarrier modulation (SCM) experimental results (using the direct detection receiver), shown in the previous chapter, are compared. The experimental results for the PI coherent receiver were taken at a bit rate of 10.7 Gb/s due to the experimental limitations. Therefore, in order to make a fair comparison, the Alamouti-coded OFDM measurements were scaled to 14 Gb/s as follows:

$$s(\text{dB}) = -10\log_{10}(10.7/14) \tag{5.6}$$

where s is the scaling factor and found to be 1.168 dB using Eq.5.6 at an OSNR resolution of 0.1 nm.

The back-to-back performance of the receivers using QPSK and 16-QAM signalling for the single channel case is shown in Fig. 5.11. For QPSK signalling, there is no significant OSNR performance difference observed between the direct detection and PI coherent receiver. However, the coherent receiver outperforms the direct detection receiver by an OSNR of 4.5 dB when the modulation format is switched to 16-QAM. The reason is that the coherent receiver does not suffer from signal-signal beating interference (SSBI) as the beating terms are removed by the balanced detector. Note that this difference can be substantially reduced through the use of SSBI compensation in the receiver DSP in the case of direct detection systems. In the direct detection case, the optical carrier is added to the signal at the transmitter and sent over the fibre in order to receive the transmitted signal with a sufficient SNR for successful demodulation. To achieve this, the CSPR needs to be significantly higher than the signal power, as discussed extensively in chapter 4. It is worth noting that the optical carrier for the coherent receiver is only used for PNC, and hence, its required power is much lower (approximately -9 dB) than the transmitted signal, as discussed in section 5.4.1.

5.6 Summary

Coherent detection provides a full optical field recovery, which is linearly translated into the digital domain by ADCs. However, the complexity of a polarization- and phase-diverse coherent receiver is not suitable for cost-effective transceiver designs for metropolitan links. Therefore, the implementation of a

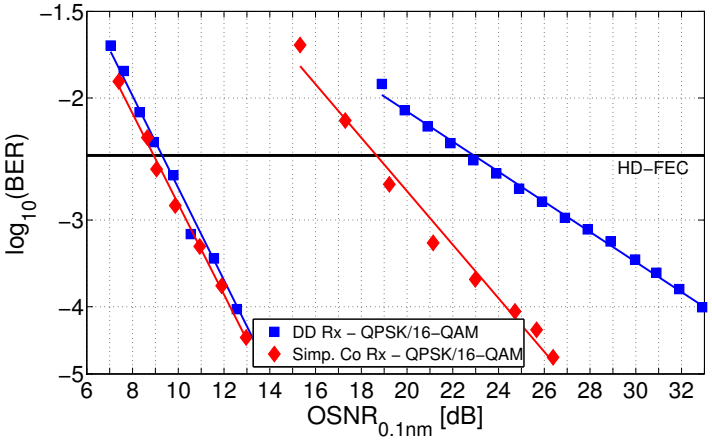

Fig. 5.11: BER vs OSNR performance of direct detection (DD) and PI (simplified) coherent receiver using SSB Nyquist-SCM and Alamouti-coded OFDM QPSK/16-QAM formats.

polarization insensitive (PI) (simplified) coherent receiver that utilizes Alamouti PTBC and heterodyne detection was assessed in this chapter. The key results of this work are as follows:

- The complexity of a conventional coherent receiver can be significantly reduced, consisting of a 3 dB coupler and single BPD, utilizing Alamouti-coded OFDM signal and heterodyne detection. However, the transmitter complexity doubles compared to the direct detection transmitter.

- Half of the OFDM symbols carry redundant data so that the achievable bit rate is halved compared to a DP-OFDM signal and receiver sensitivity decreases by 3 dB due to heterodyne detection. Despite such penalties, the back-to-back performance of the PI coherent receiver starts outperforming the direct detection receiver performance at high order M-QAM formats where $M \geq 16$. Direct detection system performance degrades significantly due to the SSBI (assuming the SSBI is not compensated), whereas it is removed by the balanced detector in the PI coherent receiver.

- The proposed transceiver architecture can be an attractive approach for access and metro applications. In particular, it can be very practical for LR-PONs due to its higher receiver sensitivity, since the main concern is the optical network unit (receiver side) complexity in access networks.

5.7 References

[1] I. Kaminow, T. Li, and A. E. Willner, *Optical fiber telecommunications VB: Systems and networks*, Academic press, 2010.

[2] E. Ip, A. P. T. Lau, D. J. Barros, and J. M. Kahn, "Coherent detection in optical fiber systems," *Optics Express*, vol. 16, no. 2, pp. 753–791, 2008.

[3] J. R. Barry and J. M. Kahn, "Carrier synchronization for homodyne and heterodyne detection of optical quadrature phase-shift keying," *J. Lightw. Technol.*, vol. 10, no. 12, pp. 1939–1951, 1992.

[4] L.E. Nelson, X. Zhou, R. Isaac, Y.-M. Lin, J. Chon, and W.I. Way, "Colorless reception of a single 100Gb/s channel from 80 coincident channels via an intradyne coherent receiver," *Proc. IPC*, 2012, paper TuE4.

[5] A. Beling, N. Ebel, A. Matiss, G. Unterbörsch, M. Nölle, J.K. Fischer, J. Hilt, L. Molle, C. Schubert, F. Verluise and L. Fulop, "Fully-integrated polarization-diversity coherent receiver module for 100G DP-QPSK," *Proc. OFC*, 2011, paper OML5.

[6] M. Schell, H.G. Bach, K. Janiak, N. Keil, M. Möhrle, P. Runge, and Z. Zhang, "Coherent receiver photonic integrated circuits," *Proc. OFC*, 2013, paper OW3J.6.

[7] C.R. Doerr, L.L. Buhl, Y. Baeyens, R. Aroca, S. Chandrasekhar, X. Liu, L. Chen, and Y.-K. Chen, "Packaged monolithic silicon 112-Gb/s coherent receiver," *IEEE Photon. Technol. Lett.*, vol. 23, no. 12, pp. 762—764, 2011.

[8] C.R. Doerr, P.J. Winzer, Y.-K. Chen, S. Chandrasekhar, M.S. Rasras, L. Chen, T.-Y. Liow, K.-W. Ang, and G.-Q. Lo, "Monolithic polarization and phase diversity coherent receiver in silicon," *J. Lightw. Technol.*, vol. 28, no. 4, pp. 520–525, 2010.

[9] R. Zhang, P. Runge, G. Zhou, R. Gan and R. Klotzer, D. Pech, H.-G. Bach, D. Perez-Galacho, A. Ortega-Murnox, R. Halir, and I. Molina-Fernandez, "56Gbaud DP-QPSK receiver module with a monolithic integrated PBS and 90^{o} hybrid InP chip," in *26th Int.'l Conf. on InP and Related Materials*, 2014, paper We-B1-4.

[10] E. Ciaramella, "Polarization-independent receivers for Low-Cost Coherent OOK Systems," *IEEE Photon. Technol. Lett.*, vol. 26, no. 6, pp. 548—551, 2014.

[11] I.N. Cano, A. Lerín, V. Polo, and J. Prat, "Polarization independent single-PD coherent ONU receiver with centralized scrambling in udWDM-PONs," in *Proc. ECOC*, 2014, P.7.12.

[12] M. Presi, F. Bottoni, R. Corsini, G. Cossu, and E. Ciaramella, "All DFB-based coherent UDWDM PON with 6.25 GHz spacing and a >40 dB power budget," *IEEE Photon. Technol. Lett.*, vol. 26, no. 2, pp. 107—110, 2014.

[13] M. Artiglia, R. Corsini, M. Presi, F. Bottoni, G. Cossu, and E. Ciaramella, "Coherent systems for low-cost 10 Gb/s optical access networks," *J. Lightw. Technol.*, vol. 33, no. 15, pp. 3338–3344, 2015.

[14] I.N. Cano, A. Lerín, V. Polo, and J. Prat, "Flexible D(Q)PSK 1.25-5 Gb/s UDWDM-PON with directly modulated DFBs and centralized polarization scrambling," in *Proc. ECOC*, 2015, paper Th.1.3.7.

[15] W. Shieh, H. Bao, and Y. Tang, "Coherent optical OFDM: Theory and design," *Optics Express*, vol. 16, no. 2, pp. 841–859, 2008.

[16] W. Shieh and I. Djordjevic, *OFDM for optical communications*, Academic Press, 2009.

[17] S.L. Jansen, I. Morita, T.C. Schenk, N. Takeda, and H. Tanaka, "Coherent optical 25.8-Gb/s OFDM transmission over 4160-km SSMF," *J. Lightw. Technol.*, vol. 26, no. 1, pp. 6–15, 2008.

[18] T.M. Schmidl and D.C. Cox, "Robust frequency and timing synchronization for OFDM," *IEEE Transactions on Communications*, vol. 45, no. 12, pp. 1613–1621, 1997.

[19] J.-J.V. De Beek, O. Edfors, M. Sandell, S.K. Wilson, and P.O. Borjesson, "On channel estimation in OFDM systems," in *IEEE Vehicular Technology Conference*, 1995, vol.2, pp. 815–819.

[20] J. Armstrong, "Analysis of new and existing methods of reducing intercarrier interference due to carrier frequency offset in OFDM," *IEEE Transactions on Communications*, vol. 47, no. 3, pp. 365–369, 1999.

[21] X. Yi, W. Shieh, and Y. Tang, "Phase estimation for coherent optical OFDM," *IEEE Photon. Technol. Lett.*, vol. 19, no. 12, pp. 919–921, 2007.

[22] S.M. Alamouti, "A simple transmit diversity technique for wireless communications," *IEEE Journal on Selected Areas in Communications*, vol. 16, no. 8, pp. 1451–1458, 1998.

[23] E. Meron, A. Andrusier, M. Feder, and M. Shtaif, "Use of space-time coding in coherent polarization-multiplexed systems suffering from polarization-dependent loss," *Optics letters*, vol. 35, no. 21, pp. 3547–3549, 2010.

[24] E. Awwad, Y. Jaouën, and G.R.-B. Othman, "Polarization-time coding for PDL mitigation in long-haul Polmux OFDM systems," *Optics express*, vol. 21, no. 19, pp. 22773–22790, 2013.

[25] S. Mumtaz, G.R.B. Othman, Y. Jaouën, J. Li, S. Koenig, R. Schmogrow, and J. Leuthold, "Alamouti code against PDL in polarization multiplexed systems," in *Proc. Signal Processing in Photonic Communications (SppCom)*, 2011, paper SPTuA2.

[26] T. Pfau, S. Hoffmann, and R. Noé, "Hardware-efficient coherent digital receiver concept with feedforward carrier recovery for M-QAM constellations," *J. Lightw. Technol.*, vol. 27, no. 8, pp. 989–999, 2009.

[27] W.T. Silfvast, *Laser fundamentals*, 2^{nd} edition, Cambridge University Press, New York, 2008.

[28] M.G. Taylor, "Phase estimation methods for optical coherent detection using digital signal processing," *J. Lightw. Technol.*, vol. 27, no. 7, pp. 901–914, 2009.

[29] W. Shieh, X. Yi, and Y. Tang, "Transmission experiment of multi-gigabit coherent optical OFDM systems over 1000 km SSMF fibre," *Electronics Letters*, vol. 43, no. 3, pp. 183–185, 2007.

[30] S.L. Jansen, I. Morita, N. Takeda, and H. Tanaka, "20-Gb/s OFDM transmission over 4,160-km SSMF enabled by RF-pilot tone phase noise compensation," in *Proc. IEEE/OSA Optical Fiber Communication Conference (OFC)*, 2007, paper PDP15.

[31] M.S. Erkılınç, D. Lavery, R. Maher, M. Paskov, B.C. Thomsen, P. Bayvel, R.I. Killey and S.J. Savory, "Polarization-insensitive single balanced photodiode coherent receiver for passive optical networks," in *Proc. IEEE European Conference on Optical Communication (ECOC)*, 2015, paper Th.1.3.3.

Chapter 6

Conclusions and Future Work

Cost-effective and spectrally-efficient optical transceiver architectures for metropolitan and regional links have been extensively studied in this thesis. The prominent results from this study are summarized in section 6.1. Moreover, the issues that can be potentially valuable to investigate in the future are discussed in section 6.2.

6.1 Summary of research

Rapidly increasing bandwidth and data demand in metropolitan links/networks has attracted the optical communications research community to develop and/or improve optical transceivers offering high spectral efficiency with reasonable reach. Among the proposed solutions, polarization- and phase-diverse coherent receivers, that enable multi-level and multi-dimensional modulation formats, such as quadrature amplitude modulation (QAM) with polarization multiplexing, offer the highest achievable bit-rates per channel and information spectral densities (ISDs). Thus, they have become a well-established technology for long-haul communication links. However, it comes at the expense of great complexity. On the other hand, the key requirement for metropolitan links is cost-effectiveness. Such coherent receivers are currently prohibitively expensive and not feasible for such links.

Based on the literature review presented in chapter 3, it was concluded that the complexity of optical transceivers employed in access, metro and regional links should be minimized and designed using low-cost optical components, *e.g.,* low-cost optical modulators and high linewidth ($1 \geq$ MHz) lasers, to meet the budget requirements. Considering rapid cost and performance innovations in silicon complementary metal oxide semiconductor (CMOS) technology, the complexity needs to shift from the optical to the electrical domain. Thus, digital signal processing (DSP) based transceivers employing direct detection receivers, *i.e.,* consisting of only a single-ended photodiode and a single analogue-to-digital converter (ADC), can offer promising and practical solutions for access, metro and regional links. Alternatively, the complexity of the polarization- and phase-diverse coherent receivers need to be simplified such as removing the need for polarization beam splitter (PBS) and 90^{o} optical hybrids.

The performance of two spectrally-efficient subcarrier modulation (SCM) formats, enabled by a DSP-based optical transmitter and direct detection receiver, have been compared in numerical simulations. SSB Nyquist-SCM and single sideband orthogonal frequency division multiplexing (OFDM) (SSB-OFDM) signals with QAM formats were assessed in back-to-back operation and transmission. One of the limiting factors for high information spectral density (ISD) in direct detection compared to

coherent detection links is signal-signal beating interference (SSBI). The signal formats' tolerance to SSBI have been studied, for the first time, in optical communication systems offering ISDs of up to 2 b/s/Hz. It was found that single sideband (SSB) Nyquist-SCM has a higher tolerance to the SSBI, and consequently, its reach is up to double that of SSB-OFDM. Thus, it has the potential to offer the combination of higher ISD, and longer transmission distances with low complexity transceiver design for metro, regional, access and back-haul applications.

Following the comparison in simulations, SSB Nyquist-SCM transmission using a Lithium Niobate ($LiNbO_3$) in-phase and quadrature (IQ)-modulator and offering ISD greater than 1 b/s/Hz has been experimentally demonstrated. Initially, the performance of wavelength division multiplexing (WDM) quadrature phase-shift keying (QPSK) system (11 GHz-spaced 7-channel operating at a bit rate of 14 Gb/s per channel) was assessed. A net optical ISD of 1.2 b/s/Hz was achieved at a transmission distance of 800 km of standard single mode fibre (SSMF). Moreover, employing the same optical transceiver architecture with 16-QAM signalling, the net optical ISD was increased from 1.2 to 2 b/s/Hz (operating at a net bit rate of 24 Gb/s per channel on a 12 GHz channel grid) with a reach of 323 km over SSMF. These reported experimental demonstrations are currently the record achieved ISDs at the given distances amongst the published experimental single polarization WDM demonstrations in direct detection links, as described in chapter 4.

To reduce the optical complexity of the SSB Nyquist-SCM transmitter, the external cavity laser (ECL) and IQ-modulator were replaced with the distributed feedback (DFB) laser and dual-drive Mach-Zehnder modulator (dual-drive MZM). First, in numerical simulations, the impact of the extinction ratio (ER) of the modulators on the optical sideband suppression ratio (OSSR) was investigated for generating spectrally-efficient SSB signals in WDM systems, together with the resulting impact on inter-channel crosstalk penalties. Subsequently, in back-to-back operation, an IQ-modulator with an ER of 30 dB and a dual-drive MZM with an ER of 18 dB were experimentally compared in a 6×25 Gb/s WDM system by varying the channel spacing. It is found out that the channel spacing needs to be increased from 12 GHz to 16 GHz for the optimum performance while using the dual-drive MZM. This is due to the reduced sideband suppression ratio of the dual-drive MZM, causing an increase in linear crosstalk between the neighboring WDM channels at lower channel spacings. Following this comparison, the transmission performance of $LiNbO_3$ and Indium Phosphide (InP) dual-drive MZMs was experimentally assessed using the SSB Nyquist-SCM 16-QAM signal. Their performance was found to be similar. WDM (6ch.×16 GHz-spaced) SSB Nyquist-SCM 16-QAM signal carrying 25 Gb/s per channel was transmitted over 242 km of SSMF at a net optical ISD of 1.46 b/s/Hz, as presented in chapter 4. The achieved transmission distance and net optical ISD, compared to the experiments using the IQ-modulator, reduced from 343 to 242 km of SSMF and 2 to 1.46 b/s/Hz, respectively. Nevertheless, this is the highest achieved ISD reported, at this distance, among the published studies using a dual-drive MZM based transmitter and direct detection receiver.

In contrast to the work on direct detection systems, and to take advantage of the superior performance of coherent detection, a simplified architecture for the polarization- and phase-diverse coherent transceiver has been explored. By employing transmit (polarization) diversity, the complexity of the required coherent receiver was found to be significantly reduced. Sending two consecutive symbols on two orthogonal polarization modes with Alamouti polarization-time block coding (PTBC), the receiver is able to detect the signal without the need for polarization tracking. The PBS used in conventional co-

herent receivers can be removed. In addition, by utilizing heterodyne detection, the 90° optical hybrids can be replaced by a simple 3 dB coupler, and the number of balanced photodetectors (BPDs) can be reduced from four to one. Consequently, a polarization-insensitive phase-diverse coherent receiver using Alamouti polarization-time block coding (PTBC) combined with heterodyne reception was realized using only a single 3 dB coupler and a single BPD, as discussed in chapter 5. Following the implementation of the polarization insensitive (PI) (simplified) coherent receiver, its performance was compared with the direct detection receiver. As expected, the coherent receiver starts offering significant required optical signal-to-noise ratio (OSNR) performance gain when M-QAM schemes are considered where $M \geq 16$. However, two transmitters, one for each polarization, are required to achieve the polarization independence. Such a receiver architecture is attractive and can be promising particularly for long-reach passive optical networks (LR-PONs) since the optical line terminal unit (transmitter side) may have high complexity whereas the optical network unit at the customer premises (receiver side) has to be quite simplified.

To sum up, the key achievements presented in this thesis are

- Generation and detection, for the first time, of spectrally-efficient SSB Nyquist pulse-shaped QPSK subcarrier modulation (SCM) using an IQ-modulator in direct detection (DD) links [16].
- Single channel transmission of Nyquist pulse-shaped QPSK SCM utilizing electronic pre-distortion in DD links [17].
- First experimental demonstration of WDM Nyquist pulse-shaped QPSK SCM transmission, achieving the highest net optical ISD of 1.2 b/s/Hz at a given distance among the reported WDM direct detection experiments [22].
- The first investigation of signal waveform symmetric clipping effect on the performance of dispersion-precompensated Nyquist pulse-shaped QPSK SCM in uncompensated DD links [6].
- First assessment of Nyquist-SCM and OFDM signal formats' tolerance to signal-signal beating interference, resulting from square-law detection [15].
- Generation, transmission and detection, for the first time, of SSB Nyquist pulse-shaped QPSK and 16-QAM SCM using a dual-drive MZM in DD links including a performance comparison between an ECL and DFB laser [21].
- Experimental demonstration, for the first time, of WDM SSB Nyquist pulse-shaped 16-QAM SCM using an IQ-modulator and achieving a record net optical ISD of 2 b/s/Hz at a given distance in DD links [21].
- First theoretical investigation and experimental evaluation, supported by numerical simulations, of the impact of the finite extinction ratio of a modulator, *i.e.,* $LiNbO_3$ IQ- or dual-drive MZ (DD-MZ) modulator, in relation to the optical sideband suppression in SSB signal generation, and the resulting crosstalk between neighboring WDM channels. Following this work, the first experimental demonstration of WDM SSB Nyquist pulse-shaped 16-QAM SCM signal, achieving a record net ISD of 1.5 b/s/Hz using a dual-drive MZM based transmitter [23].

- Experimental demonstration of WDM SSB Nyquist pulse-shaped 16-QAM SCM transmission using an InP-based tunable transmitter assembly (TTA), consisting of a wideband tunable digital supermode distributed Bragg reflector (DS-DBR) laser and an InP dual-drive Mach-Zehnder modulator (MZM) [25]. All the aforementioned studies were discussed in chapter 4.
- Implementation and experimental demonstration of the PI coherent receiver, consisting of a single BPD with a single ADC, without the need for a PBS or 90^{o} optical hybrids, [26, 31] (For the corresponding results, see chapter 5.)

Nonetheless, the aforementioned studies in this thesis can be still improved. Alternatively, they can be considered for modified/different system configurations. In this regard, suggestions for potential future research for improvements/different considerations are discussed in the following section.

6.2 Future work

Despite all the work presented in this thesis, there are still open questions concerning the achievable performance (transmission distance and ISD) of direct detection (single-ended photodiode) systems employing DSP-based transceivers and PI coherent receiver systems. Some potential research areas are briefly described as follows:

6.2.1 Transceiver-based SSBI estimation/cancellation techniques for SCM schemes

The performance of both OFDM and Nyquist-SCM formats is significantly degraded by the SSBI due to the square-law detection. The detailed literature review regarding SSBI mitigation techniques is already given in section 3.1.4.1. Optical-based mitigation schemes result in increased complexity of the receiver optical hardware [1, 2]. Therefore, DSP-based mitigation schemes appear more promising. The DSP-based methods can be divided into two groups, digital pre- or post-compensation. Digital pre-compensation takes place at the transmitter, but, it leads to an increased peak-to-average-power ratio (PAPR) and imperfect SSBI mitigation due to the extra ("unwanted") beat products after square-law detection [3,4]. On the other hand, digital post-compensation, a receiver-based mitigation scheme, causes significant increase in DSP complexity due to the iterative estimation and cancellation [5–7].

To deal with these drawbacks, it is also possible to share the DSP complexity between the transmitter and receiver. In other words, it can be mitigated both at the transmitter and receiver end to allocate the resources more efficiently. The signal can be pre-distorted and transmitted over the fibre in order to cancel some of the signal-signal mixing products. The PAPR of the driving signals and extra beating products at the receiver due to the pre-distortion are the main parameters that need to be optimized. Following the detection, the iterative estimation/cancellation scheme can be used with a minimum number of iterations. In the previous works, four iterations were found to be the optimum. Thus, the ultimate goal is to reduce it to a single iteration. Such SSBI compensation scheme can be used both for SSB Nyquist-SCM and SSB-OFDM.

6.2.2 Simulations of a 1 Tb/s (10$\lambda \times$100 Gb/s) for metropolitan links

The next generation optical transceivers will be required to achieve 1 Tb/s utilizing superchannel configuration which consists of, for example, 10 wavelength channels operating at 100 Gb/s per channel

(λ). Assuming the use of Nyquist-SCM 16-QAM signal format operating at $\geq$25 GBaud, two digital-to-analogue converters (DACs) with a sampling rate of $\geq$50 GSa/s (2 samples-per-symbol) are required to achieve 100 Gb/s per λ. However, currently, the experimental complexity is beyond the capabilities of our available lab instruments. Therefore, it can be explored in numerical simulations to find out the maximum achievable transmission distance at given channel spacings. These two parameters are inversely proportional to each other. For instance, although dense channel spacing increases the ISD, the signal quality degrades due to the linear crosstalk between the neighboring channels and fibre nonlinearities which can cause a significant reduction in transmission distance. Or, coarse channel spacing can yield excellent transmission margins, however, very low ISD.

To implement such systems, SSB Nyquist-SCM or SSB-OFDM can be utilized, as they are shown to be one of the most spectrally-efficient signalling techniques. SSB signalling demonstrated in this thesis is achieved using a dual-input optical vector modulator, *e.g.,* IQ-modulator or dual-drive MZM modulator which requires two DACs. However, SSB signals can also be generated utilizing (tight) optical filtering using a single DAC which can potentially reduce the complexity of the transmitter, referred to as vestigial sideband (VSB) signalling. Recently, it has been coupled with discrete multi-tone (DMT) and the transmission over 242 km of SSMF has been demonstrated at an ISD of 1.12 b/s/Hz [8]. Therefore, VSB signalling is worth being investigated for the Nyquist-SCM signal format. As an alternative to SCM formats, carrierless amplitude/phase modulation (CAP) modulation scheme is shown to be a promising spectrally-efficient format for cost-effective links. However, it has been only demonstrated for (ultra) short links [9–11]. Thus, it might be attractive to explore for medium-haul metro and regional links. All these modulation formats that can be recovered in direct detection links can be combined with a SSBI mitigation scheme, such as the one described in the previous section (section 6.2.1).

6.2.3 Polarization-insensitive (simplified) coherent receiver for LR-PONs

The transmission performance of the PI coherent receiver, described in chapter 5, can be assessed in ultra-dense WDM passive optical networks (PONs) to quantify the number of users that can use the network. Due to its high receiver sensitivity, a splitting ratio of 1:128, 1:256 or even 1:512 might be possible over an unamplified link with a length of up to 120 km [12]. Moreover, the linewidth tolerance of the receiver can be increased so that a relatively cheaper laser with a linewidth of 3 to 5 MHz can be used as a local oscillator (LO) laser at the receiver side. Last but not least, the PI coherent receiver can be implemented using a single-ended photodiode instead of using a BPD, making the receiver complexity almost identical to the direct detection receiver. In this scenario, the signal-signal beating interference (SSBI) distorts the signal. Therefore, common mode rejection ratio (CMRR) needs to be quantified to calculate the expected penalty, followed by its demonstration to measure the system performance.

6.3 References

[1] S.A. Nezamalhosseini, L.R. Chen, Q. Zhuge, M. Malekiha, F. Marvasti, and D.V. Plant, "Theoretical and experimental investigation of direct detection optical OFDM transmission using beat interference cancellation receiver," *Optics Express*, vol. 21, no. 13, pp. 15237–15246, 2013.

[2] J. Ma, "Simple signal-to-signal beat interference cancellation receiver based on balanced detection for a single-sideband optical OFDM signal with a reduced guard band," *Optics Letters*, vol. 38, no. 21, pp. 4335–4338, 2013.

[3] C. Sánchez, B. Ortega, and J. Capmany, "System performance enhancement with pre-distorted OOFDM signal waveforms in DM/DD systems," *Optics Express*, vol. 22, no. 6, pp. 7269–7283, 2014.

[4] C. Ju, X. Chen, N. Liu, and L. Wang, "SSII cancellation in 40Gbps VSB-IMDD OFDM system based on symbol pre-distortion," in *Proc. IEEE European Conference on Optical Communication (ECOC)*, 2014, paper P.7.9.

[5] W.-R. Peng, X. Wu, K.-M. Feng, V. R. Arbab, B. Shamee, J.-Y. Yang, L.C. Christen, A.E. Willner, and S. Chi, "Spectrally efficient direct-detected OFDM transmission employing an iterative estimation and cancellation technique," *Optics express*, vol. 17, no. 11, pp. 9099–9111, 2009.

[6] W.-R. Peng, B. Zhang, K.-M. Feng, X. Wu, A.E. Willner, and S. Chi, "Spectrally efficient direct-detected OFDM transmission incorporating a tunable frequency gap and an iterative detection techniques," *J. Lightw. Technol.*, vol. 27, no. 24, pp. 5723–5735, 2009.

[7] Z. Li, M. S. Erkilinc, S. Pachnicke, H. Griesser, R. Bouziane, B. C. Thomsen, P. Bayvel, and R. I. Killey, "Signal-signal beat interference cancellation in spectrally-efficient WDM direct-detection Nyquist-pulse-shaped 16-QAM subcarrier modulation," *Optics Express*, vol. 23, no. 18, pp. 23694–23709, 2015.

[8] A. Dochhan, H. Grieser, M. Eiselt, and J.-P. Elbers, "Flexible bandwidth 448 Gb/s DMT transmission for next generation data center inter-connects," in *Proc. IEEE European Conference on Optical Communication (ECOC)*, 2014, paper P.4.10.

[9] J. Wei, J. Ingham, D. Cunningham, R. Penty, and I. White, "Performance and power dissipation comparisons between 28 Gb/s NRZ, PAM, CAP, and optical OFDM systems for data communication applications," *J. Lightw. Technol.*, vol. 30, no. 20, pp. 3273–3280, 2012.

[10] J. Wei, L. Geng, D. G. Cunningham, R.V. Penty, and I. White, "100 Gigabit ethernet transmission enabled by carrierless amplitude and phase modulation using QAM receivers," in *Proc. IEEE/OSA Optical Fiber Communication Conference (OFC)*, 2013, paper OW4A.5.

[11] J.D. Ingham, R. Penty, I. White, and D. Cunningham, "40 Gb/s carrierless amplitude and phase modulation for low-cost optical datacommunication links," in *Proc. IEEE/OSA Optical Fiber Communication Conference (OFC)*, 2011, paper CThC5.

[12] D. Lavery, M. Ionescu, S. Makovejs, E. Torrengo, and S. J. Savory, "A long-reach ultra-dense 10 Gbit/s WDM-PON using a digital coherent receiver," *Optics express*, vol. 18, no. 25, pp. 25855–25860, 2010.

ACRONYMS

ADC	analogue-to-digital converter
ADPSK	amplitude DPSK
AMO-OFDM	adaptively modulated optical OFDM
AOM	acousto-optical modulator
APSK	amplitude- and phase-shift keying
ASE	amplified spontaneous emission
ASK	amplitude-shift keying
AWG	arrayed waveguide grating
AWG	arbitrary waveform generator
AWGN	additive white Gaussian noise
BER	bit error rate
BPD	balanced photodetector
CAGR	compound annual growth rate
CAP	carrierless amplitude/phase modulation
CD	chromatic dispersion
CMA	constant modulus algorithm
CMOS	complementary metal oxide semiconductor
CMRR	common mode rejection ratio
CO-OFDM	coherent OFDM
CP	cyclic prefix
CSPR	optical carrier-to-signal power ratio

cSSB compatible SSB

CS-RZ carrier-suppressed RZ

CW continuous wave

DAC digital-to-analogue converter

DBPSK differential binary phase-shift keying

DCF dispersion compensating fibre

DD direct detection

DDO-OFDM direct detection optical OFDM

DD-MZ dual-drive MZ

dual-drive MZM dual-drive Mach-Zehnder modulator

DFB distributed feedback

DFT discrete Fourier transform

DLI delay-line interferometer

DMT discrete multi-tone

DP dual-polarization

DPSK differential phase-shift keying

DQP differential quadrature phase

DQPSK differential quadrature phase-shift keying

DSB double sideband

DSP digital signal processing

DSF dispersion shifted fibre

DS-DBR digital supermode distributed Bragg reflector

DWDM dense wavelength-division multiplexing

D6PSK differential 6-ary phase-shift keying

D8PSK differential 8-ary phase-shift keying

D16PSK differential 16-ary phase-shift keying

ECL external cavity laser

EDC electronic dispersion compensation

EDFA Erbium-doped fibre amplifier

ENOB effective number of bits

EPD electronic pre-distortion

ER extinction ratio

FBG fibre Bragg grating

FEC forward error correction

FFT fast Fourier transform

FIR finite impulse response

FO frequency offset

FPGA field programmable gate array

FT Fourier transform

FTTx Fibre to the Node, Curb, Building or Home

FWM four-wave mixing

GVD group-velocity dispersion

HC-SCM half-cycle subcarrier modulation

HD-FEC hard-decision forward error correction

HT Hilbert transform

I in-phase

ICI inter-channel interference

IDFT inverse discrete Fourier transform

IF intermediate frequency

IFFT inverse fast Fourier transform

IM intensity modulation

InP Indium Phosphide

IP Internet protocol

IQ in-phase and quadrature

ISD information spectral density

ISDs information spectral densities

ISI	inter-symbol interference
ITU	International Telecommunication Union
$LiNbO_3$	Lithium Niobate
LMS	least mean squares
LO	local oscillator
LPF	low-pass filter
LR-PON	long-reach passive optical network
MIMO	*multi-input-multi-output*
MISO	*multi-input-single-output*
MLSE	maximum likelihood sequence estimation
MSM	multiple subcarrier modulation
MZM	Mach-Zehnder modulator
NLSE	nonlinear Schrödinger equation
NRZ	non-return-to-zero
OBPF	optical band-pass filter
OCG	optical comb generator
ODC	optical dispersion compensation
OFDM	orthogonal frequency division multiplexing
OOK	on-off keying
OSA	optical spectrum analyzer
OSNR	optical signal-to-noise ratio
OSSR	optical sideband suppression ratio
PAM	pulse amplitude modulation
PAPR	peak-to-average-power ratio
PBS	polarization beam splitter
PD	photodetector
PDL	polarization dependent loss
PI	polarization insensitive

PM	phase modulator
PMD	polarization mode dispersion
PNC	phase noise compensation
PON	passive optical network
PRBS	pseudo-random binary sequence
PS	polarization scrambler
PSBT	phase-shaped binary transmission
PSK	phase-shift keying
PTBC	polarization-time block coding
Q	quadrature
QAM	quadrature amplitude modulation
QASK	quaternary amplitude-shift keying (ASK)
QPSK	quadrature phase-shift keying
RAM	random-access memory
RC	raised cosine
RDE	radius directed equalization
RRC	root raised cosine
RZ	return-to-zero
SC-SCM	single-cycle subcarrier modulation
SCM	subcarrier modulation
SNR	signal-to-noise ratio
SoP	state of polarization
SP	single polarization
SPM	self-phase modulation
SRRC	square-root raised cosine
SSB	single sideband
SSBI	signal-signal beating interference
SSB-OFDM	single sideband OFDM

SSMF standard single mode fibre

TIA trans-impedance amplifier

ToD third-order dispersion

TTA tunable transmitter assembly

VOA variable optical attenuator

VSB vestigial sideband

WDM wavelength division multiplexing

XPM cross-phase modulation